Electrochemical Micromachining of Aluminium for Microfluidic Devices

Tobias Baldhoff
Department of Chemical and Process Engineering

A thesis submitted in partial fulfilment of
the requirements for the degree of
Doctor of Philosophy

University of Canterbury
Christchurch, New Zealand
November 2018

Acknowledgements

This work was carried out from March 2015 to June 2018 at the Department of Chemical and Process Engineering (CAPE) and at the Nanofabrication Laboratory within the Department of Electrical and Computer Engineering at the University of Canterbury (UC) in Christchurch, New Zealand. It was made feasible by financial support in the form of a UC Doctoral Scholarship and a UC Meadow Mushrooms Postgraduate Scholarship, which is gratefully acknowledged.

It is a pleasure to thank those who made this thesis possible, first and foremost my supervisory team. I would like to express my sincere gratitude to my senior supervisor, Dr Aaron Marshall, for his conception of the original idea for this project, for his unfailing support throughout my PhD study, for his encouragement, enthusiasm, and experience. I would also like to thank my co-supervisor, Dr Volker Nock, for introducing me to the Nano Lab, its facilities and people, for his expert advice on all things micro and nano, for his many ideas, suggestions and criticisms. Their guidance was an immense help throughout all stages of this project, and I could not have imagined having a better team of mentors for my PhD study.

I am indebted to all CAPE staff for their assistance, knowledge and patience, which helped me negotiate all obstacles on the practical side of research successfully, in particular Stephen Beuzenberg, Graham Furniss, Tim Moore, Michael Sandridge and Glenn Wilson. Special thanks go to Graham Mitchell for expertly machining all sorts of parts, often on extremely short notice. I would also like to thank Ranee Hearst and Joanne Pollard for helping me with all the paperwork.

Many of the UC staff outside of CAPE have made their support available in one form or another, for which I am very grateful: to Gary Turner and Helen Devereux for keeping the Nanofabrication Laboratory running and for their abiding advice and assistance, to Mike Flaws for his support with SEM imaging and EDXS analysis, to Robert McGregor for the skilled execution of vitreous designs, to Assoc Prof Mathieu Sellier for helpful discussions on COMSOL, to Prof Roger Reeves and to Kevin Stobbs for offering access to polishing equipment and supplies, as well as to Clifford Franklin for a long-term loan of several laboratory power supplies.

Outside of UC, I am grateful to both Prof Cather Simpson from the University of Auckland and to Dr Natalie Plank from Victoria University of Wellington for enabling my visits and for access to equipment and facilities on site.

Finally, my thanks go to present and former colleagues within CAPE, which made my stay here so memorable. In particular, Dr Jared Steven and the late Dr Calvin Lim have earned my gratitude for helping me get my bearings.

Abstract

Through-mask electrochemical micromachining (TMEMM) combines photolithographic masking with anodic metal dissolution and thus enables the mass fabrication of microfluidic devices made from metals. To achieve an even removal rate and surface finish, a uniform current distribution is required, which is influenced by mass-transfer effects, surface-film formation, and the mask-opening geometry. This complex interplay was studied, with the aim of machining microchannel plate-inlays for a plate-type microreactor design, with aluminium acting as the anode and phosphoric acid serving as the electrolyte.

This metal/electrolyte system was first characterised in terms of surface-film formation via an extensive electrochemical impedance spectroscopy study. A shape-evolution model based on diffusive mass-transfer was then developed for comparison with experimental shape profiles. Thereafter, micromachining experiments were conducted under potentiostatic control in a custom-built batch cell using rotating discs and stationary plates, while varying the hydrodynamic conditions, and thus the conditions of mass transfer.

Analysis of this data confirmed the presence of a compact, barrier-type alumina film along the anode surface, the thickness of which was on the order of a few nanometres only and solely depended on the applied anode potential. Uniform film coverage and thickness ensued, resulting in an even surface finish with sub-micrometre surface roughness. The model agreed well with experimental results in regards to channel depth, width and profile, thereby correctly representing the shape-evolution process in quiescent electrolyte. Deviations occurred at high anode potentials due to concurrent oxygen evolution, as well as in agitated electrolyte due to mass-transfer effects. These effects were shown to manifest themselves in different forms depending on the mask-opening size: in the presence of shearing flow, the shape profiles of individual microchannels became displaced and distorted, whereas larger cavities exhibited wedging, that is a decrease in the removal rate in flow direction. As a result, sufficient control of flow conditions and anode potential was identified as a key factor in enabling the machining of well-defined microfluidic devices into aluminium.

Based on this work, it is recommended that TMEMM of microfluidic devices proceeds via through-foil etching of thin metal shims, thus following a stacked-shim assembly for the device design. Also, impinging rather than shearing flow should be used during TMEMM. In this manner, non-uniform channel and cavity dimensions could be minimised. Future work should investigate the commercial viability of TMEMM and focus on the use of difficult-to-etch metals. In addition, preliminary work on the formation of catalytic wall coatings made from Au/Al_2O_3 via electrochemical means should be pursued further.

Deputy Vice-Chancellor's Office
Postgraduate Office

UNIVERSITY OF CANTERBURY
Te Whare Wānanga o Waitaha
CHRISTCHURCH NEW ZEALAND

Co-Authorship Form

This form is to accompany the submission of any thesis that contains research reported in co-authored work that has been published, accepted for publication, or submitted for publication. A copy of this form should be included for each co-authored work that is included in the thesis. Completed forms should be included at the front (after the thesis abstract) of each copy of the thesis submitted for examination and library deposit.

Please indicate the chapter/section/pages of this thesis that are extracted from co-authored work and provide details of the publication or submission from which the extract comes:
Chapter 3 has been accepted for publication in extended form: Baldhoff, T.; Nock, V.; Marshall, A. T. Through-Mask Electrochemical Micromachining: A Review. *J. Electrochem. Soc.*, in press.

Please detail the nature and extent (%) of contribution by the candidate:
90 % of drafting and writing the paper were performed by the candidate. 100 % of all figures (with the exception of copyright material) were designed by the candidate.

Certification by Co-authors:
If there is more than one co-author then a single co-author can sign on behalf of all. The undersigned certifys that:

- The above statement correctly reflects the nature and extent of the PhD candidate's contribution to this co-authored work.
- In cases where the candidate was the lead author of the co-authored work he or she wrote the text.

Name: Volker Nock	Signature: Volker Nock	Date: 8 November 2018

Deputy Vice-Chancellor's Office
Postgraduate Office

UNIVERSITY OF CANTERBURY
Te Whare Wānanga o Waitaha
CHRISTCHURCH NEW ZEALAND

Co-Authorship Form

This form is to accompany the submission of any thesis that contains research reported in co-authored work that has been published, accepted for publication, or submitted for publication. A copy of this form should be included for each co-authored work that is included in the thesis. Completed forms should be included at the front (after the thesis abstract) of each copy of the thesis submitted for examination and library deposit.

Please indicate the chapter/section/pages of this thesis that are extracted from co-authored work and provide details of the publication or submission from which the extract comes:

Chapter 5 is a reproduction of the publication:
Baldhoff, T.; Marshall, A. T. Characterization of Surface Films Formed on Aluminum during Mass-Transfer Limited Anodic Dissolution in Phosphoric Acid. *J. Electrochem. Soc.* **2017**, 164, C46-C53.

Please detail the nature and extent (%) of contribution by the candidate:

90 % of designing the experiments, discussing the results, and writing the paper were performed by the candidate. 100 % of the experimental work and the data analysis were done by the candidate.

Certification by Co-authors:
If there is more than one co-author then a single co-author can sign on behalf of all. The undersigned certifys that:

- The above statement correctly reflects the nature and extent of the PhD candidate's contribution to this co-authored work.
- In cases where the candidate was the lead author of the co-authored work he or she wrote the text.

Name: Aaron Marshall Signature: AMarshall Date: 29 May 2018

Deputy Vice-Chancellor's Office
Postgraduate Office

UNIVERSITY OF CANTERBURY
Te Whare Wānanga o Waitaha
CHRISTCHURCH NEW ZEALAND

Co-Authorship Form

This form is to accompany the submission of any thesis that contains research reported in co-authored work that has been published, accepted for publication, or submitted for publication. A copy of this form should be included for each co-authored work that is included in the thesis. Completed forms should be included at the front (after the thesis abstract) of each copy of the thesis submitted for examination and library deposit.

Please indicate the chapter/section/pages of this thesis that are extracted from co-authored work and provide details of the publication or submission from which the extract comes:

Chapter 7 is a reproduction of the publication:
Baldhoff, T.; Nock, V.; Marshall, A. T. Through-Mask Electrochemical Micromachining of Aluminum in Phosphoric Acid. *J. Electrochem. Soc.* **2017**, 164, E194-E202.

Please detail the nature and extent (%) of contribution by the candidate:

90 % of designing the experiments, discussing the results, and writing the paper were performed by the candidate. 100 % of the experimental work and the data analysis were done by the candidate.

Certification by Co-authors:
If there is more than one co-author then a single co-author can sign on behalf of all. The undersigned certifys that:

- The above statement correctly reflects the nature and extent of the PhD candidate's contribution to this co-authored work.
- In cases where the candidate was the lead author of the co-authored work he or she wrote the text.

Name: Aaron Marshall Signature: AMarshall Date: 29 May 2018

Contents

List of Abbreviations

AC	Alternating current
Avg.	Average
BEM	Boundary element method
CNLS	Complex non-linear least squares
CPE	Constant-phase element
CTAB	Cetyltrimethylammonium bromide
DC	Direct current
DI	De-ionised
ECM	Electrochemical machining
EDM	Electrical discharge machining
EDXS	Energy-dispersive x-ray spectroscopy
EIS	Electrochemical impedance spectroscopy
EMM	Electrochemical micromachining
EP	Electropolishing
FEM	Finite element method
IPA	Isopropyl alcohol
LBM	Laser beam machining
OFLL	Oxide film laser lithography
PCM	Photochemical machining
PDMS	Polydimethylsiloxane
PP	Polypropylene
PTFE	Polytetrafluoroethylene
RCE	Rotating cylinder electrode
RDE	Rotating disc electrode
Ref.	Reference
RMS	Root mean square

SDS	Sodium dodecyl sulphate
SEM	Scanning electron microscopy
SHE	Standard hydrogen electrode
Temp.	Temperature
TMEMM	Through-mask electrochemical micromachining
UV	Ultraviolet

List of Symbols

$\mathbf{A}$	Matrix corresponding to the second derivative of the objective function containing elements $A_{\ell,m}$, see Equations 2.26 to 2.28
a	Half-jump distance (cm)
$\mathbf{B}$	Vector corresponding to the first derivative of the objective function containing elements B_m, see Equations 2.26 to 2.28
b	Half-distance between mask openings (cm)
C	Capacitance ($\mathrm{F\,cm^{-2}}$)
C_{dl}	Double-layer capacitance ($\mathrm{F\,cm^{-2}}$)
C_{b}	Barrier-film capacitance ($\mathrm{F\,cm^{-2}}$)
C_0	Faradaic pseudo-capacitance ($\mathrm{F\,cm^{-2}}$)
c	Concentration ($\mathrm{mol\,cm^{-3}}$)
$\hat{c}^{(k)}, \hat{c}^{(N+k)}$	Concentration at the k-th and the $(N+k)$-th node point, see Equation 6.10 ($\mathrm{mol\,cm^{-3}}$)
$\hat{c}_{\mathrm{n}}^{(k)}, \hat{c}_{\mathrm{n}}^{(N+k)}$	Concentration gradient at the k-th and the $(N+k)$-th node point, see Equation 6.11 ($\mathrm{mol\,cm^{-4}}$)
D	Diffusion coefficient ($\mathrm{cm^2\,s^{-1}}$)
d	Maximum etch depth (cm)
d'	Metal-substrate thickness (cm)
d_{b}	Barrier-film thickness (cm)
E	Electrode potential, corrected for the ohmic drop (V)
$E_{\mathrm{Ag\|AgCl}}$	Electrode potential of the Ag|AgCl reference (V)
E_{appl}	Applied electrode potential, $E_{\mathrm{appl}} = E + iR_{\mathrm{s}}$ (V)
E_{F}	Electric-field strength ($\mathrm{V\,cm^{-1}}$)
F	Faraday constant ($96\,485\,\mathrm{C\,mol^{-1}}$)
$F_1^{(k)}, F_2^{(k)}, F_3^{(k)}, F_4^{(k)}$	Line integrals in Equation 6.12
f	Frequency (Hz)

h	Mask thickness (cm)
I	Current (A)
i	Current density ($\mathrm{A\,cm^{-2}}$)
$\bar{i}$	Average current density ($\mathrm{A\,cm^{-2}}$)
i_{L}	Limiting current density ($\mathrm{A\,cm^{-2}}$)
i_{n}	Normal current density ($\mathrm{A\,cm^{-2}}$)
j	Imaginary number
k, ℓ, m	Indices
L	Inductance ($\mathrm{H\,cm^{-2}}$)
L_{c}	Cabling inductance ($\mathrm{H\,cm^{-2}}$)
L_{sc}	Inductance related to the negative surface charge ($\mathrm{H\,cm^{-2}}$)
l	Characteristic length scale (cm)
M	Molecular weight ($\mathrm{g\,mol^{-1}}$)
N	Number of straight line elements
N_{A}	Pre-exponential factor in Equation 5.1 ($\mathrm{A\,cm^{-2}}$)
N_{B}	Parameter in Equation 5.1 ($\mathrm{cm\,V^{-1}}$)
N_{EF}	Etch factor (dimensionless)
N_{f}	Number of frequencies
N_{L}	Factor in Equation 2.19 (dimensionless)
N_{Pe}	Péclet number, $N_{\mathrm{Pe}} = ul/D$ (dimensionless)
N_{p}	Number of parameters
N_{Ra}	Rayleigh number, $N_{\mathrm{Ra}} = a_{\mathrm{c}}\beta(\Delta c)l^3/\nu D$ (dimensionless)
N_{Re}	Reynolds number, $N_{\mathrm{Re}} = \rho ul/\mu$ (dimensionless)
n	Normal coordinate in Cartesian coordinate system (cm)
$\mathbf{n}$	Unit normal vector, $\mathbf{n} = (n_{\mathrm{x}}, n_{\mathrm{y}})$
O	Objective function, see Equation 2.20
$\mathbf{P}$	Parameter vector for regression analysis containing elements P_ℓ or P_m, see Equation 2.20
$\mathbf{P}_0$	Vector of parameter estimates for regression analysis, see Equations 2.22 and 2.23
$\mathbf{\Delta P}$	Parameter vector for regression analysis containing elements ΔP_ℓ or ΔP_m, see Equations 2.22 and 2.23

R	Universal gas constant ($8.3145\,\mathrm{J\,mol^{-1}\,K^{-1}}$)
R_b	Resistance to vacancy movement ($\Omega\,\mathrm{cm}^2$)
R_ct	Charge-transfer resistance ($\Omega\,\mathrm{cm}^2$)
R_sc	Resistance related to the negative surface charge ($\Omega\,\mathrm{cm}^2$)
R_s	Solution resistance ($\Omega\,\mathrm{cm}^2$)
R_Ω	Electrical resistance ($\Omega\,\mathrm{cm}^2$)
r	Radial coordinate (cm)
r_0	Disc radius (cm)
S	Capture cross-section for positive defects ($\mathrm{cm}^2\,\mathrm{C}^{-1}$)
s	Arc length coordinate along the boundary Π (cm)
s_m	Arc length of the exposed metal surface (cm)
T	Absolute temperature (K)
t	Time (s)
u	Flow velocity ($\mathrm{cm\,s^{-1}}$)
V_ox	Molar volume of the oxide ($\mathrm{cm}^3\,\mathrm{mol}^{-1}$)
$\mathbf{v}$	Vector of displacement rates of the boundary ($\mathrm{cm\,s^{-1}}$)
w	Initial mask-opening half-width (cm)
w'	Final etch half-width (cm)
x, y, z	Cartesian coordinates (cm)
$x^{(k)}$	X-coordinate of the k-th boundary point (cm)
x_d	Characteristic length scale for diffusion (cm)
x_u	Undercut (cm)
$y^{(k)}$	Y-coordinate of the k-th boundary point (cm)
Z	Impedance ($\Omega\,\mathrm{cm}^2$)
$Z_\mathrm{Re}, Z_\mathrm{Im}$	Real and imaginary part of the impedance ($\Omega\,\mathrm{cm}^2$)
$\tilde{Z}_\mathrm{Re}, \tilde{Z}_\mathrm{Im}$	Real and imaginary part of the impedance model ($\Omega\,\mathrm{cm}^2$)
$\lvert Z \rvert$	Modulus of the impedance ($\Omega\,\mathrm{cm}^2$)
z_e	Charge-transfer number (dimensionless)
z_ox	Moles of electrons consumed per mole of oxide (dimensionless)
α	Polarisability of the film/solution interface (dimensionless)
Γ	Fundamental solution to the Laplace equation, see Equations 6.8 and 6.9

δ	Diffusion-layer thickness (cm)
ε_b	Barrier-film permittivity ($\mathrm{F\,cm^{-1}}$)
ε_0	Free-space permittivity ($\mathrm{F\,cm^{-1}}$)
$\eta^{(k)}, \eta^{(N+k)}$	Y-coordinate of the k-th and the $(N+k)$-th node point (cm)
η_ox	Current efficiency for film formation (dimensionless)
κ	Electrolyte conductivity ($\mathrm{S\,cm^{-1}}$)
$\lambda^{(k)}$	Length of the k-th straight line element (cm)
μ	Dynamic viscosity ($\mathrm{g\,cm^{-1}\,s^{-1}}$)
ν	Kinematic viscosity ($\mathrm{cm^2\,s^{-1}}$)
ξ, η	Cartesian coordinates of an arbitrary point along the boundary, see Figure 6.4 (cm)
$\xi^{(k)}, \xi^{(N+k)}$	X-coordinate of the k-th and the $(N+k)$-th node point (cm)
Π	Boundary, see Figure 6.4
$\Pi^{(k)}$	Element k of the boundary
ρ	Density ($\mathrm{g\,cm^{-3}}$)
$\boldsymbol{\sigma}$	Vector of weights for regression analysis containing elements σ_k, see Equation 2.20
τ	Factor in Equations 6.10 and 6.11 (dimensionless)
ϕ	Phase angle (°)
ϕ_c	Cavity wall angle (°)
ϕ_m	Mask wall angle (°)
χ^2	Chi-squared statistic
Ω	Rotation rate (rpm)
ω	Angular frequency ($\mathrm{rad\,s^{-1}}$)
$\boldsymbol{\omega}$	Vector of angular frequencies for regression analysis containing elements ω_k, see Equation 2.20

1 Introduction

1.1 Microreactors and mass fabrication

Gas-phase microreactors have been the focus of much research related to their use for the distributed and decentralised production of chemicals and electricity [1]. These reactors possess internal dimensions on the order of 50–500 µm, resulting in compact reactor designs about 1–10 cm in size [2]. Areas of application include the production of hydrogen-rich synthesis gas from fuels (steam reforming), CO removal from fuel-cell feedstocks (Water-Gas-Shift reaction, preferential CO oxidation), and the synthesis of hydrocarbons (Fischer-Tropsch reaction), methanol, dimethyl ether, and ethanol. Microreactor technology, therefore, is key in enabling mobile, on-demand fuel production and power generation [3].

From the vantage point of chemists and chemical engineers, conducting reactions via heterogeneous gas-phase catalysis within a microreactor has several important advantages [4]. Due to their small characteristic dimensions, the driving forces for heat and mass transfer increase by several orders of magnitude. This allows more precise temperature control and prevents hot-spot formation, leading in turn to higher selectivity towards the desired reaction products. Operation at high temperatures and pressures, for example within the explosive region, is intrinsically safe, because flame propagation is inhibited at small length scales [5]. Not only does process safety improve, but overall conversion from reactants to products also increases. Based on their small internal volume, microreactors also offer opportunities for swift process development and optimisation. Examples for this are rapid screening of catalysts and testing of process conditions. Thus, microreactor technology emerges as a promising tool for the chemical process industry.

The widespread use of microreactors is intimately linked to the scalability of current microfabrication methods. This is because microreactor technology has a high investment cost [6], that is unless methods of mass fabrication are employed [7]. For gas-phase microreactors made from metals, these methods encompass etching, punching, rolling, embossing and injection moulding [2]. These processes permit

the continuous fabrication of thousands of devices at low cost. Nonetheless, existing and novel microfabrication methods, with a particular focus on mass fabrication, are improved and developed continuously.

1.2 Opportunities and challenges

The combination of lithography and electrochemistry presents a promising opportunity for the large-scale production of microreactors. This is because processes, which are well-established within the microelectronics industry — like photolithography, electrochemical etching and plating — are expected to enable the low-cost mass fabrication of such devices [8]. Therein, both plating and etching processes start with covering the substrate with an insulating mask, a patterned thin-film, which is formed via lithography (Figure 1.1). Subsequently, material is either added or removed through the mask openings using electrochemical deposition or dissolution, respectively, and the mask is stripped afterwards. In this way, a pattern of micrometre-sized structures is transferred onto the substrate.

Both processes differ in their applicability. Combining lithography with electroplating is known under the German acronym LIGA (Lithographie, Galvanoformung, Abformung), meaning lithography, electroplating, and moulding [2]. Microstructures thus fabricated exhibit high precision and large aspect ratios. However, LIGA is limited to a few metallic materials amenable to electroplating, such as nickel, nickel alloys, copper, silver and gold [6]. The combination of lithography with electrochemical etching on the other hand, is termed through-mask electrochemical micromachining (TMEMM) [9]. Notably, TMEMM is applicable to any electrically conductive material, be it metal, semiconductor or conductive ceramic.

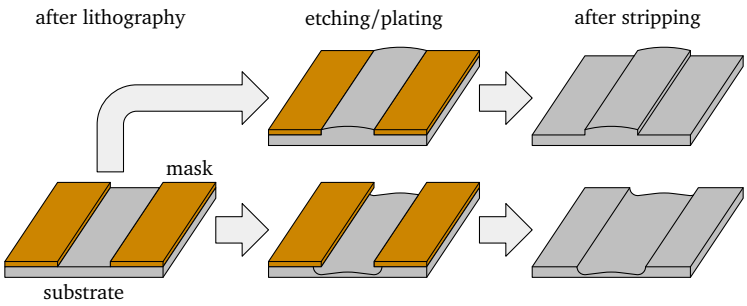

Figure 1.1: Schematic depiction of electrochemical through-mask etching and plating processes.

Compared to conventional micromachining techniques, which make use of chemical etchants, reactive plasmas, cutting tools, or laser beams for microstructuring, TMEMM offers additional advantages. In the case of difficult-to-etch metals and alloys, corrosive etchants can be replaced with benign salt solutions, thus enhancing process safety [10]. Also, the process typically operates under mass-transfer-limited conditions, leading to an improved surface finish and an accelerated machining rate [11]. Furthermore, by introducing potential control, selective machining of one metal in the presence of another is feasible [12]. In addition, TMEMM generally takes place around room temperature, and contact between a tool and the workpiece is not necessary. This avoids tool wear and subsequent surface-finishing steps, but also prevents heat-affected zones and successive heat treatments [9].

Despite its potential for mass fabrication, examples of microreactors fabricated via TMEMM are non-existent at this point. In relatively recent work [13–15] TMEMM was applied to the formation of serpentine gas-flow-field channels in stainless-steel bipolar plates for use within a proton-exchange-membrane fuel cell. A few other studies [16–18] showcase simple microstructures only, which are geared towards more fundamental microfluidic applications. However, these studies do not go into much depth in addressing process-specific challenges.

The fact that such challenges exist has long been acknowledged [19]. One problem consists in maintaining electrical contact across the whole workpiece, especially with thin-films as substrates. However, in most cases this can be solved by appropriate mask design [20]. A far greater problem exists in ensuring an even current distribution along the workpiece surface. The current distribution is linked to the rate of material removal via Faraday's law. Proper control of the current distribution is key in guaranteeing a uniform removal rate and in minimising undercutting underneath the mask, but also in ensuring a smooth surface finish [9]. Under mass-transfer-limited conditions, the current distribution is closely linked to the conditions of mass transfer [21]. Thus, the successful application of TMEMM involves not only the optimisation of the geometric cell design, but also of the hydrodynamics within the cell. In addition, surface films may form along the workpiece under mass-transfer-limited conditions, either via precipitation or passivation, which themselves affect the current distribution [22]. This picture is further complicated by the fact that different length scales are important for each of these processes [21].

Therefore, modelling TMEMM on the basis of all underlying processes, while simultaneously taking into account different length scales, has thus far not been reported. The most complex case published to date involves the multiple-length-scale modelling of the current distribution and subsequent shape evolution along a complex

printed circuit board [23, 24]. Critically, this treatment neglects the influence of mass transfer and surface-film formation. On the other hand, it highlights that solutions to the problem of non-uniform current distribution are specific for each mask design. Furthermore, the properties of the specific metal-electrolyte system play a role, for example in terms of what type of surface film forms under mass-transfer-limited conditions [22]. As a result, optimising TMEMM towards a particular application is still left to experimental trial-and-error.

1.3 Choice of metal/electrolyte system

Aluminium was chosen here as the construction material for the microreactor, instead of other metals in common use, like stainless steel, nickel or titanium [6]. These materials are compared with aluminium in terms of their physical and mechanical properties in Table 1.1. At first glance, aluminium seems clearly inferior due to its low melting point and its comparatively poor mechanical properties. One should bear in mind, however, that most microreactors are multi-component systems, wherein microstructured inlays are positioned within a reactor housing [2]. In fact, the use of aluminium is considered safe up to temperatures of 450 °C [25]. This covers a considerable number of gas-phase reactions, for example low-temperature CO oxidation, the Fischer-Tropsch reaction, as well as the low- and high-temperature Water-Gas-Shift reactions [1, 4]. Further gas-phase reactions, which have been successfully conducted in microreactors at least partly made from aluminium, include dehydrogenations [26, 27], oxidations [28–30], hydrogenations [31–33] and fuel reforming [34]. Clearly, the use of aluminium is feasible.

On the other hand, the use of aluminium also offers distinct advantages compared to other metals. The aforementioned reactions are often highly exothermic in nature; hence, its high thermal conductivity is beneficial in maintaining isothermal conditions within the reactor. In addition, the structure of aluminium surfaces may be altered via the formation of porous-oxide films, which subsequently serve as catalyst-support layers [42]. In particular, this enables noble-metal catalysts to be deposited within the pores via wash-coating or electrodeposition methods [43]. Its low density results in low-weight reactors, which is of interest in mobile applications, such as within fuel cells. Economic criteria are usually of minor importance, because little material is consumed when fabricating microreactors [6]. Nonetheless, aluminium's low price, good recyclability and widespread availability should be mentioned on the plus side, notably compared to nickel, titanium and tantalum.

The choice of electrolyte solution for TMEMM of aluminium fell on phosphoric acid. At elevated temperatures and high acid concentrations, mass-transfer-limited dissolution is observed, resulting in a polished surface finish with sub-micrometre surface roughness [44]. In fact, many mixtures intended for electrochemical and chemical polishing of aluminium are based on phosphoric acid [45]. The fabrication of micrometre-sized structures via TMEMM thus seemed attainable. Moreover, it appeared both safe and practical to use phosphoric acid on the lab-scale. Hence, this work relates to the system aluminium/phosphoric acid.

Note that several alternatives to phosphoric acid were considered initially, but then excluded for one reason or the other. Electrolytes based on alkalis were primarily eliminated to avoid problems of glass corrosion. Perchloric acid-based solutions were rejected due to safety concerns related to their tendency to ignite and detonate [46]. The use of concentrated and highly conductive salt solutions appeared attractive at first. These electrolytes are benign and enable high-rate metal dissolution [47]. Achieving an acceptable surface finish, however, requires the application of large current densities on the order of tens of amperes per square centimetre [48]. This coincides with large amounts of evolved gas and precipitated products of the metal-dissolution reaction. Therefore, the use of salt solutions requires a high-current power source and a dedicated system for electrolyte delivery and renewal [49]. These requirements were not met at the outset of this study. Based on these practical considerations, these electrolytes were not used.

Table 1.1: Typical values for physical and mechanical properties of aluminium [35], copper [36], nickel [37], type 304 stainless steel [38], tantalum [39] and titanium [40] at ambient conditions. Average US market prices for 2010 are listed as well [41]. For titanium, tantalum and stainless steel these prices refer to titanium sponge, Ta_2O_5 contained in tantalite and hot rolled bar, respectively.

Material	Density ($g\,cm^{-3}$)	Melting point (°C)	Thermal conductivity ($W\,m^{-1}\,K^{-1}$)	Young's modulus (GPa)	Yield strength (MPa)	Tensile strength (MPa)	Price (2010) (US$\,kg^{-1}$)
Aluminium*	2.71	657	220	69	93	128	2.30
Copper*	8.93	1083	394	110	80	225	7.68
Nickel	8.9	1455	88.5	200	165	495	21.80
304 steel*	8.0	1425	16.2	193	205	515	0.93
Tantalum	16.6	2996	54.4	182	555	820	119.05
Titanium	4.51	1668	21.4	105	285	515	10.74

* Mechanical properties refer specifically to annealed condition.

1.4 Thesis scope and structure

The focus of this work is to evaluate the feasibility of TMEMM for microreactor fabrication for the purpose of heterogeneous gas-phase catalysis. This refers specifically to microchannel reactors made from metals and alloys, which are used within the chemical process industry. The investigation aims at establishing a relationship between the process conditions of TMEMM on the one hand and the properties of the microreactor on the other hand. In particular, the shape, surface finish and uniformity of individual microchannels, as well as of the whole reactor, are of interest. In order to achieve this goal, the following objectives are pursued:

- Review of existing TMEMM literature, much of which focuses on current distribution, mass transfer, surface films, shape evolution and surface finish.
- Characterisation of the chosen metal/electrolyte system in terms of surface-film formation during mass-transfer-limited electrochemical dissolution.
- Development of a shape-evolution model based on diffusive mass transfer for comparison with measured shape profiles to explain the role of mass transfer.
- Scale-up of the TMEMM process to a relevant substrate size and fabrication of a complete microchannel plate-inlay for a plate-type microreactor design.
- Deposition of a catalytic wall coating, holding a noble-metal catalyst along the microchannel surface for a relevant gas-phase reaction such as CO oxidation.
- Comparison with common aluminium wet-etchants in terms of etch rate, surface roughness, undercutting, shape profile and etch uniformity.

The successive thesis chapters are briefly summarised below. In general, the structure of the results chapters follows that of a research paper, including dedicated introductory, experimental and concluding sections. By necessity some information is repeated in the process from the respective thesis chapters. Note that Chapters 5 and 7 have been published elsewhere; thus, they are reprinted in their original form with minor adjustments to fit the style of this work.

Chapter 2 – *Theory and background* covers basic electrochemical concepts such as passivity and transpassivity of metals. It also provides a compilation of information on the electrochemical behaviour of aluminium, as far as it is relevant to the present work. The latter part of this chapter presents the necessary theoretical basis for the use of disc electrodes and impedance spectroscopy, which are of importance for experimental work presented in Chapters 5 and 7.

Chapter 3 – *Through-mask electrochemical micromachining: a review* provides an in-depth summary of the current state of TMEMM and introduces key concepts relevant to this work. While previous review articles cover TMEMM to some extent, no single source exists until now, which discusses all aspects of this process in its entirety. In particular, this review constitutes an almost complete record of the TMEMM literature to date, which may be of interest to other workers.

Chapter 4 – *Experimental methods* constitutes a detailed overview of the experimental setups, methods and apparatuses. This chapter expands on the information given in each results chapter, and thereby repeats it in part. In particular, the electrochemical cell design, sample preparation, lithography protocol and surface-characterisation methods are covered in great detail.

Chapter 5 – *Characterisation of surface films formed on aluminium* presents experimental results on the type, structure and properties of surface films formed on aluminium during mass-transfer-limited anodic dissolution in phosphoric acid. A model is chosen from the literature, which describes the phenomena at the film/solution interface and within the film bulk, and several model parameters are calculated based on a fit between model and experiment.

Chapter 6 – *Modelling and simulation of current distribution and shape evolution* describes the mathematical model, which is used for the simulation of shape-evolution experiments in Chapter 7. The model derivation is performed, the underlying assumptions are justified and the numerical implementation is detailed. Model results are tested for their validity and compared with literature data.

Chapter 7 – *Through-mask electrochemical micromachining of aluminium* contains both experimental and model-based results on the shape-evolution process during TMEMM of aluminium in phosphoric acid. The effect of mass transfer under controlled hydrodynamic conditions is highlighted, and other important influences are presented. The feasibility of aluminium micromachining is demonstrated by machining a few microfluidic test structures.

Chapter 8 – *Fabrication and functionalisation of an aluminium gas-phase microreactor* gives an account of experiments on the machining of an example microreactor structure, including the formation of a catalytic wall coating made from Au/Al_2O_3. The impact of electrolyte additives, mass-transfer conditions and adjustments to the mask design is examined, all with an eye for the uniformity of the current distribution and the resulting reactor dimensions.

Chapter 9 – *Comparison with wet-chemical etching* describes results on comparative chemical and electrochemical etching of aluminium for the purpose of micro-

machining. Differences between these two types of etching processes are highlighted in terms of etch rate, surface roughness, etch factor, shape profile and etch uniformity. Their suitability for aluminium micromachining is discussed.

Chapter 10 – *Conclusions and recommendations* summarises the most significant findings of this work and puts them in context to each other. Furthermore, suggestions for future investigations are made and discussed briefly in the process.

Appendices A to D list for convenience values for the conversion between the potential of the Ag|AgCl electrode and the standard hydrogen electrode. Also included are the results of a mass-transfer study for a recessed disc electrode, which is used extensively in Chapter 7. The valence of aluminium dissolution in phosphoric acid was determined for comparison with other work. Finally, the technical drawings for the experimental apparatuses described in Chapter 4 are given.

1.5 Publications and conference contributions

Results presented in this work have in part been disseminated. The following articles have either been published or accepted for publication in peer-reviewed journals:

- Baldhoff, T.; Nock, V.; Marshall, A. T. Through-Mask Electrochemical Micromachining: A Review. *J. Electrochem. Soc.*, in press.
- Baldhoff, T.; Nock, V.; Marshall, A. T. Through-Mask Electrochemical Micromachining of Aluminum in Phosphoric Acid. *J. Electrochem. Soc.* **2017**, *164*, E194–E202.
- Baldhoff, T.; Marshall, A. T. Characterization of Surface Films Formed on Aluminum during Mass-Transfer Limited Anodic Dissolution in Phosphoric Acid. *J. Electrochem. Soc.* **2017**, *164*, C46–C53.

Results shown herein were also presented at various conference meetings, either in the form of an oral or a poster presentation. The presenting author is underlined:

- Oral presentation, Baldhoff, T.; Nock, V.; Marshall, A. T. Microfabrication and Functionalization of an Aluminum Gas-Phase Micro-Reactor via Through-Mask Electrochemical Micromachining. 233rd ECS Meeting, 13-17 May 2018 in Seattle, Washington, USA.

- Oral presentation, Baldhoff, T.; Nock, V.; Marshall, A. T. Aluminium Micromachining in Phosphoric Acid via Through-Mask Electrochemical Micromachining. 43rd International Conference on Micro and Nanoengineering (MNE2017), 18–22 September 2017 in Braga, Portugal.
- Poster presentation, Baldhoff, T.; Nock, V.; Marshall, A. T. Aluminium Micromachining via Mass-Transfer Limited, Electrochemical Dissolution in Phosphoric Acid. 68th Annual Meeting of the ISE, 27 August–1 September 2017 in Providence, Rhode Island, USA.
- Oral presentation, Baldhoff, T., Marshall, A. T., Nock, V.: Through-mask electrochemical micromachining of aluminium. 8th International Conference on Advanced Materials and Nanotechnology (AMN8), 12–16 February 2017 in Queenstown, New Zealand.
- Oral presentation, Baldhoff, T., Marshall, A. T.: Study of Anodically Formed Solid Films during Electropolishing of Aluminium using Electrochemical Impedance Spectroscopy. 67th Annual Meeting of the ISE, 21–26 August 2016 in The Hague, Netherlands.
- Oral presentation, Baldhoff, T., Marshall, A. T.: Electrochemical Impedance Study of Oxide Films Formed During Electropolishing of Aluminium in Phosphoric Acid. ISE Satellite Student Regional Symposium on Electrochemistry & 20th Australasian Electrochemistry Symposium, 17 April 2016 in Auckland, New Zealand.

2 Theory and background

The first part of this chapter addresses electrochemical phenomena, which are relevant to anodic metal-shaping and -finishing processes. To this end, Section 2.1 covers the relation between passive and transpassive behaviour on the one hand, and anodic metal removal on the other hand. Section 2.2 then presents the electrochemical behaviour of aluminium, insofar as it is relevant to this work. The second part (Sections 2.3 and 2.4) deals with the theory related to the use of disc electrodes and impedance spectroscopy, both of which are utilised extensively.

2.1 Passivity and transpassivity of metals

The anodic behaviour of metals is characterised by a complex interplay of different processes such as charge transfer, oxide-film formation, growth and dissolution, electrolyte breakdown and gas evolution. When a metal electrode is anodically polarised, different modes of dissolution are observed depending on the metal-electrolyte combination and on the magnitude of the anode potential. In general, anodic metal dissolution can be classified as active, passive or transpassive [50, 51].

Upon the application of an anodic potential, the metal surface initially dissolves in the active state. Metal cations form at the metal-electrolyte interface via a charge-transfer reaction, and subsequently undergo hydration and complexation in conjunction with ionic and molecular species in solution. As the anode potential rises, metal dissolution increases rapidly. Surface-kinetic effects are significantly involved in the accompanying charge-transfer process. Surface imperfections, such as variations in the crystal lattice, result in differences in the local dissolution rate. Thus, the final surface finish under the influence of active dissolution usually shows etch figures and a corresponding increase in surface roughness.

At sufficiently high anode potentials the metal enters the passive state. The corresponding potential is termed the passivation or Flade potential. In the passive state, metal-oxide formation is thermodynamically favoured, and hence the metal surface is covered with a thin oxide film. Metal cations are still generated at the metal-film

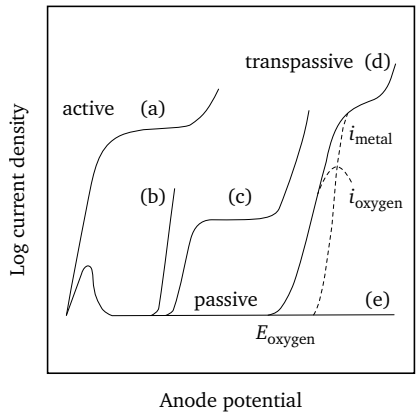

Figure 2.1: Schematic depicting the anodic polarisation behaviour of metals (adapted from Datta [47]). The letters designate typical polarisation curves: (a) active dissolution and (b–e) passive-film formation followed by (b) local film breakdown via pitting, (c) uniform film dissolution and secondary passivity, (d) oxygen evolution and transpassive metal dissolution, and (e) continued film growth.

interface, but they now have to traverse the oxide film first, before being hydrated and complexed in solution. This is accompanied by a reduction in the rate of metal dissolution, and hence a fall in current density down to a limiting value. In contrast to dissolution in the active state, the current density in the passive state is largely independent of further increases in potential.

In case the anode potential is increased even further, transpassive behaviour can be observed, such that the rate of metal dissolution increases again. Several phenomena are summarised under this term. Firstly, local film breakdown may occur due to pitting in the presence of aggressive ions in the electrolyte (Curve (b) in Figure 2.1). Secondly, the potential increase may lead to further oxidation of the metal-oxide film, yielding soluble species and resulting in uniform film dissolution below the potential for oxygen evolution (Curve (c)). At higher anode potentials, secondary passivity may occur, which is characterised by the formation of more stable oxides and a re-passivation of the metal surface. Thirdly, the oxide film may dissolve uniformly at potentials above the oxygen-evolution potential (Curve (d)). In this case, the current density rises quickly with potential and contains contributions from metal dissolution and oxygen evolution. Lastly, transpassive dissolution may fail to appear, despite further increases in anode potential (Curve (e)). In this case, highly resistive oxide films form during passivation, which may grow to considerable thickness before film breakdown occurs at much higher potentials.

Passive and transpassive dissolution phenomena are highly relevant in the study of electrochemical metal-shaping and -finishing processes. Firstly, the continued growth of oxide films is utilised in the generation of protective, anodic coatings on metals such as aluminium and titanium [52, 53] (Section 2.2.1). Secondly, uniform film dissolution below the oxygen-evolution potential is frequently limited by mass transfer, leading to an electropolished surface finish [46, 51, 54] (Section 2.2.2). Thirdly, transpassive film dissolution above the oxygen-evolution potential is accompanied by high metal dissolution rates and usually employed in electrochemical cutting and shaping [47, 55] (Section 2.2.3).

2.2 Electrochemistry of aluminium

According to its standard electrode potential ($E^0(\mathrm{Al/Al^{3+}}) = -1.663\,\mathrm{V}$ vs. SHE) [56], aluminium is highly reactive and easily oxidised in water. Despite its reactivity, aluminium exhibits passive behaviour in aqueous solutions in the pH range from about 4 to 9 (Figure 2.2). This is because in neutral and near-neutral solutions the formation of stable, passivating oxide and hydroxide films is thermodynamically favoured compared to aluminium dissolution. This fact lends the metal its high corrosion resistance under atmospheric conditions, as well as when in contact with industrial fumes and vapours, and fresh, brackish, or salt waters [57].

Aluminium is typically assumed to go into solution in the trivalent state [58]. No soluble species with a valency state larger than three exists; thus, transpassive behaviour exhibiting secondary passivity as discussed in Section 2.1 is non-existent [59]. In general, the high resistivity of aluminium oxides and hydroxides ($> 10^{15}\,\Omega\,\mathrm{cm}$ for Al_2O_3 at 25 °C) [60] limits electron transfer through the passive film; hence, oxygen evolution is negligible [61]. In consequence, passive films continue to grow in neutral electrolytes with increases in potential [52]. In both acidic and alkaline solutions, however, these films are not stable, and aluminium dissolves in the active state [62–65]. In addition, breakdown of passive films may occur in solutions containing aggressive anions due to a pitting mechanism [66–68].

2.2.1 Anodising

In the presence of air, aluminium quickly becomes covered with a duplex-structure oxide film, consisting of a compact, barrier-type layer adjacent to the metal and a

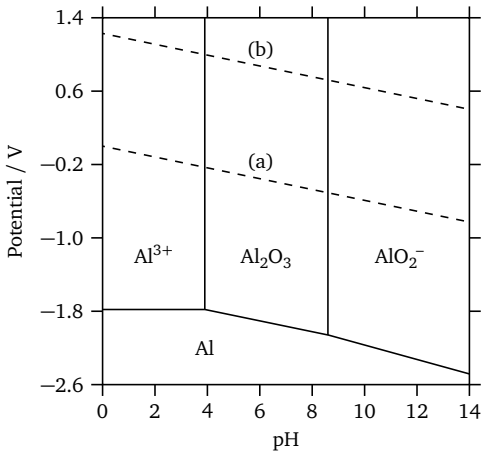

Figure 2.2: Potential-pH diagram for the system aluminium-water at 25 °C and an activity of 10^{-6} mol cm^{-3} for all aqueous species (adapted from Pourbaix [56]). The dashed lines enclose the stability region of water, where (a) and (b) designate the reversible potential for the hydrogen and oxygen electrode, respectively.

porous layer on top [69]. The thickness of the compact layer is on the order of a few nanometres [70, 71], while the overall oxide-film thickness can reach several hundred nanometres [45]. The presence of this natural oxide film lends aluminium its good corrosion resistance. Aluminium-oxide films can be grown artificially to much larger thickness, if aluminium is made the anode in an electrochemical cell using an appropriate electrolyte. The process is widely used in research and industry to produce dielectric capacitors, decorative coatings, corrosion- and wear-resistant films [52, 70], catalyst-support layers [26, 27, 33, 42, 72], and more recently nanostructure templates [71, 73, 74].

The film structure depends mainly on the electrolyte type (Figure 2.3). In near-neutral electrolytes such as borate, phosphate and tartrate solutions, compact films form; whereas porous films form in acidic solutions such as oxalic, phosphoric and sulphuric acid [52, 70, 71, 73, 74]. The thickness of compact films depends linearly on the applied potential with a proportionality constant between the two quantities on the order of 1.5 V nm^{-1} [52, 74]. At sufficiently high potentials in the range of 500–700 V the films break down; thus, their maximum thickness is usually limited to 1 µm [52, 74]. Porous films exhibit a duplex structure with a compact, barrier-type layer adjacent to the metal and a porous layer on top. As for films formed in near-neutral electrolytes, the thickness of the compact layer depends on the applied potential and is limited to a few hundred nanometres [71]. The porous-layer thickness, however, can reach several tens of micrometres [75, 76] and depends linearly

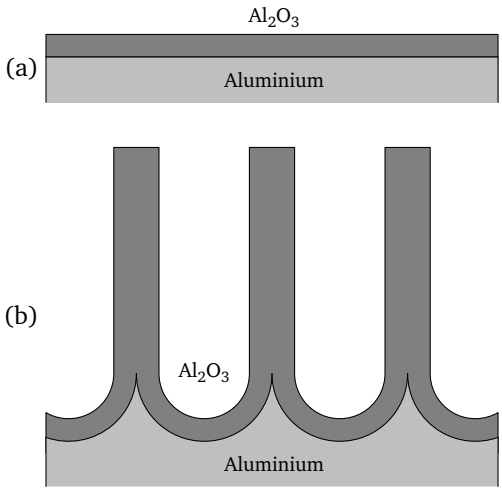

Figure 2.3: Cross-section of (a) a compact and (b) a porous aluminium-oxide film.

on the cumulative passed charge, and hence on current density and time [52, 71]. Eventually, the porous layer reaches a limiting thickness, which is characterised by a balance between film growth and dissolution. The balance between both processes varies with electrolyte type, temperature and concentration [45].

The morphology of the porous layer within duplex-structure films is itself amenable to customisation based on the anodising conditions. It is described by several parameters, namely: pore diameter, inter-pore distance, pore-wall thickness, pore density and porosity [71]. Under potentiostatic conditions, pore diameter, inter-pore distance and pore-wall thickness are linearly proportional to the anodising potential with proportionality constants on the order of 0.8–2.5 $\mathrm{nm\,V^{-1}}$ [73, 77, 78]. Considering the typical potential range for each acid electrolyte, these quantities increase in the order sulphuric (15–40 V), oxalic (20–65 V) and phosphoric acid (60–195 V) [74]. Conversely, pore density and porosity decline with an increase in potential [71, 79]. Similar trends emerge under galvanostatic conditions for a rise in current density [75, 76]. The influence of anodising time, electrolyte concentration and temperature, however, is less clear and depends on the acid in use and the mode of anodising (galvanostatic or potentiostatic) [73].

Highly ordered, porous-alumina films are obtainable under specific process conditions corresponding to the so-called self-ordering regime [73]. This regime is characterised by the prolonged application of high anodising potentials and current densities, just short of the occurrence of burning, which results in non-uniform film thickening, excessive gas evolution, and ultimately film breakdown [71]. To

limit current flow, gas evolution and heat generation during self-ordering, anodising proceeds in dilute solutions at low temperatures [80, 81]. The resulting films are distinguished by porosities close to 10 % independent of the electrolyte in use [79, 82]. Self-ordering is sensitive to the presence of surface defects; hence, aluminium surfaces are annealed and electropolished before anodising [83]. A smooth, defect-free starting surface is critical to obtain long-range-ordered pore arrays.

Porous, duplex-structure alumina films are of particular interest in this work because of their aforementioned use as catalyst-support layers. They are predestined for this role for several reasons [42, 84–86]. Firstly, pore formation leads to a more than hundredfold increase in surface area. This results in a higher number of catalytically active sites per geometric surface area, which can be formed by subsequent processes. Secondly, porous-alumina films show good adhesion strength, thus minimising the problem of catalyst loss over time during operation. Thirdly, the anodising process leads to films of uniform thickness, which are characterised by regular, unbranched, parallel-aligned pores. This results in a narrow residence time distribution of reactants, intermediates and products, and hence positively affects selectivity. Fourthly, the properties of the porous film can be tuned within limits by varying the process conditions during anodising.

2.2.2 Electropolishing

When aluminium is made the anode in an electrochemical cell in concentrated acidic or alkaline electrolytes, passive and transpassive phenomena as outlined in Section 2.1 are absent. Thermodynamically, passive films are not stable under these conditions (Figure 2.2), and the metal instead dissolves in the active state with concurrent hydrogen evolution. The resulting surface appears non-reflective, and surface roughness increases. However, at sufficiently high anode potentials, the current reaches a plateau and becomes independent of further increases in potential. In this case, dissolution is limited by mass transfer, and a smooth and polished surface is obtained. This process, termed electropolishing (EP) [54], is widely used in industry and research; applications include the preparation of metallographic samples [45, 46], the fabrication of aluminium mirrors and reflectors [87, 88] and the finishing of decorative parts, for example in the automotive industry [45].

EP is based on the combined action of a levelling and brightening process [21, 54]. Levelling results either from the concentration of current lines on the peaks of a surface profile, and thus local differences in the ohmic drop between anode and

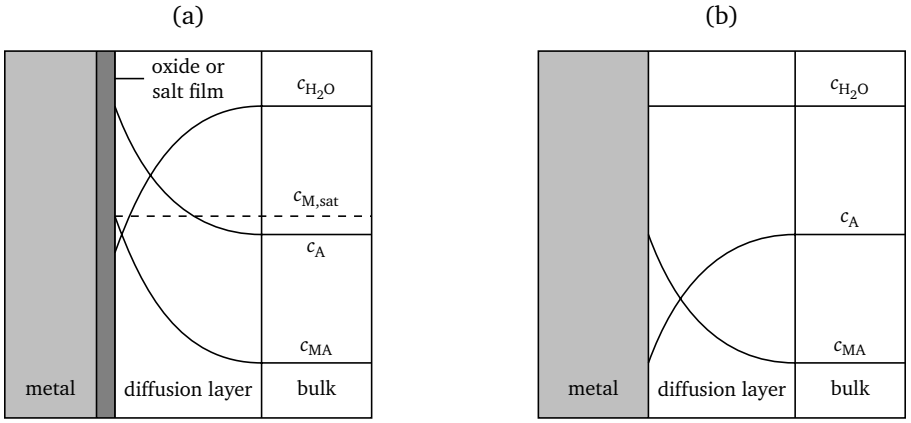

Figure 2.4: Concentration gradients along the metal/electrolyte interface for mass-transfer-limited anodic dissolution corresponding to EP via (a) an oxide- or salt-film mechanism and (b) an acceptor mechanism (adapted from Landolt [54]). The symbols c_M, c_A, c_{MA} and c_{H_2O} denote the concentration of metal cations, acceptor anions, complexed metal cations and water, respectively.

cathode [54], or from variations in the path length of diffusion between surface and bulk solution [21]. This process is responsible for the removal of surface roughness larger than 1 µm. In contrast, brightening removes surface roughness smaller than 1 µm and is governed by a random process, either the transfer of vacancies within a surface film [54] or the diffusion of metal ions within the diffusion layer [21]. Only the parallel action of levelling and brightening yields a macro- and microscopically smooth surface [54]. The necessary condition for this is the presence of a limiting-current plateau, which is controlled by mass transfer.

Two mechanisms are commonly proposed to explain the existence of these limiting-current plateaus [54] (Figure 2.4). In the salt-film mechanism the surface is covered with a surface film, either consisting of a salt or an oxide [89, 90]. The rate-limiting step is the diffusion of metal cations from the anode surface into the bulk electrolyte. The limiting current density is thus determined by the concentration of metal cations along the anode surface. In the acceptor mechanism on the other hand, the diffusion of an acceptor from the bulk electrolyte towards the anode surface is the rate-limiting step [91]. This acceptor, either water or an anion, is subsequently consumed in the solvation or complexation of surface-adsorbed intermediates of the metal-dissolution reaction. Hence, the acceptor concentration in the bulk electrolyte determines the limiting current density. Which mechanism is at work depends on the specific metal-electrolyte combination: for example, during copper EP a solid film forms in hydrochloric acid [92, 93], whereas in phosphoric acid the dissolution is limited by mass transfer of an acceptor species [94].

In the case of aluminium, the presence of solid salt or oxide films during EP is widely accepted [45, 95]. The composition and structure of these films, however, is not always clear and varies with the type of EP solution. For example, in mixtures of perchloric acid and acetic anhydride or acid, the formation of an oxide film of appreciable thickness can be excluded based on the study of plastic deformation [96, 97], open-circuit potential and electron-diffraction patterns [98, 99]. Instead, the formation of a white precipitate is observed, which contains aluminium chloride, chlorate and perchlorate [100]. Polishing in perchloric acid/ethanol solutions on the other hand clearly produces a porous-oxide film [101], which contains traces of oxygen, carbon, sulphur, nitrogen and chlorine [102]. Oxide-film formation is also evident in EP solutions based on phosphoric acid [87, 97, 103–106]. In mixtures containing butyl alcohol, this latter film is characterised by a duplex structure with a compact layer adjacent to the metal and a porous layer in contact with the solution. The presence of a phosphate film has also been proposed [107, 108].

On an industrial scale, aluminium EP is limited to four types of electrolyte, namely mixtures based on sodium carbonate/trisodium phosphate, fluoboric acid, perchloric acid, and phosphoric acid [45, 46]. Each of these have distinct areas of application. For example, the carbonate/phosphate process is only applicable to aluminium of 99.8 % purity or above. Furthermore, except for phosphoric-acid baths, these mixtures are intended for brightening operations after mechanical polishing; thus, they exhibit low dissolution rates [45]. In concentrated phosphoric acid on the other hand both levelling and brightening occur in parallel, thereby supplanting mechanical polishing. Also, note that phosphoric acid-based mixtures pose no threat of spontaneous explosion or combustion, unlike perchloric acid baths.

Phosphoric-acid baths frequently contain additives such as acids or organic components to improve certain process aspects (Table 2.1). All baths have in common the operation at elevated temperatures and low water content. For example, additions of sulphuric acid reduce pitting and increase electrolyte conductivity, hence permitting operation at lower applied potentials [45]. Chromic or nitric acid act as strong passivating agents, which promote the formation of protective films during immersion and removal of aluminium substrates. Organic solvents such as alcohols and ethers are added to vary solution viscosity [45] and surface-film thickness [87]. Surfactants modify surface tension along the aluminium surface and improve the removal of adherent gas bubbles [109]. The amount of dissolved aluminium is also of importance [45, 46]. Nonetheless, aluminium EP can be conducted at elevated temperatures in concentrated phosphoric acid alone [44].

Table 2.1: Composition of aluminium electropolishing mixtures based on phosphoric acid in terms of their acid and water content. The composition is given in weight percent. Organic components and additives are omitted, thus not all solutions add up to 100 %. Also given are typical or recommended operating conditions.

H_3PO_4 (%)	H_2SO_4 (%)	CrO_3 (%)	HNO_3 (%)	H_2O (%)	Temp. (°C)	Applied potential (V)	Current density ($mA\,cm^{-2}$)	Ref.
85	–	–	–	15	65–90	2–6	–	[44]
75	–	–	–	11	90–100	–	120–150	[45]
56	–	–	–	23	42–45	50–60	350	[46]
73	12	8	–	7	95	60	120	[46]
71–76	–	–	–	13	60–65	–	20–30	[87]
76	–	–	–	13	60–65	10–40	30–50	[104]
90	–	–	–	10	65	4	19.1	[110]
70	17	–	3	10	100	4	–	[111]

2.2.3 Electrochemical machining

When aluminium is submersed into neutral, aqueous solutions of certain inorganic salts, the passive-oxide film breaks down locally, which results in pitting corrosion. Pitting occurs due to a multi-step mechanism, which involves the adsorption of anions along the film/solution interface, the chemical reaction between anions and aluminium cations along the surface, the dissolution and thinning of the passive film, and finally the exposure and dissolution of the underlying metal [112]. The phenomenon is most notable in chloride solutions, where pitting corrosion is observed under open-circuit conditions. In order to induce pitting in the presence of other anions such as nitrate or sulphate, aluminium must be made the anode in an electrochemical cell [66, 113]. The rate of pit formation increases with a rise in salt concentration [114], leading to uniform dissolution along the whole exposed metal surface in concentrated solutions [115]. In this way, these solutions are utilised in industry for high-rate metal dissolution, cutting, milling and shaping operations, which are collectively termed electrochemical machining (ECM) [48, 49, 55].

The ECM process, like EP (Section 2.2.2), operates under the combined action of a levelling and brightening mechanism [22]. Levelling follows from large potential gradients within the interelectrode gap in conjunction with variations in ohmic drop along the peaks and valleys of the surface profile [49, 55, 116]. Brightening stems from the presence of a surface film consisting either of a precipitated salt, an oxide

or a viscous layer [48]. In this manner, ECM has the ability to produce electropolished surfaces with sub-micrometer surface roughness. Note that flow effects are of importance in governing the surface finish under ECM conditions.

In the case of aluminium, the existence of surface films is attested from a number of investigations. During high-rate dissolution in solutions of NaCl, $NaNO_3$, $NaClO_3$ and $NaCl/NaNO_3$, mass-transfer-limited current plateaus are observed at sufficiently large anode potentials in conjunction with a polished surface finish [117–119]. Whether the surface is covered with a solid or a viscous film, however, is not discernible from these studies. Recently, a multi-layer film model was proposed for ECM in $NaNO_3$ electrolytes, consisting of an oxide film adjacent to the metal and a supersaturated layer of aluminium nitrate solution on top [120].

In order to operate ECM under polishing conditions, very large current densities need to be applied. For example, anodic dissolution at 3–4 $A\,cm^{-2}$ in various salt solutions yields an etched surface, which exhibits signs of crystallographic etching [121]. In the aforesaid high-rate dissolution studies [118, 119], the magnitude of the limiting-current plateaus corresponding to polishing conditions varied from 4–12 $A\,cm^{-2}$. Under ECM conditions, current densities on the order of tens of amperes per square centimetre are routinely applied [120]. This fact alone complicates the study of ECM of aluminium under laboratory conditions. Furthermore, dissolution in NaCl and $NaNO_3$ solutions is accompanied by oxygen evolution along the anode [120], which may induce pitting superimposed with polishing [48].

2.2.4 Alternating current electrodeposition

When aluminium, which has previously been covered with a porous-alumina film, is submersed in a noble-metal salt solution and subjected to an alternating current (AC), the respective metal is reduced and deposited within the pores. Because of the valve character of aluminium [61], current flows preferentially during the cathodic half-cycles. Therefore, the reduction of metal ions is favoured over metal oxidation, and a net metal deposit forms in the process.

This technique, termed AC electrodeposition, has long been utilised for the impregnation of porous-alumina films with inorganic pigments, in particular metal salts of silver, copper, nickel and cobalt, with the aim of colouring aluminium parts [45]. Many process variations are available to produce varying colours and shades. Renewed interest in these processes stems from the possibility of using porous-alumina films as a template for the fabrication of nanostructured materials [73].

This includes the deposition of metals, metal oxides and semiconductors for the formation of nanowires, -dots and -tubes. Because the structure of the underlying oxide can be tuned by modifying the anodising conditions, nanomaterials with a wide range of properties can be formed. By using self-ordered films for this purpose, nanostructured arrays of high regularity are achievable.

In principle, the deposition of metals into porous-alumina films is possible by applying both AC and direct current (DC) signals, but in practice the latter are not used on an industrial scale. This is because the high resistivity of the underlying barrier layer (Section 2.2) necessitates the application of large deposition potentials during DC operation [122]. Also, alumina films dissolve in parallel with hydrogen evolution upon cathodic polarisation, in particular in alkaline and neutral electrolytes [123]. This results in non-uniform pore filling and film detachment [124]. For these reasons, DC deposition is mostly performed with free-standing alumina films — a process which is not amenable to scale-up [125].

The successful application of AC potential signals, while more facile than DC deposition processes, still requires that several precautions are met. Due to the aforementioned corrosion behaviour of alumina during cathodic polarisation [123], metal-salt solutions are adjusted to low pH values [122]. This reduces film damage during the cathodic half-cycles. Also, the underlying barrier layer is usually thinned first to enable deposition at lower AC potentials, either via chemical or electrochemical means [73]. Typically, 10–20 V AC are applied at frequencies of 50–300 Hz [122]. Note that barrier-layer thinning is essential for films grown in oxalic and phosphoric acid [126, 127] due to the relationship between barrier-layer thickness and anodising potential (Section 2.2.1). Conversely, for films grown in sulphuric acid this is not always necessary, unless pore widening is desired at the same time [128]. In addition, complete pore wetting is required prior to AC electrodeposition [129]; otherwise, non-uniform pore filling occurs.

Within the present work, AC electrodeposition is of special interest for the deposition of catalytically active materials, specifically noble metals, within porous-alumina films. Firstly, the process is considered to be much cheaper and simpler than other deposition methods, such as chemical and physical vapour deposition or atomic layer deposition [71]. Secondly, compared to chemical deposition techniques, additional parameters are available for process optimisation, including the AC potential, the AC frequency, and the overall shape of the AC waveform [129]. Thirdly, the method is applicable to a wide range of catalytically active metals [73]; for example copper [130], palladium [43, 130] and platinum [131]. Fourthly, uniform noble-metal deposits can be formed rapidly [131].

2.3 Rotating disc electrode

Electrochemical reactions usually proceed in several steps. In the simplest case, these steps are the diffusive transport of reactants from the bulk solution towards the electrode surface, the charge-transfer reaction at the metal-solution interface, and the diffusive transport of products away from the surface. Depending on which step is rate-controlling, different equations describe the current density [51, 132]. For an electrode reaction, which is limited by the charge-transfer reaction at the surface, the current density depends on the electrode potential; thus, it is described by the Butler-Volmer or Tafel equation. In contrast, for a mass-transfer-limited electrode reaction the current density can be expressed using Fick's first law [51]:

$$i_\mathrm{L} = z_\mathrm{e} F D \frac{c}{\delta} \tag{2.1}$$

Herein, δ denotes the thickness of the diffusion layer, z_e the charge-transfer number, F the Faraday constant and D the diffusion coefficient. For an electrode reaction which is limited by the transport of a species towards the surface, c signifies the concentration of that species in the liquid bulk. In cases where the transport of a species away from the electrode surface is rate-limiting, c corresponds to that species' saturation concentration at the metal-solution interface. If the rates of charge (i_K) and mass transfer (i_L) are of similar size, the electrode reaction proceeds under mixed control, and both processes contribute to the overall current density [51]:

$$\frac{1}{i} = \frac{1}{i_\mathrm{K}} + \frac{1}{i_\mathrm{L}} \tag{2.2}$$

Distinguishing between both contributions is possible by varying the conditions of mass transfer, such as when using a rotating disc electrode. The well-defined flow conditions along the disc surface enable the analytical solution of the Navier-Stokes equations for the flow field. From this solution, the thickness of the diffusion layer (δ) can be calculated as follows [133]:

$$\delta = 1.61\, \nu^{1/6} D^{1/3} \omega^{-1/2} \tag{2.3}$$

Herein, ν is the kinematic viscosity of the electrolyte and ω denotes the rotation rate of the disc electrode (in $\mathrm{rad\,s^{-1}}$). Inserting Equation 2.3 into Equation 2.1 yields the well-known Levich equation for the mass-transfer-limited current density [133]:

$$i_\mathrm{L} = 0.62 z_\mathrm{e} F D^{2/3} \nu^{-1/6} c \omega^{1/2} \tag{2.4}$$

Note that the validity of the Levich equation is limited to laminar flow conditions. Distinguishing between the influence of charge and mass transfer is then possible by inserting Equation 2.4 into Equation 2.2, which yields:

$$\frac{1}{i} = \frac{1}{i_\mathrm{K}} + \frac{1.61\,\nu^{1/6}}{z_\mathrm{e} F D^{2/3} c \omega^{1/2}} \tag{2.5}$$

In case of complete control by mass transfer, plotting $1/i$ against $1/\omega^{1/2}$ yields a straight line through zero. Under mixed control, the plotted line has a non-zero intercept equalling $1/i_\mathrm{K}$. In both cases, the slope equals $(1.61\,\nu^{1/6})/(z_\mathrm{e} F D^{2/3} c)$. If all other parameters in Equation 2.4 are known, it is possible to compute the diffusion coefficient of the rate-limiting species from this slope.

2.4 Electrochemical impedance spectroscopy

Electrochemical impedance spectroscopy (EIS) is a non-steady state, electrochemical analysis technique, in which the response of an electrochemical system to a sinusoidal perturbation is studied. Either the current or the potential can be perturbed, leading in turn to a potential or current response, respectively. In general, EIS is applied to the investigation of electrochemically active surfaces to elucidate their structure and the electrochemical reactions taking place thereon [51, 132, 134]. Examples include the study of the electrochemical reaction kinetics of corrosion processes, the evaluation of the thickness of surface films and coatings, or the measurement of the double-layer capacitance of metal electrodes.

The principle of EIS rests on the application of a small perturbation of varying frequency (f) on top of a steady-state input signal. The perturbation must be small — in case of an input potential perturbation below 10 mV [132, 135] — to ensure a linear response of the electrochemical system at hand. Under this condition, the output signal is independent of the magnitude of the input perturbation. Note that analysis via EIS requires the equations describing the system to be linearised. By modulating the signal frequency from megahertz down to millihertz, electrochemical phenomena occurring at different time scales can be analysed.

For the definition of the impedance, consider a sinusoidal potential perturbation of amplitude $|\Delta E|$, which results in a current response of the system of amplitude $|\Delta I|$ (Figure 2.5). The potential and the current perturbation are both complex, time-dependent quantities, which are expressed as follows [51]:

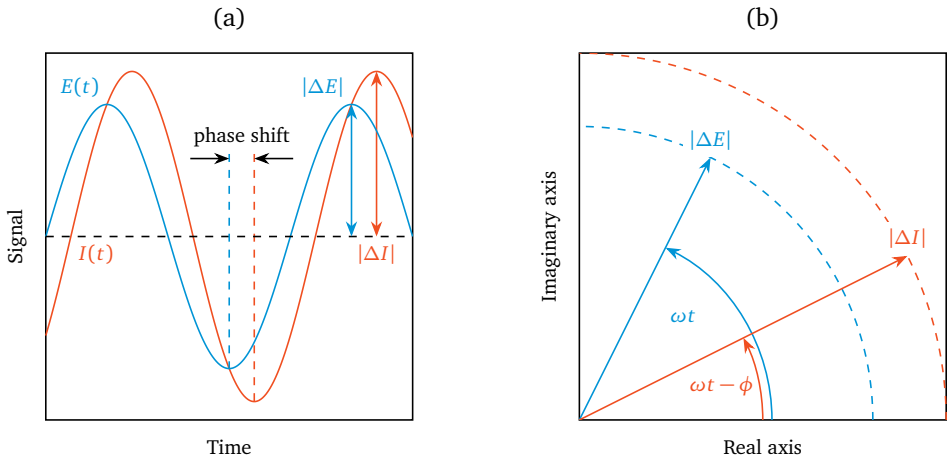

Figure 2.5: Sine-wave potential and current signal in the (a) time domain and (b) the complex plane.

$$E(t) = |\Delta E| \exp(j\omega t) \tag{2.6}$$
$$I(t) = |\Delta I| \exp(j(\omega t - \phi)) \tag{2.7}$$

Herein, $\omega = 2\pi f$ denotes the angular frequency of the perturbation in rad s^{-1}, ϕ is the phase angle, which describes the phase lag between the two signals, and j is the imaginary number defined as $j = \sqrt{-1}$. The impedance (Z) can then be seen as the complex resistance, that is as the ratio between the time-dependent potential and current signal, analogously to Ohm's law [51]:

$$Z = \frac{E(t)}{I(t)} = \frac{|\Delta E| \exp(j\omega t)}{|\Delta I| \exp(j(\omega t - \phi))} = |Z| \exp(j\phi) \tag{2.8}$$

Herein, $|Z|$ is the modulus of the impedance, which is defined as the amplitude ratio between the potential and the current perturbation. The impedance is described in the complex plane by the modulus $|Z|$ and the phase angle ϕ. Alternatively, the impedance can be expressed by its real and imaginary parts, Z_{Re} and Z_{Im}, respectively. The basic equations relating these four quantities to each other are derived from their geometrical relationship in the complex plane [51]:

$$Z = Z_{\mathrm{Re}} + jZ_{\mathrm{Im}} \tag{2.9}$$
$$|Z| = \sqrt{Z_{\mathrm{Re}}^2 + Z_{\mathrm{Im}}^2} \tag{2.10}$$
$$\tan\phi = Z_{\mathrm{Im}}/Z_{\mathrm{Re}} \tag{2.11}$$

2.4.1 Equivalent electrical circuits

Ideally, data analysis in EIS revolves around a physical model, which describes phenomena such as charge transfer and diffusive mass transfer in a rigorous manner. More often, an equivalent electrical circuit is employed to represent the data, and the influence of experimental conditions on the circuit elements is studied. These equivalent circuits contain simple elements such as resistors, capacitors and inductors. The impedance equations of these circuit elements are [51]:

$$Z_{\mathrm{R}} = R_{\Omega} \qquad \text{(for a resistor)} \tag{2.12}$$

$$Z_{\mathrm{C}} = -j/\omega C \qquad \text{(for a capacitor)} \tag{2.13}$$

$$Z_{\mathrm{L}} = j\omega L \qquad \text{(for an inductor)} \tag{2.14}$$

The behaviour of each element in the frequency domain is schematically shown in Figure 2.6 in terms of its impedance modulus. As ω goes to zero, the capacitive modulus approaches infinity, whereas the inductive modulus goes towards zero. This corresponds to open-circuit and short-circuit conditions, respectively. Conversely, as ω approaches infinity these roles are reversed. Of course, the resistive modulus is independent of frequency. More complicated behaviour is observed, if these simple elements are connected to form a composite circuit. For this purpose, simple elements are connected in series and in parallel. The resulting impedance equation is determined by basic rules for both connection types [51]:

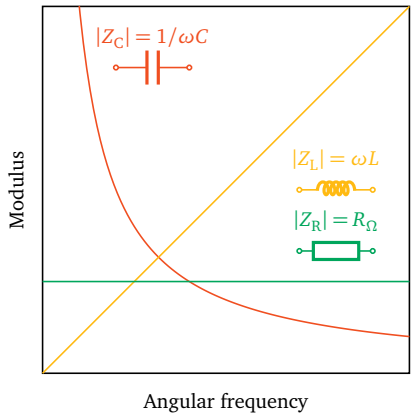

Figure 2.6: Frequency dependence of the impedance modulus for simple circuit elements.

$$Z = \sum_k Z_k \qquad \text{(for a serial connection)} \tag{2.15}$$

$$1/Z = \sum_k 1/Z_k \qquad \text{(for a parallel connection)} \tag{2.16}$$

Using the above rules, an arbitrarily complex circuit can be constructed in principle to perfectly represent any EIS data set. However, with an increase in the number of circuit elements, it becomes increasingly difficult to ascribe physical meaning to each individual element. In practice, it is thus desirable to describe the data set with as few elements as possible, with each element being physically significant.

The graphic representation of EIS data is usually carried out either in Nyquist or Bode plots. For the purpose of illustration, consider the example circuit given in the insert in Figure 2.7(a). This circuit is frequently used to represent the electrode/solution interface of bare-metal electrodes. According to Equations 2.12 to 2.16 its impedance equation is calculated as follows [51]:

$$Z = R_\mathrm{s} + \frac{R_\mathrm{ct}}{1 + j\omega R_\mathrm{ct} C_\mathrm{dl}} \tag{2.17}$$

Herein, R_s denotes the solution resistance, R_ct the charge-transfer resistance and C_dl the capacitance of the electrical double layer. At present, the resulting Nyquist plot

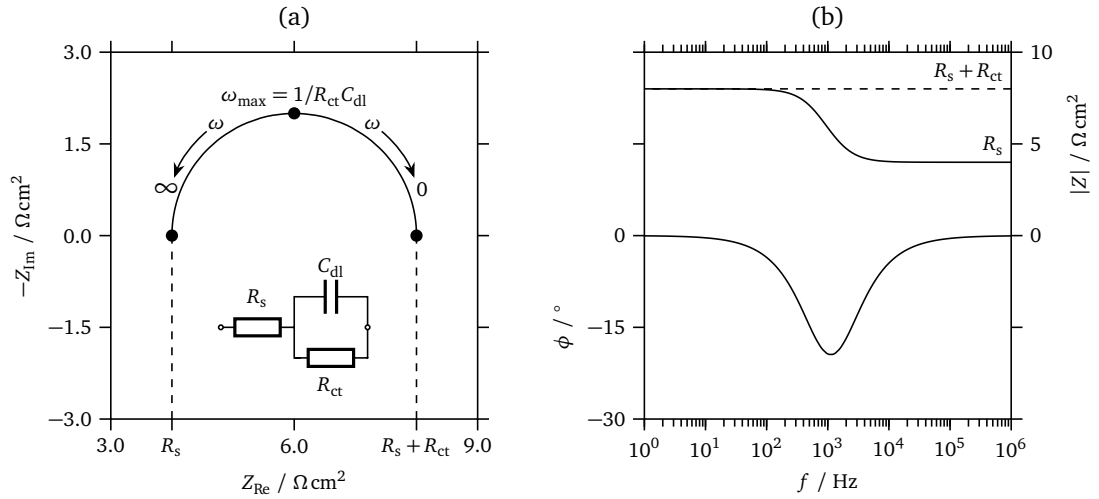

Figure 2.7: (a) Nyquist and (b) Bode plot of the circuit model in the insert, assuming $R_\mathrm{s} = 4\,\Omega\,\mathrm{cm}^2$, $R_\mathrm{ct} = 4\,\Omega\,\mathrm{cm}^2$ and $C_\mathrm{dl} = 50\,\mu\mathrm{F\,cm}^{-2}$. The parameters can be read from the plots directly.

(Figure 2.7(a)) shows a semi-circle, from which the values of the circuit elements can be read directly. The solution and charge-transfer resistances are given by the respective intercept with the ordinate. The double-layer capacitance is calculated from the frequency at the top of the semi-circle. Within the Bode plot (Figure 2.7(b)) on the other hand, both resistances are read from the corresponding intercept of the impedance modulus with the abscissa. In this plot, the double-layer capacitance is not accessible directly, but it can be computed from the characteristic frequency, at which the phase angle shows a minimum [135].

2.4.2 Inductance influence

The aforementioned graphical approach for the extraction of circuit parameters is only applicable to simple circuits, which contain only a few elements. For more-complex circuits, mathematical fitting procedures are employed exclusively towards this end. Even seemingly simple circuits can pose problems. To illustrate this point, consider the common issue of an inductance in series with the electrochemical measurement cell. Such an inductance can originate from the cell cabling, the cell arrangement [136] or the reference electrode [137].

We assume again the case of charge transfer along a bare-metal electrode. Only this time, the cabling inductance (L_c) is taken into account. Therefore, the circuit shown in Figure 2.7(a) is modified with an inductance in series. By adding Equations 2.14 and 2.17, the impedance of the modified circuit is:

$$Z = j\omega L_\mathrm{c} + R_\mathrm{s} + \frac{R_\mathrm{ct}}{1 + j\omega R_\mathrm{ct} C_\mathrm{dl}} \tag{2.18}$$

At this point, the impact of adding the cabling inductance in series is of interest. Clearly, the inductance causes a measurement error, because the cabling is not part of the electrochemical system under study. It is useful to access this error in terms of its relative magnitude compared to the inductance-free circuit. This can be done by comparing the impedance of the modified circuit with that of the inductance-free circuit, all relative to the latter [136]. In other words, it is necessary to subtract Equation 2.17 from Equation 2.18 and to divide the result by Equation 2.17. This yields the relative impedance error (ε_L):

$$\varepsilon_\mathrm{L} = -N_\mathrm{L}(1 + \omega^2 R_\mathrm{ct}^2 C_\mathrm{dl}^2) \tag{2.19}$$

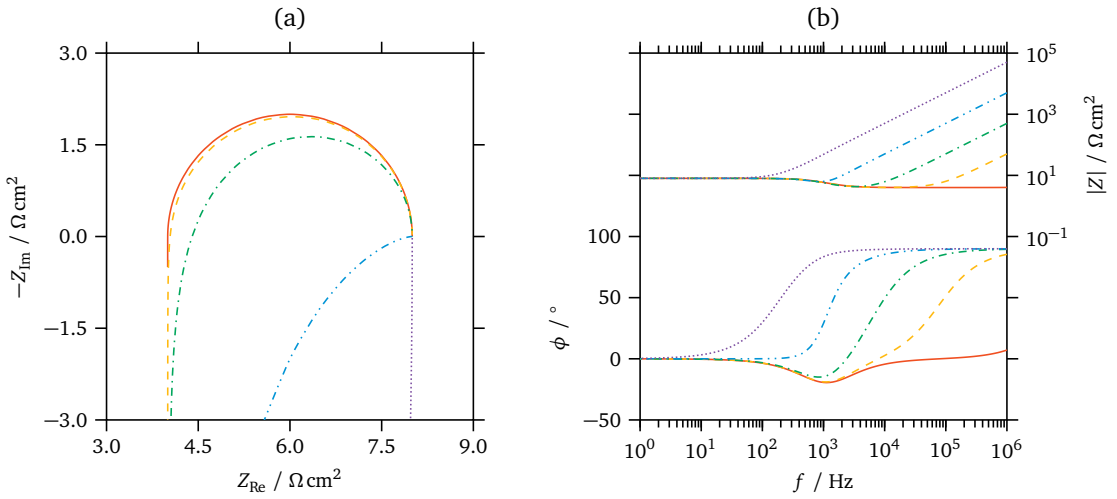

Figure 2.8: (a) Nyquist and (b) Bode plot of the circuit presented in the insert of Figure 2.7, modified with an inductance in series, for $R_s = 4\,\Omega\,\mathrm{cm}^2$, $R_{ct} = 4\,\Omega\,\mathrm{cm}^2$ and $C_{dl} = 50\,\mu\mathrm{F\,cm}^{-2}$. For the inductance ($L_c$), different values are assumed resulting in variations in the dimensionless number N_L: 0.0001 (——), 0.01 (– – –), 0.1 (–·–·–), 1 (–··–··–), 10 (·····).

Herein, N_L denotes a dimensionless number, which equals $L_c/R_{ct}^2 C_{dl}$. From Equation 2.19 it is clear that errors caused by the inductance are more severe at higher frequencies ω. In addition, the error depends on the value of the dimensionless number N_L. This is governed by the magnitude of the inductance, the charge-transfer resistance and the capacitance in relation to each other.

Returning to the Nyquist and Bode representation of the impedance (Figure 2.8), it is possible to visualise these tendencies [136]. For $N_L < 0.01$, the influence of the inductance is negligible and the Nyquist plot shows a semi-circle similar to the inductance-free circuit. One notable difference lies in a shift of the semi-circle's high-frequency limit to more positive values of the imaginary part of the impedance. With increasing values of N_L, the semi-circle becomes more distorted, and the distance between the intercepts with the abscissa shrinks. As N_L approaches unity, the impedance spectrum starts to resemble that of a purely inductive circuit. Within the Bode plot, the increase in N_L becomes manifest in a shift of the phase angle towards 90° at high frequencies and an increase in the impedance modulus. Note that the inductance influence increases with frequency.

The above error analysis shows that graphical methods for the extraction of circuit parameters can produce considerable deviations, in particular in the presence of circuit elements, which are unrelated to the system under study. The use of compu-

tational circuit fitting techniques is recommended in this case, in order to study the electrode-solution interface in isolation [136]. Advantageously, such methods allow complex circuit models to be fit to EIS data of any shape. Unlike graphical methods, they provide a measure for the uncertainty in the fitted parameter.

2.4.3 Complex non-linear least squares regression

Computational circuit-fitting techniques, which are applied to the analysis of EIS data, are termed complex non-linear least squares (CNLS) regression methods [134, 135, 138, 139]. CNLS regression methods are based on minimising an objective function, which computes the deviation between experimental and model data. To this end, squared differences between the measured and simulated impedance are calculated. This calculation is performed separately at each frequency, and the results are subsequently weighted and summed up. Therefore, the objective function $O(\mathbf{P})$ takes the form of a weighted sum of squared residuals [135]:

$$O(\mathbf{P}) = \sum_{k=1}^{N_\mathrm{f}} \sigma_k \left[\left(Z_\mathrm{Re}(\omega_k) - \tilde{Z}_\mathrm{Re}(\omega_k, \mathbf{P}) \right)^2 + \left(Z_\mathrm{Im}(\omega_k) - \tilde{Z}_\mathrm{Im}(\omega_k, \mathbf{P}) \right)^2 \right] \tag{2.20}$$

Herein, the residual value between the data, $Z_\mathrm{Re}(\omega_k)$ and $Z_\mathrm{Im}(\omega_k)$, and the model, $\tilde{Z}_\mathrm{Re}(\omega_k, \mathbf{P})$ and $\tilde{Z}_\mathrm{Im}(\omega_k, \mathbf{P})$, is formed at each frequency ω_k and multiplied with the respective weight σ_k. The data set contains N_f frequencies in total. Consequently the vectors $\boldsymbol{\sigma}$ and $\boldsymbol{\omega}$ contain as many elements. The impedance model itself takes as an input a parameter vector $\mathbf{P}$, which includes N_p elements.

The first step in any CNLS method is the choice of the correct weights. Impedance spectra usually cover several orders of magnitude in terms of frequency and modulus. Thus, varying weights are necessary; otherwise, data points of small magnitude are neglected, leading to a poor fit [134]. Ideally, the impedance measurements are repeated several times to obtain the experimental variance at each frequency. In this case, the weights equal the inverse of the variance. As this is often neither practical nor feasible, other weighting methods are used instead. In proportional weighting, the variance is assumed to equal or to be proportional to the data itself [134, 139]. In modulus weighting, the weights are related to the modulus of the impedance via some function. In the present work, the data is weighted with the inverse of the square of the modulus [138, 140] (Equation 2.10):

$$\sigma_k = \left(Z_\mathrm{Re}(\omega_k)^2 + Z_\mathrm{Im}(\omega_k)^2 \right)^{-1} \tag{2.21}$$

The second step is the transformation of the model equations. CNLS regression methods are based on linear-regression techniques [135]. However, most impedance models are non-linear in nature. Therefore, it is necessary to linearise the model equations first. A Taylor expansion is applied with respect to small changes ΔP_ℓ in each of the parameters around a set of parameter estimates $\mathbf{P}_0$ [135, 141]:

$$\tilde{Z}_{\mathrm{Re}}(\omega,\mathbf{P}) = \tilde{Z}_{\mathrm{Re}}(\omega,\mathbf{P}_0) + \sum_{\ell=1}^{N_\mathrm{p}} \left.\frac{\partial \tilde{Z}_{\mathrm{Re}}}{\partial P_\ell}\right|_{\mathbf{P}_0} \Delta P_\ell + \ldots \tag{2.22}$$

$$\tilde{Z}_{\mathrm{Im}}(\omega,\mathbf{P}) = \tilde{Z}_{\mathrm{Im}}(\omega,\mathbf{P}_0) + \sum_{\ell=1}^{N_\mathrm{p}} \left.\frac{\partial \tilde{Z}_{\mathrm{Im}}}{\partial P_\ell}\right|_{\mathbf{P}_0} \Delta P_\ell + \ldots \tag{2.23}$$

Inserting the Taylor expansions (Equations 2.22 and 2.23) into Equation 2.20, while neglecting higher-order terms, yields [135, 141]:

$$\begin{aligned} O(\mathbf{P}) = \sum_{k=1}^{N_\mathrm{f}} \sigma_k \Bigg[& \left(Z_{\mathrm{Re}}(\omega_k) - \tilde{Z}_{\mathrm{Re}}(\omega_k,\mathbf{P}_0) - \sum_{\ell=1}^{N_\mathrm{p}} \left.\frac{\partial \tilde{Z}_{\mathrm{Re}}}{\partial P_\ell}\right|_{\mathbf{P}_0} \Delta P_\ell \right)^2 \\ & + \left(Z_{\mathrm{Im}}(\omega_k) - \tilde{Z}_{\mathrm{Im}}(\omega_k,\mathbf{P}_0) - \sum_{\ell=1}^{N_\mathrm{p}} \left.\frac{\partial \tilde{Z}_{\mathrm{Im}}}{\partial P_\ell}\right|_{\mathbf{P}_0} \Delta P_\ell \right)^2 \Bigg] \end{aligned} \tag{2.24}$$

The last step is then to find the minimum of Equation 2.24. As there are N_p model parameters, an equal number of first derivatives is necessary, which must be set to zero. For this purpose, the derivative is formed in terms of a change ΔP_m in the parameter P_m ($m = 1, 2, \ldots, N_\mathrm{p}$) resulting in a set of N_p equations [135, 141]:

$$\begin{aligned} \frac{\partial O(\mathbf{P})}{\partial \Delta P_m} = -2 \sum_{k=1}^{N_\mathrm{f}} \sigma_k \Bigg[& \left(Z_{\mathrm{Re}}(\omega_k) - \tilde{Z}_{\mathrm{Re}}(\omega_k,\mathbf{P}_0) - \sum_{\ell=1}^{N_\mathrm{p}} \left.\frac{\partial \tilde{Z}_{\mathrm{Re}}}{\partial P_\ell}\right|_{\mathbf{P}_0} \Delta P_\ell \right) \left.\frac{\partial \tilde{Z}_{\mathrm{Re}}}{\partial P_m}\right|_{\mathbf{P}_0} \\ & + \left(Z_{\mathrm{Im}}(\omega_k) - \tilde{Z}_{\mathrm{Im}}(\omega_k,\mathbf{P}_0) - \sum_{\ell=1}^{N_\mathrm{p}} \left.\frac{\partial \tilde{Z}_{\mathrm{Im}}}{\partial P_\ell}\right|_{\mathbf{P}_0} \Delta P_\ell \right) \left.\frac{\partial \tilde{Z}_{\mathrm{Im}}}{\partial P_m}\right|_{\mathbf{P}_0} \Bigg] \end{aligned} \tag{2.25}$$

By setting Equation 2.25 equal to zero for one parameter at a time, a system of linear equations of the form $\mathbf{A}\boldsymbol{\Delta}\mathbf{P} = \mathbf{B}$ is formed [135, 141], where:

$$A_{\ell,m}\Delta P_\ell = B_m \tag{2.26}$$

$$A_{\ell,m} = \sum_{k=1}^{N_\mathrm{f}} \sigma_k \left(\frac{\partial \tilde{Z}_\mathrm{Re}}{\partial P_\ell}\bigg|_{\mathbf{P}_0} \frac{\partial \tilde{Z}_\mathrm{Re}}{\partial P_m}\bigg|_{\mathbf{P}_0} + \frac{\partial \tilde{Z}_\mathrm{Im}}{\partial P_\ell}\bigg|_{\mathbf{P}_0} \frac{\partial \tilde{Z}_\mathrm{Im}}{\partial P_m}\bigg|_{\mathbf{P}_0} \right) \tag{2.27}$$

$$\begin{aligned} B_m = \sum_{k=1}^{N_\mathrm{f}} \sigma_k \Bigg(& \left(Z_\mathrm{Re}(\omega_k) - \tilde{Z}_\mathrm{Re}(\omega_k, \mathbf{P}_0)\right) \frac{\partial \tilde{Z}_\mathrm{Re}}{\partial P_m}\bigg|_{\mathbf{P}_0} \\ & + \left(Z_\mathrm{Im}(\omega_k) - \tilde{Z}_\mathrm{Im}(\omega_k, \mathbf{P}_0)\right) \frac{\partial \tilde{Z}_\mathrm{Im}}{\partial P_m}\bigg|_{\mathbf{P}_0} \Bigg) \end{aligned} \tag{2.28}$$

This system of equations must be solved iteratively. For a set of starting values $\mathbf{P}_0$, the variables $A_{\ell,m}$ and B_m are calculated according to Equations 2.27 and 2.28. The system of equations is then solved to obtain values for ΔP_ℓ. With these values an updated estimate of the parameter set is calculated. This iterative process continues, until a set of parameters has been computed with the desired precision.

Apart from the parameter values themselves, their variances and covariances are accessible as well [138, 141]. The variables $A_{\ell,m}$ constitute the so-called curvature matrix of the objective function. The inverse of the curvature matrix is termed the error matrix. It contains the variances and covariances as entries. For example, the variances can be read from the diagonal elements of the error matrix.

The quality of the fit is also available from the final value of the objective function. In case the experimental variances are used as weights, the result $O(\mathbf{P})$ of the objective function equals the chi-squared statistic χ^2. Under these circumstances, a good fit implies that the final value for χ^2 divided by the degrees of freedom of the problem $(N_\mathrm{f} - N_\mathrm{p} - 1)$ equals unity [141]. This is called the reduced chi-squared statistic. When applying other weighting methods, the final value of $\chi^2/(N_\mathrm{f} - N_\mathrm{p} - 1)$ may be much smaller than unity, however, even in the case of a good fit. This usually indicates, that the error is assumed to be too large, and that the chosen weights do not correctly represent the error structure of the data set [141].

In order to estimate the parameter variances under these conditions, two assumptions are commonly made: firstly, the chosen weights are presumed to be proportional to the inverse variances in the data, and secondly the reduced chi-squared statistic is fixed to equal unity [138]. This is equivalent to presuming that the computed parameter values fit the data well. In this way, it is possible to determine

the proportionality factor between the weights and the inverse variances at the end of the CNLS algorithm. With the inverse variances in the data now estimated, both the curvature matrix and the error matrix are re-computed with the adjusted weights. This yields the estimated parameter variances from the error matrix.

Different algorithms are available for the iterative computation of a solution, such as the method of steepest descent or the Gauss-Newton method [135, 141]. Most commonly used in CNLS regression of impedance data is the Levenberg-Marquardt method [142], which is also utilised in this work. This is because, compared to the aforementioned methods, it offers improved convergence behaviour and quickly approaches the minimum of the objective function.

3 Through-mask electrochemical micromachining: a review

3.1 Introduction

Through-mask electrochemical micromachining (TMEMM) is a non-conventional machining process, in which a metal substrate is made the anode in an electrochemical cell and thereby dissolved [21, 143]. The substrate is covered with an insulating mask — a patterned thin-film — and hence partly protected. Metal dissolution proceeds only through the mask openings, thus replicating the mask pattern along the surface. The process is sometimes also referred to as electrolytic photoetching [144], electrolytic photopolishing [145], photoelectrochemical milling [146], through-mask electro-etching [14] or photoelectropolishing [147].

TMEMM is related to other methods of anodic metal removal such as electrochemical machining (ECM) and electropolishing (EP) [47, 148, 149]. In ECM the anode is brought into close proximity of a cathode tool to reproduce the tool shape [48, 49]. Concentrated, highly conductive salt solutions serve as the electrolyte to enable high current densities and removal rates (0.2–10 $\mathrm{mm\,min^{-1}}$, 10–300 $\mathrm{A\,cm^{-2}}$) [55, 148, 150]. Accordingly, copious quantities of gas and precipitated metal hydroxides form, and large amounts of heat are released, all of which are removed by pumping the electrolyte through the gap between both electrodes at high flow rates. In EP the anode is dissolved to reduce its surface roughness and to increase its reflectivity [54]. Highly viscous, concentrated mineral-acid solutions are used, so that dissolution proceeds under mass-transfer-limited conditions. Agitation is usually sparse or non-existent. Current densities and removal rates are thus much lower (1–60 $\mathrm{\mu m\,min^{-1}}$, 0.01–0.5 $\mathrm{A\,cm^{-2}}$) [46, 47]. Both ECM and EP are accompanied by the formation of anodic surface films, which determine the resulting surface finish [22, 48, 54].

The application of ECM and EP processes for the fabrication of microstructures is termed electrochemical micromachining (EMM) in general [47, 148, 150]. EMM can be performed utilising both through-mask and maskless methods. The former correspond to the aforementioned TMEMM process. The latter achieve localised

and directional material removal via different means such as a micrometre-sized cathode tool (μECM) [151], an impinging electrolyte jet (Jet-EMM) [152], pulsed current (Pulse-EMM) [153], a focused laser beam (Laser-Enhanced-EMM) [154] or a combination of these methods [152, 155].

Another related, non-conventional machining process is photochemical machining (PCM) [150, 156]. PCM combines photolithography with through-mask, chemical etching to produce intricate parts from thin metal sheets and foils. Concentrated solutions and mixtures of ferric chloride, acids and alkalis are used to this end. The efficiency of the process depends, among other factors, on the corrosion resistance of the substrate and the corrosiveness of the solution. Agitation in the form of spraying or stirring ensures the removal of gaseous reaction products and precipitates, and thus sufficient removal rates (10–100 $\mu m\,min^{-1}$) [150, 156].

All these machining processes have in common a complex interplay of several phenomena, which in sum determine the overall removal rate, the shape profile and the surface finish of the workpiece. In the case of TMEMM, the most important factors in governing these criteria are the conditions of mass transfer and the current distribution between anode and cathode. Both factors are intimately linked with each other, as they influence the presence and properties of surface films along the anode surface. In turn these dictate the mode of dissolution. An additional factor is the aforementioned existence of an insulating mask. As part of this review, these underlying factors are presented, followed by an overview of past and present applications of TMEMM and a list of more recent process developments.

3.2 Current distribution

In TMEMM the formation of cavities and through-holes is governed by temporal and spatial variations in the rate of metal removal along the exposed metal surface [21, 143]. The local metal removal rate is in turn linked to the current distribution along the surface via Faraday's law. Which type of distribution is present depends on the potential field between the electrodes and the boundary conditions along the surface. In principle, it may be of primary, secondary or tertiary kind [157]. This topic has been reviewed previously for different processes, which rely on electrochemical metal deposition [158, 159] and dissolution [21, 143].

The primary current distribution depends only on the potential field between anode and cathode and therefore on the distribution of ohmic resistances within the elec-

trolyte. In this case, surface-kinetic and concentration effects are negligible, and the potential along the anode surface is constant. For the secondary current distribution, surface-kinetic effects need to be taken into account. As a result, the anode potential is a function of current density according to relations such as the Butler-Volmer or Tafel equation. Finally, the tertiary current distribution is present, if considerable concentration variations exist between anode and cathode. The anode potential is governed both by current density and surface concentration in this context. It thus depends on mass transfer. In the presence of mass-transfer limitations, the current distribution depends entirely on concentration variations, and ohmic as well as surface-kinetic effects are negligible [21, 143].

Which type of current distribution is present in practice depends on the conditions at hand. Comparisons with experimental work suggest a primary current distribution can be assumed for large electrolyte flow rates and high average current densities, corresponding to ECM conditions [160, 161]. This is because large flow rates level concentration variations, while high current densities lead to considerable ohmic potential drops in the electrolyte. In contrast, a tertiary current distribution exists, in case surface films form along the anode surface [16, 162]. These films subsequently fix the surface concentration and limit the rate of mass transfer from the metal surface towards the bulk, leading to EP conditions.

In TMEMM the current distribution must be described on different length scales simultaneously [21, 143]. These are the workpiece scale, the pattern scale and the feature scale. On the feature scale, only the geometry in the vicinity of a single aperture in the mask is taken into account, which extends at most to neighbouring features [163]. Arrays of differently sized and spaced features constitute a pattern. The side-by-side arrangement of several such patterns on a single substrate conforms to the workpiece scale. Optimising the current distribution, especially on the pattern and workpiece scale, is a necessity to minimise dimensional variations from feature to feature and from pattern to pattern [23, 24].

The workpiece scale is concerned with the macroscopic current distribution within the electrochemical cell. As such, it is influenced by the cell geometry, the type and dimensions of the anode and cathode, as well as the presence and form of auxiliary electrodes [158, 159, 164]. It is frequently characterised by edge effects, that is maxima and minima in the current distribution positioned along the workpiece edge and in the centre, respectively [23, 24, 165–167]. Numerous treatises on the topic of workpiece-scale current distribution exist for bare electrodes of varying shape, which assume distributions of primary, secondary or tertiary type [164]. These solutions may serve as approximations to more complicated cases.

The pattern-scale current distribution describes variations in current density between different areas on the workpiece. Similarly to the workpiece scale, edge effects in the form of maxima in the current distribution are observed along the margins of a pattern [163, 165, 168, 169]. In general, maxima and minima in the pattern-scale current distribution emerge from spatial differences in the ratio of open to masked areas along the workpiece surface [158, 170–172] and from non-uniform spacing of adjacent features within a pattern [163, 168, 169].

The feature-scale distribution corresponds to the current distribution on the microscopic scale of individual mask openings. Due to the typical length scales involved, which are on the order of tens of micrometres, variations in the current distribution arise from gradients in the concentration field rather than the potential field [158, 159]. For this reason, studies on the feature-scale current distribution often incorporate a detailed treatise of the surrounding geometry [16, 20, 148, 160, 161, 173–177]. Furthermore, microscopic shape changes due to electrochemical deposition or dissolution processes become relevant on the feature scale [158, 159].

3.3 Shape evolution

The calculation of shape changes for an evolving cavity is intimately linked to the current distribution on the feature scale [21, 143] (Section 3.2). The majority of studies on shape evolution in TMEMM [16, 20, 148, 160, 161, 173–177] is in fact limited in scope to the feature scale. Their results are thus not suitable to predict differences in current density and variations in shape profile between different mask openings [163]. For complex mask designs, all length scales must be taken into account to accurately compute the current distribution for each mask opening and to predict the shape of every evolving cavity [23, 24]. Nonetheless, feature-scale studies provide information on the range of achievable aspect ratios, dimensions and shape profiles of the resulting cavities.

Shape-evolution studies distinguish between cavity and through-foil etching, and different parameters and length scales are of importance in each case (Figure 3.1). These parameters are the spacing half-width (b), the metal-substrate thickness (d'), the maximum etch depth (d), the mask thickness (h), the mask-opening half-width (w), the final etch half-width (w') and the mask wall angle (ϕ_m). In the case of cavity etching, the geometry of the problem is usually described by three scales. These are the aspect ratio of the mask opening (h/w), the spacing-to-opening ratio (b/w) and the ratio between the cavity depth and the mask-opening width (d/w) [148, 160,

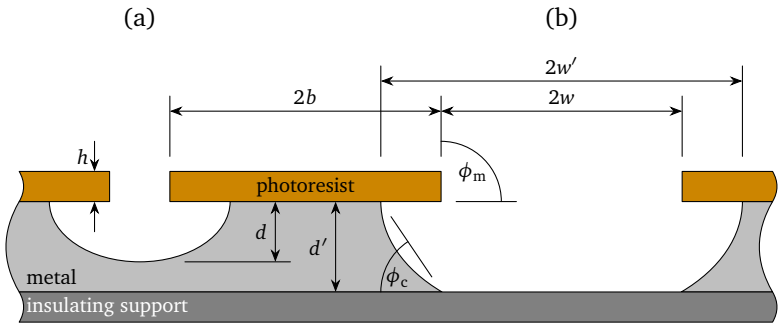

Figure 3.1: Schematic depiction of the defining geometrical dimensions during (a) cavity and (b) through-foil etching of a metal substrate through two mask openings: spacing half-width (b), metal-substrate thickness (d'), maximum etch depth (d), mask thickness (h), mask opening half-width (w), final etch half-width (w'), mask wall angle (ϕ_m), cavity wall angle (ϕ_c).

173]. For through-foil etching, the film-thickness ratio (d'/w) [148] and the cavity wall angle (ϕ_c) of the resulting aperture are also considered [173].

Apart from the assessment of the shape profile, the resulting cavities and through-holes are evaluated in terms of the undercut (x_u) of the mask and the etch factor (N_{EF}). The undercut is defined as the difference between the maximum half-width of the final etched cavity and the mask-opening half-width. The etch factor is defined as the ratio between the undercut and the maximum etch depth as follows [156]:

$$x_u = (w' - w) \tag{3.1}$$

$$N_{EF} = d/x_u \tag{3.2}$$

Both the etch factor and undercut are relevant for the mask design. By taking into account the material removal underneath the mask, the mask openings can be sized to yield the desired cavity width at the end of the process.

Shape-evolution studies usually assume either a primary [20, 148, 160, 161, 173] or a tertiary current distribution in conjunction with mass-transfer-limited dissolution [16, 174–176]. The latter investigations also distinguish between different forms of mass transfer such as diffusion, forced and natural convection. As kinetic effects can be neglected under mass-transfer control, studies on mass-transfer-limited chemical etching are relevant for this discussion as well. Note that, by mathematical analogy, the governing equations and boundary conditions of the diffusion problem are identical to shape evolution under ohmic control [132, 148, 160].

3.3.1 Diffusion

Shape evolution is dominated by diffusive mass transfer in the absence of any convective flow pattern, such as during immersion etching. Under these conditions, shape changes are solely governed by the geometry in the immediate vicinity of the mask opening [163]. To illustrate this point, consider the characteristic length scale of diffusive mass transfer (x_d) [2, 6, 178]:

$$x_\mathrm{d} \sim \sqrt{Dt} \tag{3.3}$$

In quiescent liquids ($D \sim 10^{-5}\,\mathrm{cm^2\,s^{-1}}$) [5] and at a typical time scale ranging from tens of seconds to minutes ($t \sim$ 10–1000 s), changes in the concentration of metal cations propagate at most 0.1–1 mm outwards into the bulk. Thus, features with a width and pitch of 0.1 mm influence only their nearest neighbours.

Early studies [179–182] of the diffusion problem used semi-analytical and numerical techniques to predict shape changes. Simplifications such as assuming a semi-infinite mask opening [179] or an infinitely thin mask [179–182] were used to arrive at asymptotic solutions for etching through line-shaped mask openings. Despite these simplifications, the results were found in favourable agreement with experimental observations [183]. More recently, this work was extended to cover circular geometries as well [178, 184]. A notable result of these studies is the prediction of the so-called edge effect, which describes the bulging of the shape profile in the vicinity of the mask edge (Figure 3.2) [179]. Bulging in turn may lead to so-called island formation, that is the undesirable loss of electrical contact between different parts of thin foils or sheets supported on insulating materials [20].

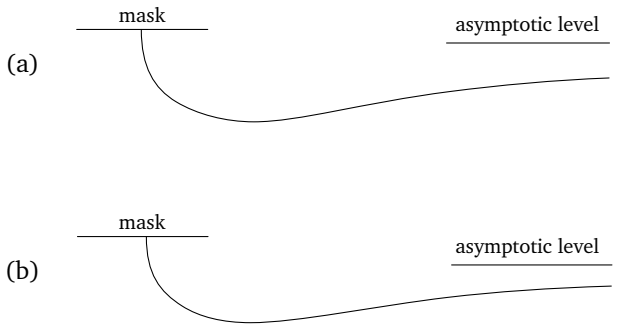

Figure 3.2: Schematic shape profile of a substrate covered with a thin mask and etched through a semi-infinite mask opening exhibiting bulging close to the mask edge: (a) higher etch rate, (b) lower etch rate. Reprinted from [179], by permission of the Royal Society.

Once these geometric simplifications are dropped, numerical methods must be used exclusively to arrive at a solution, in particular when assuming the more realistic case of a finite mask-thickness. The boundary element method has been applied extensively for this problem [16, 20, 148, 160, 161, 173–176], but solutions via finite element [185], finite volume and fixed grid approaches [186, 187] are also available. These investigations have in common that they illustrate the influence of different geometric mask parameters on the feature-scale current distribution, and thus on the shape evolution of individual features.

One important parameter is the aspect ratio of the mask opening [160]. For a thick mask ($h/w > 0.5$), a flat-bottomed cavity forms at first, which subsequently acquires a hemispherical shape (Figure 3.3(a)). The maximum etch depth always remains in the cavity centre. Note that this behaviour is independent of neighbouring features and thus the spacing-to-opening ratio [148]. In contrast, for a thin mask ($h/w = 0.08$) the maximum etch depth is initially displaced from the centre (Figure 3.3(b)). Accordingly, the profile shows an inflection point. As the cavity deepens, the points of maximum etch depth move towards the centre and merge. For the latter case, adjacent features may exert a considerable influence on shape evolution [177], unless they are widely spaced ($b/w > 3$) [20].

This difference in shape evolution stems from variations in the current distribution [160]. For a high-aspect-ratio mask opening, the initial current distribution is practically uniform. As the metal surface recedes, a maximum in the current distribution forms at the cavity centre and remains there. In the case of a low-aspect-ratio mask opening, however, the initial distribution is highly non-uniform; in particular, maxima occur along the edges. With an increase in etch depth, the current distribution becomes more uniform, and the maxima merge in the centre.

For the same reason, the amount of undercutting and the resulting etch factor vary with the mask geometry (Figure 3.4) [16, 20, 160, 173]. For a constant mask-opening half-width and etch depth, the etch factor increases with the mask thickness, thus reducing undercutting. This is because of the more uniform current distribution during the initial stages of shape evolution. Decreasing the mask wall angle has an equivalent effect on the current distribution, and hence on the etch factor. Note that the influence of geometric dimensions diminishes with increases in etch depth, and it is largely negligible for deep cavities ($d/w > 2$). In all cases, the etch factor approaches that of isotropic etching ($N_{\mathrm{EF}} = 1$) over time .

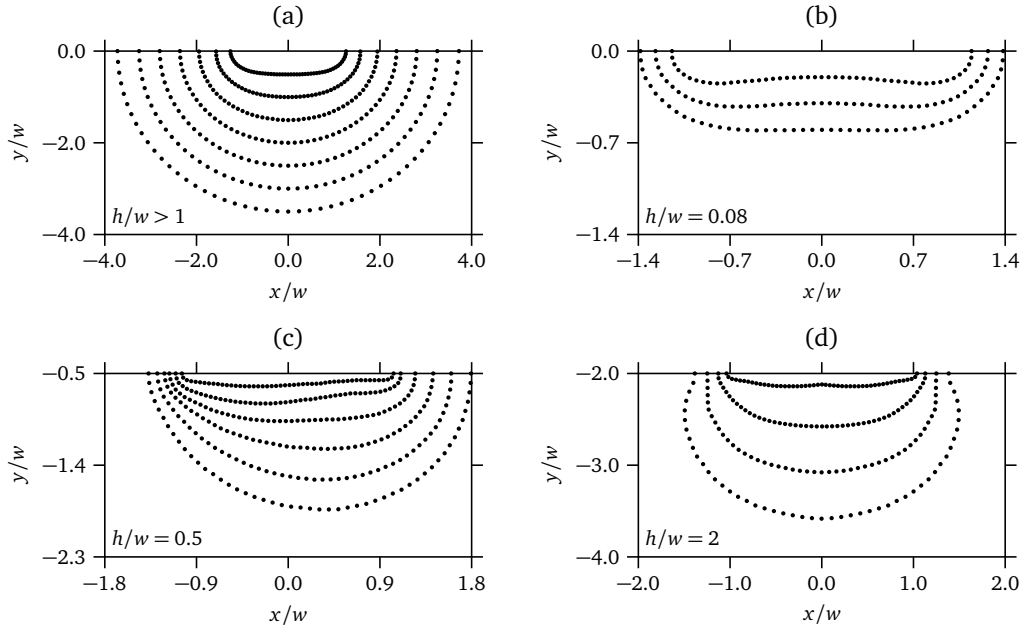

Figure 3.3: Simulated shape profiles in dimensionless coordinates assuming mass-transfer-limited dissolution in conjunction with different modes of mass transfer: (a, b) diffusion, (c) forced convection ($N_{\mathrm{Pe}} = 100$, $N_{\mathrm{Re}} = 0.1$) and (d) natural convection ($N_{\mathrm{Ra}} = 10^4$). Note the different aspect ratios of the mask opening. Data adapted from West et al. [160] and Shin and Economou [185, 188].

3.3.2 Forced convection

Shape evolution is controlled by forced convection, in case the solution is strongly agitated, for example during jet and spray etching or within a flow channel cell. The relative importance of forced-convective and diffusive mass transfer is expressed by the Péclet number [5]:

$$N_{\mathrm{Pe}} = ul/D \tag{3.4}$$

Herein, u denotes a characteristic velocity, l the characteristic length scale and D the diffusion coefficient. The length scale is usually the mask-opening half-width, because it is invariant with time [188]. For the characteristic velocity, especially in numerical studies, the velocity close to the centre of the cavity mouth is chosen [189–191]. In these studies, the Péclet number usually ranges from 10^2–10^6 [185, 188, 190, 192, 193]. For forced convection to have an appreciable effect, the Péclet number should be much larger than unity [190].

The flow pattern in the presence of forced convection depends strongly on the shape of the cavity at hand (Figure 3.5) [162, 190–195]. In the case of a shallow, rounded

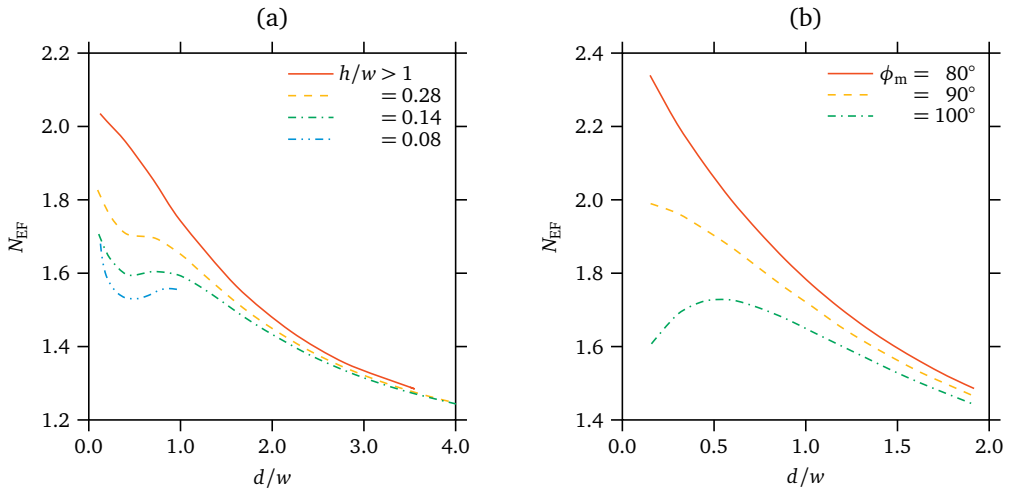

Figure 3.4: Simulated etch factor under diffusion control as a function of the ratio between the cavity depth and the mask-opening width, (a) for different aspect ratios of the mask opening and (b) mask wall angles. Data adapted from West et al. [160], Madore et al. [16], and Shenoy and Datta [173].

cavity [194] the streamlines are merely shifted and the flow field extends into the whole cavity. As the fluid flows along the substrate surface, dissolution products accumulate, decreasing the concentration gradient close to the surface. Accordingly, the mass-transfer rate declines from a maximum in the upstream half to a minimum in the downstream half of the cavity. This behaviour holds true for shallow, rectangular cavities as well, with the modification that circulating flow regions — so-called eddies — occur in the corners [162, 190–192, 195]. This results in additional minima in the local mass-transfer rate.

For round and rectangular cavities of approximately equal depth and width [190, 194, 195], the flow field no longer extends into the whole cavity. Instead, fluid circulates with clockwise rotation within the centre. The bulk solution enters close to the downstream side. Therefore, the maximum mass-transfer rate now occurs in the downstream half, where the circulating fluid first meets the cavity bottom. This eddy effectively reduces the overall mass-transfer rate between the cavity and the bulk. Very deep cavities [189] exhibit several eddies with alternating direction of rotation, which diminish in magnitude. Each subsequent eddy leads to a further decrease in mass transfer. This effect is further compounded in the case of partially covered cavities [185, 188, 191, 193].

The distribution of the mass-transfer rate along the cavity surface in turn influences the evolution of shape changes over time. In the case of a thin mask ($h/w = 0.5$)

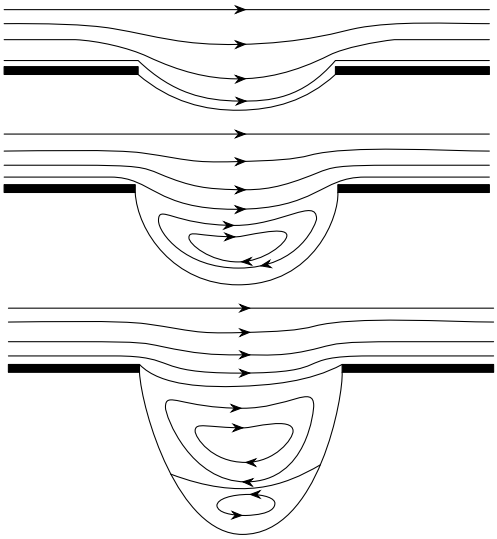

Figure 3.5: Schematic depiction of stream lines and regions of circulating flow during forced-convective flow past a cavity of varying depth. Reproduced with permission from [196]. Copyright 1983, The Electrochemical Society.

[185], material removal initially proceeds fastest in the upstream half due to the distorted flow field (Figure 3.3(c)). Hence, the maximum etch depth is shifted away from the cavity centre towards the upstream side. As the cavity deepens, an eddy forms at some point. Correspondingly, the etch rate is now largest in the downstream half, and the maximum etch depth shifts back. In the case of a thicker mask ($h/w = 2$) [188], the fluid circulates in clockwise direction from the start. Therefore, the etch rate is largest close to the downstream edge. As the cavity grows, a second, weaker eddy forms underneath the first eddy, which rotates in counter-clockwise direction. This second eddy now enhances the etch rate in the upstream half. In both cases, the shape profile conforms roughly to a semi-ellipse, whose centre is shifted away from the centre of the mask opening.

The formation of surface films — induced by the precipitation of metal-dissolution products — complicates this process further [162, 194, 195]. Assuming either a constant film coverage or a constant rate of material removal along the cavity surface, there exists a critical Péclet number for which the surface is either entirely at or below the saturation concentration. These critical Péclet numbers depend largely on the cavity shape and on the physical properties of the system at hand. Secondary flow phenomena such as eddies, which are induced by flow outside the cavity, can thus lead to differences in film coverage, and hence in the etch rate along the surface. This effectively results in anisotropic etching.

Overall, the etch rate is initially much larger in the presence of forced convection compared to diffusion-controlled shape evolution [185, 188, 193]. However, as the cavity deepens, the etch rate continuously decreases. This can be partially compensated by increasing the Péclet number. Similarly, the etch factor is initially higher than under diffusion control [185, 188]. Nonetheless, it drops off over time and approaches the result for purely diffusion-limited mass transfer. In summary, forced convection leads to enhanced etch rates and anisotropic material removal only during the formation of shallow cavities through thin masks. Conversely, forced convection is largely ineffective in achieving deep anisotropic etching [188].

3.3.3 Natural convection

Shape evolution is dominated by natural convection over diffusion, if acceleration fields several magnitudes larger than Earth's gravity are applied, for example in a centrifuge. The relative importance of natural convection and diffusion is expressed in the form of the Rayleigh number [196]:

$$N_{\mathrm{Ra}} = a_{\mathrm{c}} \beta (\Delta c) l^3 / \nu D \tag{3.5}$$

Herein, a_{c} denotes the acceleration field, β the coefficient of volumetric expansion, Δc the concentration difference, l the characteristic length scale, ν the kinematic viscosity and D the diffusion coefficient. For natural convection to dominate over diffusive mass transfer, N_{Ra} should be larger than 100 [192, 196]. Investigated Rayleigh numbers range from 10^3 to 10^5 [185, 192]. Note that the Rayleigh number depends strongly on the length scale in use (Equation 3.5). Initially, it corresponds to the mask-opening half-width, whereas the cavity depth is more appropriate later on. For the relative importance of natural convection to remain constant, a reduction in the mask-opening half-width needs to be compensated by a large increase in the magnitude of the acceleration field [192, 196].

Natural-convection-controlled dissolution within a masked cavity is characterised by a unique flow pattern (Figure 3.6) [196]. Presently, it is assumed that the accumulation of dissolution products leads to an increase in liquid density compared to the bulk, and that an outward-pointing acceleration field is applied perpendicular to the surface. Under these conditions, the liquid enters the cavity in the centre, travels upwards along the side walls and exits close to the mask edge. The liquid entering the cavity is free of dissolution products; thus, the largest concentration gradient and etch rate exist in the centre close to the cavity bottom. As the solution travels

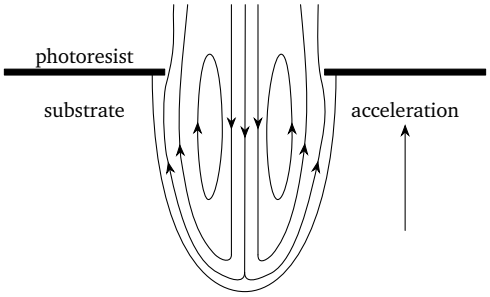

Figure 3.6: Qualitative stream lines within an etched cavity caused by an outward pointing acceleration field. Outward-flowing liquid enriched with dissolution products is denser than fresh liquid entering the cavity. The cavity is occupied by two flow cells, which rotate in opposite directions. Reproduced with permission from [196]. Copyright 1983, The Electrochemical Society.

upwards, it accumulates dissolution products. Therefore, the lowest concentration gradient and etch rate occur close to the mask edge.

Experimentally, the etch rate is found to depend on the size of the mask opening for a given acceleration [196, 197]. This is because in reality more than two of the outlined flow cells can emerge. The characteristic cell size depends on the physical properties of the system, as well as on the magnitude of the acceleration field [196]. If the mask-opening half-width is larger than a single cell, several cells emerge, as is evident from the resulting cellular pattern along the metal surface [196, 197]. In case the mask-opening half-width is on the order of the cell size, however, the aforementioned flow pattern occurs, and the highest etch rate arises. Reducing the mask-opening half-width any further leads to the diminishing importance of natural convection (Equation 3.5). Notably, the etch rate is only weakly size-dependent for mask openings much larger than the cell size [197].

The unique flow pattern induced by natural-convection phenomena reflects on the shape of the evolving cavity [188, 192]. During low-Rayleigh-number flow ($N_{\mathrm{Ra}} = 10^3$), a single rotating flow cell forms initially, resulting in an asymmetric shape profile at first. At higher Rayleigh numbers ($N_{\mathrm{Ra}} = 10^4$), however, shape evolution is symmetric from the beginning. In both cases, the aforesaid unique flow pattern emerges at longer etching times, including flow bifurcation close to the cavity bottom (Figure 3.6). Accordingly, the maximum in the mass-transfer rate occurs in the cavity centre, leading eventually to a rounded, symmetric shape profile. Note that in the latter case ($N_{\mathrm{Ra}} = 10^4$), the maximum cavity width occurs below the position of the cavity mouth [188, 197] (Figure 3.3(d)).

Overall, high-aspect-ratio cavities can be formed in this way with etch factors appreciably higher than in diffusion- or convection-controlled shape evolution [188]. In a theoretical paper, Kuiken [198] argues that more-elongated shape profiles are achievable than have thus far been observed. Experimental and numerical results [188, 196, 197] already show that anisotropic etching with etch factors as high as 10 and an acceleration of the depth etch rate by a factor of 10 to 20 are possible.

3.4 Surface finish

The average surface roughness after TMEMM is typically on the order of 0.1–1 μm [199]. Important factors in determining the appearance of metal surfaces after electrochemical dissolution are current density, electrolyte flow rate and temperature, as well as the composition and structure of the metal or alloy at hand. The influence of these variables on surface finish has been discussed extensively for related processes involving electrochemical metal removal such as ECM, EP and EMM [21, 22, 46–48, 54, 55, 143, 148, 149, 200].

In general, the magnitude of the current density along the anode determines the mode of metal removal, which is either characterised by active or mass-transfer-limited dissolution (Section 2.1) [21, 54, 143, 200]. Below the limiting current density the anode dissolves in the active state. In this case, the dissolution rate is controlled by surface-kinetic steps, such as charge transfer. Differences in the orientation of crystal grains along the surface lead to variations in dissolution rate and thus expose crystal facets. The resulting surface appears rough, dull and non-reflective [169, 201]. Conversely, anodic metal removal at the limiting current density leads to mass-transfer control (Section 2.2.2). Variations in dissolution rate are suppressed and a smooth, polished and reflective surface finish is thus obtained. Complete mass-transfer control is necessary to achieve this [11].

The composition and structure of the anode surface are also of importance in governing the surface finish, in particular during active dissolution [46–48]. When machining pure metals or single-phase alloys, higher dissolution rates are observed in the vicinity of surface defects such as grain boundaries and metallic inclusions, resulting in grain boundary attack and pitting, respectively [169, 202–204]. In multi-phase alloys, different metallic phases often exhibit a distinct polarisation behaviour; thus, adjacent crystal grains belonging to different phases dissolve at varying rates [51]. In all these cases surface roughness increases rapidly. At higher current densities, however, specifically under mass-transfer control, such variations

in the rate of metal removal are typically less pronounced or even suppressed completely. Nonetheless, when comparing mono- and polycrystalline [95, 205], as well as high- and low-purity materials [44, 206], pure single crystals exhibit lower surface roughness after dissolution under polishing conditions.

Hydrodynamic effects due to electrolyte flow also play a major role in determining the surface finish, especially during mass-transfer-limited dissolution [22, 48, 54]. One such effect is striation in flow direction. The formation of striae may be explained by the presence of microscopic protrusions and depressions in the initial surface profile. Vortices form in the wake of such imperfections, which enhance the dissolution rate in the vicinity. Similar structures occur in both ECM and EP, in case dissolution is accompanied by pit formation [207, 208] or gas evolution [46, 111, 209]. In addition, such local variations in flow rate may lead to partial passivation and uneven polishing [48, 207]. By necessity, the influence of such hydrodynamic effects is magnified in TMEMM, where localised metal removal results in height differences along the surface over time. Consequently, non-uniform mass transfer ensues. This may be followed by partial removal of surface films [162, 194, 195], and thus incomplete polishing, or large-scale surface undulations [210].

Another important factor is resistive heating, which influences both the machining accuracy and the surface finish resulting from TMEMM [21]. A well-documented example is TMEMM of titanium in a methanol/sulphuric-acid electrolyte. Electrochemical titanium dissolution at room temperature is accompanied by pitting [16] and small-scale surface undulations [21, 210]. In both studies resistive heating is reported as the likely cause. In low-conductivity solutions, such as the employed acid-in-alcohol electrolyte [211], and at high current densities, the liquid in the vicinity of the exposed metal heats up considerably. This may lead to the formation of inhibiting oxide films [16] and the establishment of small-scale, natural-convective flow cells [21, 210]. Lowering the electrolyte temperature and optimising the applied potential, however, can alleviate these problems [175, 212].

3.5 Masking methods and materials

During TMEMM the anode surface is partially protected from dissolution by a patterned thin-film, the so-called mask. Today, several methods and materials are available to create the mask, including photo-sensitive polymers, metal oxides and inert silicones. Whichever material is used to fabricate the mask, it must satisfy several criteria to fulfil its purpose [143, 156]. First and foremost, the mask material

should be an insulator to enable preferential electrochemical dissolution through the mask openings. Secondly, the material must show sufficient chemical resistance to the electrolyte. In particular, its dissolution rate must be low compared to that of the anode material. To this end, a defect-free mask of uniform thickness is advantageous. Thirdly, the mask should adhere firmly to the anode to facilitate accurate pattern transfer. Fourthly, the process and material cost need to be taken into account. Each of these points should be considered when making a choice.

3.5.1 Photoresists

By far the most widely used masking method is photolithography, which employs photo-sensitive polymer and resin coatings, so-called photoresists. These are extensively employed in silicon micromachining [213], electrochemical microfabrication [143] and the manufacture of intricate parts in aerospace, automotive, electronic and optical systems to name a few [214]. The working principle of photolithography revolves around the fact that the structure of photo-sensitive polymers changes upon exposure to ultraviolet (UV) light [215].

Photoresists are divided according to the form, in which they are supplied, and the type of photochemical reaction, which occurs during exposure to UV or near-UV light [213, 216]. Liquid resists are solvent-based, whereas dry-film resists are supplied in sheet or roll form. Their typical coating thickness ranges from 2–5 µm and 10–50 µm, respectively. Both liquid and dry-film resists may be of positive- or negative-tone type. UV exposure of positive-tone resists leads to a decrease in molecular weight and thus an increase in solubility, either via photo-catalytic scission of polymer chains or photolysis of a photo-active sensitiser. In this manner, subsequent development creates a positive image of a design. In contrast, negative-tone resists, when subjected to UV light, become less soluble, either due to cross-linking of polymer chains or the formation of products with higher molecular weight. Hence, a negative image forms after the development step.

Several pre- and post-processing steps are necessary to create a photoresist mask (Figure 3.7) [213, 216]. These are described by way of example for a liquid, positive-tone resist. At first, the substrate must be thoroughly cleaned and degreased to promote sufficient resist adhesion. Next, the surface is uniformly coated with a thin layer of liquid resist. Spin-coating is most often used for this step. Afterwards, the resist film is subjected to a pre-exposure bake to evaporate excess solvent. The photoresist is then exposed to UV light through a photo-tool, such as a patterned,

chrome-coated glass plate. With the exposed parts of the resist film thus chemically modified, the substrate is rinsed with developer solution. This leaves only the unexposed parts of the resist in place. After this, the substrate is dried, and the photoresist is strengthened via a post-exposure bake. Following a subsequent chemical or electrochemical etching step, the resist film is stripped. In the case of positive-tone resists, aqueous alkalis and organic solvents are employed for stripping. These resists are thus incompatible with alkaline electrolytes.

Photolithography and photoresist-processing technologies are well-established at this point, and many suppliers for equipment and materials exist. Numerous resists catered for different applications and processing conditions are available. Unless highly aggressive solutions are employed, a suitable resist should exist for any application. Furthermore, the parallel nature of the photolithography process enables the creation of multiple mask patterns simultaneously. Nonetheless, a few downsides need to be considered as well. The necessary clean-room facilities and multiple processing steps create considerable capital and operational costs. The lack of an option to re-use the mask adds to these costs. Also, photolithography is largely limited to planar substrates. Though exposure equipment and photo-tools for non-planar substrates exist, these are specific to each geometry [17, 176, 217–220].

3.5.2 Oxide films

In response to the drawbacks of traditional photoresists and photolithography processes, resists based on oxide films, so-called oxyresists, were developed [221]. The oxyresist technology exploits the fact that some metals like aluminium and titanium naturally form adherent, passivating, nanometre-thin oxide films. These films can be grown artificially to much larger thickness via anodising processes [52, 53]. Oxide films lend these metals their good corrosion resistance. Therefore, they were considered for use in TMEMM in conjunction with highly corrosive and aggressive electrolyte solutions, in particular for Al and Ti micromachining.

Several processes based on oxide films have been developed since the first inception of oxyresists. In the initial process variant [221, 222], an oxide film is selectively formed on the metal by first applying and patterning a positive- or negative-tone photoresist via photolithography, which is followed by anodising the exposed surface in a suitable solution. After stripping the photoresist, the oxide film remains and forms either a negative or positive image of the mask design. In this way, it acts as a protective mask during the successive electrochemical etching step. However, the

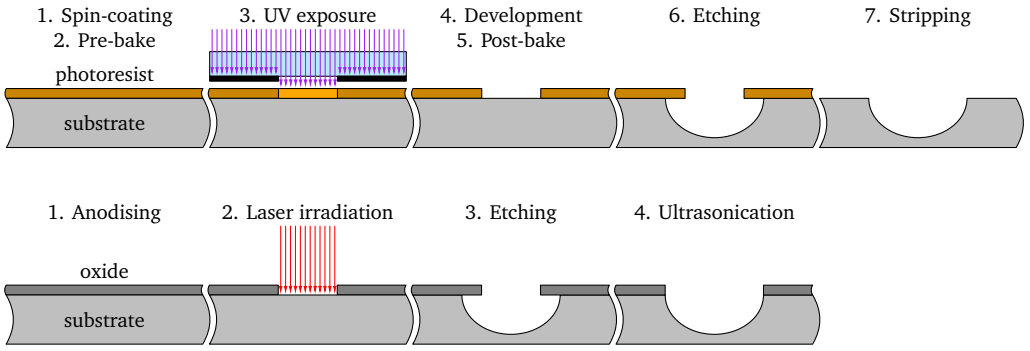

Figure 3.7: Pre- and post-processing steps of an electrochemical etching process using either photolithography in combination with a positive-tone photoresist or OFLL for pattern transfer (adapted from Madou [213] and Chauvy et al. [223]).

photolithography step can be eliminated all together by the use of oxide film laser lithography (OFLL) instead [18, 175, 212, 223–225].

OFLL consists of several process steps in series: anodising, laser irradiation, electrochemical etching and ultrasonication (Figure 3.7). The substrate in question is first anodised in an appropriate electrolyte solution by applying a sufficiently high anodic potential. The thickness of the oxide film is accurately controlled by the anodising time and current density. The oxide is then locally irradiated and removed from the substrate surface with a sequence of nanosecond-long laser pulses. Solid state (Nd:YAG) [18] and excimer (XeCl) lasers [223] have been used for this step. After the electrochemical etching step, the overhanging oxide film can be removed chemically or ultrasonically. Note that OFLL on titanium substrates has been reviewed previously by Landolt and Datta [21].

In a similar approach, the anodising step can be replaced by using a laser to create the protective oxide film directly [226]. In the case of a stainless-steel substrate, subjecting its surface to laser irradiation with an ytterbium-doped, pulsed fibre laser leads to changes in its surface structure, which render the irradiated surface more resistant to electrochemical etching. These changes include oxide formation, phase transformations, and a homogenisation of the grain structure close to the surface [226, 227]. Successful application of this approach is, however, linked to the ability to form homogeneous oxide films of uniform thickness.

When comparing OFLL with photolithography, two aspects need to be considered [210]: cost and flexibility. OFLL does without working in a clean-room environment with photoresist and developer solutions as consumables. On the downside, the cost-effectiveness of OFLL suffers from the serial nature of the laser-masking

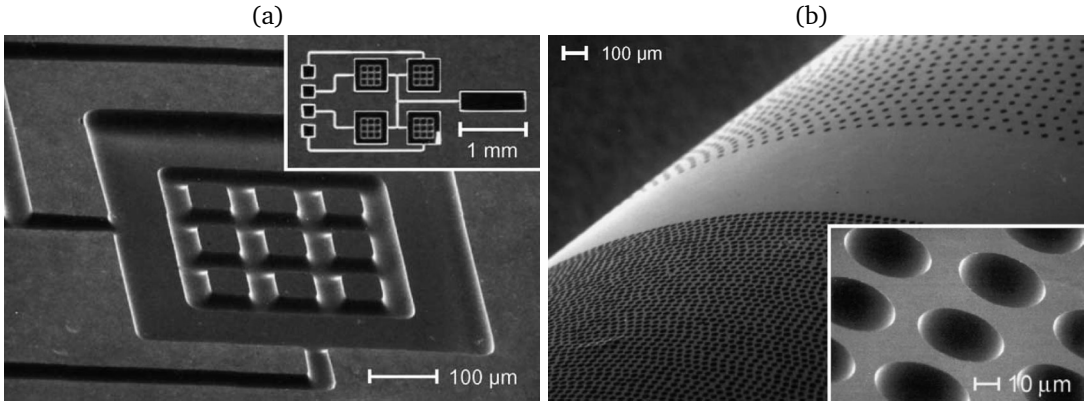

Figure 3.8: SEM images of (a) a two-level microstructure machined in titanium and (b) an array of micrometer-sized cavities on the surface of a titanium cylinder. Reprinted from [212]. Copyright 2003, with permission from Elsevier.

and -marking process. Also, the investment and operating cost of the laser need to be taken into account. For the mass production of devices, photolithography is likely the more economically viable option. Also note that OFLL is limited to metals onto which a protective, adhering oxide film can be grown [176]. Nonetheless, when it comes to Al and Ti micromachining of prototype devices, OFLL offers unparalleled flexibility. It enables the machining of both multilevel structures [174, 175, 212] and non-planar surfaces [212] (Figure 3.8). For multilevel structures, multiple steps of laser irradiation and electrochemical etching are applied in series. For non-planar substrates, the equipment for laser irradiation is combined with an automated sample stage to move and rotate the substrate [210, 223].

Initially, the good chemical resistance and spatial resolution of oxyresists, compared to photoresists in use at the time of their introduction, was mentioned as an inherent advantage [210, 221]. Traditionally, positive-tone resists are unstable in solvent-based electrolytes, whereas negative-tone resists suffer from poorer resolution [213]. Since the inception of oxyresists, however, advances in photoresist technology have lead to substantial improvements, at least partially invalidating this claim. For example, epoxy-based, negative-tone resist formulations like SU-8 enable sub-micrometre-sized features and offer high chemical resistance [228].

3.5.3 Polydimethylsiloxane

An additional downside of both photoresists and oxyresists is their lack of re-usability. Each substrate must again be treated to form a protective film, which is subsequently patterned and stripped in the end. If the mask were re-usable, these process steps could be omitted resulting in time and cost savings. The required re-usability, however, contradicts the criterion of good adherence between the mask and the substrate during the electrochemical dissolution step. One such candidate is a patterned silicone film made from polydimethylsiloxane (PDMS) [229].

The creation of a PDMS mask requires the fabrication of a mould for casting. The mould corresponds to a negative image of the desired mask design. For example, if the mask should contain an array of linear trenches, then the mould includes line-shaped crests. Photolithography in combination with a negative-tone SU-8 photoresist may be employed for this step [229]. PDMS gel is then cast into the mould, while applying a vacuum to quickly and thoroughly distribute the gel. Afterwards the gel is allowed to cure and the resulting PDMS mask is de-moulded.

While this process provides a low-cost, re-usable mask, a number of limitations exists as well. The chemical resistance of PDMS is limited, especially when exposed to concentrated acids or alkalis [230]. Accordingly, the use of PDMS masks is thus far limited to electrolytes consisting of neutral salt solutions [231–234]. In addition, re-usability is linked to simple mask designs such as hole arrays, which lack intersecting or nested features. Furthermore, good adhesion between the mask and the substrate is necessary, otherwise increased undercutting is observed [234].

3.6 Metals and electrolytes

TMEMM is in general applicable to the machining of any electrically conductive material, be it a metal, semiconductor or conductive ceramic [9, 150]. In an extensive study Almond and Allen [199] showed that an electrolyte suitable for TMEMM can in principle be found for any metal or alloy, including difficult-to-etch materials like tantalum, titanium, tungsten and nickel superalloys. In many instances, several solutions are available to machine a particular substrate. The various electrolyte solutions can be broadly classified as aqueous and non-aqueous. Aqueous electrolytes are further divided into saline, acidic and alkaline solutions. Each of these groups has distinct advantages or areas of application.

Saline electrolytes are employed most frequently and for the widest range of materials, among them the noble metals platinum, gold, silver, copper and their alloys [9, 146, 199, 201, 219, 220, 235–238]. Non-noble metals encompass hafnium [199], molybdenum [146] and zirconium [199]. In addition, iron-nickel [161, 239], nickel [199] and titanium alloys [234, 240–243], as well as a range of austenitic and martensitic stainless steels [13, 14, 146, 168, 169, 201, 226, 231–233, 235–237, 244–249] are machinable. The widespread application of saline electrolytes is based on their non-toxicity, low cost, and long-term stability [9, 10]. They are usually based on ECM solutions; thus, saline electrolytes contain NaCl, $NaNO_3$ or mixtures thereof and are used at or around room temperature. In concentrated, highly conductive solutions very high current densities and thus etch rates can be achieved (20–100 $A\,cm^{-2}$, 10–60 $\mu m\,min^{-1}$) [10, 146]. Advantageously, material removal in saline electrolytes only occurs, in case a potential or current is applied to the anode; otherwise the solution remains basically inert.

Acidic and alkaline electrolytes are typically made from viscous solutions of mineral acids like H_2SO_4 and H_3PO_4, and inorganic alkalis such as NaOH and KOH. Acidified chloride electrolytes are also in use. Machining often takes place via immersion etching; hence, current densities and etch rates are usually lower than in saline electrolytes (0.1–10 $A\,cm^{-2}$, 1–10 $\mu m\,min^{-1}$) [147, 199, 250, 251]. A wide range of metals has been machined, namely aluminium [18, 225, 252], chromium [199], copper [12, 167], hafnium [199], molybdenum [199, 253, 254], niobium [255], platinum [256], tantalum [255], titanium [257] and tungsten [199, 258]. This list is complemented by several cobalt [199, 251], copper [199, 252] and nickel alloys [199], as well as a number of stainless steels [147, 245, 250, 259, 260]. Parts machined in acidic and alkaline electrolytes often distinguish themselves by their superior surface finish. This is because frequently the specific metal-electrolyte combination permits mass-transfer limited dissolution and hence EP. Examples for this are molybdenum [261], nickel [262] and niobium [263] in acidic solutions, as well as tungsten [264] in alkaline solutions.

Non-aqueous electrolytes comprise either salt-in-alcohol or acid-in alcohol mixtures. The most common electrolyte constituents are H_2SO_4 or LiCl, which are dissolved in methanol or ethanol. These solutions are primarily applied to the machining of difficult-to-etch metals and alloys, including nickel [17, 199, 218], tantalum [265, 266], titanium [11, 16, 174–176, 212, 221, 223, 267, 268], tungsten [199], and nickel-titanium alloys [199, 269–273]. During immersion etching, typical etch rates are on the order of 5–15 $\mu m\,min^{-1}$ [11, 17, 199, 218, 272]. The main incentive for the use of alcohol-based electrolytes stems from the fact that many of the above materials form inhibiting oxide films in the presence of small amounts of water

— notably tantalum [274], titanium [275] and nickel-titanium [204] — which severely limit the dissolution process. Therefore, water-free electrolytes should be used instead. In addition, initially present oxide films must be stripped first and their regrowth prevented, either via chemical [273] or electrochemical means [274, 275]. Alcohol-based electrolytes have also proven useful when machining aluminium [276], cobalt [199] and iron alloys [17, 218], as well as steels [17, 145, 218, 259]. Nonetheless, their application is likely limited to metals and alloys, which are otherwise only machinable with difficulty. This is because specific safety concerns arise due to the toxicity, flammability and limited long-term stability of mixtures based on non-aqueous solvents [265, 266].

3.7 Technical applications

Historically, TMEMM derives from engraving processes developed for printmakers and artists in the 19th century. A first mention is made in a British patent, granted to Thomas Spencer and John Wilson in 1840 [277], which describes the fabrication of printing plates and cylinders made from copper and other metals by means of electrochemical dissolution. In this case, the resist contained asphalt, wax and various resins [278] and was drawn upon manually with a sharp tool! Shortly thereafter, a method for etching silver-coated copper printing plates, partially protected by a thin layer of mercury, was presented by William Grove in a talk given to the London Electrical Society in 1841 [279, 280]. In the following year, Gottfried Osann published a short treatise on the subject in German [281], describing his engraving experiments and showcasing some example prints (Figure 3.9).

From 1950–1970 the advent of modern photoresist technology, in the form of the KTFR- and the AZ-family of resists, stimulated rapid growth in the microelectronics industry [282]. This coincided with a renewed interest in electrochemical etching processes, as is attested by several Kodak publications from the 1960s [144]. Applications from that time include the etching of supported metal thin-films for memory arrays [283], chip metallisation on integrated circuits [252, 256, 258, 284] or diodes [285]. The goal of applying TMEMM was often to supplant an existing chemical etching process, in particular where difficult-to-etch materials were concerned. Several review articles [9, 143, 148, 149, 200, 286] have since then covered TMEMM of components for microelectronic systems. Further examples include detachable electrical contacts [236, 237], metallisation layers on printed circuit boards [9], or recording head laminations and suspensions [237, 251].

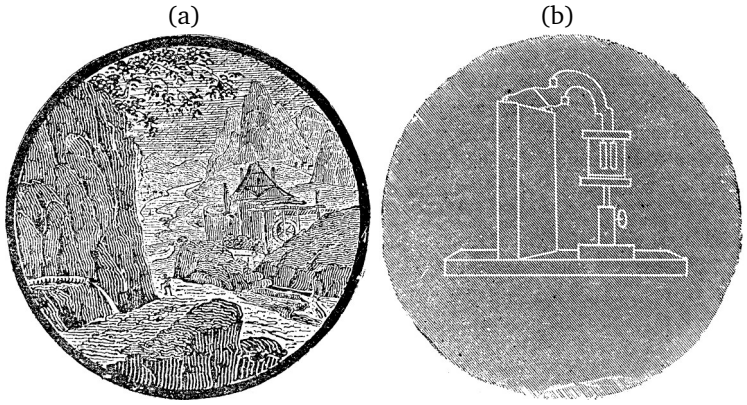

Figure 3.9: Reproduction of two prints from electrochemically etched tin plates: (a) landscape drawing and (b) sketch of the utilised electrochemical cell (reprinted from Osann [281]).

From the 1980s onwards, applications include the manufacture of precision parts from thin metal foils, often as an alternative to PCM of difficult-to-etch metals. Through-foil etching allowed a bewildering variety of parts to be formed for use in mechanical, electronic, optical, analysis and separation systems. Articles thus machined encompass stainless-steel edge filters [145, 259], tantalum specimen holders [265], molybdenum apertures [146], elgiloy springs [19], copper and stainless-steel ink-jet printer nozzle plates [201, 235], invar shadow masks [161, 239], molybdenum evaporation masks [10], Cu/Pd gas separation membranes [12], aluminium cantilevers [276], and stainless-steel bumping masks [260].

In the mid-1990s, applications of through-foil etching moved to microactuators made from thin films ($< 200\,\mu$m) of NiTi shape-memory alloys (Figure 3.10). Such devices are available via thin-film deposition, laser beam machining (LBM), PCM and TMEMM [271, 287–292]. PCM of NiTi alloys, however, necessitates the use of aggressive hydrofluoric/nitric-acid mixtures and results in severe undercutting and rugged side walls [290]. By comparison, TMEMM of NiTi alloys in acidified methanol produces smooth and straight side walls [289, 290] at similar etch rates [271, 272]. In contrast to thin-film deposition and LBM, TMEMM avoids the use of costly vacuum equipment and the creation of heat-affected zones, respectively. These microactuators were subsequently destined for use in microelectromechanical systems, microvalves [271, 291] and bending catheters [269, 270, 293].

A novel field of application lies in bulk micromachining with the aim to modify the surface structure of metals. Herein, cavity etching enables the formation of rounded, micrometre-sized pits, which are related to optical, tribological, biological and medical purposes. The parallel nature of TMEMM is key in creating thousands

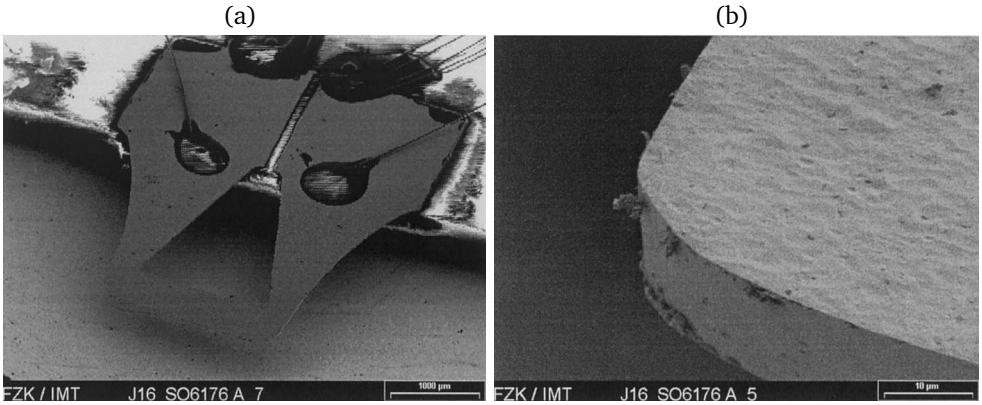

Figure 3.10: SEM images of a beam-cantilever device machined in 50 µm thin foil made from NiTi shape memory alloy: (a) overview and (b) close-up of side wall. Reprinted from [294]. Copyright 1999, with permission from Elsevier.

of pits simultaneously. These pits subsequently form microlens arrays [225], reduce the friction in bearing systems [219, 220, 231–234, 243, 249, 295, 296], or enhance the biocompatibility of medical implants [11, 242, 267] (Figure 3.8(b)).

Another recent area of interest is the fabrication of microfluidic devices. These can be manufactured from a range of relevant engineering materials such as aluminium, stainless steel and titanium. Example structures thus machined include spiral-shaped and straight microchannels [16, 223], interconnected chambers [18, 174], multi-level cavity and channel networks [210, 212] (Figure 3.8(a)) and parts of a microvalve [17]. Studies closer to the application stage [13, 14] showcase the formation of serpentine gas-flow-field channels in stainless-steel bipolar plates, which have already been tested in proton-exchange-membrane fuel cells [15].

3.8 Technical and financial considerations

Today, many machining processes are available to the engineer of microfluidic devices made from metals and alloys, such as micromixers, microreactors or micro heat exchangers [2, 6]. These include both traditional and non-traditional micromachining techniques [297]. Traditional micromachining (such as microdrilling, LBM and electrical discharge machining (EDM)) creates single through-holes and cavities in series, whereas non-traditional micromachining (for example PCM, TMEMM and stamping) forms multiple features simultaneously. For this reason, the latter processes are capable of unparalleled scalability [297].

In light of the resulting economy of scale, combining photolithography with electrochemical-deposition and -etching processes (such as in TMEMM) is expected to enable the fabrication of microfluidic components in large quantities at low cost [8]. However, verifying this claim is difficult, because data on investment and operating cost for comparison with other micromachining techniques is not available. For PCM on the other hand there exist some studies on its economic aspects [156, 298]. In addition, applications of PCM to the manufacture of microreactors are numerous [6, 28, 299–304]. PCM and TMEMM are both through-mask processes and thus resemble each other in many aspects. Hence, financial considerations towards PCM should be transferable to TMEMM, at least partly.

Allen [156, 298] compared the cost of PCM with stamping, LBM and wire-EDM for the manufacture of thin model parts of varying complexity and thickness made from stainless steel. Wire-EDM is found to be the most economic technique for small quantities, whereas stamping is most economic at large batch sizes. For an intermediate number of parts ranging from dozens to thousands, PCM and LBM compete with each other for economic feasibility. Because in PCM the machining time depends on the substrate's thickness, it becomes more viable for thinner parts. In addition, the parallel nature of the PCM process decreases the cost per part, as part complexity rises. To put this into perspective: it has been demonstrated that stainless-steel shims for a stacked microreactor/combustor assembly, which contains 340 shims in total, can be produced by way of PCM at a cost well below 1 US$ per shim [299, 300]. It is expected that these conclusions hold for TMEMM as well.

Indeed, cost savings are anticipated when switching from PCM to TMEMM [149, 150]. Consider for example stainless steel, tantalum and titanium, which are of special interest for microreactor fabrication [6]. In the PCM industry, tantalum and titanium are among the difficult-to-etch metals, which necessitate the use of aggressive etchants, such as hydrofluoric/nitric acid and aqua regia [156, 216, 305]. By comparison, safer alternatives can be used in TMEMM, like methanol/sulphuric acid [216, 265] or saline solutions [199]. In the case of stainless steel, acidified ferric-chloride etchants [156] can be substituted with concentrated NaCl electrolytes [146]. Thereby, the requirements towards equipment lining, safety precautions and waste disposal are reduced. Note that switching to TMEMM is also accompanied by time savings due to increased etch rates [10, 265].

Despite the capability to mass-produce parts at low cost, the continued use of PCM for microreactor fabrication is limited by technical constraints [2]. The isotropic nature of the process leads to combined perpendicular and lateral etching, which

result in large undercuts of the mask. Also, the etched metal surface is comparatively rough (0.5–5 μm) [305–308]. Therefore, channels and cavities are limited to shallow profiles (aspect ratio < 0.5–0.6) [6, 304] and large widths (> 300 μm) [2] in one-sided etching. For the same reason, the minimum aperture size in double-sided etching of thin sheets lies on the order of the sheet thickness [156]. Note that dimensional tolerances also depend on sheet thickness.

The above-mentioned downsides of PCM can be overcome one way or the other, if the metal substrate is instead made the anode in an electrochemical cell as in TMEMM. While undercutting occurs also in TMEMM, the phenomenon is usually less severe [10] and there exist more parameters to optimise the process in this regard [235]. Also, at sufficiently high electrode potentials electrochemical metal dissolution operates under mass-transfer-limited conditions, which results in an improved surface finish (0.1–1 μm) [18, 145, 147, 199, 240–242, 250, 257, 272, 276]. For this reason, the rate of material removal depends strongly on the hydrodynamic conditions within the cell. Immersion etching while stirring is usually slower (2–20 $\mu m\,min^{-1}$) [199] than etching in a flow cell (10–100 $\mu m\,min^{-1}$) [10, 13, 146, 161]. In general, TMEMM proceeds much faster than PCM [149, 150]. In fact, where direct comparisons are made under similar hydrodynamic conditions, the etch rate is at least one order of magnitude larger [10, 309]. In this manner, high-rate metal dissolution and polishing take place in parallel.

Compared to traditional micromachining techniques like μEDM, LBM and micromilling, TMEMM offers several advantages as well. Take for example results on the machining of through-holes in thin metal foils for each of these techniques [10, 146, 201, 310]. TMEMM produces burr-free edges thus superseding further processing steps. The mechanical properties close to the surface remain unchanged due to the absence of heat-affected zones and tool wear. This also results in a superior surface finish with sub-micrometre surface roughness. In addition, the parallel nature of the process enables the machining of thousands of through-holes in parallel, hence reducing the overall machining time.

3.9 Process variations and recent developments

3.9.1 TMEMM with sandwiched mask

In an effort to improve the current distribution and thus the uniformity of material removal during TMEMM, the use of a patterned cathode tool has been suggested

[168, 309]. In this process variation, the cathode is made from a thin metal sheet and covered on one side with an insulating film. Through-holes and slits are machined into the sheet beforehand, corresponding to the desired mask design. The patterned cathode is then placed in direct contact with the substrate, while the insulating film is sandwiched between them. Alternatively, a thin metal layer may be deposited directly on top of a protective, polymeric thin-film, for example via electroless plating [309] or sputter deposition [268].

Compared to the classic electrode arrangement, this setup leads to a more uniform current distribution on the pattern and the feature scale [168, 295, 309]. This results in more uniform material removal between adjacent features and less undercutting. In addition, the patterned cathode tool can potentially be re-used several times. However, this setup is only applicable to mask designs, where each part of the mask is connected to the whole. Another prerequisite is a sufficiently tight seal between the substrate and the cathode tool, otherwise leakage may lead to stray attack. Furthermore, depending on the cathode thickness, the removal of dissolution products from the machined cavities is hampered.

3.9.2 TMEMM with masked cathode tool

In an attempt to reduce the number of costly and time-consuming photolithography steps, the application of a masked cathode tool has been proposed [238]. In this case, the cathode is covered with a patterned mask, which represents the microstructure to be machined, and placed in close proximity to the anode. Upon the application of a current or potential, the whole anode surface dissolves, but preferential material removal occurs in areas directly opposite to the mask openings. Dissolution products are removed by pumping the electrolyte through the gap. As such, this process represents a hybrid between TMEMM and ECM [248].

The main advantage lies in time and cost savings, as only the cathode needs to be masked. Ideally, the resulting cathode tool is re-used many times. Accurate pattern transfer, however, necessitates a reduction of stray currents in areas opposing masked parts of the cathode. To this end, sufficiently large variations in the ohmic drop across the interelectrode gap are created by lowering the electrolyte conductivity, by operating at high current densities or by decreasing the gap size [167, 238, 247]. A gap size as small as 20 µm has been used, while still enabling sufficient electrolyte flow [247, 248]. Nevertheless, the depth and accuracy of machined features is expected to be limited due to a gradual rise in stray currents [167, 238].

3.9.3 Ultrasonically assisted TMEMM

Electrolyte agitation in TMEMM occurs normally by use of flow cells [169], rotating discs [16], impinging jets [10, 168] and stirrers [199]. Ultrasonic agitation has by comparison scarcely been employed, despite the well-documented benefits for electrochemical processes [311]. These include the formation of highly reactive, intermediate species and the removal of inhibiting, passive films, which are both caused by ultrasonically induced cavitation events. This is generally accompanied by a decrease in diffusion-layer thickness and the generation of convective flow patterns, leading to enhanced rates of mass transfer.

The likely cause for the sparse use of ultrasonication in TMEMM is due to the foreseeable mechanical stress, which is impressed upon the mask material at the same time. This may result in a loss in resist adhesion, cracking and ultimately in the exposure of the underlying substrate [253, 312]. Nonetheless, ultrasonically assisted TMEMM can be implemented successfully, if due care is given to the choice of ultrasound frequency, power input and overall cell geometry. For example, Allen et al. [268] report results on TMEMM of through-holes in titanium foil using a combination of ultrasonic agitation and ultra-short voltage pulses. The frequencies of the employed lead-zirconate-titanate transducer had to be carefully chosen to avoid damaging the resist layer. Using an electrolyte consisting of H_2SO_4 in methanol at room temperature, the etch rate could be increased by a factor of 1.2 to 1.5 and the average roughness of the machined surface decreased from 1.1 µm to 0.3 µm.

3.9.4 Pulse- and Pulse-Reverse-TMEMM

In general, constant currents or potentials are applied in TMEMM. However, the application of pulsed input signals — termed Pulse- or Pulse-Reverse-TMEMM — is advantageous under certain conditions. Using the superposition of different waveforms, complex input signals can be generated [256], but usually simple square waveforms are employed. Anodic (Pulse-TMEMM), as well as a combination of anodic and cathodic pulses can be used (Pulse-Reverse-TMEMM) [14, 235]. In between these pulses, the cell current or potential is turned off. Several process parameters are thus introduced, such as the pulse on-time, pulse off-time, the pulse current or potential and the pulse period. Pulse- and Pulse-Reverse-TMEMM, therefore, offer more opportunities for process optimisation.

The reasons to utilise Pulse- and Pulse-Reverse-TMEMM are manifold. The formation of inhibiting passive films and gaseous reaction products may reduce the machining rate [13, 146, 199, 201, 235, 256]. Concurrent Joule heating in the interelectrode gap can lead to a deterioration of machined structures [143, 267]. When using a small gap between anode and cathode, the deposition of dissolution products along the cathode may warrant periodic cleaning [248]. In case extremely thin substrates are machined, it may be desirable to exert more control over the machining time [235]. In all of these cases it is beneficial to periodically switch the current or potential on and off. In addition, in some studies pulsed input signals are found to lead to less undercutting compared to a constant signal [201, 235, 269]. In other cases a lower average surface roughness is found [199, 220, 238].

3.10 Conclusions

Theoretical studies on the underlying phenomena during TMEMM have been reviewed in this chapter. The rate of material removal, the shape-evolution process and the final surface finish all depend on a multitude of factors. The most important of these are the uniformity of the current distribution and the mode of mass transfer. In turn, these factors determine the formation and coverage of surface films along the workpiece, which themselves play an important role in governing the dissolution process. As this review attests, considerable efforts have been made to describe these phenomena on the scale of individual features. At this point, more work is necessary to understand TMEMM on multiple length scales simultaneously, in particular when accounting for mass-transfer limitations and surface films.

In addition, applications of TMEMM have been presented. The process has been widely used within the field of micromachining, especially in relation to microelectronics, microactuators and microstructured surfaces, but also for the manufacture of thin precision parts. The only prerequisite for its successful application is that the material be electrically conductive. As a consequence, suitable electrolytes are available for a large number of metals and alloys within the existing literature. The process is feasible for the mass fabrication of microstructured devices. Therein, it is comparable to the more widely used PCM process, while offering an improved surface finish, safer process conditions and more options for process optimisation. Efforts to modify TMEMM have picked up in recent decades, and several process variants exist today. Nonetheless, more work is clearly needed to explore these options more extensively and to increase the range of applications.

4 Experimental methods

The following chapter provides information on the experimental setups and procedures used within this work. Chapters 5, 7, 8 and 9 each already contain a section describing the respective experiments and methods in brief form. This chapter expands on that information and presents more details. In particular, the electrochemical cell designs and their assembly are presented, as well as the sample types and their preparation. This is followed by an overview of all materials in use, of the lithography protocol and of the characterisation methods.

4.1 Electrochemical cell setup

Two cells were designed within this work. The first cell was used for experiments with the rotating disc electrode (RDE) (Chapters 5 and 7), while the second cell was used in conjunction with a plate electrode (Chapters 8 and 9). All cell parts were built in-house, either in the department's mechanical or electrical workshop, or in the university's glass workshop. Technical drawings of each part are attached in the appendix for reference (Appendix D). The necessary peripheral equipment for these experiments is mentioned in each results chapter and thus not repeated here. In the following, both electrochemical cells are described in detail.

The first cell was centred around a 100 mL glass vessel made from borosilicate glass, and intended for a three-electrode setup (Figure 4.1). The glass vessel consisted of a main chamber and two side tubes, all of which were fitted with standard-tapered, ground glass joints. During an experiment, a platinum counter electrode and a Ag|AgCl reference electrode were positioned in the side tubes. The counter electrode had a total area of about 4 cm^2 and was thus several times larger than the working electrode. It was separated from the main chamber via a coarse glass frit to prevent evolving hydrogen bubbles from spilling over. The reference electrode was connected to the central chamber via a 2 mm wide Luggin capillary. This reduced the ohmic-potential drop and minimised potential leaching of chloride ions. An RDE served as the working electrode, which could be inserted via the central glass joint.

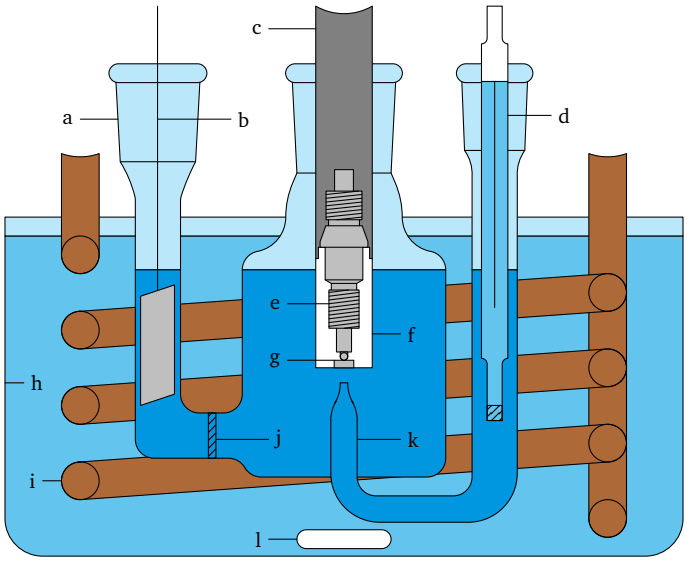

Figure 4.1: Setup for the RDE experiments consisting of (a) the glass cell, (b) platinum counter electrode, (c) rotating electrode shaft, (d) Ag|AgCl reference electrode, (e) stainless-steel adapter, (f) PTFE sample holder, (g) aluminium disc sample, (h) water bath, (i) copper coil connected to thermostat, (j) coarse glass frit, (k) Luggin capillary, and (l) magnetic flea.

Thereby, the RDE could be positioned relative to the tip of the Luggin capillary. In general, it was placed concentrically relative to the capillary tip at a distance of 4 mm or larger to avoid shielding effects. In case de-aeration was necessary, a gas bubbler could be inserted as well. The whole cell could be placed in a thermostat-controlled water bath for temperature control.

The RDE was made to enable experiments with exchangeable aluminium samples (Figures 4.2(a) and 4.3). For this purpose, 15 mm wide, cylindrical sample holders were machined from polytetrafluoroethylene (PTFE) (Dotmar NZ) to hold 5.2 mm disc samples. The discs were inserted into a 5 mm wide through-hole on one end of the holder, thus creating a firm interference fit. Prior to insertion, the disc edge was bevelled on the cylinder-facing side to prevent damage to the holder. After insertion, abrasion and polishing with SiC paper lead to a level end face. The sample holder was then screwed onto a custom-built stainless-steel adapter, which itself connected to a rotating electrode shaft (AFE6MB, Pine Research Instrumentation). Electrical contact to the disc was accomplished by adjusting the position of a set screw from the back of the stainless-steel adapter. This screw was outfitted with a spring-loaded, gold-plated contact pin (Harwin P13-4023, RS Components) at its tip, thus allowing a variable contact force to be applied. Best results in terms of low electrical resistance

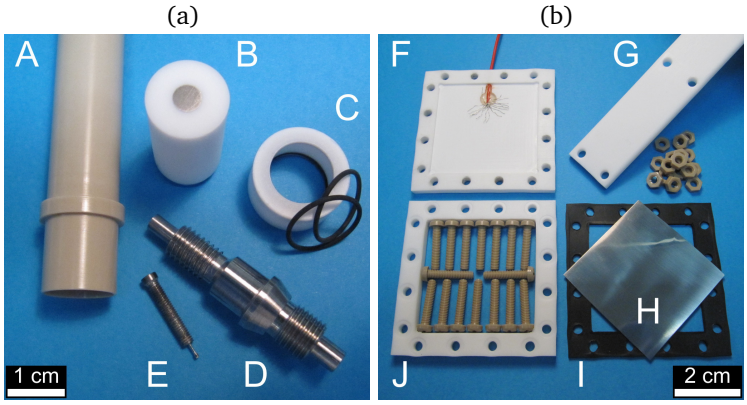

Figure 4.2: Sample holder for the (a) RDE and (b) plate-electrode setup: (A) RDE shaft, (B) PTFE sample holder, (C) PTFE cap with o-rings, (D) stainless-steel adapter, (E) set screw with contact pin, (F) PTFE sample holder, (G) PTFE fixture, (H) stainless-steel shim, (I) Viton gasket, (J) PTFE frame.

over this assembly were achieved by fixing the contact pin to the screw via silver epoxy glue ($< 0.01\,\Omega\,$cm, MG Chemicals 8331-14G, Digi-Key Electronics) and adding a small amount of silver-conductive grease to the very tip ($0.007\,\Omega\,$cm, Chemtronics Conductive Grease CW7100, RS Components).

The same setup was also suitable to hold and exchange 15 mm aluminium discs coated with photoresist (Figure 4.3(b)). These samples could be positioned at the tip of the aforementioned sample holder with a 20 mm wide PTFE cap. The cap itself was fixed in place by a press fit between the holder and two Viton 75 o-rings (MR015X1 V, Seal Imports). In this case, the correct assembly started with coating the contact area between the disc and the cap with a small amount of photoresist (AZ1518). The cap was then placed face down onto a hotplate at 100 °C for about 5 min. During this step excess solvent evaporated and resist viscosity increased. Upon insertion of the disc, the excess resist was squeezed together, effectively creating a seal between the cap and the disc. The resist was then hardened for another 30 min at 100 °C in an oven. Afterwards, the cap/disc assembly was allowed to cool down to room temperature. It was subsequently placed on the tip of the PTFE sample holder. Electrical contact to the aluminium disc was maintained via the aforesaid set screw and the stainless-steel adapter.

The second cell (Figure 4.4) had at its centre a jacketed glass vessel with an electrolyte volume of 1 L. Hot or cold water from a thermostat-controlled circulation bath could be conveyed through the jacket for temperature control. The cell came with a 20 mm thick, circular polypropylene (PP) lid, which consisted of two parts, with through-holes for the insertion of electrodes. A piece of platinum foil about

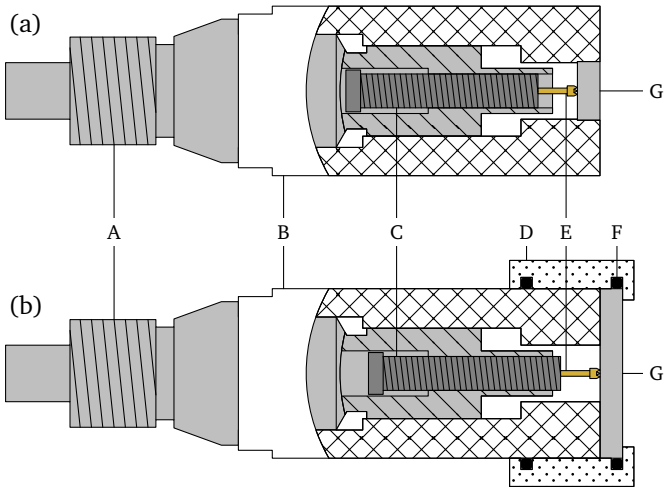

Figure 4.3: Assembled RDE for (a) 5.2 mm or (b) 15 mm wide discs: (A) stainless steel adapter, (B) PTFE sample holder, (C) set screw, (D) PTFE cap, (E) contact pin, (F) o-ring, (G) disc sample.

$20 \times 70\,\mathrm{mm}^2$ in size served as the counter electrode. The foil was connected to a short piece of platinum wire, which was soldered to a piece of copper wire to provide electrical contact. The copper wire and the solder connection were enclosed in a glass tube and thus protected from the solution. The whole counter electrode fitted into a glass sleeve with a coarse glass frit at the bottom, allowing free exchange of the electrolyte solution, while containing any hydrogen bubbles formed there. The sleeve was prevented from sliding inwards by an o-ring. A Ag|AgCl reference electrode could be positioned in a custom-made Luggin capillary, which was also fixed in place with an o-ring. The tip of the Luggin capillary was again 2 mm wide and positioned at a distance of 10 mm from the plate surface.

This cell featured a sample holder for $50 \times 50\,\mathrm{mm}^2$ aluminium plates coated with photoresist (Figure 4.2(b)). It consisted of a square holder, frame and fixture made from PTFE and a 1.5 mm thick Viton gasket (NZ Rubber and Foam). The gasket had to be cut to size manually from sheet material. The plate was placed within the holder in a 1.5 mm deep recess, the four corners of which were bored out for easy removal. The gasket and frame, both of which contained a 48 mm wide square window, were fixed to the holder with sixteen M4 screws and nuts made from polyetheretherketone (PKP420, PKN4, SolidSpot). This held the aluminium plate in place and prevented leakage at the same time. Electrical contact to the plate sample was achieved from the backside via a thin stainless-steel shim, which was pressed against stripped electrical wire. The wire itself was glued with epoxy into a circular cavity within the holder and lead through a hole in the PP lid. Where it was exposed

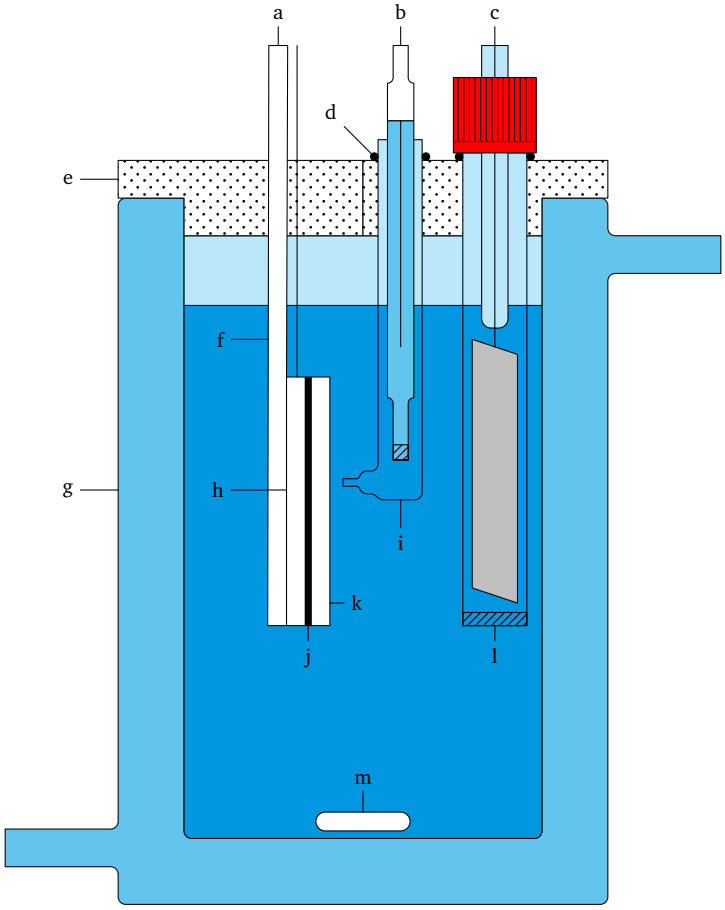

Figure 4.4: Setup for experiments with the plate electrode consisting of (a) the working electrode, (b) Ag|AgCl reference electrode, (c) platinum counter electrode, (d) Viton o-rings, (e) two-part PP lid, (f) PTFE fixture, (g) jacketed glass cell, (h) PTFE sample holder, (i) Luggin capillary, (j) Viton gasket, (k) PTFE frame, (l) glass sleave with coarse glass frit, and (m) magnetic flea.

to the solution, the wire's insulation was left in place. The assembled sample holder was bolted to the PTFE fixture with four out of the sixteen screws. As the fixture was slightly tapered on one end, it could not slide inwards by itself.

The Ag|AgCl reference electrodes used throughout this work were manufactured from materials readily available in the laboratory. The exact procedure was previously detailed by Lim [313]. In short, electrodes were made from silver wire, which was placed within a 7 mm wide glass tube and coated with AgCl by applying an anodic current ($\sim$ 20 µA) for 24 h in saturated KCl solution. A porous frit made from Vycor glass was placed at the end of the glass tube, providing sufficient ionic conduction. These electrodes were found to be stable during storage in saturated KCl at room temperature over months and during operation in 85 % H_3PO_4 up to 75 °C over several hours. Nonetheless, before any experiment, each Ag|AgCl reference was measured against a laboratory master electrode. If the absolute potential difference exceeded 10 mV, the electrode was not used and instead revived. Within this work, all electrode potentials refer to the Ag|AgCl electrode directly. For convenience, conversion factors between the potential of the Ag|AgCl electrode and the standard hydrogen electrode are listed in the appendix (Appendix A).

4.2 Sample preparation

The aluminium used almost exclusively in this work was purchased from Wakefield Metals in 2 mm thick sheet form. The material designation was 1200 corresponding to unalloyed aluminium of commercial purity. The exact composition was specified by the supplier as follows: Al $\geq$ 99.00 %, Si+Fe $<$ 1.00 %, Cu $<$ 0.05 %, Mn $<$ 0.05 %, Zn $<$ 0.10 %, Ti $<$ 0.05 %. The limits on other elements were 0.03 % individually and 0.15 % in total. The material had the temper designation H14, which specified strain-hardening without supplementary thermal treatment. In general, the material was not annealed before use.

Samples were cut from the sheet and machined to different dimensions. Firstly, discs were machined to a diameter of 5.2 mm or 15 mm either via lathing or punching. Samples machined with the lathe were burr-free along the disc circumference and perfectly round. Punched discs showed signs of tearing along the lateral surface and bending of the disc surface on one side. However, by mechanically abrading the deformed disc surface, samples of the desired diameter and flatness could still be obtained. Secondly, square platelets were sawed from the sheet and machined to a width of 50 mm. Each face except for the bottom face was machined separately

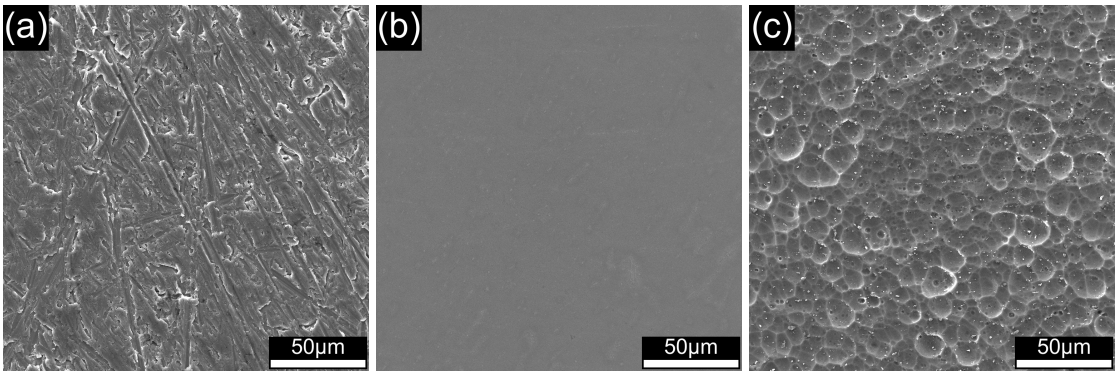

Figure 4.5: SEM images (500× magnification) of aluminium samples after preparation to different surface finishes: (a) P1200 SiC paper, (b) 0.3 µm alumina slurry, (c) 10 min etch in 5 % NaOH.

to ensure the plates were perfectly square and flat. A single high-purity aluminium sample (99.999 %, ACI Alloys) was also lathed to a diameter of 5.2 mm from an evaporation piece about 1/4 inch in size.

Subsequently, samples were mechanically abraded to provide a uniform initial surface finish. Depending on the experiment, the samples were prepared to a suitable surface morphology (Figure 4.5). For the measurement of current-potential curves and impedance spectra described in Chapter 5 the disc electrodes were mechanically polished down to P1200 SiC paper. This was sufficient so as to leave no trace of the initial scratch pattern at the end of the conditioning step. In contrast, when conducting shape-evolution experiments, samples were abraded down to P2000 SiC paper first and then polished with different grades of alumina slurry (Chapter 7), either manually or with a polishing machine (LaboPol-2, LaboForce-1, Struers). In this case, a mirror finish was necessary to accurately measure shape profiles of machined microchannels. The initial machined surface of the 50 mm wide plates already exhibited a semi-polished finish (Chapter 8). To remove remaining machining marks, these samples were polished with P1500 SiC paper and etched in 5 % NaOH for 10 min, thereby creating a uniform satin finish.

Before use, samples were subjected to different cleaning treatments. In between polishing steps with SiC paper, both types of disc samples were rinsed with deionised (DI) water. Afterwards, the discs were ultrasonicated for 5 min. Isopropyl alcohol (IPA)/DI water was used for this purpose in a 1:1 (v/v) mixture. This was followed by rinsing with DI water and then with IPA, followed by drying in air. Note that the conditioning step described in Chapters 5 and 8 prior to recording current-potential curves with the RDE constituted in effect another cleaning step. The plate

samples were only subjected to the aforementioned etching step in 5 % NaOH. This was effective in removing any adhering debris or embedded particles. In addition, all samples intended for coating with photoresist underwent additional cleaning steps, which are described in Section 4.5.

4.3 Materials and chemicals

For the majority of experiments, the electrolyte consisted of 85 % phosphoric acid, with or without the addition of surfactants. These experiments were largely conducted at applied potentials, which warranted at least a small amount of oxygen evolution along the anode. De-aeration was thus not performed. Given that the working electrode was subject to dissolution in most cases, pre-cleaning procedures for the electrolyte were not implemented. Instead, electrolytes were used as received or as prepared. An exception to this rule were measurements with the gold RDE, which are described in Appendix B. Therein, solutions prepared with sulphuric acid, ammonium iron(III) sulphate and iron(II) sulphate were always de-aerated by bubbling argon through them for at least 30 min beforehand.

For experiments with phosphoric acid and any of the three employed surfactants (cetyltrimethylammonium bromide (CTAB), sodium dodecyl sulphate (SDS) and Triton X-100), 0.1 M surfactant stock solutions were prepared with DI water. This was done because none of the surfactants dissolved readily in 85 % phosphoric acid. For these and all other solutions, high-purity DI water with a resistivity of 18.2 MΩ cm was used. This was supplied either by an arium 611UV system (Sartorius Stedim Biotech) or by a Milli-Q system (Merck). The purity and supplier of all other metals, chemicals and gases used in this work are listed in Table 4.1.

4.4 Mask design and fabrication

The masks for the patterning of photoresist films were designed using the software Tanner L-Edit (version 2016.1). An example pattern depicting the coat of arms of the University of Canterbury and its evolution from the initial design to the final mask are shown in Figure 4.6. In addition to the desired pattern, each design also contained mask openings meant for alignment between the mask and the sample prior to ultraviolet (UV) exposure. These mask openings had to be large enough to account for the spread in sample size and to allow easy alignment using the 5× to

Table 4.1: Composition, purity and supplier of all metals, chemicals and gases.

Substance	Purity	Supplier
Acetic acid, $\geq 99.7\,\%$ CH_3COOH	ACS grade	Sigma-Aldrich
Acetone, $(CH_3)_2CO$	Analytical grade	Thermo Fisher Scientific
Aluminium, Al	$\geq 99.0\,\%$	Wakefield Metals
	$\geq 99.999\,\%$	ACI Alloys
Ammonium cerium(IV) nitrate, $(NH_4)_2Ce(NO_3)_6$	Analytical grade	Thermo Fisher Scientific
Ammonium iron(III) sulphate dodecahydrate, $99\,\%$ $(NH_4)Fe(SO_4)_2 \cdot 12\,H_2O$	ACS grade	Sigma-Aldrich
Argon, Ar	$\geq 99.999\,\%$	BOC
AZ1518	*	Microchem
AZ MIF 326	*	Microchem
CTAB, $[(C_{16}H_{33})N(CH_3)_3]Br$	$\geq 99\,\%$	BDH
Gold(III) chloride trihydrate, $HAuCl_4 \cdot 3\,H_2O$	$\geq 99.9\,\%$	Sigma-Aldrich
Hydrochloric acid, $37\,\%$ HCl	Analytical grade	Thermo Fisher Scientific
IPA, $(CH_3)_2CHOH$	Analytical grade	Thermo Fisher Scientific
Iron(III) chloride, $97\,\%$ $FeCl_3$	Reagent grade	Sigma-Aldrich
Iron(II) sulphate heptahydrate, $99.5\,\%$ $FeSO_4 \cdot 7\,H_2O$	Analytical grade	VWR
Methanol, CH_3OH	Analytical grade	Thermo Fisher Scientific
Nitric acid, $70\,\%$ HNO_3	Analytical grade	Thermo Fisher Scientific
Nitrogen, N	*	UC Physics Department
Perchloric acid, $70\,\%$ $HClO_4$	AnalaR grade	VWR
Phosphoric acid, $85\,\%$ H_3PO_4	ACS grade	Thermo Fisher Scientific
Potassium chloride, $99.8\,\%$ KCl	Analytical grade	Thermo Fisher Scientific
Silver, Ag	$\geq 99.9\,\%$	Sigma-Aldrich
SDS, $CH_3(CH_2)_{11}SO_4Na$	$\geq 98.5\,\%$	Sigma-Aldrich
Sodium hydroxide, $\geq 99\,\%$ NaOH	Analytical grade	VWR
Sulphuric acid, $95.0–98.0\,\%$ H_2SO_4	Analytical grade	Thermo Fisher Scientific
Triton X-100	Laboratory grade	Sigma-Aldrich

* not specified

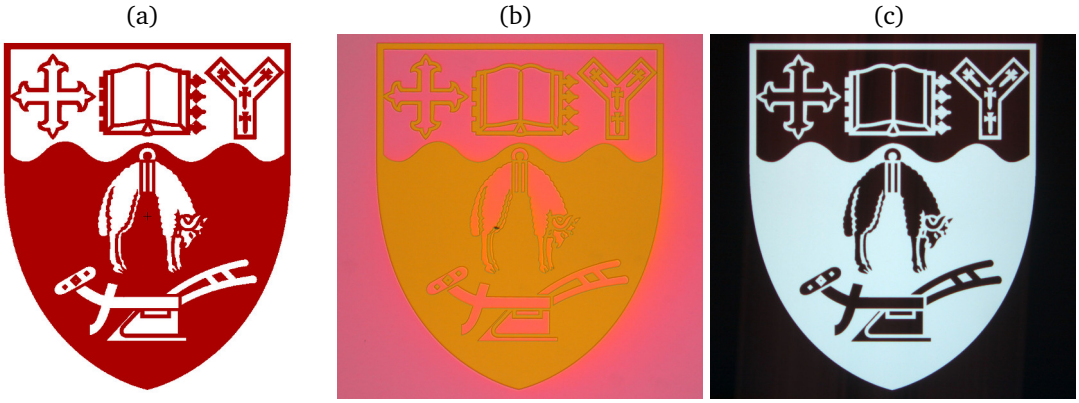

Figure 4.6: Mask fabrication from the initial design to the final mask, depicting the coat of arms of the University of Canterbury in this example: (a) screenshot from Tanner L-Edit, (b) optical micrograph of the developed photoresist pattern (in magenta) exposing the underlying chrome layer (in orange), (c) optical micrograph of the etched chrome layer. The design is approximately $2.0 \times 2.4\,\mathrm{mm}^2$ in size.

20× magnification objectives of the Karl Suss MA6 mask aligner. Note that asymmetric patterns were mirror-inverted during the design process.

A Heidelberg uPG101 Laser Mask Writer was used to write the patterns with a resolution down to 1 µm on 3 or 4 inch, chrome-coated glass plates (3x3x .060 SL LRC 10M 1518 5k, 4x4x .060 SL LRC 10M 1518 5k, Nanofilm), which were pre-coated with a layer of positive-tone photoresist (AZ1518). At the end of the writing process, the exposed resist was removed by rinsing with AZ MIF 326 developer for 30 s. After rinsing with tap water and drying, the laid open chrome layer was etched in a solution containing 33 g ammonium cerium(IV) nitrate and 8.6 mL perchloric acid made up to a volume of 200 mL with DI water. The remaining resist was then washed off by rinsing with acetone, methanol and IPA. Finally, the mask was dried with pressurised nitrogen, and the pattern was inspected for its dimensions and for flaws with an Olympus BX60 light microscope.

4.5 Photolithography

All lithography-related work was conducted within the premises of the Nanofabrication Laboratory. Firstly, each sample was ultrasonically cleaned for 5 min in a solvent bath and rinsed with copious amounts of solvent to remove any particles, grease and residues from previous preparation steps. Thereby, the samples were treated

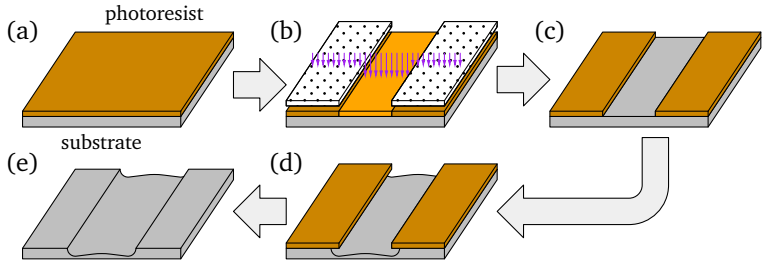

Figure 4.7: Schematic depiction of the photolithography process: (a) spin-coating and pre-bake, (b) UV exposure, (c) development and post-bake, (d) etching, (e) stripping.

in sequence with acetone, methanol and IPA, dried with pressurised nitrogen and stored in separate containers for further processing.

Throughout this work positive-tone AZ1518 resist was used exclusively for the coating of samples in conjunction with a PWM32-PS-R790 spinner (Headway Research) (Figure 4.7). Each sample was positioned on an o-ring in the centre of the spinner chuck and held in place by a vacuum. Before applying the resist, particles were removed from the sample surface once more with pressurised nitrogen. The resist was then dispensed carefully in the sample centre via a 1 mL autopipette or a 25 mL Combitip (Eppendorf) and allowed to fully wet the surface. On the 15 mm discs about 0.1–0.2 mL have proven sufficient to achieve a good coating, whereas 1–2 mL were necessary for the 50 mm square plates. Standard parameters were used for spin-coating (acceleration 3000 rpm s^{-1}, final spin speed 3000 rpm, duration 90 s). Subsequent edge-bead removal was not necessary, because UV exposure was conducted in proximity mode. Samples were then subjected to a pre-bake on a hotplate (100 °C, 90 s) to remove excess solvent and to harden the resist. Afterwards, each sample was stored in a container wrapped in aluminium foil and allowed to cool down to room temperature before further processing.

For the subsequent UV-exposure step a Karl Suss MA6 mask aligner was used. Prior to that, the mask was rinsed with acetone, methanol as well as IPA and dried in a nitrogen stream. After inserting the sample, wedge-error correction was performed by bringing it in contact with the mask, thus aligning both in parallel to each other. Sample alignment and UV exposure in proximity mode were conducted at distances of 100 and 10 µm, respectively. A dose of 50 mJ cm^{-2} at 365 nm corresponding to an exposure time of 8 s was applied in general. The resist was developed straight away via immersion in AZ MIF 326 developer for 30 s, rinsed with DI water and dried with pressurised nitrogen. Afterwards, the resist mask was strengthened with a post-bake on a hotplate (120 °C, 120 s). Finally, samples were inspected for flaws

with a light microscope and stored in separate containers for subsequent use. After pattern transfer via etching, samples were rinsed with copious amounts of acetone, methanol and IPA to strip the resist mask.

4.6 Characterisation

Optical inspection of the surface was possible using an Olympus BX60 light microscope in conjunction with a Leica DFC320 microscope camera mounted on several adapters (Olympus U-TVO 5X, Olympus U-CMAD-2). Each objective was calibrated beforehand with a stage micrometer 1 mm in length with 10 µm graduation marks. This way, the dimensions of machined microstructures could be measured accurately from microscope images with the software ImageJ (version 1.50i).

For scanning electron microscopy (SEM) a JSM 7000F field-emission, high-resolution scanning electron microscope (JEOL) was available in the University of Canterbury Electron Microscopy Center. This enabled imaging with secondary and backscattered electrons and qualitative elemental analysis via energy-dispersive x-ray spectroscopy (EDXS). The latter method was solely employed to detect elemental gold within Au/Al_2O_3 films (Chapter 8). SEM imaging was performed at an acceleration voltage of 15 kV, whereas EDXS was conducted at 5 kV. At this lower acceleration voltage, the signal ratio between gold and aluminium was amplified, thus facilitating the detection of smaller amounts of gold. These analyses were repeated in a sufficient number of locations to yield representative results.

Prior to SEM imaging, samples were mounted on a holder with conductive carbon tape, in order to minimise charging effects during the imaging process. For poorly conductive samples, such as cross-sectioned samples mounted in epoxy, it was possible to coat the surface with a thin conductive layer made from chromium or carbon (EMS150T ES, Electron Microscopy Sciences). Coating with chromium and carbon was usually done for 2×180 s at 120 mA and for 5×5 s at 60 A, respectively. In preparation for sputter-coating, mounted samples were first abraded with different grades of SiC paper to create a level surface. Subsequently, they were polished either with alumina slurry (ProSciTech) or polycrystalline diamond suspension (Buehler) of 1 µm particle size. This was done manually or with the help of a polishing machine (Beta Grinder-Polisher, Buehler) on velvet cloth.

For further characterisation of the surface morphology several instruments were accessible: a DEKTAK 150 stylus profilometer (Veeco), a Profilm3D optical profilo-

meter (Filmetrics), both available at the University of Canterbury Nanofabrication Laboratory, as well as a ContourGT optical profilometer (Bruker) at the University of Auckland Photon Factory. Another DEKTAK 150 was on hand within the Cleanroom Fabrication Facility at Victoria University of Wellington. These instruments were used to measure surface roughness, to determine resist thickness or to acquire two-dimensional height profiles and three-dimensional surface maps of whole samples. Data evaluation was subsequently conducted with Gwyddion (version 2.44) and Matlab (version R2013b).

5 Characterisation of surface films formed on aluminium

The following chapter was originally published in the Journal of The Electrochemical Society under the title 'Characterization of Surface Films Formed on Aluminum during Mass-Transfer Limited Anodic Dissolution in Phosphoric Acid', corresponding to reference [314]. The content is the same apart from grammatical and stylistic corrections, the adoption of British instead of American English, and adjustments to the appearance of figures and tables in line with the remainder of the manuscript. As such, the reader may already be familiar with the content of the introductory and experimental sections from other parts of this work.

Abstract

Electrochemical impedance spectra recorded during the mass-transfer-limited dissolution of commercially pure aluminium rotating disc electrodes in concentrated phosphoric acid are presented. The influence of rotation rate and potential on the observed capacitive and inductive semi-circles is discussed and the presence of a salt film on top of the oxide film is debated. The impedance spectra are interpreted, hypothesising the presence of a compact, barrier-type Al_2O_3 film only. The capacitive and inductive features are explained in terms of the capacitive charging of the barrier film, the relaxation of a surface charge at the film/solution interface and the perturbation of the film thickness. The properties of the film such as electric-field strength, half-jump distance and polarisability of the film/solution interface are calculated in agreement with literature values.

5.1 Introduction

The formation of surface films during the mass-transfer-limited anodic dissolution of metals is of great importance for processes such as electrochemical planarisation or through-mask electrochemical micromachining (TMEMM). In electrochemical planarisation the surface roughness of electrodeposited thin-films is reduced, which arises from differently sized features on an underlying layer [315]. In TMEMM a metal substrate is anodically dissolved through a thin, insulating mask for the

fabrication of microstructures [21, 143]. In both cases, the presence and properties of surface films influence the amount of removed material necessary for a desired reduction in surface roughness or the final shape of the evolving, micrometre-sized structures [21, 143, 315]. Depending on the film's thickness and composition, complex phenomena such as charge-transfer processes within the film or the hydrodynamic conditions in the interelectrode gap have to be considered, greatly affecting the complexity of shape-evolution simulations.

Due to its high thermal conductivity, easy machinability, and the ability to modify its surface roughness and porosity, aluminium has been widely used for the fabrication of microfluidic devices [18, 26, 29, 42, 316]. Phosphoric acid is a suitable electrolyte for TMEMM of such devices, as aluminium dissolution at elevated temperatures in concentrated phosphoric acid leads to a concurrent reduction in surface roughness and an increase in reflectivity and brightness [44]. To achieve smooth surfaces in either electrochemical planarisation or TMEMM, the metal dissolution must be limited by mass transfer, which is characterised by the presence of a limiting-current plateau [54]. Often, the formation of surface films — consisting either of a salt or an oxide — is thought to be responsible for the observed mass-transfer limitation.

The formation of surface films during aluminium anodising in dilute phosphoric acid at room temperature has long been studied and used in industry to form thick, duplex-structure alumina films [52, 70, 71, 317] (Section 2.2.1). In comparison, less information is available on the composition, structure and properties of films, which are present during aluminium electropolishing (EP) in concentrated phosphoric acid, conforming to mass-transfer-limited anodic dissolution (Section 2.2.2). Electrochemical impedance spectroscopy (EIS) combined with a rotating disc electrode (RDE) can be used to study systems, which exhibit film formation during EP [101, 263, 274, 275, 318–321]. In the first extensive EIS study by Vidal and West [44] on aluminium EP in concentrated phosphoric acid, it was proposed that a non-porous, compact film was present. However, in other work, scanning electron microscopy (SEM) images of thin-films formed during anodic dissolution of aluminium in phosphoric acid with the addition of butyl alcohol revealed a porous film structure [104]. In EIS studies on the dissolution of aluminium in an organic $AlCl_3$ electrolyte [321], as well as in mixtures of perchloric acid and ethanol [101], a duplex and a porous film were found, respectively. Therefore, it is the aim of this work to investigate the nature and properties of the film present during aluminium EP in concentrated phosphoric acid.

5.2 Experimentation

For all experiments a commercially pure aluminium RDE was used (Al $\geq$ 99.00 %, Si+Fe $<$ 1.00 %, Cu $<$ 0.05 %, Mn $<$ 0.05 %, Zn $<$ 0.10 %, Ti $<$ 0.05 %, Wakefield Metals). 2 mm thick discs were machined to a diameter of 5.2 mm and embedded in a 15 mm wide polytetrafluoroethylene holder. Prior to each experiment, the RDE was polished with SiC paper of grit sizes P320, P600 and P1200. In between these polishing steps, the disc surface was rinsed with de-ionised (DI) water with a resistivity of 18.2 MΩ cm. After the final polishing step, the RDE was ultrasonicated for 5 min in a 1:1 (v/v) mixture of isopropyl alcohol (IPA) and DI water, thoroughly rinsed first with DI water and then with IPA, and finally left to dry in air.

For all electrochemical studies, either a Reference 3000 or an Interface 1000 (Gamry Instruments) served as the potentiostat. The Gamry Frameworks software (version 6.31) was used to setup and control single or multiple experiments in series and to record the data. Data analysis was conducted with the Gamry Echem Analyst software package (version 6.25) and with Matlab. The RDE was mounted on a AFE6MB RDE shaft, which was used in conjunction with a Modulated Speed Rotator (Pine Research Instrumentation). All experiments were conducted using a custom-made glass cell with a volume of 100 mL. Before each experiment, the cell was ultrasonically cleaned with IPA and DI water, rinsed several times with DI water, and dried in an oven at 105 °C. The glass cell was immersed in a water bath, the temperature of which was maintained within $\pm$1 °C, using a copper coil connected to a GD120 thermostat and a LTC1 circulation bath (Grant Instruments). The counter electrode was made from a 4 cm^2 platinum foil connected to a platinum wire. As the reference, a Ag|AgCl electrode connected to a Luggin capillary was used ($c_{\mathrm{KCl}} = 4.77\,\mathrm{mol\,kg^{-1}}$, $E_{\mathrm{Ag|AgCl}}(25\,^{\circ}\mathrm{C}) = 0.197\,\mathrm{V}$ vs. SHE, $E_{\mathrm{Ag|AgCl}}(75\,^{\circ}\mathrm{C}) = 0.153\,\mathrm{V}$ vs. SHE). The Luggin capillary, with an outer diameter of 2 mm, was held concentrically underneath the RDE at a distance of 4 mm. All potentials are reported against this reference. The electrolyte was made from 85 % phosphoric acid (ACS grade, Thermo Fisher Scientific) and used as received.

Potential sweeps were conducted at 25, 50 and 75 °C and at rotation rates of 100, 400, 900, 1600 and 2500 rpm. The potential was swept from 1.4 to $-$0.6 V at a sweep rate of 5 mV s^{-1}. In order to gain reproducible results, the sweeps started at positive potentials, to avoid the entrapment of gas bubbles underneath the RDE. Prior to these sweeps, the anode was conditioned at 1.4 V for 400 s, and the electrolyte resistance was determined using EIS. The duration of the conditioning step was chosen long enough for successively measured impedance spectra to overlap. In addition, the

RDE was rotated at 2500 rpm during the first 50 s of the conditioning step. In total, the largest material removal at the end of the potential sweep corresponded to a recess depth of 120 μm.

EIS was performed at 75 °C for rotation rates 100, 400, 900, 1600 and 2500 rpm and at applied potentials of 1.4, 2.4, 3.4, 4.4 and 5.4 V. The amplitude of the potential modulation was set to 5 mV rms^{-1} with a frequency range of 500 kHz to 5 Hz. This lower-frequency limit was chosen to restrict the recess depth at the end of a measurement. Ten data points per decade were acquired, and for each data point several Lissajous curves were measured to account for 99.9 % of the variation. The applicability of the Kramers-Konig relations was tested for each data set, and only those data points that conformed to them were subsequently used for analysis. The same conditioning as for the potential sweeps was applied.

Samples for SEM analysis (JSM 7000F, JEOL) were etched at 25, 50 and 75 °C, an applied potential of 5.4 V and a rotation rate of 2500 rpm for a cumulative charge of 25 C, corresponding to a final disc recess of approximately 40 μm. The discs were subsequently rinsed with DI water and IPA, and left to dry in air.

5.3 Results and discussion

5.3.1 SEM results

As many studies report that films formed during mass-transfer-limited anodic dissolution can be either porous or non-porous, the surface of etched substrates was examined via SEM. The visual inspection of etched samples showed a marked increase in brightness and reflectivity with temperature, with samples anodically dissolved at 75 °C exhibiting an almost perfect mirror finish.

SEM images taken at 500× magnification revealed different surface structures, depending on the electrolyte temperature (Figure 5.1). At 25 °C hemispherical, partially overlapping depressions covered the whole surface, giving it a shallow-dimpled appearance. The size of these depressions varied between 5 and 20 μm. At 50 °C the depressions were fewer and appeared to be much shallower. At 75 °C the surface appeared smooth by comparison, with no surface structures present larger than a few micrometres. Using a Veeco DEKTAK 150 stylus profilometer, the average surface roughness was found to decrease from an initial value of about 0.19 μm to 0.02 μm after anodic dissolution at 75 °C. The disappearance of the

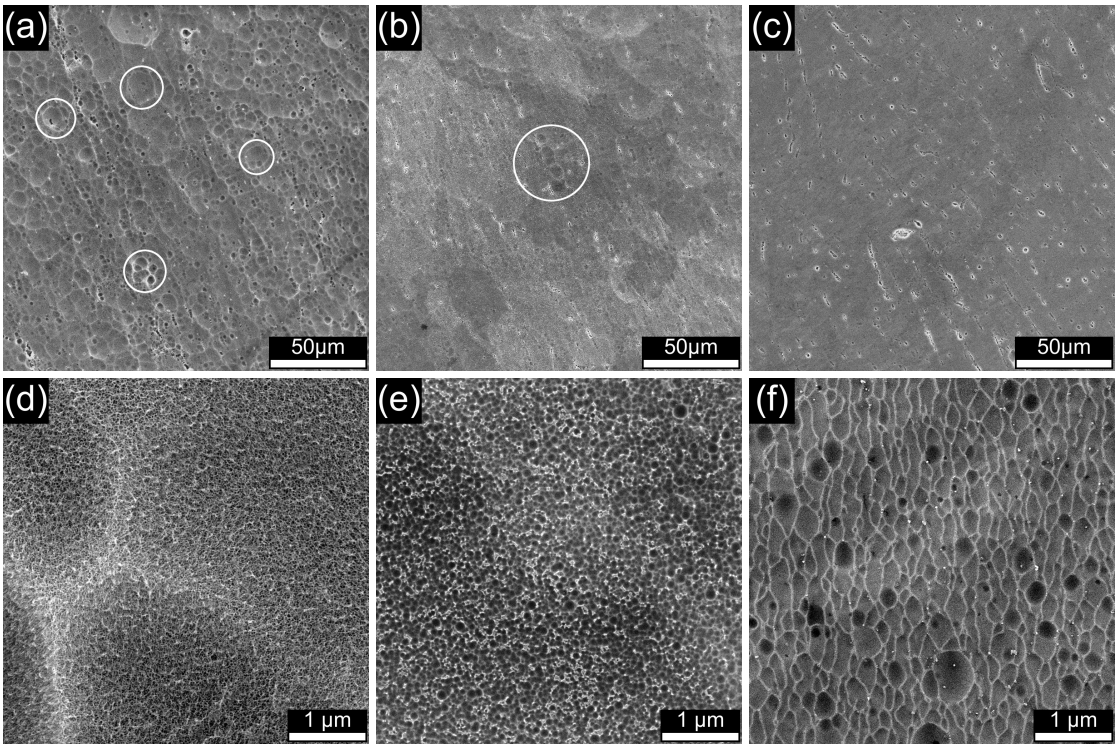

Figure 5.1: SEM images of aluminium at 500× (a, b, c) and 20000× magnification (d, e, f) anodically dissolved at 25 (a, d), 50 (b, e) and 75 °C (c, f), an applied potential of 5.4 V and a rotation rate of 2500 rpm for a cumulative charge of 25 C. The circled areas contain the hemispherical depressions mentioned in the text, which can only be observed at 25 °C and to a lesser degree at 50 °C.

hemispherical depressions reduced the overall surface roughness, and hence the scattering of inclined light, resulting in the observed brightening effect. At all temperatures micrometre-sized, aligned pits were present. These aligned pits were not caused by the rotational flow pattern, as their orientation was the same across the whole disc. It was assumed that these pits formed due to small amounts of other elements within the commercially pure aluminium, as a comparison with high-purity aluminium (99.999 %) showed far fewer pits (Figure 5.2).

At 20000× magnification, differences in the sub-micrometre structure became apparent. At 25 °C the surface was covered by a pore structure with pore diameters on the order of tens of nanometres, similar to films formed in dilute phosphoric acid at high anode potentials [322, 323]. At 50 °C the pore diameters ranged from tens of nanometres to about 100 nm. At 75 °C no pores were present and the surface appeared to be covered by small depressions with characteristic dimensions on the

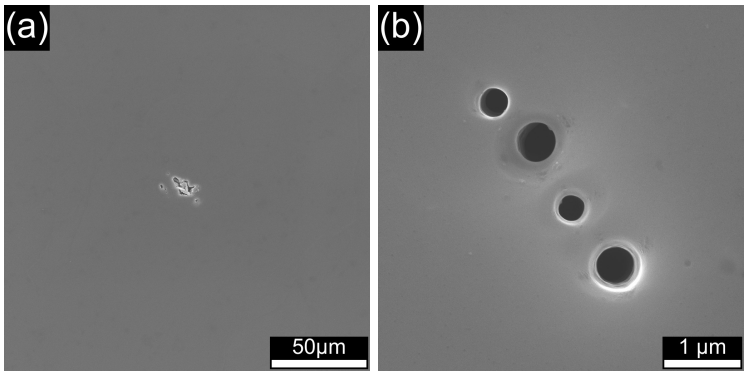

Figure 5.2: SEM images of 99.999 % aluminium at 500× (a) and 20000× magnification (b) dissolved at 75 °C, an applied potential of 5.4 V and a rotation rate of 2500 rpm for a cumulative charge of 25 C.

order of a few hundred nanometres, which were separated by thin ridges. Strong similarities existed to film structures obtained in dilute phosphoric acid at 25 °C during the initial phase of pore formation on top of an alumina barrier film [324]. It should be noted though that any porous film could have dissolved between the end of a dissolution experiment and the retrieval of the RDE from the solution, due to the open-circuit conditions at 75 °C; thus, the absence of a porous film could only be confirmed in conjunction with the analysis of the EIS data.

5.3.2 Results of linear sweep voltammetry

Potential sweeps at all temperatures exhibited current plateaus, which started at −0.2 to 0.3 V, depending on temperature and rotation rate, and extended over several volts (Figure 5.3). The influence of rotation rate on the magnitude of the limiting current density at any given potential increased with temperature, leading to an almost equidistant spacing between the plateaus at 75 °C. For a mass-transfer-limited, electrochemical reaction on a RDE the limiting current density can be described by the Levich equation [133]. Plotting the inverse of the limiting current density ($1/i_{\mathrm{L}}$) against the inverse of the square root of rotation rate ($1/\omega^{1/2}$) should yield a straight line through the origin, if the anodic dissolution is completely controlled by mass transfer. Taking the inverse limiting current density from the current-density plateaus at 1 V, corrected for the ohmic drop in the solution, generated a straight line at each temperature (Figure 5.4). However, at 25 and 50 °C the data showed a non-zero intercept with the ordinate, suggesting partial control by a kinetic step. Only at 75 °C was the dissolution completely controlled by mass

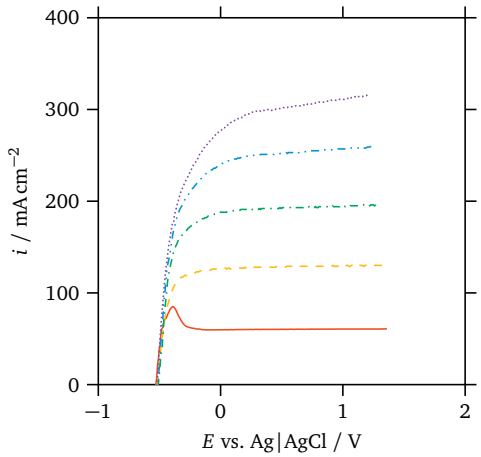

Figure 5.3: Linear potential sweeps from 1.4 V to −0.6 V recorded at a sweep rate of 5 mV s^{-1} at 75 °C for five different rotation rates, corrected for the ohmic drop in the electrolyte: 100 rpm (——), 400 rpm (– – –), 900 rpm (– · –), 1600 rpm (– ·· –), 2500 rpm (·····).

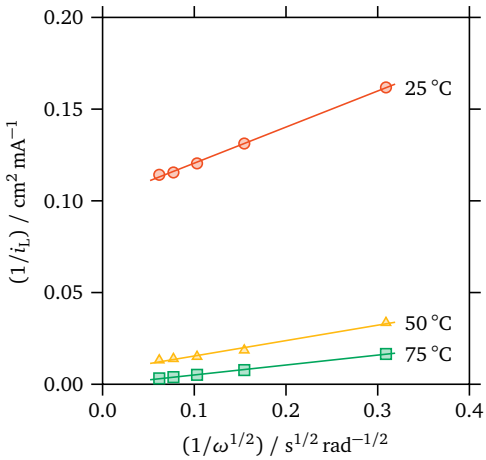

Figure 5.4: Levich-Koutecky plot showing the dependence between inverse limiting current density and inverse square root of disc rotation rate at different electrolyte temperatures. The values for the limiting current density were taken from the linear potential sweeps at a potential of 1 V. The low intercept at 75 °C indicates that the aluminium dissolution is completely controlled by mass transfer.

transfer, in accordance with the observed changes in surface structure and the results presented by Vidal and West [44] for high-purity aluminium.

5.3.3 EIS results

EIS was performed at potentials along the limiting-current plateau only. The impedance data is reported in the form of Nyquist plots (Figures 5.5, 5.6 and 5.7), as this presentation is more sensitive to discrepancies between model and experiment than traditional Bode plots [135]. In the high-frequency range, the data exhibited a capacitive semi-circle, which extended down to approximately 2–15 kHz at 75 °C, depending on rotation rate and applied potential. This was followed by an inductive semi-circle, which extended down to roughly 100–800 Hz. The size of both the capacitive and inductive semi-circle decreased with increases in temperature (Figure 5.7). At constant temperature, the diameter of both semi-circles depended also on applied potential and rotation rate. For the same rotation rate, and hence almost constant current density, the size of both semi-circles grew with increases in applied potential (Figure 5.6). Holding the applied potential constant and decreasing the rotation rate had the same effect (Figure 5.5). Note that this was accompanied by a concurrent decrease in current density. As the electrolyte resistance was constant (Table 5.1), this lead to a reduction in the ohmic drop and an increase in the effective anode potential. At frequencies below 100 Hz, a second capacitive semi-circle was found, the size of which increased with a rise in applied potential, and which approached purely capacitive behaviour. At the highest frequencies, a purely inductive feature could be observed below the real axis, which caused a slight depression of the high-frequency, capacitive semi-circle.

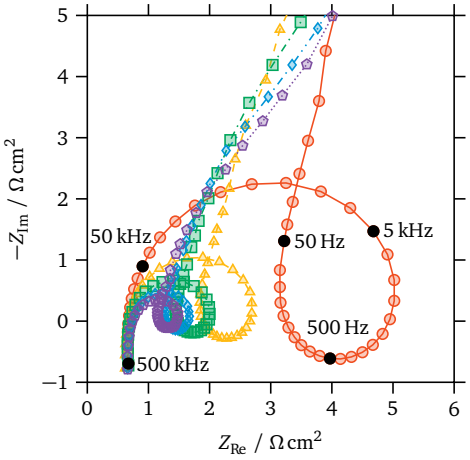

Figure 5.5: EIS data recorded at 75 °C, an applied potential of 1.4 V and five different rotation rates: 100 rpm (—○—), 400 rpm (- -△- -), 900 rpm (- -□- -), 1600 rpm (- -◇- -), 2500 rpm (···⬠···).

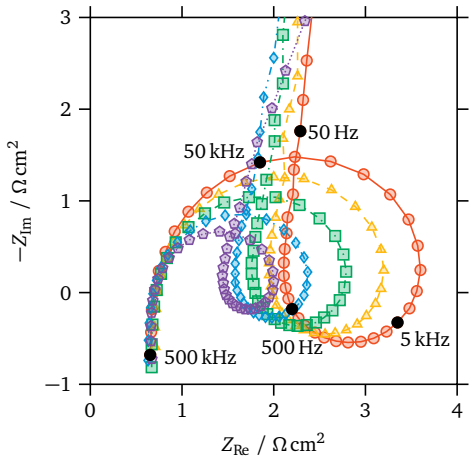

Figure 5.6: EIS data recorded at 75 °C, a rotation rate of 900 rpm and five different applied potentials: 1.4 V (⬠), 2.4 V (◇), 3.4 V (□), 4.4 V (△), 5.4 V (○).

This inductive feature appeared for different potentiostats, varying positions of the Luggin capillary, and various orientations of the current carrying and sense leads, and it was also present using a pseudo-reference electrode [137] in parallel with the Ag|AgCl reference. However, it could be largely removed by reducing the amount of cabling. Thus, we believe it was most likely linked to the intrinsic inductance of the cabling and of the measurement cell itself [136] (Section 2.4.2). To ensure the correct fitting of other circuit elements though, especially in the high-frequency

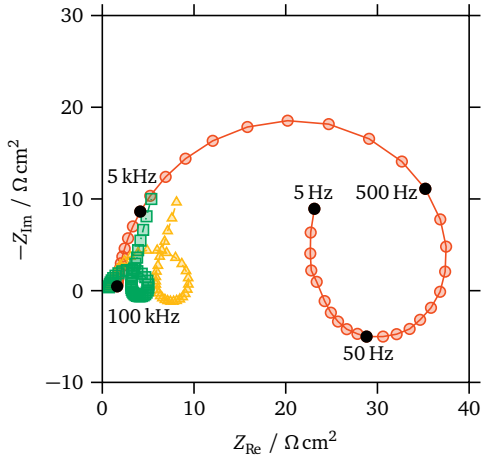

Figure 5.7: EIS data recorded at an applied potential of 1.4 V, a rotation rate of 100 rpm and three different electrolyte temperatures: 25 °C (○), 50 °C (△), 75 °C (□).

range, it was included in the equivalent electrical circuit. Beyond that, the inductive feature is not discussed any further.

The observed impedance features are found in several studies on the dissolution or corrosion of aluminium, using aqueous and non-aqueous electrolytes alike [44, 64, 67, 68, 325–329]. The capacitive semi-circle at high frequencies is usually attributed either to the formation of an oxide film, or to the transport of ionic species through said film [44, 67, 68, 327–329]. The inductive semi-circle in the mid-frequency range is associated with relaxation phenomena in the oxide bulk or on the surface [67, 327], as well as with the adsorption of reaction intermediates [326, 329]. The dissolution of the oxide film [64, 67], the competing adsorption of electrolyte anions [329], or diffusion processes within the oxide film [68] are suggested to be responsible for the capacitive semi-circle at low frequencies. Notably, the measured impedance spectra strongly resembled data obtained during the study of passive, compact films covering other valve metals such as bismuth, niobium, molybdenum and tungsten in acidic solutions [263, 330–338].

5.3.4 Model identification

Several models, specifically developed for film formation on aluminium, were considered to fit the EIS data. Bessone et al. [68] studied passive films in NaCl solutions. They explained the observed capacitive semi-circle at low frequencies in terms of diffusion processes within the passive film, modelling it via a Warburg impedance with a transmissive boundary condition for finite-length diffusion. A satisfactory fit using their model could not be obtained. A reaction scheme based on the Point Defect Model [339–344] was modified by de Wit and Lenderink [329] to incorporate the dissociation reaction of water and the formation of adsorbed oxygen ions on the film/solution interface, in order to explain the inductive time constant observed in the system Al/H_2SO_4. Their model predicts four time constants in total: two possibly overlapping time constants in the high-frequency range, due to the passive film and the charge transfer at the film/solution interface; followed by an inductive time constant in the mid-frequency range, resulting from oxygen-ion adsorption; and a capacitive time constant at low frequency caused by the competing adsorption of electrolyte anions. Only three time constants were observed in the present case and no overlap of time constants in the high-frequency range occurred. Furthermore, these authors presume that film growth and dissolution are small. In the present work, the surface-charge approach developed by Bojinov and co-workers [330, 331, 333, 334, 345] was adopted to model the EIS data. This model has been

frequently used to describe the formation and dissolution of barrier films on valve metals in acidic solutions [330, 331, 333–338]. Moreover, it matches the number and type of observed impedance features, namely a capacitive time constant at high and low frequency, and an inductive time constant in the mid-frequency range.

5.3.5 Surface-charge approach

The surface-charge approach is based on ideas drawn from Dignam's dielectric-relaxation model [347] and on the work of de Wit et al. [325], who assumed that relaxation phenomena within the anodic oxide film can be accounted for by the assumption of a time-dependent surface charge, as well as on the defect chemistry of barrier films developed by MacDonald et al. [339–344] within the Point Defect Model. The reactions in the barrier film, which is thought to contain a high number of defects in the form of oxygen and metal vacancies, are assumed to be localised at the metal/film and the film/solution interface [342–344] (Figure 5.8). Oxygen vacancies are generated at the metal/film interface and are consumed at the film/solution interface, while metal vacancies are formed at the film/solution interface and annihilated at the metal/film interface. The faster movement of oxygen vacancies leads to the formation of a negative surface charge at the film/solution interface. While both oxygen and metal vacancies contribute to the current through

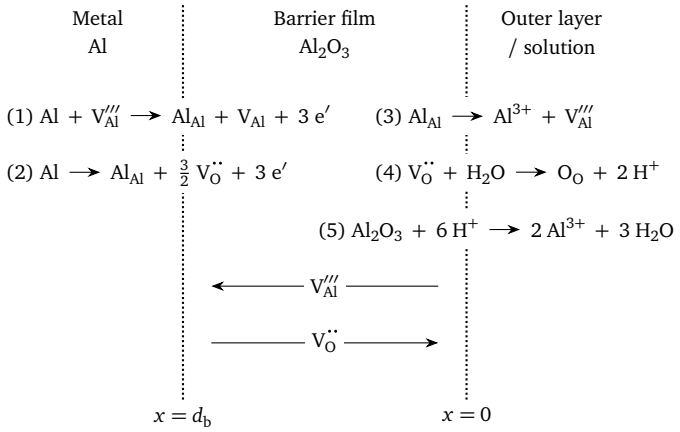

Figure 5.8: Defect chemistry of an alumina barrier film according to the Point Defect Model using the Kröger-Vink notation: V_{Al} (vacancy in the metal phase), Al_{Al} (aluminium atom at a cation site in the cation sub-lattice), $V_O^{\cdot\cdot}$ (oxygen vacancy in the anion sub-lattice), V_{Al}'''' (aluminium vacancy in the cation sub-lattice), O_O (oxygen atom at an anion site in the anion sub-lattice). The role of cation interstitials has been neglected for simplicity (adapted from Sikora et al. [346]).

the film, only the flux of oxygen vacancies leads to film formation at the metal/film interface under steady-state conditions. Film dissolution takes place at the film/solution interface, either via an electrochemical or a chemical reaction, depending on the oxidation state of the metal in the oxide and in solution. The thickness of the barrier film (d_b) depends linearly on potential. The electric field (E_F) is assumed to be constant throughout the film and independent of film thickness and potential. The potential drop across the film/solution interface depends linearly on the applied potential, and it is proportional to the polarisability of the film/solution interface (α). The presence of an outer layer, such as a salt film, has been considered, but the impedance of the system is thought to be dominated by the barrier film.

In contrast to the Point Defect Model, the flux of oxygen and metal vacancies is not obtained by solving the Nernst-Planck equations, but via a mechanistic approach, assuming an ion-hopping mechanism within the film, as described by Fromhold [348]. At steady state and in the limit of high electric-field strengths, the current density through the film can thus be described by an exponential law [333, 334]:

$$i = N_A \exp(N_B E_F/(1-\alpha)) \tag{5.1}$$

The pre-exponential factor N_A and the parameter N_B are related to the diffusion coefficient of oxygen vacancies (D_O), the oxygen-vacancy concentration at the metal/film interface (c_O), the ideal gas constant (R), the absolute temperature (T), the Faraday constant (F), the half-jump distance (a), and the charge-transfer number (z_e), respectively, yielding [333, 334]:

$$N_A = z_e F D_O c_O/2a \tag{5.2}$$

$$N_B = z_e F a/RT \tag{5.3}$$

The resulting impedance equation can be represented by the equivalent electrical circuit given in Figure 5.9. Herein, R_s denotes the solution resistance, C_b the capacitance of the barrier film, R_b the resistance to vacancy movement, R_{sc} and L_{sc} are associated with the relaxation of the negative surface charge, and C_0 is the faradaic pseudo-capacitance. The inductance L_c represents the inductive behaviour in the high-frequency range caused by the cabling and the measurement cell, and thus has no relevance to the formation or dissolution of the barrier film. The relations between the model parameters and the elements of the equivalent electrical circuit are as follows [333, 334]:

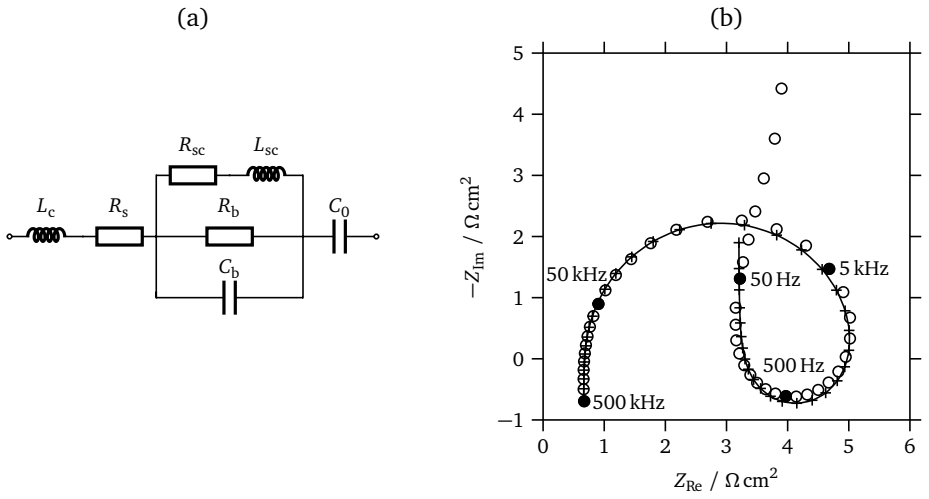

Figure 5.9: (a) Equivalent electrical circuit representing the surface-charge approach, as well as (b) comparison between EIS data recorded at an applied potential of 1.4 V at 75 °C and 100 rpm (○) and the respective circuit fit (—+—). Data at low frequencies was omitted from the fit.

$$iR_b = d_b/N_B(1-\alpha) = E/N_B E_F \tag{5.4}$$

$$iR_{sc} = d_b/N_B\alpha \tag{5.5}$$

$$L_{sc}i^2 = d_b/SN_B\alpha \tag{5.6}$$

$$1/C_b = d_b/\varepsilon_b\varepsilon_0 = E(1-\alpha)/\varepsilon_b\varepsilon_0 E_F \tag{5.7}$$

$$C_0 = z_{ox}F(1-\alpha)/V_{ox}\eta_{ox}E_F \tag{5.8}$$

Herein, S designates the capture cross-section for positive defects by the negative surface charge, ε_b the relative permittivity of the barrier film, ε_0 the permittivity of free space, V_{ox} the molar volume of the oxide, z_{ox} the number of moles of electrons consumed per mole of oxide, and η_{ox} the current efficiency for film formation.

5.3.6 CNLS regression

The EIS data recorded at 75 °C was subsequently fit to the equivalent electrical circuit representing the surface-charge approach, using a complex non-linear least squares (CNLS) regression method (Section 2.4.3). Within the CNLS regression method, the χ^2 statistic was minimised [138, 141]. As the variance at each frequency was unknown, the data was weighted using the square of the modulus of the impedance instead [140]. The minimum of χ^2 was found using a Levenberg-Marquardt

algorithm [142] combined with an initial parameter search [141]. The final value for χ^2 divided by the degrees of freedom ranged between 10^{-3} and 10^{-4}, and the real and imaginary residuals were smaller than ±5 % in the frequency range of the fit. The parameter variances were estimated at the end of the CNLS regression by assuming that the weights were proportional to the inverse variance of the experimental data, and that the model represented a good fit to the data [138].

The inductive behaviour observed in the high-frequency range was accounted for by choosing a value of 0.15 to 0.30 µH cm^2 for the cabling inductance in series (L_c). This ensured a correct estimation of the other circuit elements, especially of the solution resistance in series [136]. Comparing the results of the CNLS regression to a graphical method for the estimation of the solution resistance yielded values that were up to 24 % too large relative to the graphical approximation.

Replacing the film capacitance with a constant-phase element (CPE) was considered, but resulted in a CPE coefficient close to unity in all cases; hence, a pure capacitor could be used instead. Effectively, the introduction of the cabling inductance accounted for the slight depression of the high-frequency semi-circle. Replacing the faradaic pseudo-capacitance with a CPE resulted in a superficially better fit at the lower frequencies. However, the final value of χ^2 divided by the degrees of freedom remained almost unchanged. Furthermore, the effective capacitance values calculated from the CPE coefficients [349] were on average only 5 % larger than values obtained using a pure capacitor. Hence, to minimise the number of model parameters, data points at the lowest frequencies, which deviated from a purely capacitive behaviour, were omitted from the fit, and a pure capacitance was used instead. Note that a deviation from purely capacitive behaviour in the low-frequency range can be expected, if the slope of the current-potential curve is not zero — that is, if the experimental polarisation resistance is finite [336, 350]. In fact, the linear potential sweeps showed that the slope along the limiting-current plateaus increased with rotation rate (Figure 5.3). The same relationship could be inferred from the increasing deviation from purely capacitive behaviour in the low frequency EIS data at constant applied potential and different rotation rates (Figure 5.5).

Several dependencies of the fitted parameters on applied potential and rotation rate could be observed (Table 5.1). The barrier-film capacitance (C_b) ranged from 1–4 µF cm^{-2}, decreasing as the applied potential rose, whereas rotation rate had only a negligible effect. Notably, it was about one order of magnitude smaller than a typical double-layer capacitance on a bare-metal electrode [135]. The resistance associated with the movement of vacancies (R_b), as well as the circuit elements linked to the negative surface charge (R_{sc}, L_{sc}) behaved similarly, increasing as applied potential

Table 5.1: Example data showcasing the effect of applied potential and rotation rate on the fitted circuit elements of the equivalent electrical circuit in Figure 5.9(a).

E_{appl} (V)	Ω (rpm)	i ($mA\,cm^{-2}$)	R_s ($\Omega\,cm^2$)	C_b ($\mu F\,cm^{-2}$)	R_b ($\Omega\,cm^2$)	R_{sc} ($\Omega\,cm^2$)	L_{sc} ($mH\,cm^2$)	C_0 ($mF\,cm^{-2}$)
1.4	100	60.7	0.661	3.08	4.47	5.87	2.39	2.53
2.4	100	64.5	0.673	2.21	5.56	6.23	2.55	2.12
3.4	100	63.8	0.650	1.70	7.00	7.61	3.02	1.95
4.4	100	63.5	0.673	1.40	8.40	8.33	3.61	1.87
5.4	100	66.4	0.661	1.19	9.37	8.79	3.74	1.78
5.4	400	139	0.665	1.24	4.51	4.45	0.870	1.81
5.4	900	209	0.624	1.27	3.02	3.03	0.396	1.84
5.4	1600	280	0.637	1.31	2.25	2.25	0.218	1.85
5.4	2500	347	0.651	1.35	1.79	1.74	0.139	1.85

rose and decreasing at higher rotation rates. The faradaic pseudo-capacitance (C_0) showed the same trends as the barrier-film capacitance.

5.3.7 Discussion of the presence of a porous film

Under the conditions of mass-transfer-limited anodic dissolution, the charge transfer across a porous film can be presumed to happen mainly via migration within the electrolyte-filled pores. Such a film is found to contribute to the uncompensated solution resistance, depending on its thickness and porosity, both of which are influenced by rotation rate and/or applied potential [318, 319, 321]. In the present case, the fitted solution resistance in series (R_s) varied between 0.61 and 0.68 $\Omega\,cm^2$ (Table 5.1). Using the conductivity data from Chin and Chang ($\kappa = 0.279\,S\,cm^{-1}$) [351], the electrolyte resistance at virtual infinity could be determined according to the formula $R_s = \pi r_0/4\kappa$ [352], assuming a primary current distribution along the RDE. For a reference electrode at the described position and at virtual infinity, R_s was calculated as 0.46 and 0.73 $\Omega\,cm^2$, respectively. The measured solution resistance was slightly larger than expected, probably due to other resistances in series with the electrochemical cell. Nonetheless, no influence of applied potential or rotation rate on the solution resistance was found. Hence, the presence of a porous film covering the anode during the anodic dissolution of aluminium at 75 °C could be dismissed, confirming the observations made by way of SEM.

5.3.8 Discussion of the presence of a salt film

Mass-transfer-limited anodic dissolution may be accompanied by the precipitation of a salt film, the thickness of which depends on rotation rate and applied potential. In this work, the most likely candidate for salt film formation was $AlPO_4$. In agreement with Equations 5.4 to 5.7, plotting the quantities iR_b, iR_{sc}, $L_{sc}i^2$ and $1/C_b$ against potential yielded the expected linear relationship between film thickness and potential (Figure 5.10). The data obtained at different rotation rates,

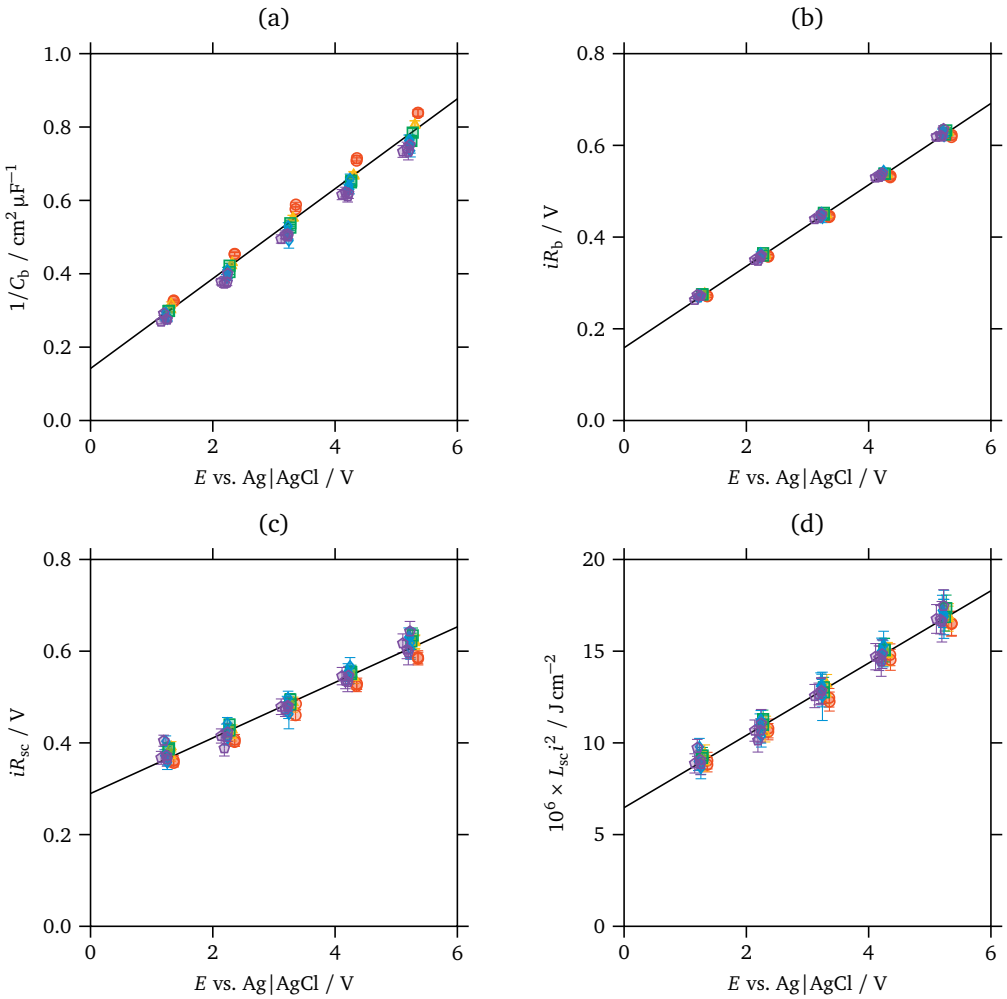

Figure 5.10: Potential dependence of (a) $1/C_b$, (b) iR_b, (c) iR_{sc} and (d) $L_{sc}i^2$, corrected for the ohmic drop, for an aluminium RDE at different rotation rates: 100 rpm (○), 400 rpm (△), 900 rpm (□), 1600 rpm (◇), 2500 rpm (⬠). The error bars signify one standard deviation.

however, fell at the same line in each case, indicating that rotation rate had a negligible effect on the film's thickness. This is in contrast to the analysis of EIS data measured in systems that exhibit the precipitation of a salt film during high-rate anodic dissolution [318, 319, 321]. In order to rule out the presence of $AlPO_4$ along the aluminium surface, the saturation concentration of $AlPO_4$ was compared with an estimate of its surface concentration. The solubility of $AlPO_4$ was extrapolated as 5 g per 100 g of solution in 85 % H_3PO_4 from equilibrium data in the system $AlPO_4/H_3PO_4/H_2O$ [353]. Assuming the density ($\rho = 1.645\,g/cm^3$) [354] and viscosity ($\mu = 9.67 \times 10^{-2}\,g\,cm^{-1}\,s^{-1}$) [351] for 85 % H_3PO_4 at 75 °C were unchanged by the small amount of $AlPO_4$ present, this corresponded to a saturation concentration of roughly $0.67\,mol\,cm^{-3}$. From the slope in the Levich-Koutecky plot at 75 °C (Figure 5.4) the surface concentration of Al^{3+} ions was estimated using the Levich equation [133]. Assuming $z_e = 3$, $D_{Al^{3+}} = 10^{-7}\,cm^2\,s^{-1}$ and 100 % current efficiency for aluminium dissolution, this yielded a surface concentration of $0.15\,mol\,cm^{-3}$. Given that the assumed diffusion coefficient was already on the lower end, the precipitation of $AlPO_4$ along the anode surface could be safely dismissed. It was hypothesised instead that the surface film present during anodic dissolution in phosphoric acid consisted of a non-porous Al_2O_3 barrier film.

5.3.9 Barrier film properties

The properties of the Al_2O_3 barrier film could be calculated from the obtained potential dependence of the circuit elements (Table 5.1). From Equations 5.4 to 5.6 the relations for the parameters α and S are [333, 334]:

$$R_b/R_{sc} = \alpha/(1-\alpha) \tag{5.9}$$

$$L_{sc}i/R_{sc} = 1/S \tag{5.10}$$

In accordance with the model, a linear relationship was obtained when plotting R_{sc} against R_b and $L_{sc}i$ against R_{sc} (Figure 5.11). From the respective slope, the polarisability of the film/solution interface (α) was calculated as 0.508 ± 0.002 (Table 5.2). A similar value was computed for films formed on molybdenum and tungsten in concentrated phosphoric and sulphuric acid [333, 334]. The capture cross-section for positive defects (S) equalled $(36.6 \pm 0.5)\,cm^2\,mC^{-1}$, corresponding to an interaction radius for positive-defect capture of (0.432 ± 0.003) nm. Similar values for alumina films are listed by Dignam [347] and have also been calculated by de Wit et al. [325] and Frers et al. [67] for alumina films formed in ammonium pentaborate/glycol and in NaCl solutions, respectively.

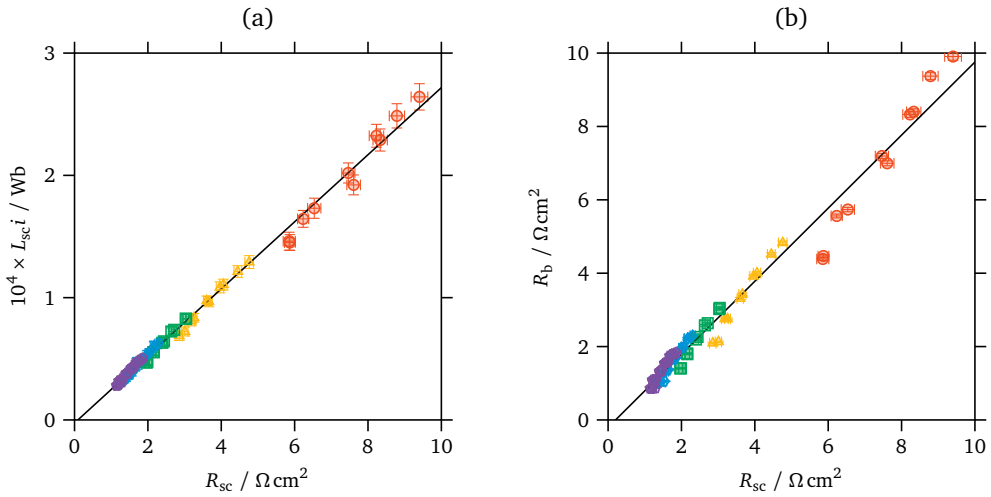

Figure 5.11: Relationship between (a) $L_{sc}i$ and R_{sc} and between (b) R_b and R_{sc} for an aluminium RDE at different rotation rates: 100 rpm (○), 400 rpm (△), 900 rpm (□), 1600 rpm (◇), 2500 rpm (⬠). The error bars signify one standard deviation.

Using this value for the polarisability of the film/solution interface and assuming $\varepsilon_b = 9.6$ for alumina [61], the electric field across the barrier film was calculated from the potential dependence of the inverse film capacitance according to

Table 5.2: Results for linear regression of the data presented in Figures 5.10 and 5.11 including the standard deviation and resulting model parameters of the surface-charge approach according to Equations 5.3, 5.4, 5.7, 5.9 and 5.10.

Slope			
$\mathrm{d}(1/C_b)/\mathrm{d}E$	($\mathrm{cm^2\,\mu F^{-1}\,V^{-1}}$)	(1.225	± 0.007) × 10^{-1}
$\mathrm{d}(iR_b)/\mathrm{d}E$		(8.83	± 0.04) × 10^{-2}
$\mathrm{d}(L_{sc}i)/\mathrm{d}R_{sc}$	($\mathrm{Wb\,\Omega^{-1}\,cm^{-2}}$)	(2.73	± 0.04) × 10^{-5}
$\mathrm{d}R_b/\mathrm{d}R_{sc}$		1.032	± 0.009
Model parameter			
E_F	($\mathrm{MV\,cm^{-1}}$)	4.7	± 0.3
a	(nm)	0.36	± 0.03
N_B	($\mathrm{cm\,MV^{-1}}$)	2.4	± 0.2
S	($\mathrm{cm^2\,mC^{-1}}$)	36.6	± 0.5
α		0.508	± 0.002

Equation 5.7 to equal $(4.7 \pm 0.3)\,\mathrm{MV\,cm^{-1}}$. Assuming $z_e = 2$ for mobile oxygen vacancies, the half-jump distance for oxygen vacancies moving through the film was $(0.36 \pm 0.03)\,\mathrm{nm}$, and the parameter N_B equalled $(2.4 \pm 0.2)\,\mathrm{cm\,MV^{-1}}$. The obtained values agreed well with data for Al_2O_3 films in the limit of high electric-field strengths [61]. With the above values, the film thickness could be calculated from the capacitance data given in Table 5.1 using Equation 5.7. At 100 rpm and an applied potential of 1.4 V this gave a thickness of 2.8 nm. At 2500 rpm and 5.4 V the film thickness was 6.3 nm. The anodising ratio was calculated as $(1.042 \pm 0.006)\,\mathrm{nm\,V^{-1}}$ in agreement with literature data [52, 61, 67, 71].

According to Equation 5.1, assuming the electric-field strength and the parameter N_B are constant, the observed increase of the limiting current density with rotation rate is only possible, if the pre-exponential factor N_A is proportional to $\Omega^{1/2}$ (Figure 5.12). Previously, this linear relationship between N_A and $\Omega^{1/2}$ was attributed to an increase in the number of charge carriers within the film, as the current density increases [318, 319]. According to Equation 5.2, the concentration of oxygen vacancies at the metal/film interface has to increase for the pre-exponential factor N_A to rise, presuming that the diffusion coefficient for oxygen vacancies and the half-jump distance are independent of the current passing through the film. This change in concentration leads to an increase in the flux of oxygen vacancies across the film. The same conclusion can be drawn starting from the reaction scheme of the Point Defect Model (Figure 5.8). Within this scheme, only Reactions (2) and (5) lead to a change in barrier-film thickness [346]. Reaction (2) describes the growth of the barrier film, which concurrently generates oxygen vacancies, and Reaction (5) its dissolution. As rotation rate and thus current density rise, the film dissolves at a higher rate. For film thickness to be independent of rotation rate, an increase in the dissolution rate must be matched by a rise in the rate of film growth at the metal/film interface, in line with Reaction (2). In parallel, this creates more oxygen vacancies, resulting in a larger flux of oxygen vacancies through the barrier film.

The faradaic pseudo-capacitance (C_0) deserves special mention. According to Equation 5.8, it represents the stored charge per volume of film formed for a given variation in film thickness and potential [325, 330]. At 75 °C the faradaic pseudo-capacitance varied from 1.78–2.59 $\mathrm{mF\,cm^{-2}}$, in the usual range obtained for other valve metals (Figure 5.13). The value of the faradaic pseudo-capacitance corresponding to a current efficiency for film formation (η_{ox}) of unity was calculated as $1.77\,\mathrm{mF\,cm^{-2}}$ (assuming $V_{ox} = 3.40 \times 10^{-5}\,\mathrm{m^3\,mol^{-1}}$ and $z_{ox} = 6$ for Al_2O_3) [61]. Hence, as the faradaic pseudo-capacitance decreased, the current efficiency for film formation increased on average from 0.70 at 1.4 V to 0.97 at 5.4 V. This was in contrast to other studies, which found the faradaic pseudo-capacitance to be inde-

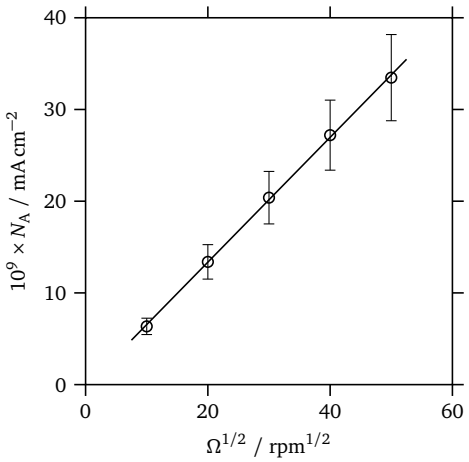

Figure 5.12: Variation of the pre-exponential factor N_A with the square root of rotation rate. The error bars signify one standard deviation.

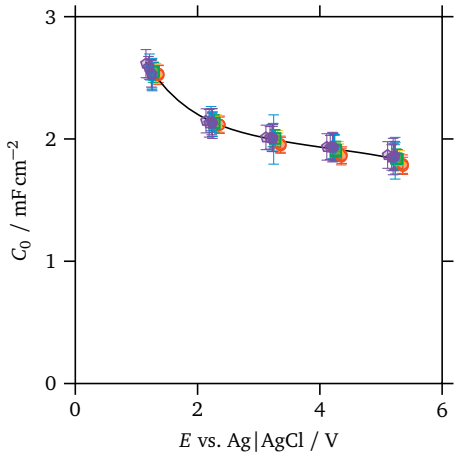

Figure 5.13: Variation of the faradaic pseudo-capacitance with shifts in applied potential, corrected for the ohmic drop in the electrolyte: 100 rpm (○), 400 rpm (△), 900 rpm (□), 1600 rpm (◇), 2500 rpm (⬠). The error bars signify one standard deviation.

pendent of potential [330, 333–336, 350]. The high value found for η_{ox} could be interpreted as evidence that few side reactions beside oxide formation took place [335]. Possible side reactions are field-induced dissolution of the oxide, direct ejection of Al^{3+} ions into the electrolyte, and oxygen evolution — all of which decrease the current efficiency for film formation. By fitting the surface-charge approach to EIS data measured at an applied potential of 1.4 V at 25 and 50 °C, the respective values for the faradaic pseudo-capacitance were estimated as 2.75 and 3.23 mF cm^{-2},

corresponding to a current efficiency for film formation of about 0.55 and 0.65. Shimizu and Kobayashi [324] determined a similar value of 0.535 for η_{ox} under galvanostatic control during the initial stages of barrier-film growth in 0.4 M H_3PO_4 at 16 °C. The increase of the current efficiency for film formation with temperature coincided with the observed change in film structure from a porous to a compact-alumina film. This matches the general observation that films formed in barrier-film-forming electrolytes grow at a higher current efficiency than films formed in porous-film-forming electrolytes [71].

5.4 Conclusions

EIS data recorded during the mass-transfer-limited dissolution of aluminium in concentrated phosphoric acid could be adequately fit to an equivalent electrical circuit, which assumed the presence of a compact, barrier-type Al_2O_3 film. The presence of a precipitated salt film consisting of $AlPO_4$ could be excluded based on the negligible influence of rotation rate on the circuit elements. The capacitive and inductive semi-circles could be clearly linked to the capacitive charging of the oxide film in the high-frequency range, the relaxation of a negative surface charge at the film/solution interface, and the perturbation of the film thickness in the low-frequency range. Several parameters relevant to the transfer processes within the barrier film were calculated such as the electric-field strength, the half-jump distance for the underlying ion-hopping mechanism, and the polarisability of the film/solution interface, all in good agreement with previous studies on films formed on aluminium and other valve metals. Based on the film capacitance, the barrier-film thickness was calculated to range from 2–7 nm in the potential range of 1.4–5.4 V.

With TMEMM in mind several conclusions can be drawn on the basis of remarks by West [315] towards electrochemical planarisation. As the film thickness during mass-transfer-limited dissolution is on the order of nanometres under the present conditions, the film/solution interface is well defined and known *a priori*. The calculation of the position of the film/solution interface, taking into account the hydrodynamics in the interelectrode gap, is thus not necessary. For the same reason, the charge transfer within the film can be treated in a simplified, one-dimensional manner, and the redistribution of current density within the film can be neglected. This greatly simplifies the calculation of the local etch rate along the cavity surface and of the final shape of the evolving cavity.

6 Modelling and simulation of current distribution and shape evolution

The following chapter describes in greater detail the mathematical model, which is used for the simulation of shape-evolution experiments in Chapter 7. In particular, the model derivation is performed, each underlying assumption is justified, and the numerical implementation is detailed. In addition, model results are tested for their validity and compared with literature data. Note that an introduction to the topic of shape-evolution simulation is given in Sections 3.2 and 3.3.

6.1 Mathematical model

The geometry of the problem consists of a 15 mm wide aluminium disc, which is covered with a thin, insulating photoresist film. The resist film contains a 5 mm wide pattern of openings, which expose the underlying aluminium surface. The pattern contains five annular openings with radii ranging from about 0.5–2.5 mm, which are concentrically aligned with the disc centre. Electrochemical aluminium dissolution proceeds through these openings, leading to a displacement of the metal surface over time. At all times the dissolution rate is limited by mass transfer, corresponding to the formation of a surface film and a tertiary current distribution along the metal surface. The disc and the liquid are both stationary, that is mass transfer occurs only via diffusion. Several simplifications are necessary at this point.

Firstly, the different geometric length scales are considered (Figure 6.1). Note that both the thickness of the photoresist film ($\sim 2\,\mu m$) and the width of each annular opening ($\sim 10\,\mu m$) are small compared to the overall dimensions of the disc and the pattern. The shape-evolution problem on the scale of a single mask opening is solely determined by the geometry in its immediate vicinity [163]. Thus, each opening can be viewed independently and in isolation from the whole of the pattern. Furthermore, on the mask-opening scale the curvature of each annulus is small and can be neglected. The initial geometry of the problem can therefore be simplified

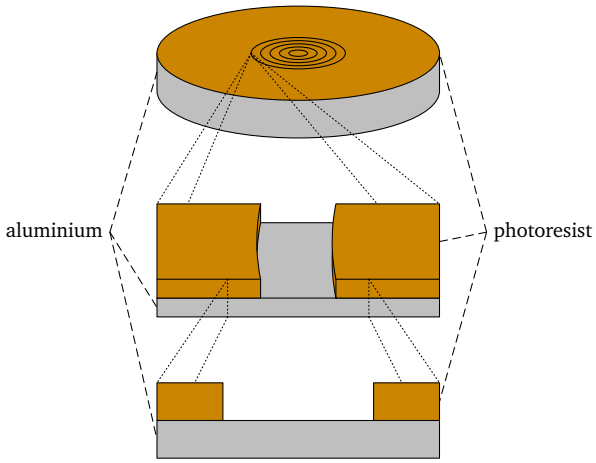

Figure 6.1: Schematic of the geometric simplifications for the shape-evolution model from the initial, three-dimensional disc geometry to the simplified, two-dimensional model geometry.

to yield an isolated, infinitely long line-electrode. Based on these simplifications the problem is solved in two dimensions only.

Secondly, the characteristic time scale (Equation 3.3) of diffusive mass transfer must be accounted for. In viscous liquids ($D \sim 10^{-6}\,\mathrm{cm^2\,s^{-1}}$, Section 7.4.2) and at the discussed length scale ($x_\mathrm{d} \sim 10\,\mu\mathrm{m}$), the characteristic time of diffusive mass transfer lies on the order of a second. By comparison, changes in the position of the metal surface occur over the course of minutes. Initial variations in the shape of the diffusion layer can therefore be neglected, and the diffusion-layer boundary may be represented by a semi-circle at all times (Figure 6.2). Subsequently, a pseudo steady-state assumption may be utilised when solving the model.

It is thus possible to finalise the model geometry (Figure 6.3). The key dimensions to describe the problem are the mask height (h), the mask-opening half-width (w) and the radius of the diffusion-layer boundary. As becomes clear later (Section 6.2), the position of the latter can be presumed to stay constant without affecting the validity of the model results. Two different cases are considered, corresponding to variations in mask thickness and mask-opening half-width [160]. In case the aspect ratio of the mask opening is small ($h/w \leq 1$), the diffusion-layer boundary is represented by a semi-circle of radius $2w$ centred at the coordinate $(0,h)$. For a large-aspect-ratio mask-opening ($h/w \geq 1$), the geometry is further simplified by placing the boundary in parallel with the metal surface at a distance h. This is justified by the fact that the results of shape-evolution models for deeply recessed electrodes are largely unaffected by the position of this boundary [160, 175].

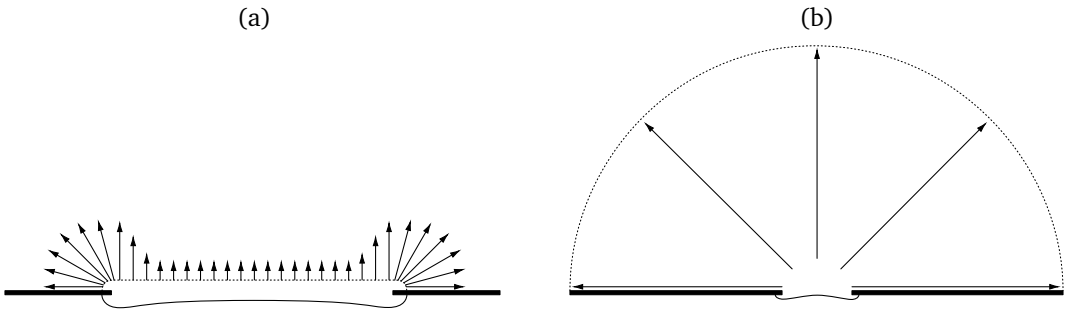

Figure 6.2: Schematic depicting the shape of the diffusion-layer boundary in the vicinity of a single, isolated mask opening at (a) short ($t \ll x_\mathrm{d}^2/D$) and (b) long times ($t \gg x_\mathrm{d}^2/D$) after the beginning of the machining process (adapted from Kuiken [178]). The arrows indicate the relative magnitude of concentration gradients within the diffusion layer.

With the model geometry in place, the governing equations are determined. In general, the concentration (c) in the vicinity of the mask opening and its dependence on mass transfer are described by the convection-diffusion equation [132]. However, this equation can be simplified in the present case, because forced and natural convection are both absent. In addition — when computing the displacement — the aforesaid difference in the time scales associated with diffusive mass transfer and shape changes allows temporal variations in the concentration field to be neglected. This is the aforementioned pseudo steady-state assumption [16, 148]. The convection-diffusion equation is thus transformed into the Laplace equation, which in a two-dimensional Cartesian coordinate system reads [16]:

$$\nabla^2 c = \frac{\partial^2 c}{\partial x^2} + \frac{\partial^2 c}{\partial y^2} = 0 \tag{6.1}$$

Once the concentration is known, the normal current density (i_n) at any point along the metal surface can be calculated, which is linked to the concentration gradient via Fick's law [16]:

$$i_\mathrm{n} = z_\mathrm{e} F D \left(\frac{\partial c}{\partial x} + \frac{\partial c}{\partial y} \right) \tag{6.2}$$

Here, z_e is the charge-transfer number and F the Faraday constant. Assuming 100 % current efficiency, the rate of displacement ($\mathbf{v}$) can in turn be computed via Faraday's law [16, 160]:

$$\mathbf{v} = \frac{M}{z_\mathrm{e} F \rho} i_\mathrm{n} \mathbf{n} \tag{6.3}$$

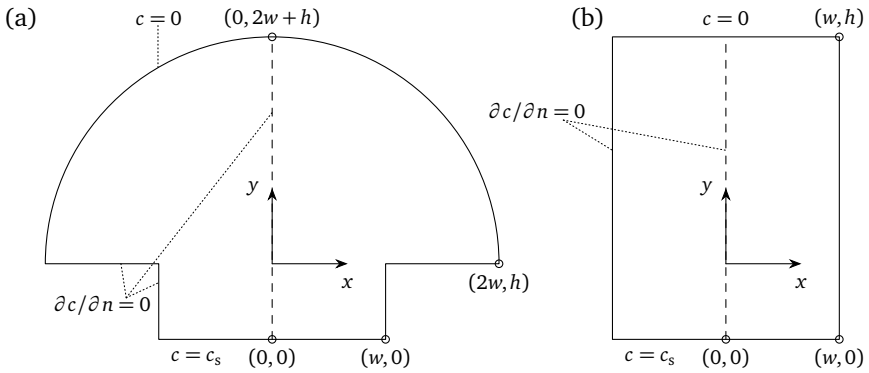

Figure 6.3: Schematic depiction of the two-dimensional geometry of the boundary problem together with the respective boundary conditions for the Laplace equation: for small mask-opening aspect-ratios (a) a semi-circular diffusion-layer boundary centred at $(0, h)$ is assumed, whereas for large aspect ratios (b) the boundary is placed in parallel with the metal surface.

Herein, M denotes the molar mass of the metal, ρ the metal density and $\mathbf{n}$ the unit normal vector relative to the surface. The boundary conditions for the solution of the Laplace equation can now be formulated (Figure 6.3). These are as follows:

$$\partial c/\partial n = 0 \qquad \text{(along the insulator and symmetry line)} \tag{6.4}$$

$$c = c_s \qquad \text{(along the metal surface)} \tag{6.5}$$

$$c = 0 \qquad \text{(along the diffusion-layer boundary)} \tag{6.6}$$

The concentration gradient normal to the symmetry line and to the insulator surface is assumed to be zero, as there is no flux of metal cations across those boundaries. The concentration along the metal surface is assumed to be constant, corresponding to the presence of a surface film. The concentration along the boundary of the diffusion layer equals the bulk concentration.

6.2 Numerical implementation

The mathematical model was solved using two different approaches: the boundary element method (BEM) and the finite element method (FEM). The BEM was utilised extensively in previous studies [16, 20, 148, 160, 161, 173–176] to solve similar problems; hence, it presented a good starting point for the development of a numerical implementation. For this purpose, a program was written in Matlab to solve the model equations and to visualise the results. The performance of this program

was compared with a FEM implementation using the proprietary software Comsol Multiphysics. This also allowed the independent validation of model results. Due to the software being proprietary, the description of the FEM implementation herein necessarily remains more superficial.

6.2.1 Boundary element method

The BEM is a numerical technique for the solution of partial differential equations, which describe the behaviour of a variable along the boundary and within the interior of a domain. To this end, the partial differential equation in question is reformulated as a boundary-integral equation, which involves only the variable values along the boundary. The boundary is discretised, and the boundary-integral equation is subsequently solved numerically. After the solution is known along the boundary, it can be calculated for any point in the interior. The main advantage of the BEM compared to other numerical techniques consists in the fact that the reformulation as a boundary-integral equation reduces the number of spatial dimensions of the problem. For example, for a two-dimensional domain the solution has to be obtained along a line, for a three-dimensional domain along a surface. The main disadvantage of the method lies in its limitation to certain types of partial differential equations, such as the Laplace equation. For more details on the BEM, the reader is referred to the pertinent literature [355–357].

In the present case, the Laplace equation is solved in a two-dimensional geometry using a Cartesian coordinate system. The solution is limited to the positive half-plane depicted in Figure 6.3 due to the inherent symmetry. The boundary-integral formulation of the Laplace equation thus corresponds to a line integral along the perimeter Π, enclosing the interior domain (Figure 6.4) [357]:

$$\begin{aligned}\frac{1}{2}c(\xi,\eta) = \int_{\Pi}\Bigg(&c(x,y)\frac{\partial}{\partial n}(\Gamma(x,y,\xi,\eta)) \\ &-\Gamma(x,y,\xi,\eta)\frac{\partial}{\partial n}(c(x,y))\Bigg)\mathrm{d}s(x,y)\end{aligned} \tag{6.7}$$

This equation relates the concentration c at an arbitrary point (ξ,η) along Π to the concentration and its normal derivative along the whole boundary. The integration variable $s(x,y)$ represents the arc length along the curve. The centre of the cavity bottom corresponds to the start and end point for integration. By convention, integration proceeds counter-clockwise, and the normal vector $\mathbf{n} = (n_x, n_y)$ points

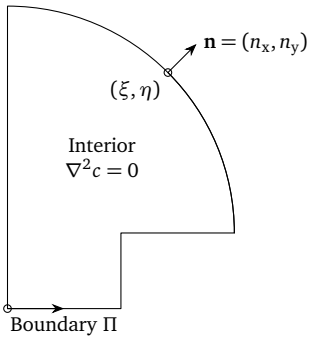

Figure 6.4: Notation and geometry for the boundary-integral formulation of the Laplace equation.

outwards. Γ and $\partial\Gamma/\partial n$ designate the fundamental solution of the Laplace equation and the normal derivative of the fundamental solution, respectively [357]:

$$\Gamma(x,y,\xi,\eta) = \frac{\ln((x-\xi)^2+(y-\eta)^2)}{4\pi} \tag{6.8}$$

$$\frac{\partial}{\partial n}(\Gamma(x,y,\xi,\eta)) = \frac{n_x}{2\pi}\frac{(x-\xi)}{(x-\xi)^2+(y-\eta)^2} + \frac{n_y}{2\pi}\frac{(y-\eta)}{(x-\xi)^2+(y-\eta)^2} \tag{6.9}$$

Due to the complexity of the geometry and the boundary conditions in the present case, Equation 6.7 must be solved numerically. In order to calculate the concentration c at a point (ξ,η), the boundary is discretised into N straight line segments $\Pi^{(k)}$ $(k = 1,2,\ldots,N)$ of length $\lambda^{(k)}$ connecting $N+1$ boundary points (Figure 6.5). The integration is performed over each element individually, with the final results summed to determine the concentration at the specified point.

The position of each line element is governed by the coordinates of its boundary points $(x^{(k)}, y^{(k)})$ and $(x^{(k+1)}, y^{(k+1)})$, which correspond to each element's end points (Figure 6.6). Therein, the coordinates $(\xi^{(k)}, \eta^{(k)})$ and $(\xi^{(N+k)}, \eta^{(N+k)})$ belong to the so-called node points, where a solution to the Laplace equation is subsequently sought. The functions c and $\partial c/\partial n$ must be approximated along each element to facilitate integration. In the present work, this is achieved by using discontinuous linear approximations for both functions [357]:

$$c(x,y) \simeq \frac{\hat{c}^{(k)}(s(x,y)-(1-\tau)\lambda^{(k)}) - \hat{c}^{(N+k)}(s(x,y)-\tau\lambda^{(k)})}{(2\tau-1)\lambda^{(k)}} \tag{6.10}$$

$$\frac{\partial}{\partial n}(c(x,y)) \simeq \frac{\hat{c}_n^{(k)}(s(x,y)-(1-\tau)\lambda^{(k)}) - \hat{c}_n^{(N+k)}(s(x,y)-\tau\lambda^{(k)})}{(2\tau-1)\lambda^{(k)}} \tag{6.11}$$

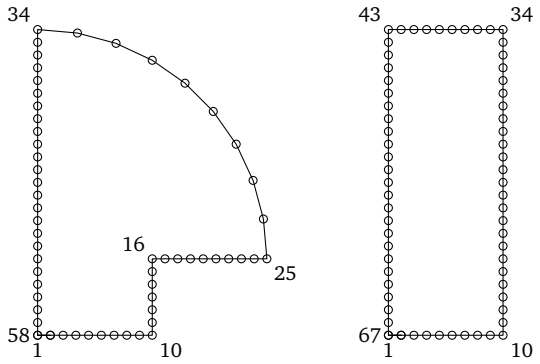

Figure 6.5: Discretisation of the positive half-plane of the two domains shown in Figure 6.3 into line segments and respective numbering of the boundary points. In both cases, the metal surface is represented by nine elements. The first and the last boundary point have the same coordinates.

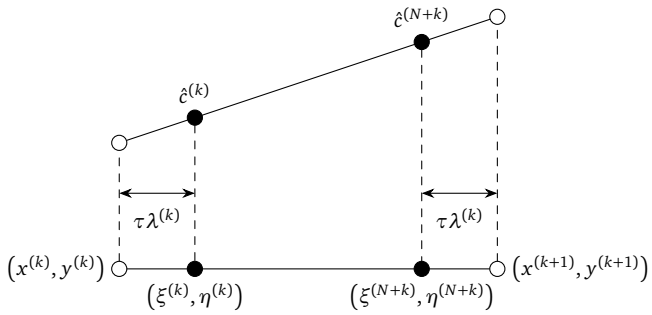

Figure 6.6: Schematic depiction of the geometry and coordinate system for a straight line element $\Pi^{(k)}$ of length $\lambda^{(k)}$, using a linear approximation for the function $c(x, y)$ along the element.

Both approximation functions are defined by their function values for the concentration ($\hat{c}^{(k)}$, $\hat{c}^{(N+k)}$) and for the normal derivative of the concentration ($\hat{c}_{\mathrm{n}}^{(k)}$ and $\hat{c}_{\mathrm{n}}^{(N+k)}$), respectively, at each of the aforementioned node points. Every line element contains two such points, which results in a total of $2N$ node points. Within each element, the node points are positioned at a distance $\tau\lambda^{(k)}$ away from the boundary or end points. The value of the factor τ may range between 0 and 0.5, but in this work a value of 0.25 is adopted [357]. After discretising the boundary into line segments and inserting Equations 6.10 and 6.11 into Equation 6.7, the boundary-integral equation may be written as follows [357]:

$$\begin{aligned}\frac{1}{2}c(\xi,\eta) \simeq \sum_{k=1}^{N} \frac{1}{(2\tau-1)\lambda^{(k)}} \Bigg(& \hat{c}^{(k)} \Big[-(1-\tau)\lambda^{(k)} F_2^{(k)}(\xi,\eta) + F_4^{(k)}(\xi,\eta) \Big] \\ & + \hat{c}^{(N+k)} \Big[\tau\lambda^{(k)} F_2^{(k)}(\xi,\eta) - F_4^{(k)}(\xi,\eta) \Big] \\ & - \hat{c}_{\mathrm{n}}^{(k)} \Big[-(1-\tau)\lambda^{(k)} F_1^{(k)}(\xi,\eta) + F_3^{(k)}(\xi,\eta) \Big] \\ & - \hat{c}_{\mathrm{n}}^{(N+k)} \Big[\tau\lambda^{(k)} F_1^{(k)}(\xi,\eta) - F_3^{(k)}(\xi,\eta) \Big] \Bigg)\end{aligned} \tag{6.12}$$

Within the boundary-integral equation, $F_1^{(k)}(\xi,\eta)$, $F_2^{(k)}(\xi,\eta)$, $F_3^{(k)}(\xi,\eta)$ and $F_4^{(k)}(\xi,\eta)$ designate the remaining line integrals to be solved [357]:

$$F_1^{(k)}(\xi,\eta) = \int_{\Pi(k)} \Gamma(x,y,\xi,\eta)\,\mathrm{d}s(x,y) \tag{6.13}$$

$$F_2^{(k)}(\xi,\eta) = \int_{\Pi(k)} \frac{\partial}{\partial n}(\Gamma(x,y,\xi,\eta))\,\mathrm{d}s(x,y) \tag{6.14}$$

$$F_3^{(k)}(\xi,\eta) = \int_{\Pi(k)} s(x,y)\Gamma(x,y,\xi,\eta)\,\mathrm{d}s(x,y) \tag{6.15}$$

$$F_4^{(k)}(\xi,\eta) = \int_{\Pi(k)} s(x,y)\frac{\partial}{\partial n}(\Gamma(x,y,\xi,\eta))\,\mathrm{d}s(x,y) \tag{6.16}$$

Because straight-line elements and discontinuous linear functions are used to approximate the geometry and function values, the above integrals can still be solved analytically. For a detailed solution see the treatise by Ang [357].

At this point the boundary conditions are used to solve the boundary-integral formulation of the Laplace equation. The values for the concentration and the normal derivative at all node points $\hat{c}^{(k)}$, $\hat{c}^{(N+k)}$, $\hat{c}_{\mathrm{n}}^{(k)}$ and $\hat{c}_{\mathrm{n}}^{(N+k)}$ are assigned according to the known boundary conditions along the boundary Π. In this way, either the function value c or the normal derivative $\partial c/\partial n$ is prescribed along any given line element. By successively positioning the point (ξ,η) in Equations 6.12 to 6.16 at $(\xi^{(k)},\eta^{(k)})$ and $(\xi^{(N+k)},\eta^{(N+k)})$ for each of the N line elements, a system of $2N$ linear equations is obtained. This system of equations is matched by $2N$ unknowns, because at each node point either c or $\partial c/\partial n$ must be determined. The system can thus be solved by the methods of linear algebra, such as Gaussian elimination.

The algorithm to determine the unknowns and to solve the Laplace equation was implemented in Matlab (version R2013b) based on the Fortran programs DPF, DLELAP1 and DLELAP2 presented by Ang [357]. It was necessary to modify these programs to increase their calculation speed. To this end, the algorithm was vectorised as much as possible to make use of Matlab's ability to solve large equation systems quickly and efficiently. In this manner, it was possible to reduce the computation time from several hours down to minutes. For a given geometry, number of line elements and boundary conditions, the resulting Matlab program calculates the concentration and the normal derivative along the boundary for each node point. From this the current distribution is readily available via Equation 6.2.

The resulting amount of displacement in x- and y-direction, Δx and Δy, of each boundary point along the metal surface during a time step Δt is calculated by splitting Equation 6.3 into its x- and y-component. This is achieved by applying a finite-difference approximation [160] to Equation 6.3:

$$\begin{pmatrix} \Delta x \\ \Delta y \end{pmatrix} = \frac{M i_\mathrm{n}}{z_\mathrm{e} F \rho} \begin{pmatrix} n_\mathrm{x} \\ n_\mathrm{y} \end{pmatrix} \Delta t \tag{6.17}$$

The boundary points then move according to their position along the surface. Points located along the metal surface move normal to the surface by an amount dictated by Equation 6.17. As each boundary point belongs to two line elements of equal length, the direction of displacement is determined by averaging the normal vectors of both line elements. Similarly, the amount of displacement is resolved by calculating the normal current density for each element separately via Equation 6.11 and then averaging the results. If a boundary point belongs to the metal surface and the insulator boundary at the same time, it is moved tangentially relative along the latter. The amount of displacement is in this case calculated from the normal current density along the line element belonging to the metal surface only.

A special case arises when moving the boundary during the first time step. As a result of the initial current distribution along the metal surface, the displacement of the boundary point — which lies on the metal surface and the insulator boundary at the same time — is not properly defined. In order to compensate, this node is moved artificially by an amount $2.5 \times 10^{-4} w$ along the insulator boundary during the first time step. An additional line element is introduced to restore the corner in the insulator boundary. According to West et al. [160] the error introduced by a small modification of the boundary is negligible after a few time steps.

The length of a time step Δt is chosen to be small, so that the displacement of the boundary point in the centre of the evolving cavity at $x = 0$ equals $5 \times 10^{-3} w$, thus avoiding convergence problems [160]. The displacement of all other boundary points along the metal surface is adjusted in proportion to the relative magnitude of the normal current distribution. Shape profiles are thus simulated at an equidistant spacing in relation to the cavity centre, not for specific times. This has the side effect that the charge-transfer number, Faraday constant, diffusion coefficient, molar weight, density, as well as the surface concentration along the metal boundary need not be known; they can be chosen arbitrarily. These parameters need only be specified in case the time it takes for a cavity to form is of interest. As another side effect, the position of the diffusion-layer boundary may remain constant. This is because the concentration gradient, and hence the current distribution, is effectively normalised with respect to the cavity centre.

Within the algorithm, the initial number of line elements — and hence node points — is set by specifying the number of elements along the metal surface. The same spacing of node points is then used along the insulator boundaries. The diffusion-layer boundary is approximated by the same number of elements as the metal surface, resulting in a lower density of node points. The spacing of node points is kept roughly constant during the simulation by redistributing the boundary points along the metal surface after each time step, and by adding line elements along the insulator boundaries if necessary. The point-redistribution algorithm was implemented via the Matlab functions interparc and arclength [358, 359].

6.2.2 Finite element method

The FEM is a numerical technique, which is applied to boundary-value problems in arbitrarily shaped domains. A solution is obtained by first dividing the domain into smaller sub-domains of simple geometric form. The variable of interest is then represented via simple, parameter-based functions within each sub-domain. The boundary-value problem is thus transformed into the simpler problem of determining the parameter values for each sub-domain. By applying the boundary conditions along the domain boundary and between the sub-domains, a system of linear equations can be constructed and subsequently solved. The main advantage of the FEM lies in the possibility to solve problems in domains of varying shape. The FEM is also applicable to a wide range of problems including heat and mass transfer, fluid mechanics, and structural mechanics [360–363].

In this work the FEM was implemented in Comsol Multiphysics (version 4.3b). Two components, the convection-diffusion equation and the moving-mesh interface, were used to this end. The convection-diffusion equation was modified to yield the Laplace equation by setting the convection and damping coefficient, as well as sink and source terms, to zero. The zero flux and Dirichlet boundary conditions were employed to represent the boundary conditions of the model. The convection-diffusion equation was coupled to the moving-mesh interface by specifying a normal mesh velocity along the metal surface, which represented the concentration gradient along the x- and y-coordinate. Applying two separate boundary conditions for the displacement in x- and y-direction lead to instabilities instead.

The two-dimensional model geometry shown in Figure 6.3 was halved and represented by three sub-domains: a quarter-circle of radius $2h$, a rectangle of height h and width w, as well as a pre-defined etch form [364]. The latter was sized with a width of $1.005w$ and depth of $0.01h$, and was thus small compared to the whole geometry. Introducing a pre-defined etch form was necessary to solve the problem of modifying the geometry during a simulation. To this end, the pre-defined etch form allowed the evolving cavity to expand correctly underneath the insulator.

When forming a unified domain, the boundaries between each sub-domain were preserved. Firstly, this resulted in a higher number of mesh elements close to the metal surface, notably at early times during the simulation (Figure 6.7). Secondly, different boundary conditions for the moving-mesh interface could be applied to each sub-domain separately. In general, it was found that limiting mesh deformations and movements to the pre-defined etch form lead to higher stability.

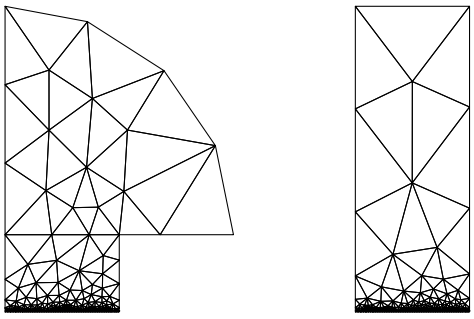

Figure 6.7: Discretisation of the positive half-plane of the two domains shown in Figure 6.3 into triangular mesh elements. Both domains contain a pre-defined etch form, thus leading to smaller elements along the metal surface. The mesh-element size corresponds to the setting ‘extremely coarse’.

A fixed time step was implemented in the model, after which the concentration field within the domain was re-calculated each time. Simultaneously, the perimeter along the metal surface was displaced. As with the BEM before, all other model parameters were chosen arbitrarily. Both the time step and the simulation time were simply chosen to generate about 200 successive shape profiles. After each time step, a criterion based on the maximum element distortion was checked to evaluate the mesh quality. The mesh quality was found to decrease rapidly over the course of the simulation, due to large deformations of the model geometry. Hence, it was necessary to employ automatic re-meshing. In addition, the mesh was smoothed via a Laplace algorithm after each time step. Furthermore, linear shape functions were used to define the geometry within the moving-mesh interface. This step resulted in a more stable simulation compared to higher-order shape functions.

6.3 Model validation

For the purpose of validating the model results, the influence of the number of line and mesh elements was studied for both numerical methods. Two different initial model geometries were tested, corresponding to a large ($h/w = 1$) and small ($h/w = 0.1$) mask-opening aspect-ratio. In the BEM implementation, the number of line elements along the metal surface was varied between 10 and 150; thus, the total number of line elements initially ranged from 52–1050. For the FEM, several mesh-element sizes were used, corresponding to 787–14 882 elements for both initial geometries. Model results were then computed for different ratios of etch depth to initial mask-opening width (d/w), ranging from 0.05–4.00. The results were compared on the basis of the etch factor.

For both the BEM and FEM, the number of line and mesh elements had only a negligible influence on the shape profile and etch factor of deeper channels ($d/w > 2$). When comparing results for the smallest and largest element number, the largest deviation amounted to 0.5 % and 2.1 %, respectively. Varying the number of elements mainly affected the results for shallow channels ($d/w < 2$) (Figures 6.8 and 6.9). When increasing the number of line elements along the metal surface from 100 to 150, the etch factor varied at most by 2.9 % and on average by 0.2 % for the range $0.05 < d/w < 2$. Subsequent BEM simulations were thus conducted with 100 line elements only. Note that increasing the number of line elements to 200 necessitated a decrease in the time step within the BEM algorithm, thereby avoiding convergence problems. For the FEM, changing the mesh quality from ‘finer’

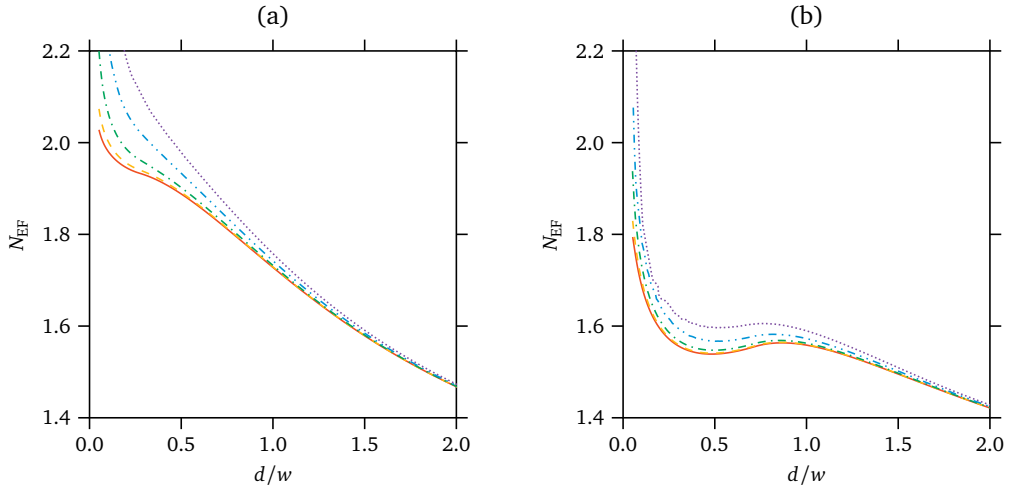

Figure 6.8: Influence of the initial number of line elements along the metal surface, and hence the node-point density, on the accuracy of model results, calculated via the BEM. Results are shown on the basis of changes in the etch factor (N_{EF}), assuming (a) a large ($h/w = 1$) and (b) a small ($h/w = 0.1$) aspect-ratio mask-opening: 10 (·····), 20 (-·-·-), 50 (-··-··-), 100 (- - -), 150 (——).

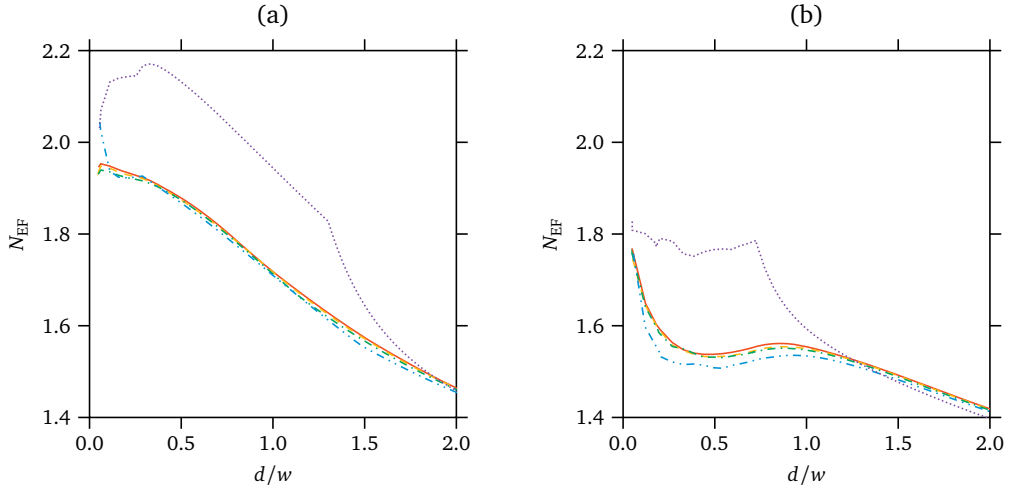

Figure 6.9: Influence of successive mesh refinements on the accuracy of model results, calculated via the FEM. Results are shown on the basis of changes in the etch factor (N_{EF}), assuming (a) a large ($h/w = 1$) and (b) a small ($h/w = 0.1$) aspect-ratio mask-opening: 'extremely coarse' (·····), 'coarser' (-·-·-), 'normal' (-··-··-), 'finer' (- - -), 'extremely fine' (——).

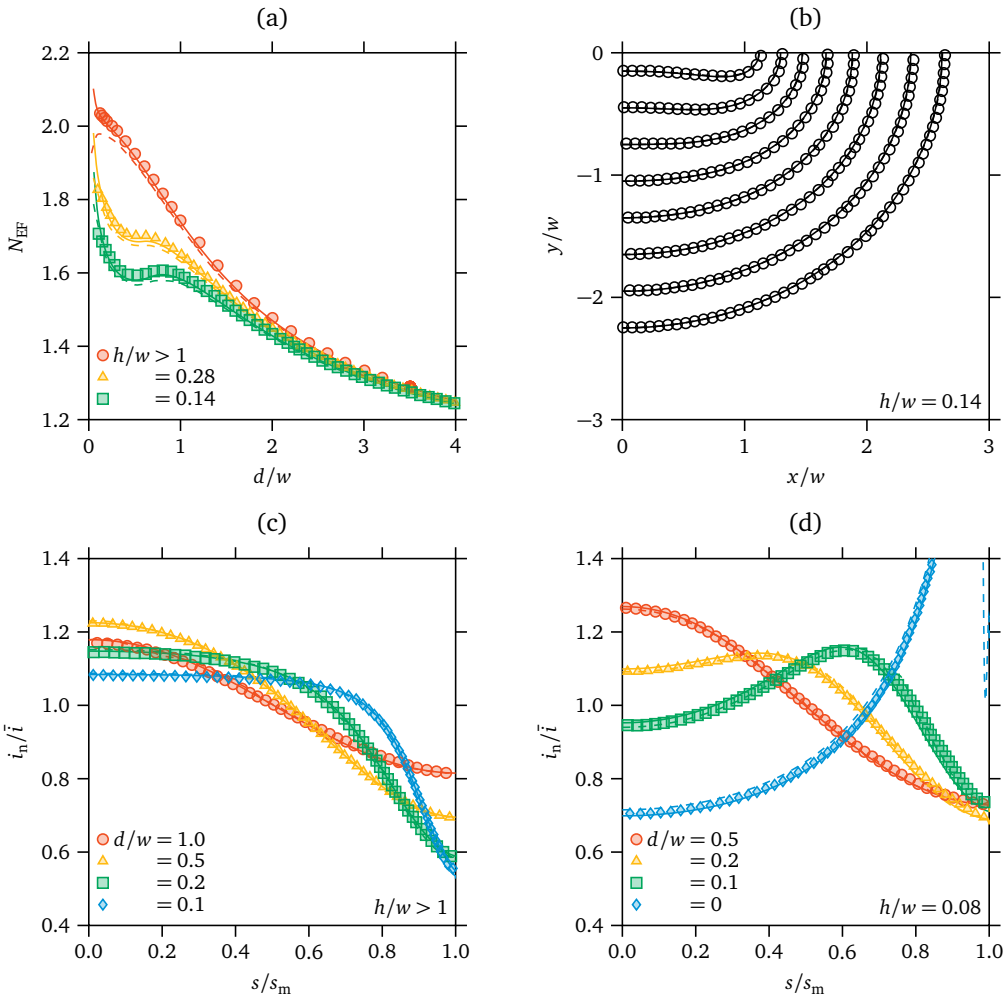

Figure 6.10: Comparison of simulated results with data presented in Figures 5, 6 and 12 in reference [160], as well as with results shown in Figures 5 and 7 in reference [16]: (a) relation between etch factor (N_{EF}) and dimensionless channel depth (d/w), (b) dimensionless shape profile for different times during the dissolution process, (c, d) normalised current distribution along the metal surface for a large ($h/w > 1$) and small ($h/w = 0.08$) aspect-ratio mask-opening. In each case, the solid and dashed lines represent the BEM and FEM results, respectively, and the symbols the referenced data.

to 'extremely fine' resulted in a variation in etch factor of at most 0.6 %, and 0.2 % on average. Hence, the 'finer' setting was used in all simulations.

In a second step, the model results were compared with data from West et al. [160] and Madore et al. [16] (Figure 6.10). Their data was solely available in graphical form and was thus extracted from a digital scan. Results were compared for the etch factor, the dimensionless shape profile and the normalised current distribution ($i_n/\bar{i}$). The latter was normalised with respect to the average current density ($\bar{i}$). The normalised current distribution was then plotted over the normalised arc length (s/s_m), relative to the arc length of the exposed metal surface (s_m).

Given that the literature data had to be extracted from graphs with a limited resolution, the overall agreement was very good. For the BEM, the largest deviation in terms of the etch factor amounted to 2.3 %, with the average discrepancy being 0.4 %. The FEM results showed a slightly larger aberration, with the maximum deviation equal to 2.8 % and an average value of 0.8 %. In general, the error lay below 2.0 % for both methods, except for shallower channels ($d/w < 0.5$). The modelled current distribution at different ratios of channel depth to mask-opening half-width (d/w) deviated at most by 3.8 % with an average error of 0.9 % for the BEM, as well as by 3.4 % and 0.9 %, respectively, for the FEM. For both methods, the largest deviation occurred when calculating the initial current distribution ($d/w = 0$); thereafter, the figures for the relative error decreased. At each value for d/w, the deviation increased towards the corner between the metal surface and the insulator (Figure 6.10 (d)), in particular with the FEM. Nonetheless, the shape profiles simulated via both methods closely resembled the data presented by Madore et al. [16]. The influence of these errors was thus deemed small.

Note that differences between the literature data and the present simulation results may have also had other causes. The initial number of elements, into which the perimeter was discretised, is not specified in either study. Also, in both studies a larger time step ranging between $0.01w$ and $0.02w$ was employed. Finally, in the work by West et al. [160] the element type used for the BEM is not clearly specified. Given the expected experimental uncertainties in determining the shape profile and the etch factor, the accuracy of the results was deemed sufficient.

6.4 Conclusions

The shape-evolution model was successfully implemented using both the BEM and FEM. Both model implementations yielded results in good agreement with literature data, deviating a few percent at most, with the average aberration within one percent. This fact lends validity to the model results for the subsequent comparison with experimental data in Chapter 7. The overall computation time was similar for both methods, on the order of ten to twenty minutes with the same work station (3.40 GHz quad-core CPU, 16 GB RAM).

The main differences between the BEM and the FEM within the scope of this work emerge from the type of model geometry at hand, and from the capabilities of the respective software package. The FEM computes the current distribution at singular points less accurately, such as at the corner between insulating and conducting boundaries. However, results for the etch factor and shape profiles seem unaffected by this inaccuracy, as is evident from the similar error figures. In contrast to the BEM implementation, using a proprietary software for the FEM bestows several key advantages. Firstly, changes to the model geometry, boundary conditions and discretisation method are implemented more swiftly. Secondly, the port from a two- to a three-dimensional model geometry is conducted more easily. This is of importance for shape-evolution studies on more-complex mask patterns.

7 Through-mask electrochemical micromachining of aluminium

This chapter was originally published in the Journal of The Electrochemical Society under the title 'Through-Mask Electrochemical Micromachining of Aluminum in Phosphoric Acid', corresponding to reference [365]. The content is the same apart from grammatical and stylistic corrections, the adoption of British instead of American English, and adjustments to the appearance of figures and tables in line with the remainder of the thesis. As such, the reader may already be familiar with the content of the introductory and experimental sections from other parts of this work.

Abstract

Aluminium microchannels have been machined in phosphoric acid via mass-transfer-limited electrochemical dissolution through photoresist masks. The results of shape-evolution experiments using a rotating disc electrode are presented in terms of the dimensions, shape profile and uniformity of the machined microchannels. The influence of applied potential, cumulative passed charge and hydrodynamic conditions on the shape-evolution process is discussed. Experimental results are compared with a shape-evolution model assuming the rate of aluminium removal is solely controlled by diffusive mass transfer. The extent of agreement between experimental and simulated results depends mainly on the hydrodynamic conditions in the electrochemical cell and indicates a shift from purely diffusive to mixed convective-diffusive mass transfer. The feasibility of electrochemical aluminium micromachining is demonstrated by fabricating microfluidic test structures with well-defined geometries and smooth surfaces.

7.1 Introduction

Through-mask electrochemical micromachining (TMEMM) is an unconventional machining process, in which a metal substrate is made the anode in an electrochemical cell and thereby dissolved [21, 143]. Localised material removal is achieved by covering the substrate with an insulating mask. The use of common photolithography processes for the creation of the mask enables the fabrication

of micrometre-sized structures. Thereby, TMEMM can be used in two ways to fabricate microfluidic devices: firstly, cavities and channels can be machined into the substrate surface; and secondly, through-holes and slits can be machined into metal foils or shims [143]. Compared to classical wet-chemical and dry etching processes, TMEMM offers higher rates of material removal, better control of surface finish, more selective machining of substrates, and enhanced process safety [10, 19, 149]. Moreover, combining photolithography with electrochemical-dissolution processes is expected to enable the fabrication of a large number of microfluidic devices in parallel and at low cost [8].

Aluminium is widely used as a construction material for the manufacture of microfluidic devices such as micro heat exchangers [366], microreactors [1] and micro fuel cells [367]. Other areas of interest are the fabrication of intricate parts in optical, electronic, automotive and aerospace systems [308, 368]. Its chief advantages compared to other materials used in these fields are its high thermal conductivity, low electrical resistivity, easy machinability and low density. In addition, it is possible to modify the surface structure of aluminium substrates via the formation of highly ordered, porous-oxide films along the surface [70, 71]. It has been demonstrated that these films can be subsequently used to incorporate noble-metal catalysts along the surface of microchannels within a microreactor [27, 29, 42].

Electrochemical dissolution of aluminium in phosphoric acid yields polished aluminium surfaces with sub-micrometre surface roughness at sufficiently high electrolyte concentration and temperature [44]. This property makes it attractive for TMEMM of micrometre-sized structures made from aluminium. The observed levelling and brightening effect is caused by the mass-transfer limitation of the dissolution process [54], and it is frequently linked to the formation of oxide or salt films along the surface [22]. Which type of mass transfer dominates the dissolution process — whether it is diffusion, natural or forced convection — thus has a marked influence on the resulting shape profiles [178, 182, 183, 185, 188, 191, 192], and depends on the hydrodynamic conditions in the electrochemical cell.

The use of TMEMM of aluminium has thus far been demonstrated for the fabrication of micrometre-sized cantilevers [276], channels [18], lenses [225] and pits [369]. The majority of this work [18, 225, 276] was conducted in mixtures of perchloric acid, acetic acid and ethanol, which are linked to specific safety concerns due to their reactivity, flammability and limited long-term stability. In addition, previous studies focused mainly on device fabrication and the influence of current density, electrolyte composition, machining time or initial surface structure. At present,

few numerical or experimental studies of TMEMM exist with a focus on the influence of mass-transfer conditions on the resulting depth, width, shape profile and uniformity of machined microchannels. Rosset and Landolt [168] and Rosset et al. [169] presented results on shape evolution during TMEMM of stainless steels, using spray-etching equipment and a flow channel cell, respectively. Winkelmann and Lang [247] studied the effect of conductivity variations on the shape evolution of a steel anode, using a flow channel cell for a modified TMEMM process in combination with a masked cathode tool. This work is complemented by shape-evolution studies pertaining to chemical etching. Shin and Economou [185, 188, 192] were the first to numerically study shape changes during mass-transfer-limited chemical etching, with natural and forced convection present in the vicinity of the mask opening. More recently, other studies [191, 193, 197, 370] have employed different numerical methods to solve similar problems.

The aim of this study is to investigate the effect of mass transfer, namely the change from diffusion to mixed convection-diffusion control, on shape evolution during TMEMM of aluminium in phosphoric acid. To this end, shape-evolution experiments were conducted using a rotating disc electrode (RDE), which allowed experiments to be executed under controlled hydrodynamic conditions. From the analysis of electrochemical impedance spectra [314] it is known that during aluminium dissolution in phosphoric acid the surface is covered with a thin alumina film at all times. As the film's thickness lies on the order of nanometres, its presence can be neglected for the study of shape evolution during TMEMM. The experimental results were thus compared with a shape-evolution model previously developed by Madore et al. [16] for TMEMM of titanium, assuming that shape changes are determined by diffusive mass transfer only. The model was solved numerically using both a boundary element method (BEM) and a finite element method (FEM). The influence of applied potential on the dimensions and uniformity of machined channels was also studied. The feasibility of TMEMM for the fabrication of microfluidic devices made from aluminium was demonstrated by machining several test structures.

7.2 Experimentation

All experiments were performed with a recessed RDE made from commercially pure aluminium (Al $\geq$ 99.00 %, Si+Fe $<$ 1.00 %, Cu $<$ 0.05 %, Mn $<$ 0.05 %, Zn $<$ 0.10 %, Ti $<$ 0.05 %, Wakefield Metals). Disks were machined from 2 mm thick sheet material to a diameter of 15 mm. Prior to each experiment, the discs

were mechanically polished with SiC paper of different grit sizes down to P2000, and then brought to a mirror finish by polishing with alumina slurry of 1 µm and 0.3 µm particle size for one hour each on velvet cloth (ProSciTech), using a LaboPol-2 polishing machine with a LaboForce-1 sample mover (Struers). Afterwards, grease and particles were removed via ultrasonication in acetone, methanol and isopropyl alcohol (IPA) (analytical reagent grade, Thermo Fisher Scientific) for 5 min each, and the discs were dried with pressurised nitrogen. The polished discs were coated with positive-tone AZ1518 photoresist (Microchem) with an average thickness of 1.95 µm using a spin-coater (PWM32, Headway Research), and subsequently pre-baked for 90 s on a hotplate at 100 °C. The photoresist film was exposed to ultraviolet light on a Karl-Süss MA6 mask aligner via proximity exposure, and then developed in AZ MIF 326 (Microchem) for 30 s. Afterwards, the samples were post-baked for 120 s on a hotplate at 120 °C to harden the photoresist mask. The discs were inserted into a polytetrafluoroethylene (PTFE) cap, thus creating a 1 mm deep and 13 mm wide recess (Figure 7.1), and mounted on a AFE6MB RDE shaft. The rotation rate was adjusted with a Modulated Speed Rotator (Pine Research Instrumentation).

Electrochemical experiments were controlled with a Reference 3000 potentiostat (Gamry Instruments) in a custom-made 100 mL glass cell. A 4 cm^2 platinum foil connected to a platinum wire served as the counter electrode in all cases. All potentials are reported against a Ag|AgCl electrode ($c_{KCl} = 4.77\,mol\,kg$, $E_{Ag|AgCl}(75\,°C) = 0.153\,V$ vs. SHE). The reference electrode was connected to a Luggin capillary with an outer diameter of 2 mm. This capillary was held concentrically underneath the

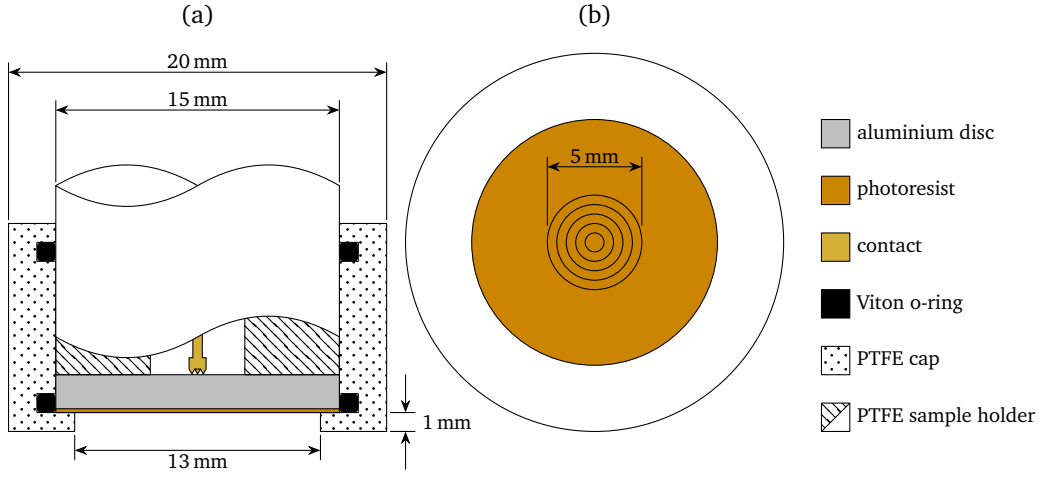

Figure 7.1: (a) Cross-sectional and (b) top view of the recessed RDE, showing the test pattern to be machined consisting of five concentric rings. Photoresist thickness is exaggerated drastically.

RDE at a distance of 10 mm. Before each experiment, the glass cell was ultrasonically cleaned in a 1:1 (v/v) mixture of IPA and de-ionised (DI) water (18.2 MΩ cm, arium 611UV system, Sartorius Stedim Biotech), rinsed several times with DI water, and dried in an oven at 105 °C. During an experiment, the glass cell was immersed in a water bath, the temperature of which was thermostat-controlled at 75 °C within ±1 °C via a copper coil connected to a GD120 thermostat and a LTC1 circulation bath (Grant Instruments). The electrolyte was made from 85 % phosphoric acid (ACS grade, Thermo Fisher Scientific) and used as received.

For shape-evolution experiments, a mask pattern consisting of five concentric rings with centre-line radii of 0.5, 1.0, 1.5, 2.0 and 2.5 mm was used (Figure 7.1). This pattern was chosen to limit the influence of convective mass transfer to the radial flow component along the disc surface only, and to minimize the influence of neighbouring mask-openings on the shape-evolution process of a particular ring. On average, the difference between the inner and the outer radius of each annular mask-opening amounted to 11.5 µm, resulting in a mask-opening aspect-ratio of 0.34 and an initially exposed aluminium surface of 0.542 cm^2. Prior to the shape-evolution experiments, it was tested whether the recess created by the PTFE cap (Figure 7.1), as well as the cap itself, impacted the hydrodynamic conditions in the vicinity of the aluminium disc surface. To this end, the uniform accessibility to mass transfer and the absence of edge effects were confirmed by determining the diffusion coefficient of Fe^{2+} and Fe^{3+} on a gold RDE (AFE2M050AU, Pine Research Instrumentation) with an active area 5 mm in diameter in 0.5 M H_2SO_4, with and without a recess (Appendix B). No influence of the recess or the cap was detected, and the results were found in good agreement with literature values.

Current transients of electrochemical aluminium dissolution through this mask pattern were recorded at an applied potential of 1.4 V in a quiescent solution and at different rotation rates of 100, 400 and 900 rpm, as well as at 5.4 V and 100 rpm. The amount of removed material was governed by adjusting the cumulative passed charge during an experiment to 0.2, 0.5, 1.0 or 2.0 C. All experiments were conducted at least in duplicate. Afterwards, the photoresist was stripped, and the discs were rinsed with IPA, methanol and acetone. Subsequently, the samples were examined via light microscopy (Olympus BX60, Leica DFC320), scanning electron microscopy (SEM) (JEOL JSM 7000F) and optical profilometry (Bruker ContourGT). Cross-sections for further microscope examination were obtained by encasing samples in epoxy, sectioning them, and polishing the cross-sectioned surface to a mirror finish with alumina slurry. For SEM imaging, cross-sectioned samples were also coated with a thin chromium film in an EMS150T ES sputter-coater to reduce charging at the edge between the aluminium and the epoxy.

7.3 Simulation

7.3.1 Mathematical problem

The formulation of the mathematical problem describing the shape evolution during TMEMM has been presented in detail by West et al. [160] and Madore et al. [16], as well as in Chapter 6 within this work. In the case of mass-transfer-limited electrochemical dissolution, a tertiary current distribution can be presumed to govern the local etch rate along the metal surface; hence, the influence of ohmic resistances and electrode kinetics can be neglected. In the absence of convective mass transfer and using a pseudo steady-state assumption for the relaxation of the concentration field (c), the convection-diffusion equation simplifies to yield the Laplace equation:

$$\nabla^2 c = 0 \tag{7.1}$$

Assuming 100 % current efficiency, the rate of displacement ($\mathbf{v}$) of any point along the metal is related to the normal current density (i_n) via Faraday's law:

$$\mathbf{v} = \frac{M}{z_\mathrm{e} F \rho} i_\mathrm{n} \mathbf{n} \tag{7.2}$$

Herein, M denotes the molar mass of the metal, z_e the charge-transfer number, F the Faraday constant, ρ the metal density and $\mathbf{n}$ the unit normal vector. The current distribution along the metal is in turn linked to the gradient of the concentration field close to the surface via Fick's law, where D is the diffusion coefficient:

$$i_\mathrm{n} = z_\mathrm{e} F D \nabla c \tag{7.3}$$

The following boundary conditions apply in order to solve the Laplace equation along the boundary (Figure 7.2):

$$\partial c / \partial n = 0 \qquad \text{(along the insulator and symmetry line)} \tag{7.4}$$

$$c = c_\mathrm{s} \qquad \text{(along the metal surface)} \tag{7.5}$$

$$c = 0 \qquad \text{(along the diffusion-layer boundary)} \tag{7.6}$$

The concentration gradient normal to the symmetry line and to the insulator surface is assumed to be zero, as there is no flux of metal cations across those boundaries. The concentration along the metal surface is assumed to be constant, corresponding

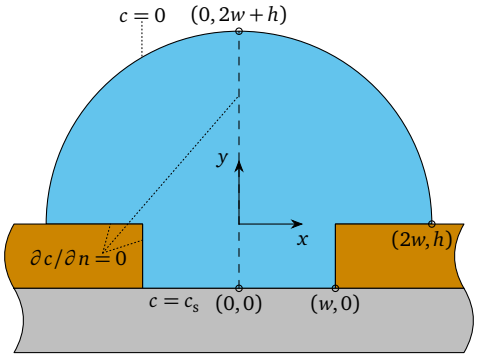

Figure 7.2: Schematic depiction of the calculation domain for a recessed, isolated line electrode. The boundary conditions necessary for the solution of the Laplace equation of the concentration field and the relevant geometrical dimensions are also given.

to the presence of a surface film. The concentration along the boundary of the diffusion layer equals the bulk concentration.

For simplicity, we assume that the curvature of each ring is negligible due to its small width and large radius. Thus, the initial geometry of the problem corresponds to an isolated, infinitely long line-electrode, which is recessed into an insulator. The key dimensions to describe the geometry are the mask height (h) and the mask-opening half-width (w). As the mask-opening aspect-ratio is small ($h/w < 1$) in the present case, the boundary of the diffusion layer can be described by a hemi-cylinder with radius $2w$, which is centred at the coordinate $(0, h)$.

7.3.2 Numerical implementation

The numerical implementation of the shape-evolution simulation using a BEM was based on earlier work on moving-boundary problems [16, 20, 160, 161, 173]. The boundary was first discretised into line segments, where the concentration was approximated along each segment using discontinuous linear functions [357]. Such boundary elements are easy to implement and allow for discontinuities at corner points and at the edge between the metal and the insulator. Subsequently, the Laplace equation was solved, yielding the current distribution along the boundary. At each time step, the amount of displacement in x- and y-direction of every point along the metal surface was calculated by splitting Equation 7.2 into its x- and y-component using a finite-difference approximation [371]. The length of a time step was chosen to be small, so that the displacement in y-direction in the centre of the

evolving cavity ($x = 0$) equalled $5 \times 10^{-3} w$, in order to avoid convergence problems [160] and to increase accuracy. Due to symmetry, only half of the depicted solution domain was considered, in order to reduce the computational effort. The metal surface and the boundary of the diffusion layer were both represented by 100 line segments each. Increasing the number of elements further lead only to negligible changes in the results. The same node density was used along the insulator and the metal surface; hence, the initial boundary consisted of 570 elements in total. At each time step, node points were added and shifted along the metal and insulator boundaries to keep the node density approximately constant.

For comparison, the problem was also implemented in Comsol Multiphysics 4.3b using a FEM. Shape changes during TMEMM were simulated with the convection-diffusion equation and the moving-mesh interface. A pre-defined etch form [364] was introduced into the geometry to allow the mesh to move along the bottom surface of the insulator. This was dimensioned with a half-width of $1.005w$ and an initial depth of $0.01w$, and was thus small compared to the rest of the geometry.

7.4 Results and discussion

7.4.1 Comparison between simulation and experiment

The solutions to the problem of shape evolution during TMEMM, using either the BEM or FEM, were generally found to be in excellent agreement with one another. Differences between the numerical results could be expected due to variations in the implementation of both methods in terms of initial geometry, time stepping, mesh size and re-meshing. However, such variations were negligible compared to the uncertainty of the experimental results, and were thus ignored. In both cases, simulations were conducted using a mask height of 1.95 µm and mask width of 11.5 µm, corresponding to a mask-opening aspect-ratio of 0.34. Afterwards, the computed shape profiles were integrated to yield the cross-sectional area, and multiplied with the sum of the centre-line length of each ring to obtain the removed volume and thus the cumulative passed charge. A valence of three for aluminium dissolution and 100 % current efficiency were assumed in the process.

Results for the channel width and depth were obtained from optical-profilometer data and from cross-sections for each ring. Both width and depth were found to increase non-linearly with the cumulative passed charge (Figure 7.3) and with time.

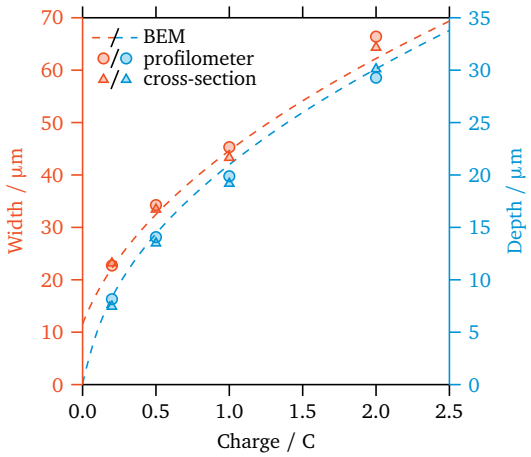

Figure 7.3: Dependence of the channel width and depth on the cumulative passed charge, corresponding to the amount of removed material in a quiescent solution. The dashed lines represent the results of BEM simulations.

The width and depth values of rings machined in a quiescent solution were found in good agreement with the simulation results. Under forced convection, the channel dimensions increased with the distance from the axis of rotation, the variation being larger at higher rotation rates. This is explained by the dependence of the angular velocity of the RDE on radial position. However, when averaging the channel depth and width of samples machined at 100, 400 and 900 rpm over all rings, similar values to the ones in a quiescent solution were obtained.

SEM and microscope images of experimental cross-sections revealed a semi-elliptic channel profile, which is characteristic for diffusion-limited dissolution through a mask [16, 182]. One such example is shown in Figure 7.4. From these images experimental shape profiles were obtained via image processing and then overlaid with simulated profiles. The best agreement between the two was determined according to the overall profile shape. Comparing cross-sections with respect to the position of the mask opening was not possible, because the fragile photoresist film was stripped before encasing and cross-sectioning samples. Overall, the agreement with simulated profiles was good up to 100 rpm (Figure 7.5), the only difference being the slightly larger width of experimental profiles towards the channel top. As rotation rate was increased to 400 and 900 rpm, the profiles tended to be asymmetric, with the position of the maximum etch depth shifted radially outward. At 900 rpm the profiles were also noticeably deeper and narrower than expected.

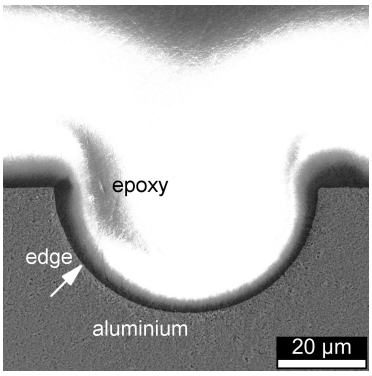

Figure 7.4: SEM image (1000× magnification) of the cross-section of a channel etched at an applied potential of 1.4 V at 100 rpm for a cumulative passed charge of 2.0 C.

Based on experimental cross-sections, the etch factor (N_{EF}) was calculated for each ring separately from the maximum etch depth (d) and the undercut (x_{u}) underneath either side of the mask opening according to the following formula:

$$N_{\mathrm{EF}} = d/x_{\mathrm{u}} \tag{7.7}$$

For a given experiment, no influence of radial position on etch factor was detected even at high rotation rates; hence, the results are reported as average values. This is because the difference in the amount of removed material between the five rings was small compared to the total amount. In a quiescent solution and under the conditions of forced convection up to 400 rpm, the etch factor was found to decrease with increasing channel depth and ranged between 1.4 and 1.1 (Figure 7.6). Up to 400 rpm the experimental results agreed with each other, but deviated from the simulated etch factor, the difference being larger for shallower channels. In contrast, the etch factor stayed roughly constant just below 1.3 at 900 rpm.

The deviations in terms of channel width and etch factor — even in the absence of convection — can be explained on the basis of SEM images of machined channels (Figure 7.7). On either side of each channel, where the channel wall met the mechanically polished surface, a small 0.5 to 2 µm wide region with a surface structure similar to the machined channel surface was frequently observed. On cross-sections, this region was not detectable; thus, only a small amount of material was removed in this place. In contrast, the simulation results predicted a 90° angle at the intersection between the channel wall and the bottom surface of the mask. In practice, the channel wall followed a wedge-like shape in the vicinity of the mask, exposing a larger surface area than expected to the electrolyte. From previous work, it is known

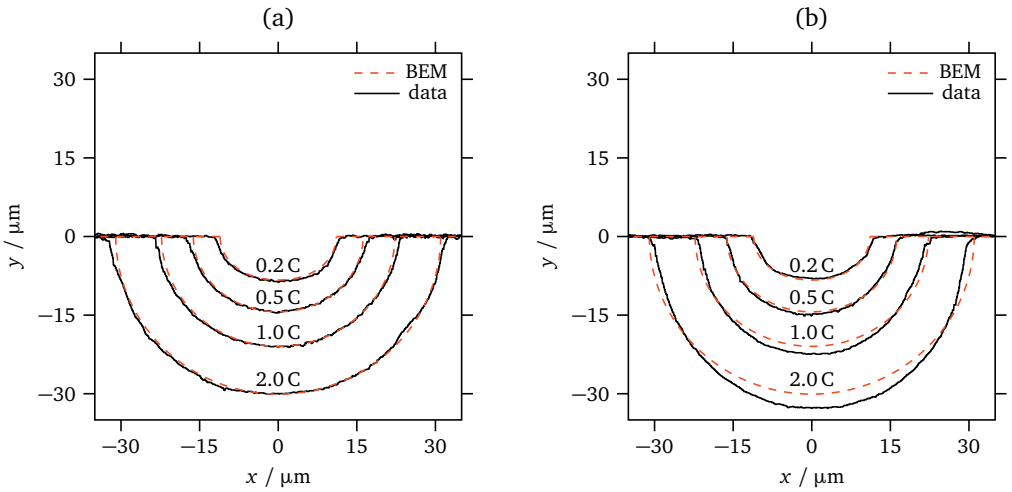

Figure 7.5: Comparison between simulated and experimental shape profiles for different values of the cumulative passed charge of 0.2, 0.5, 1.0 and 2.0 C at (a) 100 rpm and (b) 900 rpm.

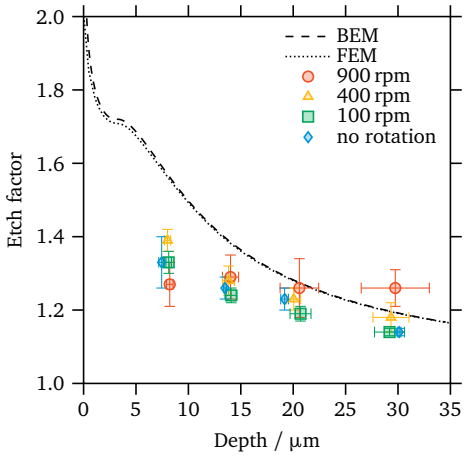

Figure 7.6: Relation between the etch factor and the maximum channel depth. Results are presented for experiments with and without electrode rotation. Also given are the results of BEM and FEM simulations. The error bars designate one standard deviation.

that aluminium oxide continuously forms and dissolves during mass-transfer-limited electrochemical dissolution in phosphoric acid [314] (Chapter 5). In the present work, the disc samples were handled in the presence of air; hence, a thin air-formed alumina film presumably covered the surface underneath the photoresist mask in all cases. We hypothesise that this air-formed film may have been dissolved preferentially, leading to more undercutting of the mask. Alternatively, adhesion problems

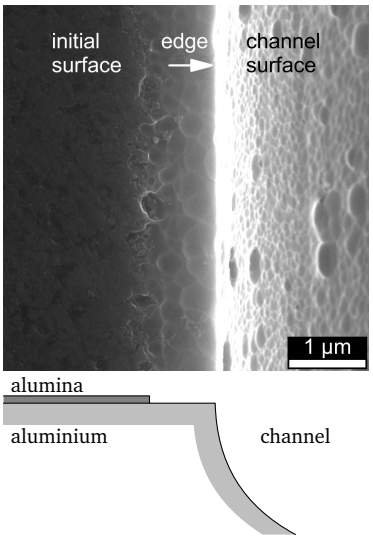

Figure 7.7: SEM image (20000× magnification) of the border region between the mechanically polished initial surface and the machined channel surface. The arrow marks the position where the vertical channel side wall meets the horizontal plateau. Also shown is a schematic cross-section, indicating partial removal of the air-formed oxide film in the vicinity of the channel edge.

between the photoresist and the aluminium substrate may have caused a larger part of the surface to be exposed to the electrolyte.

The machined rings were also characterised in terms of their surface roughness. Values for the average surface roughness (R_a) and root mean square roughness (R_q) were determined from line scans taken from optical-profilometer data along the mechanically polished surface and at the bottom of machined microchannels. Both quantities and their standard deviation were computed for the ring with the largest diameter only. For the initial mechanically polished surface, these values were determined as $R_a = (14 \pm 4)\,\mathrm{nm}$ and $R_q = (18 \pm 6)\,\mathrm{nm}$. After shape-evolution experiments, these figures increased slightly to $R_a = (28 \pm 6)\,\mathrm{nm}$ and $R_q = (40 \pm 9)\,\mathrm{nm}$, where aluminium had been electrochemically dissolved. Similar results have been obtained after electropolishing [101] and electrochemical micromachining [276] of aluminium in viscous electrolytes. Surface roughness values determined after TMEMM of aluminium in a mixture of acetic and perchloric acid [18] are about one order of magnitude higher compared to the present work. Neither rotation rate nor the passed charge had an effect on surface roughness.

7.4.2 Influence of forced convection

On an aluminium RDE, the magnitude of the mass-transfer-limited current depends directly on the square root of rotation rate [44, 314]. Likewise, the form of current transients measured during shape-evolution experiments at an applied potential of 1.4 V depended on the conditions of mass transfer (Figure 7.8). In a quiescent solution, the current quickly attained a peak value and then continuously decreased over time. This behaviour is known from TMEMM of titanium in a methanol/sulphuric-acid electrolyte [16], and arises from the establishment and subsequent levelling of concentration gradients along the metal surface, while the etch depth increases in parallel. Increasing rotation rate to 100 and 400 rpm lead to similarly shaped current transients. At 900 rpm, however, the current quickly reached a plateau and stayed constant. This indicated a change in the relative importance of diffusive and convective mass transfer during the dissolution process.

Likewise, the etch rate — here defined as the ratio of maximum etch depth to etch time — was found to depend on the conditions of mass transfer (Figure 7.9). In the absence of convection, the etch rate ranged between 0.6 and 2.4 $\mu m\,min^{-1}$, which is typical for TMEMM of aluminium in electrolytes consisting of viscous mineral acids [18, 276]. At 900 rpm etch rates ranging between 1.9 and 5.3 $\mu m\,min^{-1}$ were calculated. In all cases, the etch rate decreased sharply with the cumulative passed charge. This is explained by the aforementioned decrease in the total current over time, a decline in the average current density as the channel surface grows, and

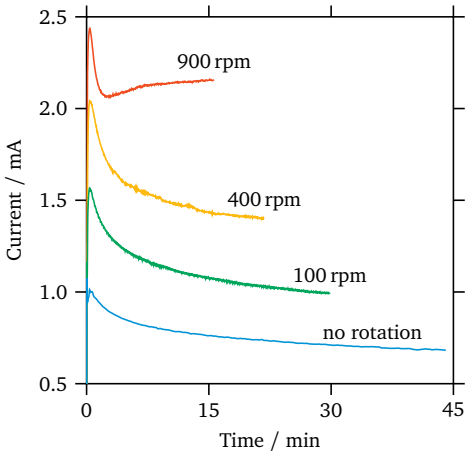

Figure 7.8: Current transients measured at an applied potential of 1.4 V and different rotation rates for a cumulative passed charge of 2.0 C.

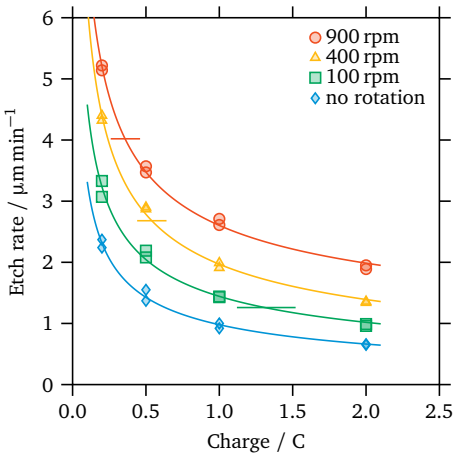

Figure 7.9: Variation of the etch rate for different amounts of the cumulative passed charge. The solid lines were added for clarity and represent a linear regression fit assuming the etch rate is proportional to the inverse square root of the cumulative passed charge. The horizontal lines indicate the etch rate for a mask opening of infinite size at the respective rotation rate.

an increase in the amount of lateral to vertical material removal as the channels deepen. The shift from purely diffusive to mixed convective-diffusive mass transfer was determined from a double-logarithmic plot of etch depth and etch rate against time (Figure 7.10), respectively. For a purely diffusion-limited etch process, the maximum etch depth is proportional to the square root of time [182, 183], corresponding to a slope of 0.5 in a log-log plot. Similarly, the etch rate depends on the inverse square root of time, in this case yielding a slope of −0.5. In the absence of convection, the slopes computed via linear regression agreed favourably with the theoretical values. As rotation rate increased, the slopes deviated more and more from these values, indicating the growing influence of convective mass transfer.

Note that lower etch rates must be expected when etching more tightly spaced patterns consisting of larger features. It is generally understood that the etch rate depends strongly on the geometry, size and spacing of the mask openings within a pattern [372]. For comparison with the above results, we have estimated the etch rate for a mask opening of infinite size from limiting-current data measured on an aluminium RDE [314] via Faraday's law at 100 % current efficiency ($M = 26.98\,\mathrm{g/mol}$, $\rho = 2.70\,\mathrm{g/cm^3}$, $z_\mathrm{e} = 3$). The results at 100, 400 and 900 rpm for this theoretical etch rate correspond to the horizontal lines in Figure 7.9. It was found that etching through a mask opening of finite size proceeded faster for shallow channels. In contrast, deep channels etched at a lower rate compared to the theoretical value. This observation coincides with theoretical results and interpretations thereof

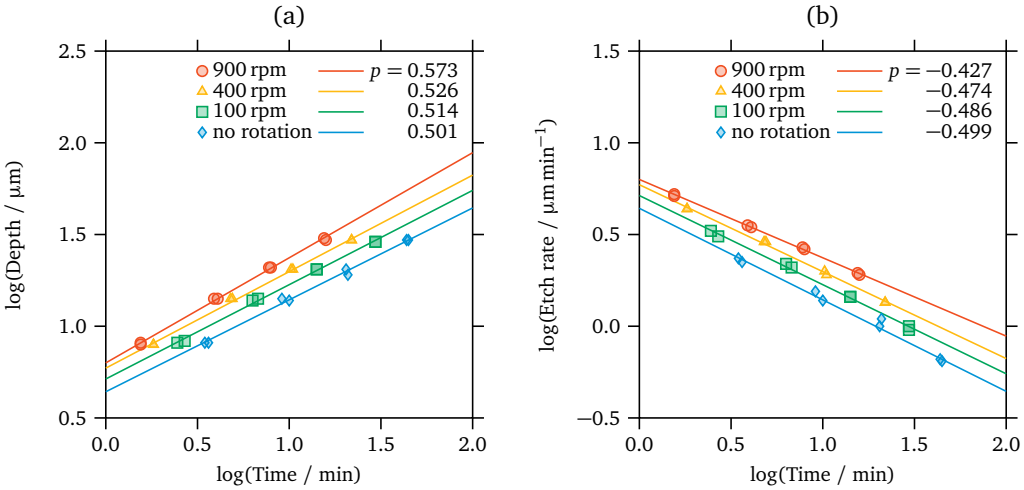

Figure 7.10: Double-logarithmic plot of (a) maximum etch depth and (b) etch rate against etch time. Also given is the slope (p) of a linear regression fit under the respective hydrodynamic conditions.

obtained by Kuiken [178] for purely diffusion-limited, chemical etching. During the early stages of etching, a decrease in the mask-opening size leads to steeper concentration gradients in the vicinity of the opening. At later times, however, smaller mask-openings also limit the flux of material more severely.

As mentioned before, increasing rotation rate also lead to changes in the overall shape profile of machined channels. In addition to the changes in depth and width, a shift in the position of the left and right channel wall was observed. In a quiescent solution and when etching at 100 rpm, material removal occurred at equal rates to the left and right side of the mask opening. The channel profile was thus centred on the middle of the mask opening. In contrast, microscope images of channels etched at 400 and 900 rpm showed uneven undercutting between both sides of the mask opening (Figure 7.11). In general, more undercutting occurred underneath the part of the mask that lay further away from the axis of rotation. The difference in undercutting increased with radial position at constant rotation rate, and with rotation rate at constant radial position. These observations overlap with results of shape-evolution simulations [185, 188, 191, 193] for flow past a partially covered trench, namely that under forced convection and in the presence of a thin mask more undercutting occurs along the downstream edge of the trench. Additionally, the difference in undercutting depends on the velocity in the vicinity of the mask opening. In the present case this corresponds to radial flow past a recessed ring.

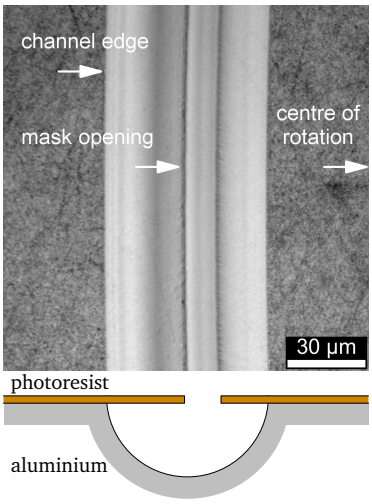

Figure 7.11: Microscope image (50× magnification) of a channel machined at an applied potential of 1.4 V at 900 rpm for a cumulative passed charge of 2.0 C. The centre of rotation lies to the right outside of this image. The schematic cross-section highlights the displacement of the channel profile relative to the mask opening.

Typically, the relative importance of convective and diffusive mass transfer is expressed in the form of the Péclet number ($N_{\mathrm{Pe}} = ul/D$), using a characteristic velocity (u) and length scale (l), and the diffusion coefficient (D) (Section 3.3.2). In studies on cavity etching through an insulating mask in the presence of convection [185, 188, 192, 193], the mask-opening half-width is used as the characteristic length; hence, in this work l was taken to equal 5.75 µm. Data on the diffusion coefficient of Al^{3+} ions in phosphoric acid is unavailable to our knowledge. Instead, the reasoning of Datta et al. [202] was adopted, and it was assumed that the diffusion coefficient of metal ions in concentrated electrolytes depends mainly on viscosity and electrolyte temperature, and not on the type of metal ion. Thus, a least-squares fit of diffusion coefficient and viscosity data was used to estimate D, which had been determined for Cu^{2+} in phosphoric acid at 25 °C [373]:

$$D = 5.7 \times 10^{-6}\, \nu^{-1.06}\ (\mathrm{cm^2\,s^{-1}}) \tag{7.8}$$

Using density ($\rho = 1.685\,\mathrm{g\,cm^{-3}}$) [354] and viscosity data ($\mu = 0.393\,\mathrm{g\,cm^{-1}\,s^{-1}}$, $\nu = 0.233\,\mathrm{cm^2\,s^{-1}}$) [351] of 85 % phosphoric acid yielded $D = 2.0 \times 10^{-7}\,\mathrm{cm^2\,s^{-1}}$ at 25 °C. This value was subsequently corrected for viscosity and temperature changes via the Stokes-Einstein equation, resulting in $D = 9.5 \times 10^{-7}\,\mathrm{cm^2\,s^{-1}}$ at 75 °C. Finally, the characteristic velocity in the vicinity of the mask opening was estimated from

the velocity gradient and the characteristic length via $u \sim \nabla u l$ [178]. Due to axial symmetry and the proximity to the surface, only the radial velocity component (u_r) close to the surface was of interest, which for a RDE is given by [133]:

$$u_r = 0.51 r \omega^{3/2} \nu^{-1/2} y \tag{7.9}$$

Close to the surface ($y \sim 0$), the axial and tangential derivatives of Equation 7.9 equal zero. Thus, only the derivative with respect to the longitudinal coordinate (y) was considered, resulting in the following equation for the characteristic velocity:

$$u \sim (\partial u_r / \partial y) l = 0.51 r \omega^{3/2} \nu^{-1/2} l \tag{7.10}$$

Effectively, the velocity of the undisturbed fluid a small distance away from the mask opening is used as the characteristic velocity [189–191]. By inserting the radius of each of the five rings into Equation 7.10, it was possible to estimate the characteristic velocity at each rotation rate. In this manner, the Péclet number could be evaluated for shape-evolution experiments at 100, 400 and 900 rpm.

In order to identify a range of Péclet numbers, for which mass transfer shifts from diffusion to mixed convection-diffusion control, the radial displacement of each ring was plotted over the Péclet number (Figure 7.12). The data was limited to samples machined for a cumulative passed charge of 2.0 C, where the displacement was

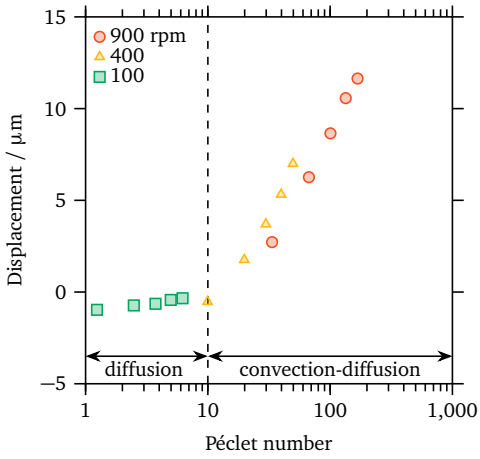

Figure 7.12: Variation of the radial displacement of rings machined into the surface of an aluminium RDE, depending on the Péclet number in the vicinity of the respective mask-opening. The Péclet number range is indicated, for which the shape-evolution model based on diffusive mass transfer is in good agreement with experimental results.

most noticeable. For $N_{Pe} \leq 10$, no preferential undercutting on either side was observed, and the channels remained centred relative to the mask opening. This coincided with the observation that experimental results obtained at 100 rpm still agreed well with the model based on diffusive mass transfer. For $N_{Pe} \geq 20$, however, the radial displacement became noticeable and increased approximately linearly with the logarithm of the Péclet number. We conjecture that these results are transferable to other flow conditions, for example to TMEMM of aluminium in a flow channel or an impinging jet cell. This would enable the estimation of an electrolyte flow rate and velocity, for which the displacement of machined channels in the direction of flow is non-existent or negligible. The above results show that a RDE itself is not suitable for TMEMM at higher Péclet numbers, due to the radial dependence of the etch rate and the channel displacement. However, note that it enables one to test for the influence of flow conditions over a wide range of Péclet numbers. Only a few experiments are necessary to that end.

7.4.3 Influence of potential

Mass-transfer-limited anodic dissolution of aluminium in concentrated phosphoric acid at elevated temperatures is characterised by a limiting-current plateau, which starts at about −0.2 to 0.3 V vs. Ag|AgCl and extends over several volts [44, 314]. Thus, a wide potential range is in principle accessible for TMEMM of aluminium. In practice, current transients measured during TMEMM differ depending on the

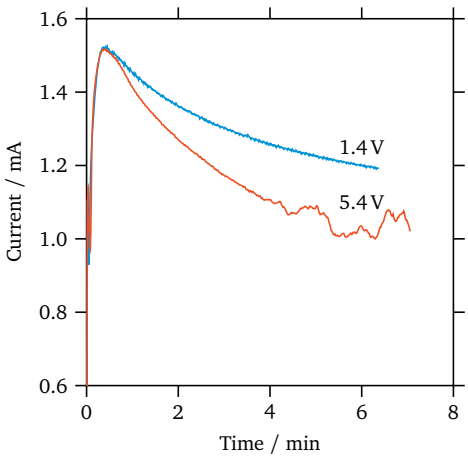

Figure 7.13: Current transients measured at a rotation rate of 100 rpm at two different applied potentials along the limiting-current plateau for a cumulative passed charge of 0.5 C.

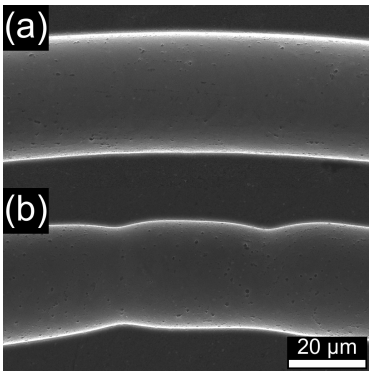

Figure 7.14: SEM images (1000× magnification) depicting channels machined at 100 rpm and an applied potential of either (a) 1.4 V or (b) 5.4 V for a cumulative passed charge of 0.5 C.

applied potential along the limiting-current plateau (Figure 7.13). At 1.4 V the current decreased steadily over time, whereas it fluctuated after a few minutes at an applied potential of 5.4 V. A larger decrease from the peak current value preceded these fluctuations. Both observations indicated the gradual formation of gas bubbles along the metal surface, which subsequently detached at periodic intervals. These bubbles were not observable themselves due to their small size, but their presence was evident from SEM images of machined channels (Figure 7.14). At 5.4 V the channel shape was non-uniform, and the channel width and depth varied considerably. This was due to partial or complete blockage of the openings in the photoresist film with gaseous reaction products, leading to locally lower rates of material removal. The most likely cause was oxygen evolution. This is backed up by earlier reports, namely the observation that gas evolves at sufficiently high potentials [374] and that the apparent valence of aluminium dissolution in phosphoric acid is slightly lower than three [44], corresponding to a current efficiency of less than 100 % (Appendix C). Note that a small percentage of the current going towards oxygen evolution is sufficient to explain the observed effects because of the large molar volume of gaseous oxygen.

7.4.4 Microfluidic example structures

To investigate the feasibility of TMEMM of aluminium for the fabrication of microfluidic devices, several test patterns were machined into the surface of disc samples. Based on previous experience, electrochemical dissolution was conducted at an applied potential of 1.4 V in a quiescent solution. The amount of removed material

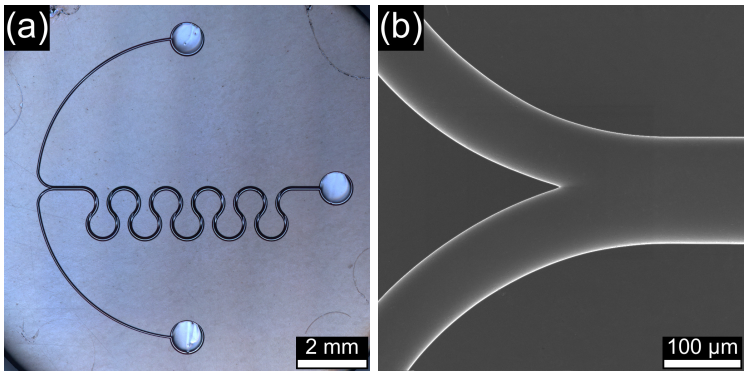

Figure 7.15: (a) Micromixer with two inlet channels leading into a meandering mixing channel. The micromixer was machined into the surface of a 15 mm wide aluminium disc at an applied potential of 1.4 V at 75 °C in a quiescent solution for a cumulative passed charge of 10 C. (b) SEM image (200× magnification) showing where the inlet channels merge into the mixing channel. The two inlets are 90 µm wide and 45 µm deep, while the mixing channel is 140 µm wide and 50 µm deep.

was controlled by measuring the cumulative passed charge. One such pattern represents a micromixer structure based on a meandering-channel design [375] (Figure 7.15). The structure consists of two inlet chambers, which lead into respective inlet channels. Both inlet channels merge in a mixing section followed by a single meandering channel and an outlet chamber. The mask opening was 50 µm wide for each inlet channel and 100 µm wide for the mixing channel. The inlet and outlet chambers were designed with a diameter of 1 mm. After TMEMM the width of the inlet and the mixing channel was 95 and 145 µm, respectively. Optical-profilometer data showed that the channels reached similar depths of 30 and 35 µm. SEM images revealed a smooth and even surface finish and well-defined channel walls. The inlet and outlet chamber showed large variations in etch depth, however. Along the edge of each chamber ran a trench, which was about 20 µm deeper relative to the chamber centre. A similar variation in etch depth occurred when machining arrays of parallel microchannels, which may be used within a microreactor or a micro heat exchanger. In this case, the outermost channel of the pattern showed the highest etch rate, leading to a larger maximum etch depth compared to the rest of the pattern.

The problem is known from experimental and theoretical studies [17, 19, 20] and arises due to differences in the shape of the diffusion-layer boundary [372]. Over large mask-openings or dense patterns of small mask-openings, the diffusion-layer boundary is parallel to the surface, and mass transfer occurs in one dimension only. In contrast, the diffusion layer attains a curved shape at the edge of mask openings

or patterns, leading to enhanced mass transfer in this region. Several solutions to the problem have been proposed, some of which are applicable to TMEMM under mass-transfer-limited conditions. For example, concentration gradients along the edge of a pattern of mask openings can be levelled by introducing sacrificial etch bands — so-called current-robber areas — which surround the pattern [19]. Also, large mask-openings can be divided into a number of smaller mask-openings, a large chamber thus being formed by the merging of many smaller cavities [17, 20]. In theory, reducing the thickness of the diffusion layer via forced convection should also reduce the dependence of the etch rate on size effects [372]. In future work these options will be explored for TMEMM of aluminium in order to yield more uniform etch rates over the whole of a pattern of mask openings.

7.5 Conclusions

In this work, aluminium discs were electrochemically dissolved through photoresist masks in 85 % phosphoric acid at 75 °C, using a custom-made RDE setup under controlled hydrodynamic conditions. The influence of applied potential, cumulative passed charge and hydrodynamic conditions on the dimensions, shape profile and uniformity of the resulting microchannels was studied, and compared with a shape-evolution model based on diffusive mass transfer [16]. The channels and their cross-sections were characterised via SEM, light microscopy and optical profilometry. The experimental and model results agreed well with each other in terms of the ratio of vertical to lateral material removal, the resulting channel dimensions and the overall shape profile up to a rotation rate of 100 rpm. At higher rotation rates, deviations between model and experiment indicated a shift from purely diffusive to mixed convective-diffusive mass transfer. This shift was characterised by estimating the Péclet number in the vicinity of each mask opening, and a range of Péclet numbers were identified, for which the shape-evolution process was described well by the model. In addition, preliminary results on the machining of complex microfluidic structures demonstrated that TMEMM of aluminium is a feasible alternative to other micromachining techniques.

8 Fabrication and functionalisation of an aluminium gas-phase microreactor

8.1 Introduction

Microreactors are of great interest for the operation of heterogeneously catalysed gas-phase reactions, and accordingly much research has focused on this area [1, 4]. They benefit from their small internal dimensions in several ways: heat- and mass-transfer limitations are negligible; safe operation within the explosive regime is possible; and accurate control of the residence time distribution is feasible. For the same reason, microreactors are characterised by small volumes and low throughputs. In order to circumvent this problem, their capacity is increased via the numbering-up approach. For this purpose, hundreds of microchannels are positioned in parallel on a single plate and tens of plates are piled up to form a plate stack [2] (Figure 8.1). However, this introduces a new problem: optimum reactor performance now depends on a uniform feed distribution among all channels and plates. Therefore, measures to ensure gas-flow uniformity have been studied extensively, including the geometry of inlets and flow distributors [376].

An often overlooked factor is the influence of manufacturing tolerances on gas-flow uniformity. On the level of an individual plate, variations in channel diameter lead to a broadening of the residence time distribution [377]. This in turn affects conversion and selectivity. For example, Delsman et al. [378] estimated that a relative standard deviation of 10 % in terms of the channel diameter results in up to 5 % lower conversion, assuming first order kinetics. In a study on the performance of fuel-cell stacks, Shimpalee et al. [15] found that changes in channel depth increased the pressure drop over a serpentine gas-flow-field channel. The same work highlights the importance of uniform channel-wall thickness for heat-transfer management and hot-spot prevention. In the same manner, the gas-flow uniformity from plate to plate needs to be considered [379]. The investigation of manufacturing tolerances is thus a priority to ensure optimum reactor performance.

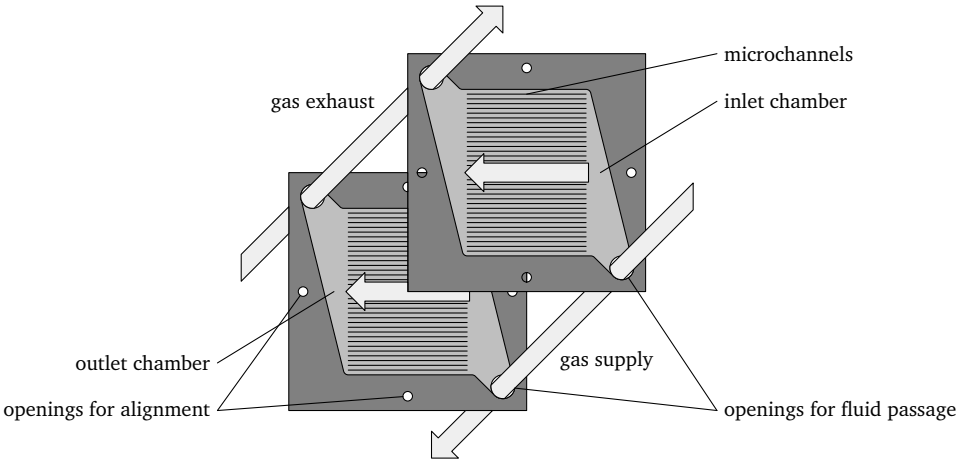

Figure 8.1: Design and flow configuration for a plate-type microreactor (adapted from Ehrfeld [2]).

In through-mask electrochemical micromachining (TMEMM), non-uniform dimensions stem from variations in the current distribution on the workpiece and pattern scale (Section 3.2). Several approaches exist to ensure uniform dimensions, which are applicable to different experimental conditions. In case of a primary current distribution, the potential field between anode and cathode needs to be optimised. This is possible by modifying the overall cell geometry [14, 380] or by introducing an auxiliary electrode — also termed current thief [24, 244, 381]. In the presence of a tertiary current distribution on the other hand, uniform concentration gradients are sought after. The latter case applies to TMEMM of aluminium in phosphoric acid. Unfortunately, few studies focus on this topic. Previously, the incorporation of dummy artwork into the mask has been suggested to level the current distribution in the vicinity of wide mask-openings [17, 20, 237] (Figure 8.2). In the case of a non-uniform current distribution along the edge of a pattern, the use of sacrificial etch bands has been proposed to even concentration gradients in this region [291, 382]. However, studies towards the success of such measures are rare.

Another source of non-uniform dimensions is gas pitting, especially during TMEMM of aluminium in phosphoric acid. At high applied potentials, gas evolution occurs in parallel with electropolishing (EP) [46, 374]. Gas evolves on energetically favoured sites, such as initially present surface defects, and creates a continuous stream of bubbles [209]. This enhances local mass transfer and hence creates pits, depressions and tails. The presence of imperfections and impurities in the initial surface may also lead to short-lived, localised gas evolution [108, 111]. In this case pits exhibit a central mound, because evolved gas adheres to the surface. During both types of

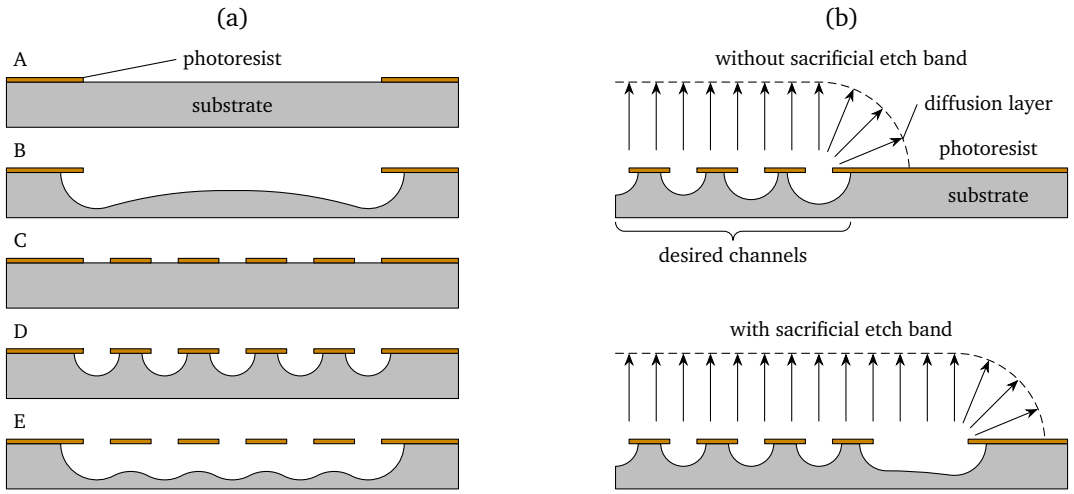

Figure 8.2: Non-uniformities in the current distribution during TMEMM can be minimised by introducing (a) a dummy mask or (b) a sacrificial etch band. In the first case, a wide mask-opening (A, B) is divided into several narrow openings (C–E), a large chamber thus being formed by the merger of a few smaller cavities. In the latter case, the presence of a sacrificial etch band along the pattern edge levels concentration gradients in that region. Thereby, the desired pattern is formed accurately.

gas pitting, the pit surface appears polished, as the dissolution process is still limited by mass transfer. Note that etching and concurrent hydrogen evolution also occur upon immersion of the anode — corresponding to open-circuit conditions — unless an anodic current or potential is applied. Several measures can be taken to minimise gas pitting, for example live immersion of the anode, etch-cleaning — either before [111] or after immersion [383] — and the addition of surfactants as wetting agents [109]. The influence of surfactants on the mechanism of EP, however, is not well understood, and studies on aluminium EP appear to be non-existent.

Apart from the microchannel dimensions, the uniformity of the catalytic wall coating is of interest for optimum reactor performance [378]. Gas-phase microreactors constructed from metals rarely possess intrinsic activity towards any given reaction; instead, activity needs to be imparted via catalyst deposition along the reactor surface. The most common deposition method is wash-coating followed by wet impregnation [384, 385]. Therein, the microreactor is filled with a suspension of finely dispersed metal-oxide particles, for example made from alumina, ceria, titania or zirconia [25, 302, 386]. After drying and calcination, the porous support is impregnated with a metal salt via immersion before being dried and calcinated once more. The chief advantage of this method lies in its general applicability to different reactor geometries, independent of the reactor material [387]. However,

forming a uniform wall coating is challenging, both across the channel profile and along the channel length [303, 384, 388, 389]. In addition, the process takes several hours until completion and is thus time-consuming.

An alternative deposition method combines electrochemical techniques instead, specifically anodising (Section 2.2.1) and alternating current (AC) electrodeposition (Section 2.2.4). Anodising is widely used in conjunction with aluminium microreactors to produce porous-alumina coatings along the channel walls, which act as catalyst-support layers [25–27, 29, 31, 42]. Advantageously, the anodising process can be monitored precisely to form uniform coatings of controlled thickness and porosity. Afterwards, noble metals may be deposited within the pores of these films via AC electrodeposition. This process has long been in use to colour aluminium articles [45]. More recently, it has been adapted to the synthesis of metal nanomaterials according to the template method [73]. By comparison, the application of AC electrodeposition towards catalyst deposition is scarcely reported. Noble metals deposited for this purpose thus far include copper [130], palladium [43, 130] and platinum [131]. The deposition behaviour is likely specific for each metal [130]. For platinum at least, it has been shown that uniform catalytic coatings can be formed in a matter of minutes under optimum conditions [131].

The aim of this study is therefore threefold. Firstly, the effect of surfactants on aluminium EP was investigated. To this end, mass-transfer-limited aluminium dissolution was studied with a rotating disc electrode (RDE). The influence of surfactant additions on surface morphology was studied via scanning electron microscopy (SEM) and optical profilometry. Secondly, the impact of mass-transfer conditions and mask design on the current distribution during TMEMM of aluminium was examined. For this purpose, a typical design for a gas-phase microreactor was fabricated from aluminium plates and afterwards analysed in terms of dimensional uniformity. Lastly, the microstructures thus machined were functionalised with a catalytic wall coating made from Au/Al_2O_3. This system is catalytically active for a number of gas-phase reactions, including low-temperature CO oxidation [390], which is why gold was chosen for AC electrodeposition.

8.2 Experimentation

All samples were made from 2 mm thick, commercially pure aluminium sheet material (Al $\geq$ 99.00 %, Si+Fe $<$ 1.00 %, Cu $<$ 0.05 %, Mn $<$ 0.05 %, Zn $<$ 0.10 %, Ti $<$ 0.05 %, Wakefield Metals). Two different sample types were machined. For

the RDE setup, 5.2 mm wide discs were punched from the sheet and embedded in a 15 mm broad polytetrafluoroethylene holder. As described previously (Section 5.2), the RDE was then mechanically polished with successively finer grades of SiC paper down to P1500, ultrasonicated for 5 min in a 1/1 (v/v) mixture of isopropyl alcohol (IPA) and de-ionised (DI) water, rinsed first with copious amounts of DI water and then with IPA, and finally left to dry in air. For the plate-electrode setup on the other hand, square plates with 50 mm side length were machined. These were abraded with P1500 SiC paper and subsequently etch-cleaned for 10 min in 5 % NaOH solution ($\geq$ 99 %, VWR) at room temperature. This was followed by cleaning in acetone, methanol and IPA for 5 min each in an ultrasonic bath, and drying in a nitrogen stream. Afterwards, the plate samples were coated with a positive-tone photoresist film (AZ1518, Microchem) about 2 µm in thickness. Depending on the experiment at hand, the resist film was patterned with different mask designs. The details for the subsequent exposure, development, and baking steps have been described already (Section 7.2).

Experiments were conducted with two different electrochemical cell setups. Firstly, a RDE was used in conjunction with a 100 mL glass cell, which was placed in a thermostat-controlled water bath. Secondly, a plate electrode held in a vertical position was employed in a 1 L jacketed glass cell. Therein, agitation was provided by a magnetic stirrer. In each case, the electrolyte temperature was controlled with a GD120 thermostat and an LTC1 circulation bath (Grant Instruments). Both electrochemical cells were operated with a Ag|AgCl reference electrode ($c_{\mathrm{KCl}} = 4.77\,\mathrm{mol\,kg}$, $E_{\mathrm{Ag|AgCl}}(75\,^{\circ}\mathrm{C}) = 0.153\,\mathrm{V}$ vs. SHE) connected to a 2 mm wide Luggin capillary and a counter electrode made from Pt foil. These cells are described in Section 4.1.

The impact of surfactant additions on aluminium EP was studied by recording linear potential sweeps under controlled hydrodynamic conditions with the RDE. Prior to these measurements, the RDE was conditioned for 400 s at 1.4 V and 75 °C. At the start of the conditioning step, the RDE was rotated at 2500 rpm for 50 s to remove adherent gas bubbles. Subsequently, the rotation rate was lowered to 100 rpm. This was followed by electrochemical impedance spectroscopy to determine the ohmic drop between the RDE and the Luggin capillary (1.4 V, 5 mV rms^{-1}, 500 kHz to 5 Hz). Afterwards, linear potential sweeps were recorded by sweeping the potential from 1.4 to -0.6 V at 5 mV s^{-1}. Three different surfactants were chosen for this investigation: sodium dodecyl sulphate (SDS) ($\geq$ 98.5 %, Sigma-Aldrich), cetyltrimethylammonium bromide (CTAB) ($\geq$ 99 %, BDH), and Triton X-100 (laboratory grade, Sigma-Aldrich). Each belongs to the group of anionic, cationic or non-ionic surfactants, respectively. Electrolyte solutions were all made from concentrated phosphoric acid (85 % H_3PO_4, ACS grade, Thermo Fisher Scientific), to which each surfactant

was added at different concentrations (0.001, 0.01, 0.1 and 1 mM). Surfactant stock solutions had to be prepared with DI water (18.2 MΩ cm, Milli-Q, Merck) due to their low solubility in concentrated phosphoric acid. Thus, the final acid content was slightly lowered to 84.5 % in the surfactant-containing solutions. By conducting control experiments in 85 % and 84.5 % H_3PO_4, it was found that this decrease in acid content was negligible. For characterisation and imaging purposes, aluminium discs were also electrochemically dissolved at 1.4 V, 100 rpm and 75 °C for a cumulative passed charge of 25 C. Potential-control was provided by a Reference 3000 potentiostat (Gamry Instruments).

For the study of porous-oxide formation and subsequent AC gold electrodeposition, the RDE was first electrochemically polished for 10 min in 85 % H_3PO_4 (1.4 V, 2500 rpm, 75 °C), thus removing a thin surface layer about 65–70 µm in thickness. Afterwards, alumina films of varying thickness were formed by anodising in 0.5 M H_2SO_4 (analytical grade, Thermo Fisher Scientific) at 10 °C and at different anodising times and potentials. During the anodising step, the solution was agitated vigorously via electrode rotation. Anodising was conducted with a two-electrode cell setup and a high-voltage power supply (SF-9585, Pasco Scientific). The film-forming current was monitored by logging the potential drop over a 1 kΩ (±1 %) resistor in series with the cell (USB-5106, Measurement Computing). Finally, AC gold electrodeposition was performed at 25 °C in a solution containing 1 g L^{-1} $HAuCl_4 \cdot 3\,H_2O$ (≥ 99.9 %, Sigma-Aldrich) and 7 g L^{-1} H_2SO_4 [126]. Again, a two-electrode cell setup was utilised, this time driven by an AC power supply (3616.00, Frederiksen). Gold particles and deposits were thus formed by applying different AC potentials for various times at a fixed AC frequency of 50 Hz.

Large-scale TMEMM experiments were performed with the square plate samples in an electrolyte solution made from 84.5 % H_3PO_4 + 1 mM Triton X-100. These experiments were conducted at an applied potential of 1.4 V at 75 °C, with and without agitation via stirring. The plate samples were immersed live, that is with a potential already applied to the anode. During an experiment, the current was recorded with a Reference 3000 potentiostat. The amount of removed material was controlled simultaneously by monitoring the cumulative passed charge.

Three different mask designs were used (Figure 8.3), which are referred to as designs A, B and C. Design A — the base case — was modelled on existing layouts for plate-type microreactors and micro heat exchangers [2, 391]. It consisted of a flow manifold in the top and bottom half, which were both connected via 59 parallel microchannels. Within the photoresist mask, these microchannels were initially dimensioned as 200 µm wide line-openings 300 µm apart from one another.

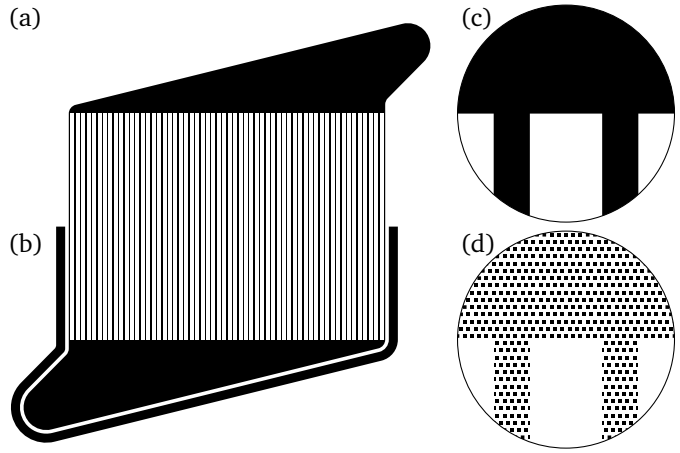

Figure 8.3: Schematic of the three different mask designs: (a) design A/C, (b) design B including a sacrificial etch band, (c) detail of designs A/B, (d) detail of design C. The initially exposed metal surface area for design A, B and C is 7.095, 8.702 and 1.774 cm^2, respectively.

Design B represented a modification of design A, in that it also contained a 1 mm wide sacrificial etch band surrounding the whole structure at a distance of 300 μm. Design C occupied the same area as design A. However, instead of a single, connected mask-opening, the flow manifolds and microchannels were realised as an array of square openings. The size of an individual opening in the photoresist mask was $20 \times 20\,\mu m^2$, with a pitch of 20 μm between each square. Designs A and C were dissolved for a cumulative passed charge of 1200 C. Due to its larger size, design B was dissolved for the same time as Design A for a charge of 1440 C.

For the characterisation of surface morphology, high-resolution images were taken via SEM (JSM 7000F, JEOL) by detecting either secondary or back-scattered electrons. The latter imaging mode was useful in enhancing the contrast between gold and the lighter elements (Al, O, C, S). For cross-section views, samples were encased in epoxy, sectioned, mechanically polished (Beta Grinder-Polisher, Buehler), and sputter-coated with carbon (EMS150T ES, Electron Microscopy Sciences). Energy-dispersive x-ray spectroscopy (EDXS) was utilised for qualitative elemental analysis. This was augmented by light-microscope images taken with an Olympus BX60. In addition, large-scale surface datasets were acquired with an optical profilometer (Profilm 3D, Filmetrics) equipped with 10× and 20× magnification objectives (CF IC EPI Plan, Nikon). This raw data was subsequently processed via data binning (Matlab, version R2013b) and levelling (Gwyddion, version 2.44). Thereafter, several surface parameters were determined, such as average and root mean square (RMS) surface roughness as well as etch depth.

8.3 Results and discussion

8.3.1 Influence of surfactants on aluminium electropolishing

In an attempt to minimize gassing defects during TMEMM of aluminium in phosphoric acid, the addition of surfactants as wetting agents was investigated. Without surfactants, incomplete wetting of the surface was frequently observed, in particular upon immersion of the anode. Gas bubbles thus immobilized at the metal/electrolyte interface tended to produce peaks and flow tails. While these defects generally exhibited a polished surface finish, their presence negatively affected the uniformity of machined microstructures. Apart from improving the overall wetting behaviour, lowering the surface tension of the electrolyte was also expected to minimise the bubble diameter, thus reducing defect size.

In order to assess the impact of surfactant additions during aluminium dissolution, the linear potential sweeps are discussed first. These can be divided into two regions (Figure 8.4). Below approximately −0.1 V active dissolution proceeded in parallel with gas evolution along the anode, leading to a dull surface finish. At higher potentials a mass-transfer-limited current plateau existed, which extended over several volts and was accompanied by EP (Section 5.3.2). Adding to the electrolyte any of the three surfactants at a concentration of 0.001 mM had no discernible effect on the linear sweeps compared to the surfactant-free solution. Increasing the surfactant concentration to 0.01–1 mM, however, caused a decrease in current density in the active region in all cases. Simultaneously, a thin foam layer formed along the anode surface. Both CTAB and Triton X-100 had no effect on the magnitude of the limiting-current plateau. In contrast, the presence of 1 mM SDS was accompanied by a substantial decrease in the limiting current density.

Visual inspection of the RDE afterwards showed no influence on surface finish in the case of CTAB and Triton X-100 at concentrations as high as 1 mM. Conversely, the presence of 1 mM SDS caused a marked decrease in reflectivity. SEM images of the disc surface after electrochemical dissolution demonstrated this difference in surface finish (Figure 8.5). Therein, the surface appeared macro- and microscopically flat with Triton X-100 in solution, which was also representative of the effect of CTAB. Adding SDS, however, induced changes in the surface structure. At 100 rpm smooth peaks and ridges with dimensions on the order of tens of micrometres formed. In contrast, dissolution at 2500 rpm lead to the formation of pits, which were aligned in the shape of log-spirals. The results of the measurement of surface roughness para-

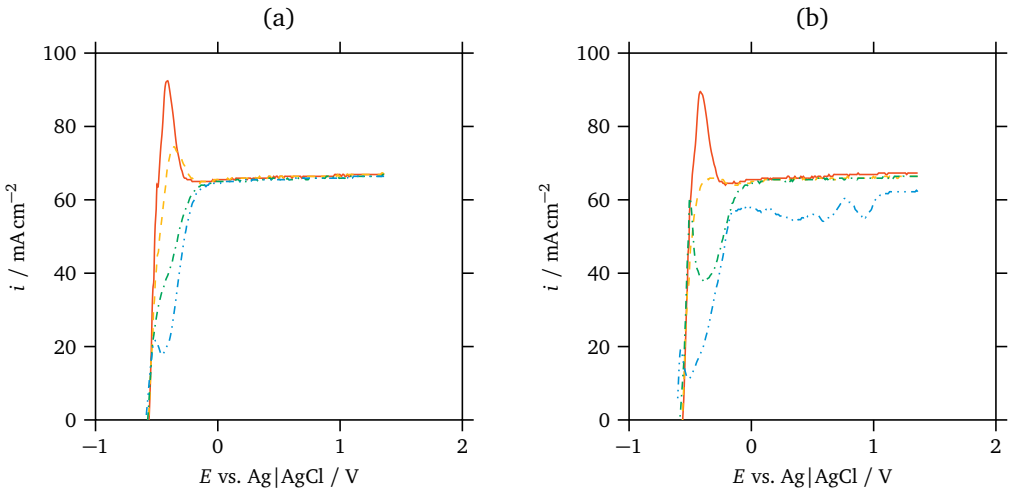

Figure 8.4: Linear potential sweeps from 1.4 V to −0.6 V at a sweep rate of 5 mV s^{-1} measured on a RDE at 75 °C and 100 rpm in 84.5 % H_3PO_4 with additions of either (a) Triton X-100 or (b) SDS at different concentrations: 0.001 mM (——), 0.01 mM (- - -), 0.1 mM (-·-·-), 1 mM (-··-··-). Corrected for the ohmic drop in the electrolyte.

meters also underlined this effect (Table 8.1), and showed that surface roughness had increased drastically in the case of SDS additions.

At present, it is difficult to explain these variations in polarisation behaviour and surface finish, given that concentration-dependant data on surface tension, viscosity and density was not collected. In general, aluminium EP in phosphoric acid is characterised by the presence of a thin, barrier-type oxide film, which continuously forms and dissolves (Chapter 5). Organic compounds — surfactants among them — act as corrosion inhibitors in acidic media for aluminium and its alloys via adsorption onto this oxide film [392]. Anionic surfactants in particular, including SDS, form a hydrophobic adsorption layer along the surface, as is evidenced by an increase in contact angle, which may prevent electrolyte ions from reaching the oxide [393, 394]. In comparison with the present work, copper EP in 8 M H_3PO_4 at 25 °C in the presence of SDS results in an improved surface finish and lower surface roughness [395]. Notably, this process proceeds without oxide formation. Thus, it may be hypothesised that the surface coverage of SDS interferes with the balance between oxide formation and dissolution during aluminium EP, causing local film thickening and non-uniform metal removal. Furthermore, the log-spirals (Figure 8.5(a)), which appear at high rotation rates and reproduce the laminar flow pattern, resemble the effect of organic inhibitors on the corrosion of carbon steel [396]. This indicates that the film structure depends on the hydrodynamic conditions close to the surface.

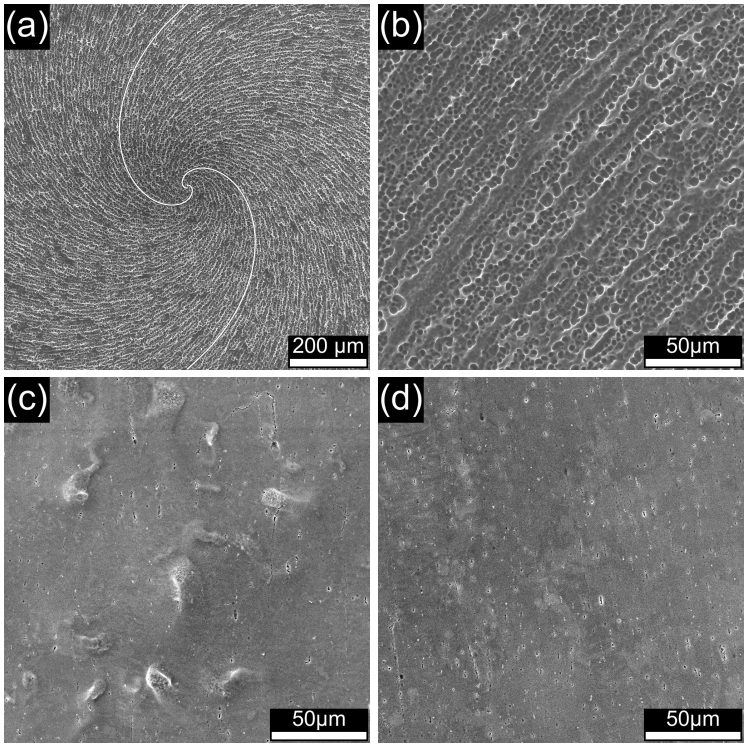

Figure 8.5: SEM images of aluminium electrochemically dissolved in 84.5 % H_3PO_4 at 75 °C and an applied potential of 1.4 V for a cumulative charge of 25 C, in the presence of (a, b, c) 1 mM SDS or (d) 1 mM Triton X-100 at (a, b) 2500 rpm or (c, d) 100 rpm. The solid lines in (a) depict logarithmic spirals, which correspond to streamlines close to the surface of a RDE under laminar flow conditions.

Table 8.1: Surface parameters in terms of average and RMS roughness after dissolution of an aluminium RDE in 84.5 % H_3PO_4 (1.4 V, 75 °C, 25 C), with and without the addition of a surfactant at two rotation rates. The standard deviation is based on scans in five locations per sample.

Surfactant content	Rotation rate (rpm)	Avg. roughness (µm)	RMS roughness (µm)
blank	100	0.017 ± 0.002	0.035 ± 0.008
1 mM SDS		0.32 ± 0.04	0.8 ± 0.1
1 mM CTAB		0.018 ± 0.008	0.03 ± 0.01
1 mM Triton X-100		0.015 ± 0.003	0.033 ± 0.007
blank	2500	0.16 ± 0.01	0.21 ± 0.02
1 mM SDS		1.00 ± 0.06	1.26 ± 0.08
1 mM CTAB		0.15 ± 0.02	0.21 ± 0.03
1 mM Triton X-100		0.16 ± 0.01	0.21 ± 0.01

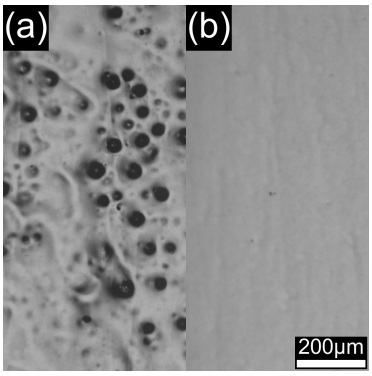

Figure 8.6: Microscope images (5× magnification) showcasing the difference in surface finish (a) in the presence and (b) absence of gas pitting after 10 min dissolution of a 1 mm wide line electrode.

In conclusion, both CTAB and Triton X-100 were identified as suitable wetting agents for TMEMM of aluminium up to a concentration of 1 mM. For subsequent experiments, however, only Triton X-100 was used. This was added at the highest concentration level tested in this study, in order to cause the largest possible decrease in surface tension. The positive effect of the cumulative efforts to minimize gas pitting during TMEMM — etch-cleaning the samples in NaOH solution, enclosing the counter electrode, immersing the samples live and using a wetting agent — is exemplified by the microscope images shown in Figure 8.6. These highlight the importance of avoiding gas pitting in TMEMM of aluminium.

8.3.2 Influence of mass transfer and mask design on TMEMM

In the absence of agitation, a natural-convective flow pattern developed quickly after the start of TMEMM experiments. This was partly because the anode was stored at ambient conditions before immersion. Upon contact with the anode, the solution in the vicinity cooled down, leading to an increase in liquid density and buoyancy motion. As a result, streamline flow from the top to the bottom edge of the anode could be observed. This downward motion continued throughout the duration of an experiment, even after the anode presumably reached thermal equilibrium with the electrolyte. This was due to simultaneous metal dissolution, which resulted in a rise in the concentration of metal ions close to the surface. This again produced a density gradient and a downwards buoyancy force.

The effect of natural convection was studied with mask design A and two different sample orientations, with the channels aligned either horizontally or vertically

(Figure 8.7(a) and (b)). In both cases, the downwards motion of the electrolyte produced large variations in etch depth in flow direction. Both leading and trailing edges were identified along the mask outline. Along a leading edge, the solution moved from the mask onto the exposed metal. Here the largest etch-depth values were observed. Conversely, trailing edges were characterised by solution flow from the metal onto the mask. This coincided with low etch depths. Overall, the etch rate along leading edges was about three to four times higher than in the vicinity of trailing edges. In between, the etch rate decreased continuously.

This effect — the decrease in etch rate in flow direction — is also known as wedging [183, 251, 291]. It stems from non-uniform concentration gradients during streamline flow. Along any line of flow, the concentration of metal ions initially equals the bulk value, which is in this case zero. In the presence of mass-transfer limitations, the etch rate is not governed by the concentration difference between the surface and bulk solution, but by the thickness of the boundary layer over which this difference occurs. Where the streamline first comes into contact with the metal surface, this layer is thinnest; therefore, the etch rate is highest. Subsequently, the boundary layer thickness increases along the flow path and the etch rate drops. Accordingly, wedging occurs not only due to natural convection, but can also be observed under laminar flow conditions in a flow channel cell [247].

In an effort to minimise wedging, electrolyte agitation with a magnetic stirrer was tested in conjunction with mask design A (Figure 8.7(c)). The channel array was oriented vertically for this and all subsequent experiments. Stirring was effective in breaking up the natural-convective flow pattern. However, leading and trailing edges could still be identified as before, their position merely shifted in comparison to the former two experiments. Based on their location, the convective flow field along the surface could be inferred indirectly (Figure 8.7(d)). This flow field ran roughly in an arc from the top right corner towards the bottom left corner. Notwithstanding the presence of electrodes, the hydrodynamics within the electrochemical cell approximately corresponded to the case of an unbaffled stirred tank [397, 398]. Therein, the flow field is dominated by the tangential and axial components, which explains the position of leading and trailing edges in the present case. In principle, it is possible to break up this flow field by adding baffles and impellers or by modifying the stirrer shape and position. This should reduce wedging.

The results of TMEMM experiments in terms of etch uniformity are summarised in Table 8.2, for the aforementioned tests, as well as all subsequent trials. For each plate sample, the channel dimensions were evaluated from three-dimensional surface data along three profiles corresponding to the top, middle and base position

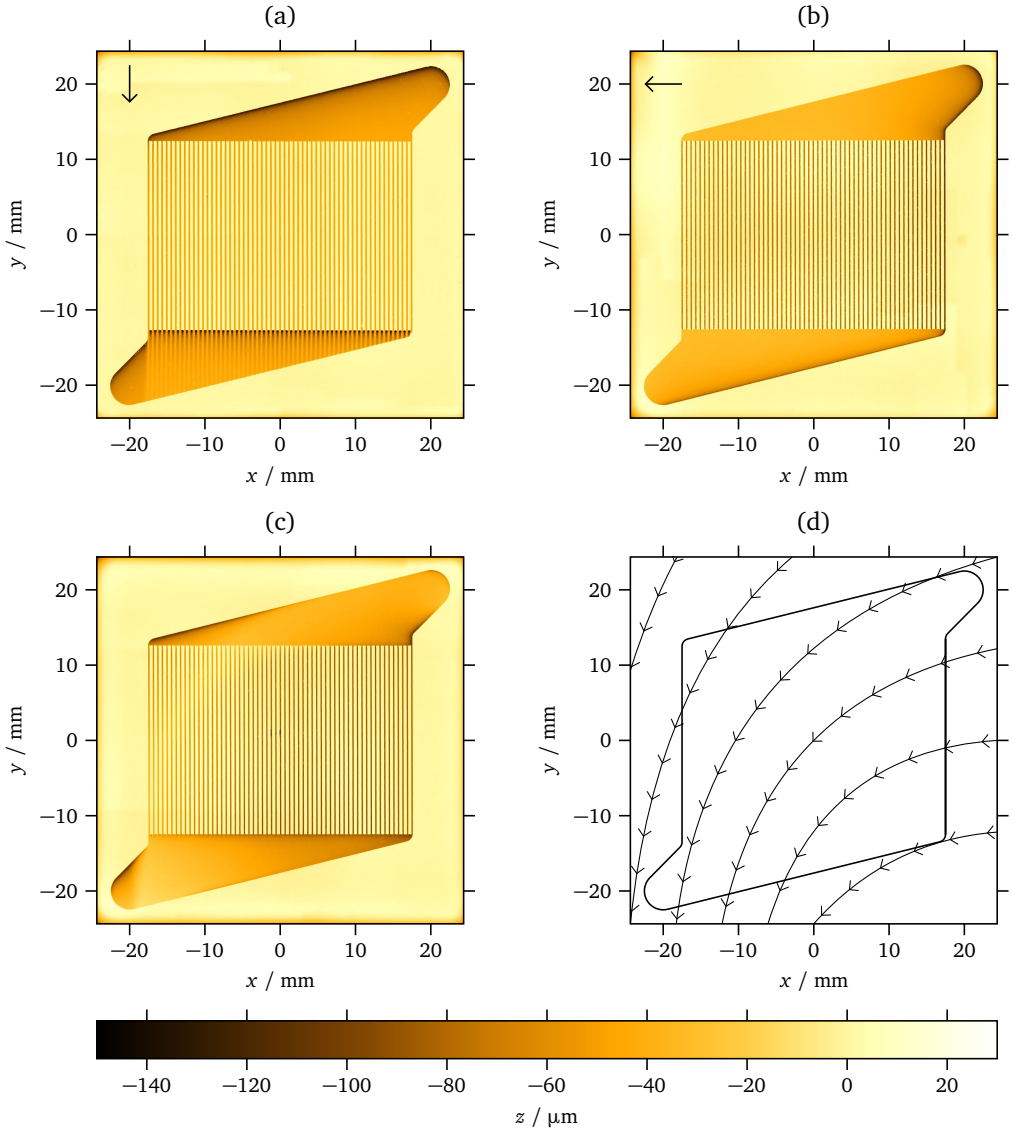

Figure 8.7: (a–c) Surface height maps of mask design A after TMEMM under different mass-transfer conditions: (a) vertical channel orientation without agitation, (b) horizontal channel orientation without agitation, (c) vertical channel orientation with agitation. The arrows (a, b) indicate the direction of the natural-convective flow pattern. (d) Schematic flow field in the presence of agitation.

Table 8.2: Summary of results for all TMEMM experiments performed in this work in terms of etch uniformity, either for the microchannel array or the overall microreactor. Average and standard deviation values are presented.

Mask design	Agitation	Channel depth (μm)	Channel width (μm)	Channel etch factor	Average depth (μm)	Average etch rate (μm min^{-1})
A	–	50 ± 3	261 ± 6	1.63 ± 0.09	51 ± 18	0.55 ± 0.19
A*	–	83 ± 8	270 ± 8	1.9 ± 0.3	50 ± 20	0.7 ± 0.3
B	–	48 ± 3	257 ± 4	1.68 ± 0.10	50 ± 16	0.53 ± 0.17
C	–	57 ± 4	260 ± 4	–	54 ± 15	0.40 ± 0.11
A	✓	79 ± 16	263 ± 14	2.52 ± 0.19	50 ± 20	1.1 ± 0.5
B	✓	80 ± 20	258 ± 14	2.7 ± 0.3	50 ± 20	1.1 ± 0.5
C	✓	66 ± 8	260 ± 10	–	54 ± 13	0.70 ± 0.17

* 90° sample rotation, that is the channel array was oriented horizontally.

of the channel array. From these profiles, average and standard deviation values were computed for the channel depth. Similarly, the channel width was measured from microscope images. The channel etch factor was calculated according to Equations 3.1 and 3.2. Finally, the average etch depth and etch rate were determined from the three-dimensional surface data by including only the etched area.

The results for design A show that the most uniform channel dimensions were obtained when the natural-convective flow pattern was oriented in parallel with the channel array (Figure 8.8). This is because the electrolyte moved past the upper flow-manifold before reaching the channels. At this point, the concentration boundary layer was well-established. Accordingly, the channel depth and etch factor were smallest. In the other two cases, the boundary-layer thickness, and hence the etch rate, varied more over this area, leading to larger standard deviations in the channel dimensions. Overall, however, the same average etch depth was reached — a change in mass-transfer conditions only affecting the average etch rate.

In terms of gas-flow uniformity, it follows that larger variations in channel cross-sectional area will lead to more maldistribution amongst the channels. In line with the work of Delsman et al. [378], it was possible to quantify the ensuing variation in gas flow rate. Several assumptions were made for this purpose. Fully developed laminar flow was assumed to be driven by a constant pressure gradient across each channel. The channel cross-section was presumed to be semi-elliptical. The friction-factor data of Velusamy et al. [399] was used. The gas flow rate was calculated for each channel with the dimensions shown in Figure 8.8. It was then possible to

compute the normalised gas-flow rate with respect to the average value. In the case of vertically oriented channels machined without agitation, 95 % of the channels had a flow rate ranging from 85–115 % of the average flow rate. In contrast, the horizontally oriented channel array yielded flow rate variations from 26–174 %. Finally, machining of channels in a vertical orientation and in the presence of agitation resulted in the widest range of gas flow rates from 11–189 %. For this estimation, deviations in the dimensions of the inlet and outlet manifold, which would result in a non-uniform pressure gradient, were not considered. This would increase maldistribution even further. Nonetheless, this approximate calculation illustrates the importance of consistent channel dimensions.

Different designs for the mask artwork were also tested, both with and without agitation. Adding a sacrificial etch band (design B) or using a dummy mask (design C) had no influence on the average etch depth within the experimental uncertainty (Table 8.2). The impact of the etch band in terms of the uniformity of the channel dimensions was also minimal. Even in the vicinity of the mask edge, the etch band had only a small effect on the etch depth (Figure 8.9). The introduction of dummy artwork resulted mainly in a drop in etch rate, which was caused by the decrease in area of the initially exposed metal surface. Notably, the individual square-openings merged to form larger cavities across the whole mask design. This lead to locally smooth channels and flow manifolds. Nonetheless, variations in the channel dimensions occurred due to non-uniform mass transfer.

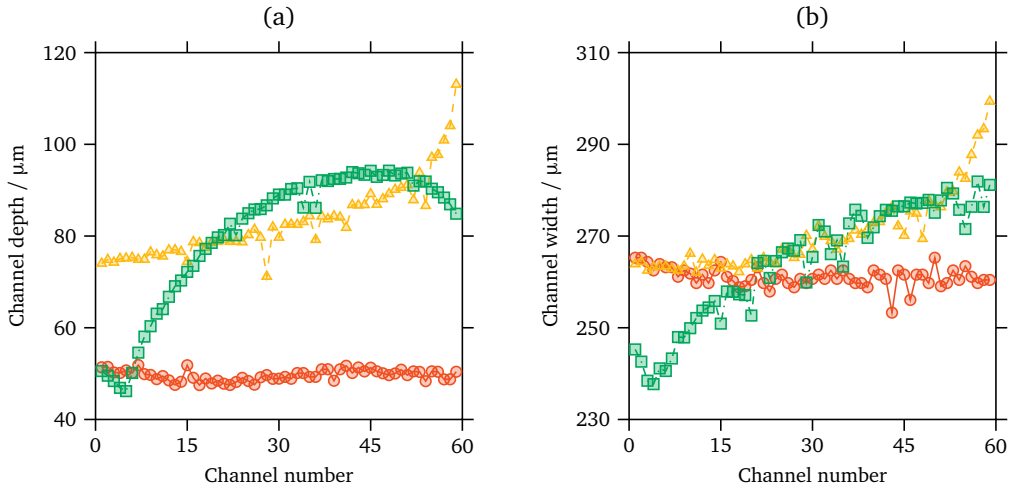

Figure 8.8: Variation in (a) channel depth and (b) width for design A along a perpendicular profile in the middle of the channel array: vertical channel orientation without agitation (—○—), horizontal channel orientation without agitation (- △ -), vertical channel orientation with agitation (- □ -).

Closer examination of existing work shows that the positive impact of adding a sacrificial etch band is tied to certain conditions. Tjerkstra [382] in his work on chemical etching of silicon in HF/HNO_3 etchant added a set of sacrificial etch bands 7 mm in width, thus compensating for non-uniform etching along the mask edge. Presumably, the etching process was limited by diffusive mass transfer in the absence of convection. Etch bands of similar size were used in electrochemical etching of NiTi shape-memory devices [291]. Therein, samples were oriented vertically within the cell, consequently leading to the wedging effect. Based on the depth profile shown in Figure 8.9, an etch band on the order of several millimetres would be necessary in the present case. This has two important consequences. Firstly, increasing the etch-band width results in a corresponding rise in current, which adds to the power consumption of the cell. Secondly, the metal content of the electrolyte rises more quickly, thus necessitating electrolyte renewal at shorter intervals. This casts some doubt on the usefulness of such compensating structures.

Likewise, dummy masks are most useful in specific cases. They have been primarily used for though-foil etching of thin substrates, which are mounted on an insulating support [20, 237]. In this case, all features are usually etched all the way through, and the dummy artwork prevents island formation, thus ensuring correct feature widths. Conversely, during cavity etching both the width and pitch of features within the dummy mask must be chosen carefully in relation to the etch depth; otherwise, the metal surface remains wavy afterwards [17]. Theoretical studies, which conform to diffusion-controlled TMEMM, show that the initial current distribution on the

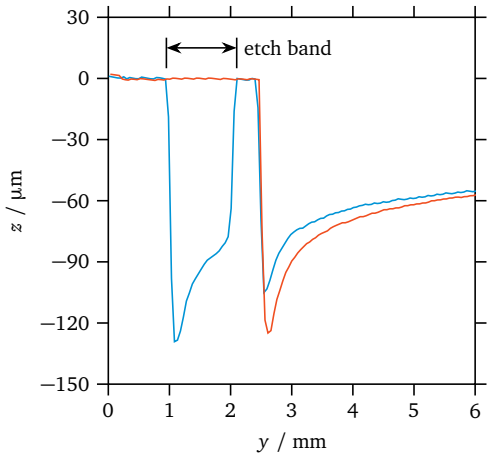

Figure 8.9: Surface profile near the upper edge of the top flow-manifold, with (——) and without (——) a sacrificial etch band in the vicinity. Solution flow was from left to right.

pattern scale exhibits distinct maxima at features located along the edge of a pattern [163, 165, 400]. Dividing such features into smaller ones can reduce but not eliminate non-uniformities in the current distribution, because edge effects still persist. Similarly, leading and trailing edges are still present during convection-controlled TMEMM, with variations in mass transfer only being attenuated by a change in feature size and spacing. The present work shows that achieving uniform mass-transfer conditions is the more critical factor.

8.3.3 AC gold electrodeposition

In preparation for gold deposition, porous-alumina films were formed in sulphuric acid under potentiostatic conditions at 10–20 V. After the initial stages of oxide growth — barrier-layer thickening, crack formation and pore initiation [73] — the current density attained stable values on the order of 1–3 mA cm^{-2} after a few minutes (Figure 8.10(a)). Concurrent gas evolution was not observed; therefore, sample orientation was not critical. Based on SEM images, porous films exhibited a random pore distribution, with pore diameters ranging from 10–20 nm. From polished cross-sections, the porous-film thickness was determined for varying anodising times of 1–4 h at each potential. Porous films were thus formed in the thickness range from 1–19 µm (Figure 8.10(b)). Due to the stable current density, film thickness increased linearly with the cumulative passed charge, and hence with anodising time. The film-growth rate was found to range roughly from 1–5 µm h^{-1} and to approximately double for a 5 V increase in anodising potential. Accurate control of the thickness of porous-alumina films was hence possible.

Gold electrodeposition was subsequently performed on anodised samples under differing AC conditions. Firstly, the properties of the porous-oxide film were varied under constant deposition conditions (13.2 V AC, 180 s). Secondly, AC gold electrodeposition was conducted with porous films grown to the same thickness of about 1.3 µm at constant anodising conditions (10 V, 1 h). With the latter samples, deposition was either carried out for 180 s at different AC potentials (2.15 V, 4.30 V, 6.45 V and 13.2 V) or at 13.2 V AC for varying deposition times. Gold deposits were formed and confirmed via EDXS in all cases, except at 2.15 V AC. This is likely because this AC potential is too low compared to the reduction potential for Au^{3+} ions ($E^0(Au/Au^{3+}) = 1.498$ V vs. SHE) [58], once resistive losses within the barrier layer are factored in. This is in accordance with earlier findings that the minimum deposition potential depends on the barrier-layer thickness [128].

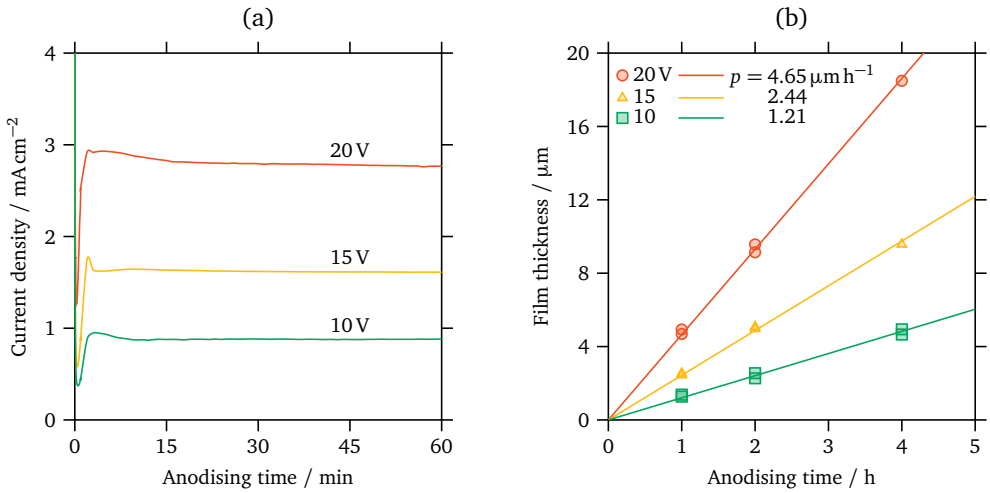

Figure 8.10: Dependence of (a) anodising current density and (b) porous-film thickness on anodising time at different applied potentials in 0.5 M H_2SO_4 at 10 °C. Also given is the slope (p) of a linear regression fit through the origin at each potential.

After electrodeposition, top and cross-section views were acquired, and the deposit morphology was studied by way of SEM (Figure 8.11). Thereby, three different deposit types were observed. During the initial deposition stage, finely dispersed gold particles formed within a thin region at the pore bottom. As the deposition continued, further gold was reduced, and gold wires grew towards the pore mouth. Once the pores were filled completely, gold was reduced along top surface, thus creating gold particles again. The growth rate of the gold deposit was found to increase with higher AC potentials. While the AC current was not monitored simultaneously, it seems reasonable to assume that this is because the deposition charge during each cycle rose accordingly. In addition, deposit thickness depended on the thickness of the porous-oxide film, and hence on pore length. The reason is that, once the electrolyte within the pores was depleted of Au^{3+} ions, the deposition rate was limited by the mass-transfer rate from the pore mouth to the deposit front.

The feasibility of scaling up both processes was tested with square samples machined according to mask design A. For this purpose, the photoresist mask was left in place after machining. The samples were then anodised at 10 V (∼1 mA cm^{-2}) for 1 h, followed by gold deposition at 13.2 V AC for 180 s. A porous-oxide film was formed in this manner, which was successfully impregnated with gold. This produced an even Au/Al_2O_3 coating over the whole microreactor structure, as was evidenced by the uniform red tone of the surface (Figure 8.12).

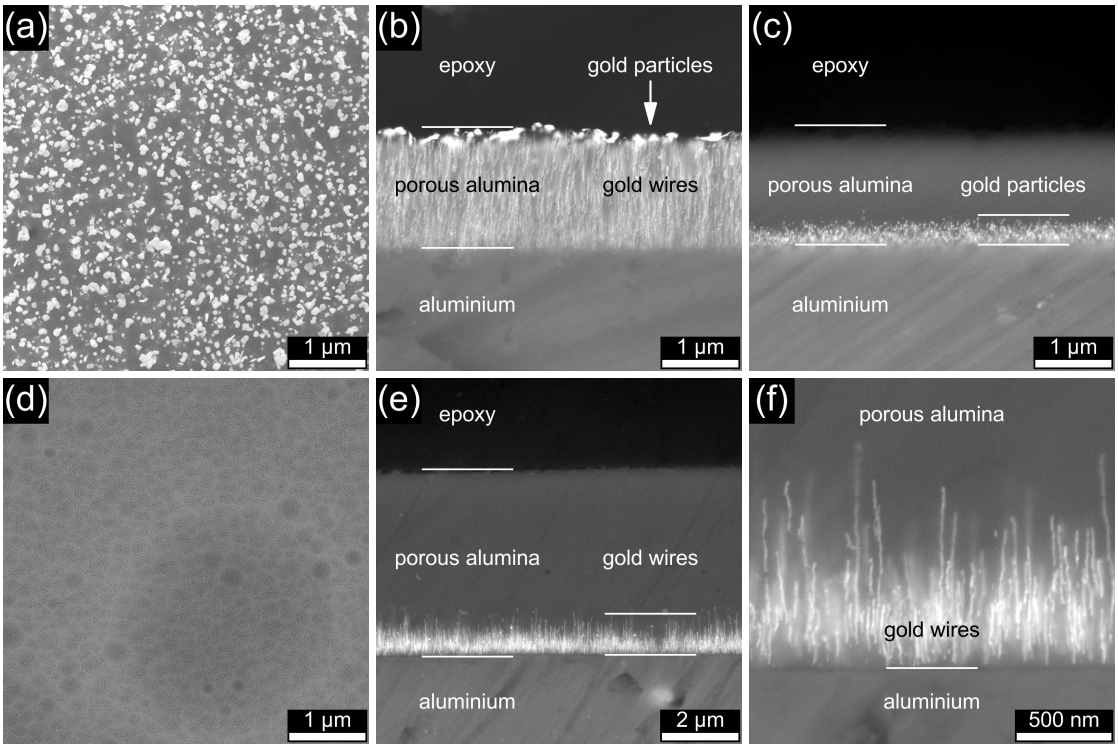

Figure 8.11: SEM images offering (a, d) top and (b, c, e, f) cross-section views of anodised aluminium samples after AC gold electrodeposition. Samples were anodised at 10 V for (a, b, c) 1 h and (d, e, f) 4 h. AC gold electrodeposition was performed at 13.2 V AC for (a, b, d, e, f) 180 s and (c) 10 s.

From the vantage point of heterogeneous catalysis, these preliminary results are promising. The prospect of optimising the deposition conditions with respect to catalyst performance seems possible. For example, if the deposition charge was monitored, the gold loading within the porous-oxide film could be controlled accurately by varying either the conditions of AC gold electrodeposition or the properties of the porous-oxide film. This is of great interest considering the cost of noble-metal catalysts. In addition, catalytic activity will presumably depend on the structure of the pores and on the gold deposit within them. In line with previous work on platinum deposition [131], there likely exist optimum deposition conditions, which maximise catalyst activity and minimise catalyst loading. At present, the formation of gold particles at the pore bottom seems most favourable, as this should increase the ratio between exposed and deposited gold. However, further work is necessary to assess and compare the catalytic performance of gold deposits formed via AC electrodeposition with chemical and physical methods in common use.

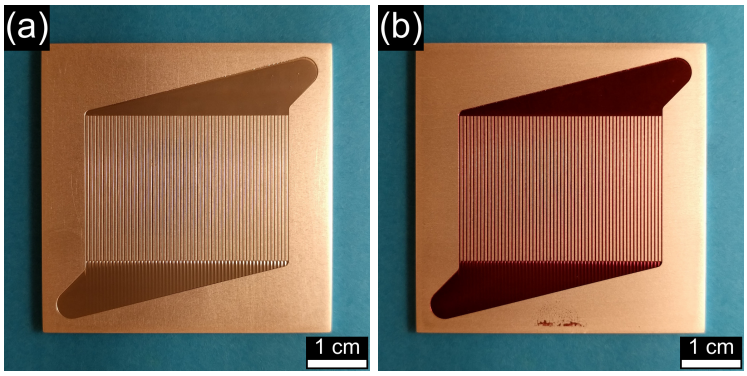

Figure 8.12: Photographs of square samples (a) after anodising and (b) AC gold electrodeposition.

8.4 Conclusions

In this work, three different aspects of fabricating and functionalising an aluminium gas-phase microreactor were studied. Firstly, the importance of avoiding gas pitting was highlighted. To this end, the influence of surfactants on aluminium EP was investigated via the recording of linear potential sweeps and via SEM imaging of the surface morphology. Thereby, both CTAB and Triton X-100 were identified as suitable wetting agents for TMEMM of aluminium. Secondly, the impact of mass transfer and mask design on the uniformity of the current distribution during TMEMM was examined. For this purpose, different designs for a gas-phase microreactor were machined — with and without agitation — and afterwards characterised via microscopy and optical profilometry. Mass transfer effects were observed in the form of wedging and found to dominate the shape-evolution process. By comparison, variations in the mask design in the form of a sacrificial etch band and a dummy mask had only a negligible effect. Thirdly, preliminary results on the formation of a catalytic wall coating made from Au/Al_2O_3 along the microchannel walls were presented. By combining anodising and AC electrodeposition, uniform catalytic coatings showcasing finely dispersed gold particles were formed.

The observed influence of mass transfer, either with or without agitation, has important implications for the cell design in TMEMM. Electrode configurations based on shearing flow, that is flow in parallel to the anode surface, inevitably suffer from wedging in flow direction. This includes, for example, rotating discs [210] and flow channel cells [169, 247, 309]. The successful application of hydrodynamic electrodes hinges on careful consideration of the flow conditions. The problem is certainly less severe in the case of simple mask designs, such as line [169] or hole

arrays [10], where non-uniformities in the current distribution can be compensated by changing feature spacing and orientation. However, with complex masks — such as the designs presented in this work — shearing flow appears to be unable to ensure uniform material removal. Instead, entirely different modes of agitation need to be considered, such as ultrasonication or impinging flow.

9 Comparison with wet-chemical etching

9.1 Introduction

Through-mask electrochemical micromachining (TMEMM) and photochemical machining (PCM) are similar to each other in many ways. Both employ an insulating mask to achieve pattern transfer onto a substrate, and both rely on electrochemical processes for material removal [156, 372]. Regarding TMEMM, the anode potential is controlled by an external device, and the current flows through an outer circuit. Within the PCM process on the other hand, the anode potential is governed by an oxidising agent in solution, and etching proceeds without external current flow. Both processes are used for the manufacture of precision parts from thin sheet material. Compare for instance applications listed in Section 3.7 with those presented by Allen [156, 214, 401]. They are also similar in terms of their economic feasibility, because the machining time depends on the substrate thickness and is independent of part complexity (Section 3.8). Moreover, TMEMM is often seen as an alternative to PCM, especially for difficult-to-etch materials [10, 216].

Given these similarities, it seemed advisable to compare the performance of a selection of typical aluminium wet-etchants with the phosphoric acid-based electropolishing solution used throughout the rest of this work. For this purpose, a simple test pattern consisting of differently sized, straight lines was machined into the surface of aluminium plates. Due to its amphoteric character, both acidic and alkaline etchants are in use for aluminium wet-etching [402]. In order to ensure compatibility with the employed positive-tone photoresist, only acid mixtures were tested here. From this group, five wet etchants were chosen, based on their use for the surface structuring [308] and finishing [45] of aluminium on an industrial scale. In the process, preliminary results were gathered and analysed in terms of etch rate, surface roughness, undercutting, shape profile and etch uniformity.

9.2 Experimentation

Commercially pure $50 \times 50\,\mathrm{mm}^2$ aluminium samples were used for all experiments (Section 4.2). These samples were prepared as described previously, with one exception: samples intended for chemical etching were not etch-cleaned in 5 % NaOH prior to photolithography. This is because continuous gas evolution is an inherent feature of chemical etching. After the usual polishing and cleaning steps, these plates were coated with a patterned mask made from positive-tone photoresist (AZ1518) according to the process outlined in Section 7.2.

During the lithography step, a mask pattern consisting of 8 mm long, straight lines of different width and orientation was created. The base pattern contained seven parallel-aligned lines in total, which increased in width from 0.01–1 mm at a constant pitch of 1.02 mm (Figure 9.1). Four of these line patterns were arranged in a 2×2 square at a distance of 8 mm from each other. The lines were oriented either horizontally or vertically in steps of 90° to one another.

The setup for both chemical and electrochemical experiments was identical to the one for the large-scale TMEMM experiments (Chapter 8). In brief, the plate samples were held vertically in a polytetrafluoroethylene holder, providing electrical contact and preventing leakage. This holder was positioned within a 1 L jacketed glass cell. A thermostat-controlled, external water bath (GD120 and LTC1, Grant Instruments) provided temperature-control. During electrochemical etching, the applied anode potential was regulated by a potentiostat (Reference 3000, Gamry Instruments),

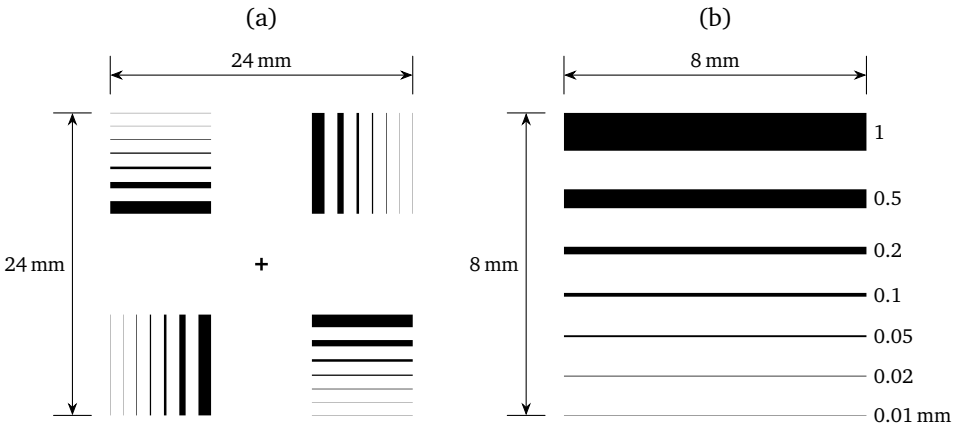

Figure 9.1: Design and dimensions of the mask pattern for comparative chemical and electrochemical etching experiments: (a) complete pattern, (b) base pattern.

Table 9.1: Composition and temperature of chemical and electrochemical etching solutions. The identifier in the first column is used for reference.

#	Solution composition	Temp.	Ref.
C1	2.4 M HCl	50 °C	[308]
C2	0.5 M $FeCl_3$, 0.25 M HCl	50 °C	[308]
C3	$H_3PO_4/HNO_3/CH_3COOH/H_2O$ (16/1/1/2, v/v)	50 °C	[403]
C4	$H_3PO_4/HNO_3/H_2O$ (20/1/4, v/v)	90 °C	[45]
C5	$H_3PO_4/HNO_3/H_2SO_4$ (14/1/5, v/v)	85 °C	[46]
E	84.5 % H_3PO_4 + 1 mM Triton X-100	75 °C	*

* this work

which was connected to a Ag|AgCl reference electrode and a Pt counter electrode. During chemical etching these electrodes were removed.

Five different wet etchants were tested and compared with electrochemical etching in 84.5 % H_3PO_4 with 1 mM Triton X-100 at an applied potential of 1.4 V. The composition and temperature of each solution is listed in Table 9.1. Therein, the first table column specifies the designation used throughout this chapter to refer to each solution. Etchants C1 and C2 are primarily used in the PCM industry [308], and both contain chloride ions as the active species. In contrast, solutions C3, C4 and C5 are all based on phosphoric and nitric acid. Etchant C3 is a common aluminium thin-film etchant [403], whereas C4 and C5 are representative mixtures used for chemical polishing [45, 46]. Concentrated reagents and de-ionised water (Milli-Q, Merck) were used to make up these solutions and to arrive at the specified concentrations or volume ratios. All acids were either of analytical or ACS grade; only the employed iron(III) chloride was of reagent-grade quality. The composition, purity and supplier of each chemical is listed separately in Table 4.1.

The etching experiments were conducted by immersing each sample for 10 min while stirring. The resulting flow pattern along the plate surface ran roughly from right to left and from top to bottom (Figure 8.7(d)). This meant that each of the four base patterns was subject to flow from a different direction. Afterwards, the aluminium plates were rinsed with copious amounts of water, cleaned with acetone, methanol and isopropyl alcohol, and left to dry in air. The resulting channels were characterised in terms of surface morphology via scanning electron microscopy (SEM) (JSM 7000F, JEOL). Depth profiles and surface roughness were acquired with an optical (Profilm 3D, Filmetrics) and a stylus profilometer (Dektak 150, Veeco), while the channel width was measured from microscope images (Olympus BX60).

9.3 Results and discussion

The surface structure of etched aluminium surfaces was examined via SEM imaging (Figure 9.2), and surface roughness (Table 9.2) was evaluated with the optical profilometer. The average values and the respective standard deviations presented in Table 9.2 were calculated from data in five different locations. The widest line was chosen for these measurements in order to exclude the effect of channel curvature. Both average and root mean square (RMS) values were gathered.

Etchants C1 and C2 both showed signs of chloride attack in the form of cubic etch pits. The rough appearance of the surface on SEM images was corroborated by profilometer data, yielding large roughness values on the order of several micrometres. In contrast, etchant C3 produced overlapping, circular etch pits, which ranged in size from 1–10 µm. Surface roughness was about one order of magnitude

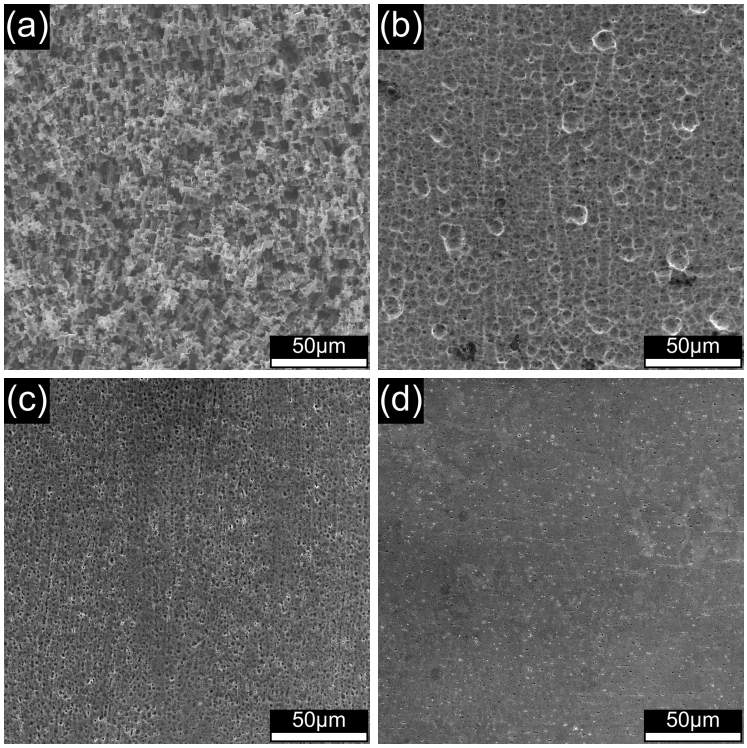

Figure 9.2: SEM images (500× magnification) of aluminium after 10 min chemical or electrochemical etching in solutions (a) C1, (b) C3, (c) C4 and (d) E. The images shown for etchants C1 and C4 are also representative for the results in mixtures C2 and C5, respectively. All images depict the channel surface for an initial line width of 1 mm.

Table 9.2: Results of chemical and electrochemical etching experiments in terms of roughness parameters, etch rate and average etch factor. Note that the etch rate was determined for an initial line width of 1 mm only.

#	Avg. roughness (μm)	RMS roughness (μm)	Etch rate ($\mu m\,min^{-1}$)	Etch factor
C1	4.4 ± 0.2	5.5 ± 0.3	30.2 ± 0.6	1.20 ± 0.02
C2	4.8 ± 0.2	6.0 ± 0.3	4.5 ± 0.4	–
C3	0.36 ± 0.04	0.53 ± 0.07	0.73 ± 0.02	0.45 ± 0.04
C4	0.07 ± 0.01	0.11 ± 0.02	7.2 ± 0.3	0.62 ± 0.02
C5	0.05 ± 0.01	0.08 ± 0.02	4.9 ± 0.3	–
E	0.04 ± 0.01	0.06 ± 0.01	2.6 ± 0.5	1.88 ± 0.10

lower compared to the former two solutions. Etching solutions C4 and C5 produced an even smoother surface finish, which was characterised by finely dispersed etch pits about 1 μm in diameter. In these three chloride-free etchants, crystallographic etching was suppressed, due to the formation of a solid surface-film made from alumina [45]. As before, electrochemical dissolution in mixture E lead to a polished surface, which included randomly scattered pits due to the presence of metallic inclusions (Section 5.3.1). This yielded the lowest surface-roughness values, but the difference to the two chemical polishing solutions was not large.

On the basis of profilometer data (Figure 9.3), the average etch rate after 10 min dissolution was determined. This was done for the widest line only, so as to yield a value, which was independent of the line width. As the profile scans show, the etch depth remained fairly constant for initial line widths of 0.1 mm and larger with all tested etchants; hence, this seemed justified. The etch factor was calculated according to Equation 3.2 in conjunction with etch widths measured from microscope images. An average value over all lines was computed for each etchant, except for solutions C2 and C5. In the case of etchant C2, the images indicated that the maximum etch width did not coincide with the channel opening; thus, results for the etch factor were deemed too high and unreliable. In etchant C5 on the other hand, the photoresist was not sufficiently stable. Pin holes and excessive undercutting occurred, likely because sulphuric acid acted as a strong oxidant towards the resist and removed it [404]. Again, measurements of the etch width were considered inaccurate. The remaining values are listed in Table 9.2.

Out of all solutions, etchant C1 showed the highest etch rate. Despite deep etching across all lines, undercutting remained modest with an average etch factor above unity. The etch rate decreased with the initial line width, which is frequently

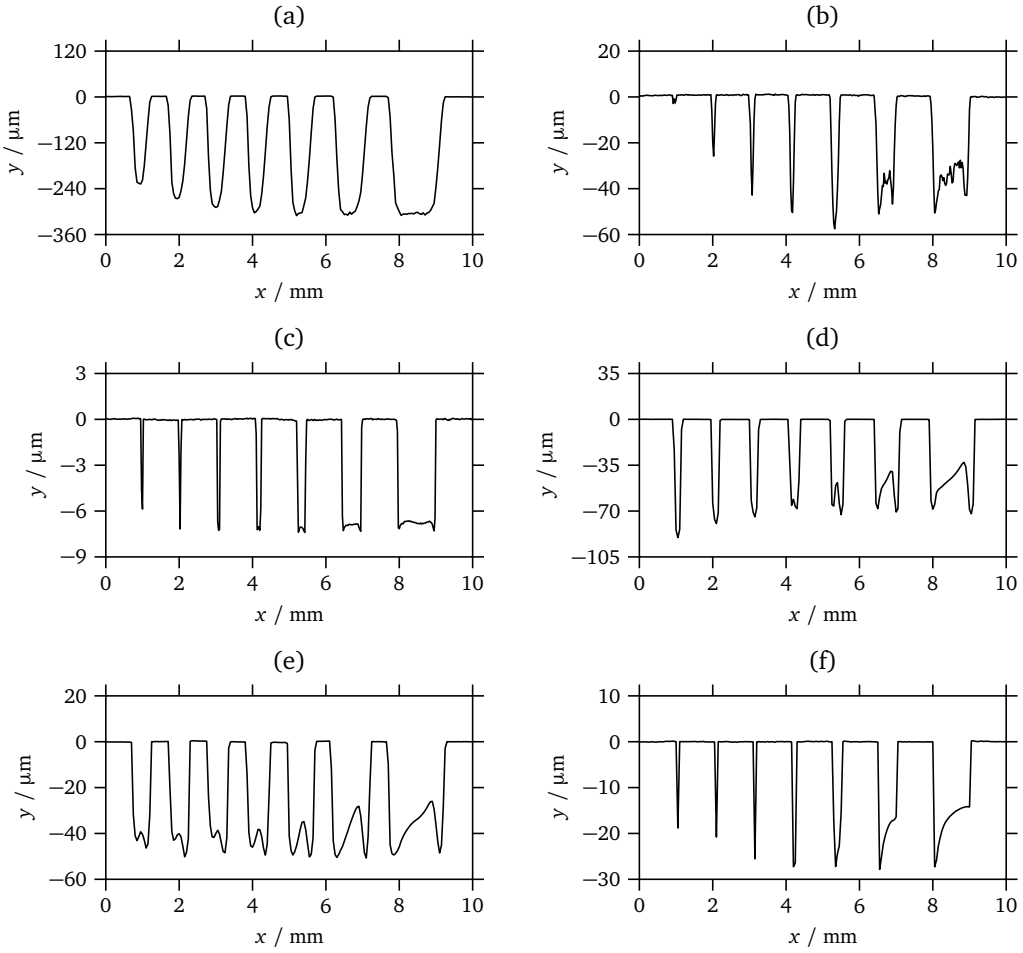

Figure 9.3: Profilometer data of etched channel profiles after chemical or electrochemical dissolution for 10 min in solution (a) C1, (b) C2, (c) C3, (d) C4, (e) C5 or (f) E.

observed when etching in chloride media [405, 406] and stems from mass-transfer limitations [156]. The channel edge appeared jagged, and thin lines varied visibly in width (Figure 9.4(a)). This is because material was removed via crystallographic etching. In this case, the orientation of crystal facets and the presence of grain boundaries both affect the etch rate. Thereby, the grain size puts a limit on the smallest resolvable feature. The observed non-uniformity was similar to that witnessed in concentrated $FeCl_3$ solutions [308]. In this case, it stems from the exothermic reaction heat, which evolves upon metal dissolution and locally accelerates the etching process. The channel profiles were either semi-elliptical or flat-bottomed with round corners, which corresponds to isotropic chemical etching [156, 405].

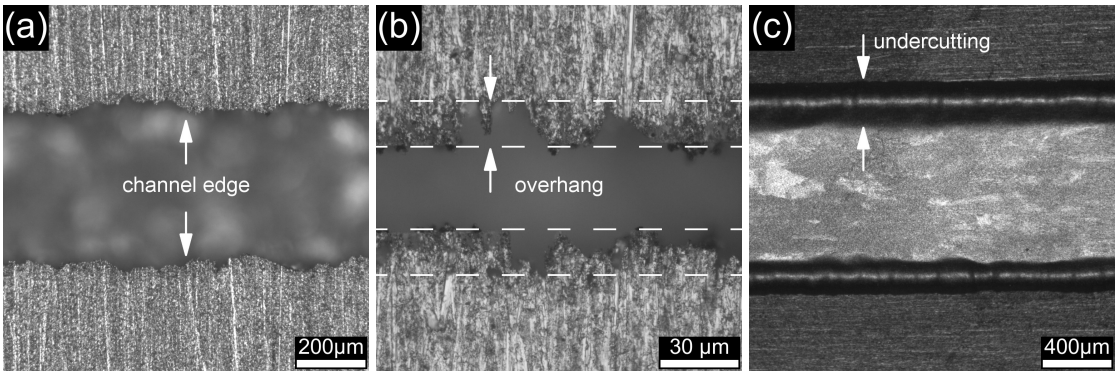

Figure 9.4: Micrographs of chemically etched channels after 10 min immersion in etchant (a) C1, (b) C2 and (c) C4. The initial line width was 0.01 mm, 0.05 mm and 1 mm, respectively.

By comparison, the etch rate in etchant C2 was smaller by a factor of about seven. Also, a more distinct line-width dependence of the etch rate occurred. The 0.01 mm line, for instance, was etched to a depth of less than 5 µm. Higher etch rates can be achieved by increasing the $FeCl_3$ concentration, with maximum values reported at 3 M $FeCl_3$ under spray-etching conditions [65]. However, such high concentrations are not suitable for immersion etching, due to the aforementioned exothermic reaction heat [308]. As was referred to before, the amount of undercutting was impossible to measure, because an overhang formed, as indicated by microscope images (Figure 9.4(b)). A possible explanation for this observation stems from the relatively low $FeCl_3$ content in solution. When etching stainless steels, a minimum amount of $FeCl_3$ is required to depassivate the surface [401]. Similarly, the air-formed alumina film along the surface may dissolve slowly, while etching proceeds more quickly underneath this film. The channel profiles, as far as they were not obstructed by the overhang, were either semi-elliptical or w-shaped.

The lowest etch rate was observed in etchant C3, with a value similar to previous reports [403]. In spite of the low overall etch depth, severe undercutting took place, with an average etch factor of only 0.4–0.5. At the same time, the uniformity of the etch rate over all lines was best. This is to be expected given that this mixture is used as a thin-film etchant. In the context of this application, the etch-rate uniformity over varying line widths is most important, and little material on the order of a few hundred nanometres is usually removed.

The other two phosphoric acid-based etchants, C4 and C5, showed a considerably higher etch rate on the order of several micrometres per minute. In both solutions, thin lines were severely undercut, and wide lines showed wedging in flow direction

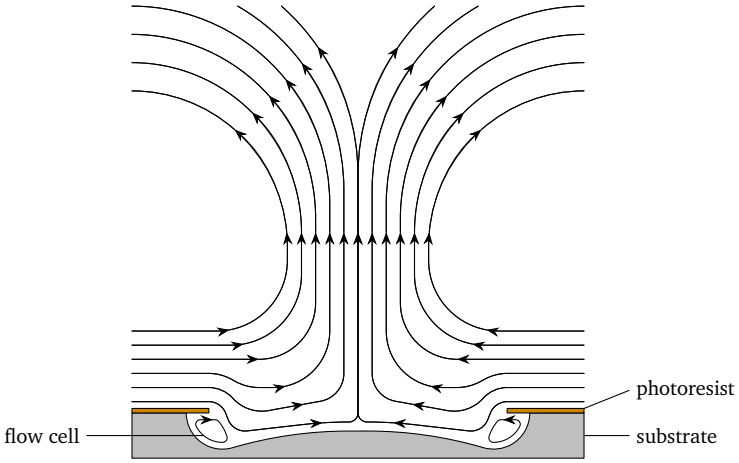

Figure 9.5: Schematic flow pattern induced by gas evolution along the exposed metal surface. Circulating flow cells develop in the process in the vicinity of the mask edge, leading to more undercutting.

and a distinct w-shape (Figure 9.4(c)). The latter two phenomena point towards a dependence of the etch rate on mass-transfer effects, at least in part. It may be hypothesised that the establishment of local hydrodynamic flow cells is responsible for this anisotropy (Figure 9.5). Gas evolution along the exposed metal surface might create two circulating flow cells at each resist edge. As the ascending gas bubbles entrain the surrounding etchant, fresh etchant is supplied from both sides. This may have lead to the formation of large concentration gradients and thus etch rates along the edge, which decreased towards the channel centre. In the case of etchant C5, insufficient resist stability was an additional factor in this regard.

In comparison to the above results, the etch rate during electrochemical dissolution in solution E was substantially lower. In addition, the etch rate varied more between all four patterns for a mask opening of the same initial width. Furthermore, wedging in flow direction was observed. These results stem from the absence of gas evolution compared to chemical etching. As a consequence, variations in the macroscopic flow pattern induced by stirring played a greater role in determining the local etch rate along the exposed metal surface. By comparing data for chemical and electrochemical etching (Figure 9.3), it is clear that gas evolution enhances local mixing and thus mass transfer. Thereby, any macroscopic flow pattern is disrupted, and differences in flow rate and direction are in part compensated.

Undercutting in solution E was less severe with an average etch factor of about 1.9. However, in judging this result, one should be aware of the influence between etch depth and etch factor. As was shown previously (Chapter 7), the etch factor

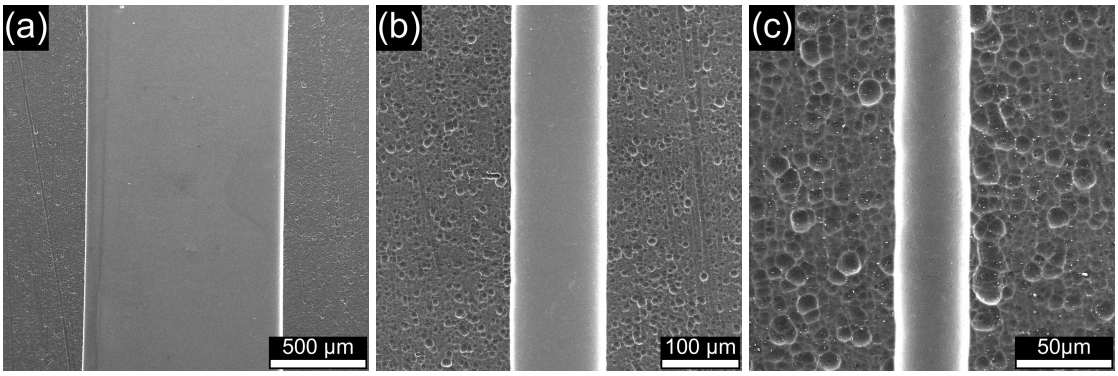

Figure 9.6: SEM images of channels after electrochemical dissolution for 10 min in solution E. The initial line width was (a) 1 mm, (b) 0.1 mm and (c) 0.01 mm. The respective average values for the etch width were (1.025 ± 0.003) mm, (0.128 ± 0.003) mm and (0.040 ± 0.002) mm.

decreases over time. With that caveat in mind, this result is difficult to compare to etchant C1, where a much larger etch depth was reached. Conversely, electrochemical dissolution clearly yielded superior results in comparison to etchants C3 and C4, which were characterised by a ratio between lateral and perpendicular etching greater than one. From a theoretical point of view [160, 188], the etch factor approaches or remains above unity during mass-transfer-limited dissolution, regardless of the mode of mass transfer. Therefore, lateral etching will never outpace perpendicular etching during electrochemical dissolution in solution E.

Regarding the channel shape and uniformity after etching in solution E, the present results agree with trends already discussed in Chapters 7 and 8. Therein, the etch depth and width of thinner lines depended less on the macroscopic flow pattern and more on the initial line width (Figure 9.3). This is explained by mass-transfer limitations caused by the smaller mask-opening size. Channels with an initial line width of 0.1–1 mm were not affected by this bottleneck, and accordingly the maximum in the etch depth remained constant. In terms of how straight the channel edge appeared after dissolution, solution E produced the best results out of all experiments. This became clear when comparing SEM (Figure 9.6) and microscope images (Figure 9.4) for the different etchants with each other. In solution E for instance, the thinnest line was widened from an initial value of 10 µm to a width of (40 ± 2) µm, yielding a relative standard deviation of 5 %. For the same initial line width, a relative standard deviation this low was only reached in etchant C1 at an etch width of (490 ± 20) µm — more than one order of magnitude larger.

9.4 Conclusions

In terms of their suitability for the purpose of micromachining microfluidic devices, the above preliminary results on wet-chemical etching present a mixed picture. The use of chloride etchants, while accelerating the etching process, is clearly disadvantageous, due to non-uniform material removal and substantial surface roughening. For these reasons, the accurate machining of small features on the order of tens of micrometres is prohibited. This has been demonstrated previously in work on aluminium etching in chloride media [62, 222]. Another point of interest is the existence of chlorine residues along the etched surface, which may subsequently lead to catalyst deactivation. As a consequence, these must first be removed via elaborate thermal or electrochemical treatments [303].

Thin-film etchants, as the one used in this work, are also not suitable, although for different reasons. While features of different size can be machined accurately and uniformly, the etch rate is too low at well below $1\,\mu m\,min^{-1}$. As has been noted before [308], this value is insufficient within an industrial context. Also, undercutting is substantial, even at very small etch depths.

This leaves chemical polishing solutions based on phosphoric acid as an alternative for aluminium micromachining. They exhibit sub-micrometre surface roughness after the dissolution process, which makes it possible in principle to resolve very small features on the order of a few micrometres. However, this gain in accuracy is literally undercut by excessive lateral etching. Whether this is due to resist instability only or because of local hydrodynamic flow-phenomena in the vicinity of the mask edge is not clear at this point. At present, this limits their use to the micromachining of features on the order of a few hundred micrometres.

In summary, TMEMM of aluminium in phosphoric acid appears to be the most suitable option for micromachining of microfluidic devices. The etch rate is larger than $1\,\mu m\,min^{-1}$, which presents at least a good starting point for further improvements. Because the process operates under mass-transfer-limited dissolution conditions, an intensification of mass transfer should lead to additional increases in the etch rate. In addition, the machining process can be accelerated even further by raising the solution temperature [44, 407] or the water content [107, 408]. Given the great similarity between chemical and electrochemical polishing solutions [45], literature data on improvements to the former may also be useful to optimise the latter. The main disadvantage, which remains at this point, consists in the dependence of the etch rate on the mask-opening size and on the flow direction.

10 Conclusions and recommendations

This chapter aims to conclude this work by presenting in turn its main contributions, as well as by summarising the major findings and conclusions. This leads to a short discussion of practical implications and recommendations. Finally, recommended avenues for future research are outlined briefly.

10.1 Thesis summary and contributions

Through-mask electrochemical micromachining (TMEMM) has been extensively used in the past for the manufacture of precision-engineered microstructures, such as microelectronics and microactuators to name a few. This is because TMEMM is able to mass-produce parts; it is applicable to difficult-to-etch materials and operable under electropolishing (EP) conditions. Parts thus machined are burr-free, and heat-affected zones are absent. Despite these benefits, the use of TMEMM for the fabrication of microfluidic devices in general and microreactors in particular is rare to non-existent at this point. The reluctance to adopt TMEMM for this purpose can be ascribed to process-specific challenges, namely to the current-distribution problem. A uniform current distribution is key in controlling material removal, undercutting and surface finish. The problem is complicated by the role of mass-transfer effects, the onset of surface-film formation and the existence of multiple length-scales. The aim of this work was, therefore, to study in detail the viability of TMEMM for the fabrication of microfluidic devices.

By way of example, the manufacture of parts for a gas-phase microreactor was studied. The ultimate goal was the fabrication and functionalisation of a complete microchannel plate-inlay for a plate-type microreactor design. For this purpose, aluminium was chosen as the substrate material, and phosphoric acid served as the electrolyte. This metal/electrolyte system exhibits EP conditions at elevated temperatures and high acid concentrations [44]. Thereby, the formation of micrometre-sized structures with sub-micrometre surface roughness seemed possible. In parallel, Au/Al_2O_3 was selected as the catalyst/support system to serve as a test case for the

subsequent formation of a catalytic wall coating. In order to achieve the above goal, this study was carried out by several means, namely: a review of the literature, an electrochemical impedance spectroscopy (EIS) study of the metal/electrolyte system, an experimental and model-based investigation of the shape-evolution process, and a series of experiments on the fabrication of microfluidic structures.

In line with the objectives stated in the introduction (Section 1.4), the research has resulted in the following original contributions:

- An in-depth literature review on the topic of TMEMM, summarising a large fraction of the existing literature and emphasising knowledge gaps (Chapter 3).
- The interpretation of EIS data in the system aluminium/phosphoric acid, thereby confirming the presence of a compact, barrier-type alumina film (Chapter 5).
- The implementation (Chapter 6) and validation (Chapter 7) of a feature-scale shape-evolution model, highlighting the influence of mass-transfer effects.
- The fabrication and functionalisation of microchannel plate-inlays by electrochemical means, namely TMEMM, anodising and electrodeposition (Chapter 8).
- A comparison with chemical wet-etching methods for the purpose of aluminium micromachining, showcasing the advantages of TMEMM in this area (Chapter 9).

10.2 Main findings and conclusions

10.2.1 Literature review

As has been established in this (Chapter 3) and previous reviews [21, 143], TMEMM is a highly complex electrochemical process, combining metal shaping and finishing into one operation. Predicting the removal rate, the shape profile and the surface finish is not straightforward, because of the interaction between current distribution, mass transfer and surface films. Over the past few decades, a considerable body of work has accrued, pertaining to the problem of shape-evolution modelling in particular. These studies are largely concerned with conditions corresponding or equivalent to diffusive mass transfer alone. Unlike electrodeposition [158, 159], the pattern- and workpiece-scale problem has received far less attention, in particular when taking into account mass-transfer limitations and surface films. As a result, optimising the conditions of TMEMM towards a particular application is still left to

experimental trial-and-error. Modelling approaches, which include multiple length-scales, are still rare [23, 24, 400], but necessary in alleviating this problem and in extending the use of TMEMM. More work in this area is clearly needed.

Another problem, the correct choice of electrolyte for a particular substrate, appears less daunting today. A pool of experimental studies is available, covering many engineering metals and alloys [199]. Water-based electrolytes used in electrochemical machining and EP will suffice in most cases, yielding high removal rates or a smooth surface finish. Likewise, there exists now a long list of TMEMM applications within the fields of thin-film and bulk micromachining, which presents examples for its successful implementation. Simultaneously, novel masking methods aimed at replacing traditional photoresists have been developed, such as metal oxides [221] and silicones [229], with the goal to introduce less costly and more environmentally friendly materials. In terms of applicability, however, photolithography is still unparalleled, with other methods limited to niche areas. Also, various process variants have been proposed, adapting particular aspects of TMEMM, such as electrode configuration [168, 309], electrolyte agitation [268] and potential waveform [235]. A systematic comparison of these process variants is due to assess their merit.

10.2.2 Surface-film formation

As part of this work, the chosen metal/electrolyte system was characterised in terms of surface-film formation during mass-transfer-limited dissolution (Chapter 5). Based on linear potential sweeps and imaging via scanning electron microscopy such conditions were confirmed for aluminium in 85 % phosphoric acid at 75 °C in agreement with previous work [44]. Thereafter, the composition, structure and properties of the surface film were studied by measuring impedance spectra under controlled hydrodynamic and potentiostatic conditions with a rotating disc electrode (RDE). A suitable circuit model following the surface-charge approach [333, 334] was identified and successfully fitted to the data, thus clearly representing the dominant impedance features over a wide range of frequencies, namely: capacitive charging within the film, relaxation of a negative surface charge at the film/solution interface and perturbation of the film thickness.

In the following, the effect of changes in the dissolution conditions on the magnitude of the circuit parameters was determined, and the presence of different film types was evaluated. Firstly, a porous film structure could be excluded on the basis of a constant solution resistance. Secondly, the existence of an $AlPO_4$ salt film was

dismissed, because the calculated model parameters were independent of the hydrodynamic conditions. Instead, the model parameters were consistent with surface coverage with a compact, barrier-type alumina film. The thickness of this film was found to be on the order of a few nanometres only, and it depended solely on the applied potential. Several parameters related to charge transfer through the film and the surface-charge formation at the film/solution interface were estimated from the data and found to agree well with literature values. Thereby, the presumed film structure and composition were confirmed.

As a result, several conclusions relevant to the description and execution of TMEMM of aluminium in phosphoric acid can be drawn. The dependence of the film's thickness on the applied potential alone has two important consequences. Firstly, constant film coverage can be assumed throughout the process, thus yielding uniform polishing conditions. Secondly, as film thickness remains constant, a well-defined film/solution interface exists at all times. Furthermore, because the film thickness equals a few nanometres only, changes in the current distribution within the film can be ignored. Similarly, the influence of hydrodynamic effects can be disregarded when computing film thickness and coverage. Accordingly, modelling the shape-evolution process can be simplified greatly, and constant boundary conditions can be presumed along the exposed metal surface.

10.2.3 Shape-evolution modelling

On the basis of the above findings TMEMM of aluminium in phosphoric acid was modelled (Chapter 6). Based on published work [16, 160], a feature-scale shape-evolution model solely governed by diffusive mass transfer was derived. The model implementation was performed in Matlab via the boundary element method and in Comsol via the finite element method, and both numerical methods were found to agree well with each other with regards to current distribution, shape evolution and etch factor. The model results were validated with published data and compared to experimental shape profiles. To this end, shape-evolution experiments were conducted with a recessed RDE (Chapter 7), while varying the hydrodynamic conditions, the applied potential and the cumulative passed charge.

The machined microchannels attained a characteristic hemi-spherical cross-section in the process. Good agreement between model and experiment was observed in terms of depth, width and shape profile for conditions pertaining to mass transfer dominated by diffusion. Deviations in the measured etch factor were attributed to a

small degree of etch anisotropy caused by the presence of an air-formed alumina film. It was estimated that the range of applicability of the model extended up to a Péclet number of ten. Upon shifting from purely diffusive to mixed convective-diffusive mass transfer, secondary flow phenomena formed within the evolving cavity, as was attested by several observations, namely: the increase in etch rate, the displacement of the channel walls and the distortion of the channel profile. While a wide limiting-current plateau was available in principle to conduct this work, gas evolution — presumably oxygen evolution — interfered with the shape-evolution process at large applied potentials. Gas bubbles thus formed stuck to the channel surface and resulted in the formation of a jagged channel outline.

From the above results, the feature-scale shape-evolution process is clearly dominated by mass-transfer effects. For any practical implementation of TMEMM, flow effects will certainly play an important role; thus, uniform flow conditions are desirable to achieve even dimensions. Similarly, it is necessary to choose a suitable operating window to prevent concurrent gas evolution. Because dissolution proceeds along a limiting-current plateau, control of the potential rather than the current is necessary to this end. Prediction of the etch factor was shown to depend on initially present alumina films. Freshly formed films are only on the order of a few nanometres in thickness and can probably be neglected. Thicker oxide scales on the other hand should be removed before machining commences.

10.2.4 Microreactor fabrication and functionalisation

The next step was then the fabrication of a complete microchannel plate-inlay for a plate-type microreactor design (Chapter 7). Small-scale micromachining experiments with 15 mm disc samples had already demonstrated the viability of TMEMM towards the formation of microfluidic structures, containing simple channel networks. As an example, a micromixer design based on a meandering channel was realised, exhibiting sub-micrometre surface roughness and well-defined channel walls (Chapter 8). In order to achieve the scale-up to a more relevant sample size, micromachining experiments were conducted with 50 mm square plate samples in a custom-built cell, which was designed for immersion etching.

During these experiments, gas pitting was found to be a particular problem in the chosen metal/electrolyte system. Sources for gas pitting were chemical etching, surface impurities, incomplete wetting and hydrogen evolution at the counter electrode. These gas bubbles lead to non-uniform channel dimensions and an uneven

surface finish. The problem of gas pitting could be overcome by an improved cell design, as well as by sample cleaning and live immersion. Furthermore, two surfactant additives — cetyltrimethylammonium bromide and Triton X-100 — were identified as suitable wetting agents, as they did not lead to a reduction in the magnitude of the limiting-current plateau or to an increase in surface roughness.

Mass-transfer effects were shown to also play an important role. In general, TMEMM experiments were conducted in the presence of shearing flow, either due to natural or forced convection. Either way, a distinct decrease in the etch rate in flow direction — so-called wedging — was observed. This resulted in the establishment of large differences in etch depth, especially along the mask edge. This behaviour stemmed likely from a variation in the thickness of the concentration boundary layer across the exposed metal surface. Modifications to the mask design, such as adding a sacrificial etch band or using a dummy mask, were ineffective in overcoming this problem. As a consequence, it was not possible to fabricate microchannel plate-inlays within acceptable tolerances of a few percent. Accordingly, substantial non-uniformities within the gas-flow distribution were anticipated.

From these observations several conclusions relating to the cell design in TMEMM can be drawn. Cells based on shearing flow, that is flow in parallel to the substrate surface, should be avoided in general. Wedging can presumably be minimised by modifying the flow pattern. Within a flow-channel cell for example, the flow direction may be changed via periodic flow reversal or continuous sample-rotation. In a batch cell, flow-reversal can be achieved via a reciprocating paddle or by moving the substrate itself. In this way, differences in the etch depth along the mask edge can be reduced. However, this will still introduce variations between the centre and the edge of a mask pattern. Another measure may consist in changing the feature spacing or orientation within a pattern. Apart from simple mask designs like line or hole arrays though, this is not feasible, unless the microstructure is compromised with regard to its intended function. For complex designs containing closely packed features at different angles, as is common for microfluidic devices, shearing flow is not able to yield uniform dimensions. Therefore, different modes of agitation need to be considered instead, like impinging flow.

Finally, a Au/Al_2O_3 coating was formed along the channel walls via anodising followed by alternating current (AC) electrodeposition. In this way, catalyst deposits of varying morphology were created by changing either the thickness of the porous-alumina film or the parameters of the deposition process. Most interestingly, finely dispersed gold nanoparticles could be formed within a few seconds, and scale-up to a relevant sample size was successful. On the basis of these preliminary results,

this method appears attractive compared to common catalyst-deposition techniques, such as wash-coating followed by wet impregnation, in particular for the fabrication of aluminium microreactors. The prospect of optimising this method with respect to catalyst loading and activity should be explored in future work.

10.2.5 Wet-chemical etching

TMEMM is often presented as an alternative to photochemical machining (PCM), which relies on wet-chemical etchants for material removal. Therefore, a selection of aluminium wet-etchants was compared with aluminium EP in phosphoric acid for the purpose of micromachining (Chapter 9). The comparison was made on the basis of typical performance criteria, namely: etch rate, surface roughness, undercutting, shape profile and etch uniformity. Thereby, chloride media and chemical etchants based on phosphoric/nitric acid were found to be not suitable for aluminium micromachining for one reason or the other. The observed problems included non-uniform material removal and surface roughening for the former, as well as excessive undercutting in the latter case. In comparison, electrochemical etching in phosphoric acid, while relatively slow, generated smooth and well-defined features. Options for accelerating the machining process include raising the electrolyte temperature and water content, as well as optimising the flow conditions.

10.3 Implications and recommendations

10.3.1 Impinging flow

As was pointed out previously, a different mode of electrolyte agitation is necessary to overcome problems associated with shearing flow. Impinging flow, such as in an impinging jet electrode [409] (Figure 10.1), is proposed as a solution to overcome these problems. This would have several advantages. Firstly, impinging flow should lead to larger etch rates, because it supplies metal-free bulk electrolyte directly to the anode surface. For these reasons, this flow regime is routinely used in the PCM industry within spray-etching machines [156]. By comparing etch rates in chemical immersion and spray etching with one another [65, 367, 405, 406, 410], a tenfold increase in the rate of material removal seems achievable at the least. Secondly, the wedging effect should be less severe, in particular if the electrolyte jet traverses the

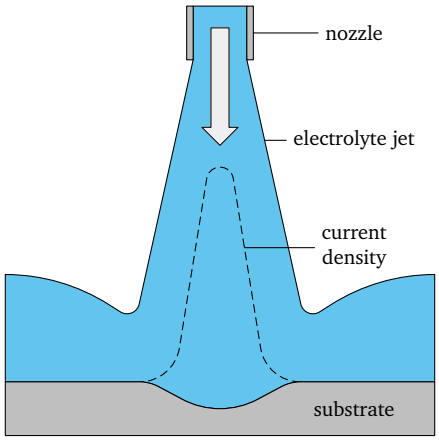

Figure 10.1: Schematic jet contour and current distribution for an impinging jet electrode.

anode surface in a regular pattern. Alternatively, a whole nozzle array may be used as well. Either way, this will result in more uniform and less severe undercutting along the mask edge [10, 168, 309]. Thirdly, any form of gas pitting would presumably be less problematic, as gas bubbles should be easier to displace with an electrolyte jet, even in high-viscosity electrolytes such as phosphoric acid. For these reasons, the use of an impinging jet electrode should be pursued.

10.3.2 Through-foil etching

Another important recommendation concerns the modification of the original microreactor design (Figure 8.1), taking into account the characteristics of the TMEMM process. In this work, microchannel plate-inlays for a plate-type microreactor were machined into the substrate surface via cavity etching. This process is governed by combined perpendicular and lateral material removal. It therefore requires simultaneous control of the depth and width of micrometre-sized features. In contrast, through-foil etching creates features, which vary in width only. This certainly reduces the complexity of the control problem. When switching from cavity to through-foil etching, the original microreactor design would need to be modified towards a stacked-shim assembly, which alternates between feed and channel shims (Figure 10.2) [411]. This would have several advantages. Firstly, the mask artwork could be simplified. For example, large through-holes may be formed by etching the perimeter only [156]. Secondly, monitoring the process would be easier. This is because the current drops sharply once through-holes form, and it decreases as the

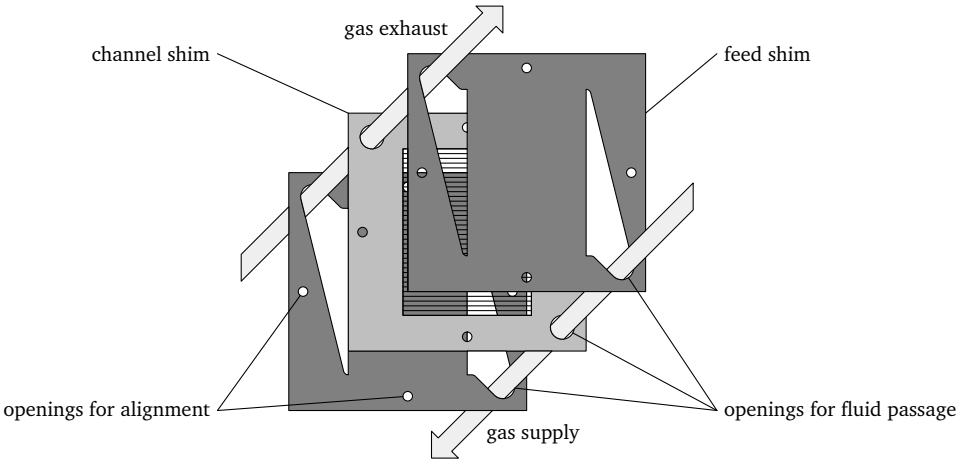

Figure 10.2: Microreactor design in the form of a stacked-shim assembly made from thin metal shims.

area of the exposed metal surface shrinks [240]. Thirdly, two-sided TMEMM would be available, resulting in larger etch factors at constant machining time [6]. This process variant is routinely used in the PCM industry. For this purpose, metal sheets can be laminated with dry-film resist on both sides, which is protected by a thin peel-off coating during the whole process, thus eliminating handling issues [401]. Accurate alignment and registration with a double-sided photo-tool comprising mirror images of the design is then possible in a vacuum printing frame. Note that this reactor design demands forming the catalytic wall coating in the assembled state. For aluminium anodising this has already been shown to be feasible [412]. The same remains to be seen for AC electrodeposition.

10.4 Suggestions for further work

10.4.1 Techno-economic study

At this point, a feasibility study under technical and economic criteria is needed to assess the potential commercial interest in TMEMM. Given the broad range of available micromachining techniques, TMEMM faces strong competition in terms of economic viability. Such a study must therefore identify the major cost components with regard to capital expenditure and operation. Likewise, an analysis of potential environmental impacts is due. In line with similar studies [413, 414], these factors need to be considered as a function of the production volume. Thereby, a suitable

production volume can be identified and compared with other methods. Based on previous research [156, 298], PCM and laser beam machining are likely candidates for such a comparison. To this end, a few technical and financial considerations of TMEMM were already summarised within this work (Section 3.8). However, much of the considered literature is now over twenty years old and thus outdated. Hence, this data can only serve as a starting point for a more detailed and up-to-date study. Ultimately, this techno-economic study would aid the engineer of microfluidic devices to choose the correct micromachining technique for a particular application.

10.4.2 Characterisation of Au/Al_2O_3 catalysts

AC electrodeposition represents a promising method for the deposition of noble-metal catalysts within gas-phase microreactors made from valve metals (Al, Ta, Ti), mainly because it is cheaper, simpler and quicker than other methods in common use (Section 2.2.4). Characterisation studies comparing electrochemically deposited catalysts with deposits formed via other techniques are rare [43]; hence, questions regarding their benefits remain, for instance:

- How do catalyst loading and dispersion vary with the deposition conditions?
- How do variations in deposit morphology affect catalyst activity?
- Where lies the optimum between catalyst loading and activity?

In the specific case of catalytic wall coatings made from Au/Al_2O_3, low-temperature CO oxidation is proposed as a suitable test case [390]. For this purpose, activity studies could be combined with investigations of the deposit morphology [131]. Note that the AC potential and deposition time alone were varied in this work, and preliminary results were gathered only. Based on published work [129], the result of AC electrodeposition also depends on the type and frequency of the AC waveform, as well as on the concentration of the metal salt in solution. All these parameters are important in explaining the structural properties of the deposit. In addition, this work can be extended to include other noble-metal catalysts.

10.4.3 Extension to other materials

The selection of an appropriate construction material for microfluidic devices, such as a gas-phase microreactor, must involve a host of different criteria. Practical

aspects like availability, material cost and workability are as much of importance as a material's electrical, mechanical, thermal and physical properties [6]. The present work focused entirely on aluminium of commercial purity as the substrate material. This does not preclude the use of other engineering metals and alloys in the context of TMEMM of microfluidic devices. Commercially pure aluminium is characterised by relatively poor mechanical properties and a low melting point, which limit its applicability to low-temperature gas-phase reactions. Some of these shortcomings can certainly be improved by applying heat treatments or by adding alloying elements. Nonetheless, other construction materials need to be considered as well. Nickel alloys, stainless steel, tantalum and titanium are all alternatives, which are of particular importance for the construction of microreactors [6]. Within this group of materials, nickel super-alloys, tantalum and titanium are classified as difficult-to-etch [199, 401]. They would, therefore, benefit the most from the application of TMEMM. This creates a strong incentive for future work on TMEMM of microfluidic devices to focus on these materials in particular.

A Conversion between reference electrodes

In this work, the Ag|AgCl reference electrode was used, due to its easy manufacture, non-hazardous components, and long-term stability. The potential of the Ag|AgCl electrode relative to the standard hydrogen electrode (SHE) is listed at relevant temperatures in the last column of Table A.1. The respective calculation steps and assumptions are outlined below and also in more detail elsewhere [415]. Thereby, experiments conducted with different reference electrodes can be compared.

The potential of the Ag|AgCl reference electrode in relation to the SHE at temperature T and chloride activity $a_{\mathrm{Cl}-}$ is described by the Nernst equation [415]:

$$E_{\mathrm{Ag|AgCl}}(T, a_{\mathrm{Cl}-}) = E_{0,\mathrm{Ag|AgCl}}(T) - RT/F \ln(a_{\mathrm{Cl}-}) \tag{A.1}$$

Herein, $E_{0,\mathrm{Ag|AgCl}}(T)$ is the standard potential against the SHE at temperature T, for which empirical equations exist for different temperatures [416, 417]. In this work, the standard potential was calculated from the formula given by Greeley et al. [417] for the temperature range from 25–200 °C, where T is the Kelvin temperature:

$$\begin{aligned} E_{0,\mathrm{Ag|AgCl}}(T) = 0.23755 &- (5.3783 \times 10^{-4})(T - 273.15) \\ &- (2.3728 \times 10^{-6})(T - 273.15)^2 \end{aligned} \tag{A.2}$$

Table A.1: Temperature and concentration correction of the Ag|AgCl reference electrode potential relative to the SHE at a KCl molality of 4.77 mol kg^{-1}. The calculation follows Equations A.1 and A.2, and assumptions outlined in the text.

Temp. (°C)	$E_{0,\mathrm{Ag|AgCl}}(T)$ (V)	$-RT/F \ln(a_{\mathrm{Cl}-})$ (V)	$E_{\mathrm{Ag|AgCl}}(T, a_{\mathrm{Cl}-})$ (V)
25	0.223	−0.026	0.197
50	0.205	−0.029	0.176
75	0.184	−0.031	0.153

All Ag|AgCl reference electrodes were manufactured at room temperature using a saturated solution of KCl. The respective molality could be calculated from solubility data at 25 °C [58] yielding a value of 4.77 mol kg^{-1}. This molality was also assumed at all other temperatures, because all reference electrodes were filled with solids-free solution during manufacture. From mean activity-coefficient data at 25 °C [418] a value of 0.588 was interpolated. By assuming equal values for the activity of chloride and potassium ions, the corresponding chloride activity was calculated as 2.81 mol kg^{-1}. Due to the lack of data in the desired molality and temperature range, changes in the activity coefficient with temperature were neglected, and the value at 25 °C was also used at 50 and 75 °C. Note that variations in the activity coefficient of ±10 % result in a change in potential of less than 5 mV. In the present work, this difference was negligible; hence, this simplification seemed justified.

B Mass transfer to a recessed disc electrode

A recessed rotating disc electrode (RDE) was used for shape-evolution experiments under mass-transfer control (Chapter 7). Before commencing with this work, it was necessary to confirm that, despite the recess, the electrode surface was still uniformly accessible to mass transfer. Prior work [419] shows that the recessed RDE largely adheres to the theory outlined in Section 2.3. However, with increasing recess depth, the magnitude and uniformity of the limiting current density decrease. For this reason, mass transfer in the Fe^{2+}/Fe^{3+} redox system was studied on a gold RDE, with and without a recess. Linear and cyclic potential sweeps, and electrochemical impedance spectroscopy (EIS) were performed in order to determine the diffusion coefficients of the Fe^{2+} and Fe^{3+} ion for comparison with literature data.

Before each experiment, the gold RDE with a geometric surface area of $1/16\pi\,\mathrm{cm}^2$ (AFE2M050AU, PINE Research Instrumentation) was mechanically polished with 0.05 µm alumina slurry on a velvet cloth for 5 min, rinsed with de-ionised (DI) water, and subsequently ultrasonicated in a 1:1 (v/v) mixture of isopropyl alcohol and DI water for 5 min. Before and after a set of experiments, the electrode was cleaned electrochemically by applying a constant potential of −0.3 V vs. Ag|AgCl for 30 s, followed by cycling the potential fifty times between −0.3 and 1.7 V in de-aerated 0.5 M H_2SO_4. When not in use, it was covered with a plastic cap to prevent the settling of dust on the surface. The reproducibility of the electrode surface area was checked by calculating the area of the gold-oxide reduction peak at approximately 0.9 V, corrected for the baseline (Figure B.1). The area-specific charge used for gold-oxide reduction was found to range between 815 and 915 $\mu\mathrm{C\,cm}^{-2}$, corresponding to a roughness factor of 2.1–2.4. This estimate was based on the assumption that the reduction charge for a gold-oxide monolayer equals $386\,\mu\mathrm{C\,cm}^{-2}$ [420].

All experiments were conducted at $(25.0 \pm 0.6)\,^\circ\mathrm{C}$ with the equipment previously described in Chapter 5. The RDE with an outer diameter of 12 mm was either used as is, or fitted with a polytetrafluoroethylene (PTFE) adapter and cap to create a 1 mm deep and 13 mm wide recess (Figure B.2). A 4 cm^2 platinum foil connected to a platinum wire served as the counter electrode. All potentials are reported against a Ag|AgCl electrode connected to a Luggin capillary. The 2 mm wide capillary was

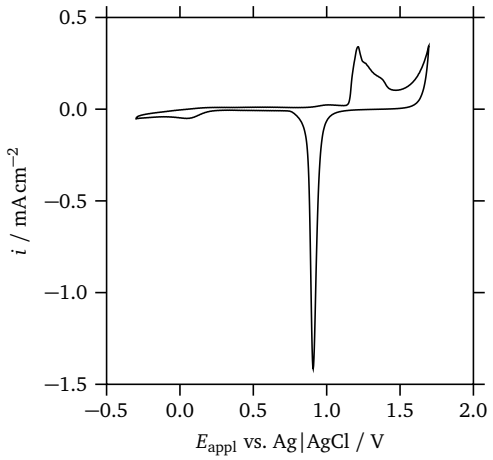

Figure B.1: Typical cyclic voltammogram of a clean gold RDE after 50 cycles recorded at a scan rate of 0.1 V s^{-1} in 0.5 M H_2SO_4 between −0.3 and 1.7 V (not corrected for the ohmic drop).

held concentrically underneath the RDE at a distance of 12 mm. Experiments were conducted in 0.5 M H_2SO_4 (analytical grade, Thermo Fisher Scientific), which also contained 5 mM $(NH_4)Fe(SO_4)_2 \cdot 12\,H_2O$ (ACS grade, Sigma-Aldrich) and $FeSO_4 \cdot 7\,H_2O$ (analytical grade, VWR) each. Beforehand, the electrolyte was de-aereated for 30 min by bubbling Argon (≥ 99.999 %, BOC) through the solution. During an experiment the bubbler was re-positioned near the electrolyte surface.

Linear potential sweeps were conducted at ten different rotation rates, ranging from 100–1000 rpm in increments of 100 rpm. The potential was swept from 1.1 to −0.3 V at a sweep rate of 5 mV s^{-1}. Before each sweep, the anode was held at 1.1 V for 30 s. Cyclic potential sweeps were performed at four different scan rates of 0.1, 0.2, 0.5 and 1.0 V s^{-1} without agitation. The potential was cycled between 0 and 1 V ten times. Prior, the anode was conditioned at 0 V for 30 s. The electrolyte resistance was determined via EIS before and after each series of experiments. EIS was conducted in an unstirred solution at a potential of 0.5 V with a potential modulation of 5 mV rms^{-1}. The potential was modulated in the high-frequency range from 1 MHz to 10 kHz, as only the uncompensated electrolyte resistance was sought. Ten data points per decade were recorded. Prior to the impedance measurement, the electrode was conditioned at 0.5 V for 30 s.

Firstly, the solution resistance (R_s) was determined from the intercept of the impedance data with the real axis in a Nyquist plot. The measured values for R_s ranged between 0.89 and 1.2 Ω cm^2. Using conductivity data ($\kappa = 0.2092$ S cm^{-1}) [421] for 0.5 M H_2SO_4, the resistance could be calculated for the case of a primary current

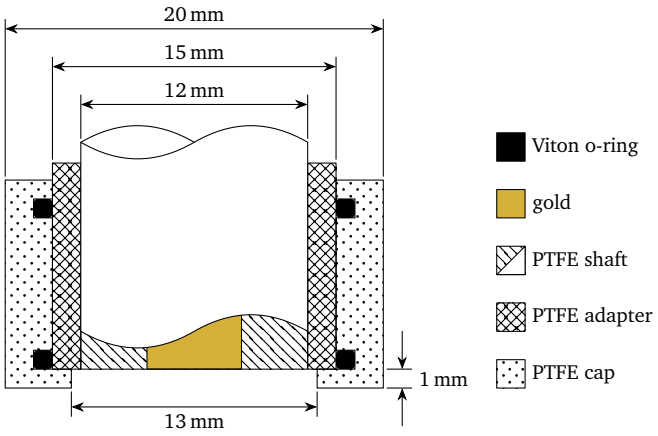

Figure B.2: Cross-sectional drawing of the recessed gold RDE fitted with the PTFE adapter and cap.

distribution by applying the formulae given by Newman [352]. This yielded values of 0.82 and 0.94 $\Omega\,\mathrm{cm}^2$ for the described position of the Luggin capillary and with the reference electrode at virtual infinity, respectively. The small discrepancy between these values can be readily explained by additional resistances in series with the measurement cell. Given that the current density was on the order of a few milliamperes per square centimetre in subsequent measurements, the error due to the ohmic drop was expected to be smaller than 10 mV. Accordingly, only the cyclic voltammetry data was corrected post-run for the ohmic drop.

Secondly, the reproducibility of the procedure for electrode preparation and cleaning was verified by way of extracting quantitative data from the cyclic potential sweeps (Figure B.3). The half-wave potential, peak-potential separation and the anodic and cathodic peak current density were determined for this purpose [132] (Table B.1). The presence of the PTFE cap and adapter had no influence on these results, and the data was thus lumped together according to the sweep rate. As an indicator of sufficient cleanliness, only experiments exhibiting a peak-potential separation of about 70 mV or smaller at $0.1\,\mathrm{V\,s}^{-1}$, and peak current densities larger than $5\,\mathrm{mA\,cm}^{-2}$ at $1.0\,\mathrm{V\,s}^{-1}$ were analysed. In this manner, reproducible mass-transfer-limited current plateaus were measured during the linear potential sweeps.

Lastly, the linear potential sweeps (Figure B.3) were analysed via Equation 2.4 ($z_\mathrm{e} = 1$, $\nu = 9.8 \times 10^{-3}\,\mathrm{cm}^2\,\mathrm{s}^{-1}$ [422], $c = 5 \times 10^{-3}\,\mathrm{mol\,cm}^{-3}$) to compute the diffusion-coefficient data. To this end, the limiting current density was extracted from the anodic and cathodic current plateaus at potentials from −0.3 to 0.2 V and from 0.8 to 1.1 V in increments of 0.1 V. Thereby, the diffusion coefficient of the ferrous ion

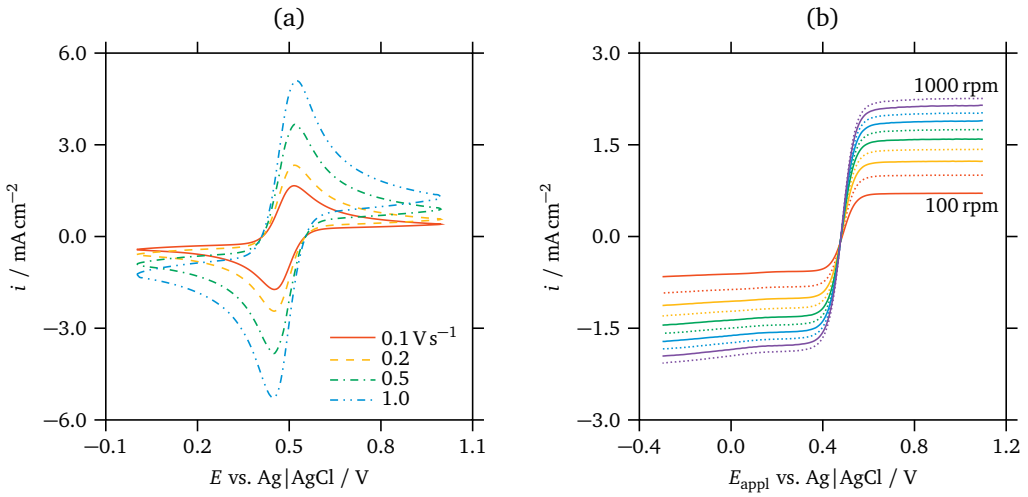

Figure B.3: Data from (a) cyclic potential sweeps at different scan rates and (b) linear potential sweeps measured at a scan rate of 5 mV s^{-1} and different rotation rates for the redox couple Fe^{2+}/Fe^{3+} at a concentration of 5 mM each in 0.5 M H_2SO_4 at 25 °C.

$D_{Fe^{2+}}$ was found to be approximately constant, whereas the coefficient of the ferric ion $D_{Fe^{3+}}$ depended linearly on potential between −0.3 and 0.2 V. A possible explanation for the observed potential dependence is the presence of another cathodic process in this potential range in parallel with the reduction of Fe^{3+}.

Despite this phenomenon, the data fell in the correct order of magnitude compared to literature values and adhered to $D_{Fe^{2+}} > D_{Fe^{3+}}$ (Table B.2). The agreement was best with the values presented by Tobias et al. [423] and Angell et al. [424]. By

Table B.1: Average values and standard deviations for the half-wave potential, the peak-potential separation, as well as the anodic and cathodic peak current densities, which were extracted from the cyclic potential sweeps. The standard deviation was calculated from ten separate experiments at each sweep rate.

Sweep rate ($V\,s^{-1}$)	Half-wave potential vs. Ag|AgCl (mV)	Peak-potential separation (mV)	Anodic peak current density ($mA\,cm^{-2}$)	Cathodic peak current density ($mA\,cm^{-2}$)
0.1	483 ± 1	65 ± 2	1.91 ± 0.08	1.99 ± 0.05
0.2	483 ± 1	68 ± 3	2.7 ± 0.1	2.82 ± 0.08
0.5	484 ± 1	74 ± 6	4.1 ± 0.2	4.3 ± 0.1
1.0	485 ± 2	77 ± 5	5.7 ± 0.2	5.9 ± 0.1

Table B.2: Summary of diffusion-coefficient data for the Fe^{2+} and Fe^{3+} ions in sulphuric acid. Also given is the electrolyte concentration, as well as the type and material of the working electrode. The standard deviation for both ions was calculated from a set of five experiments each.

Material	Electrode	$c_{H_2SO_4}$ ($mol\,cm^{-3}$)	$10^6 \times D_{Fe^{2+}}$ ($cm^2\,s^{-1}$)	$10^6 \times D_{Fe^{3+}}$ ($cm^2\,s^{-1}$)	Ref.
Fe	RDE	0.5	–	5.2	[423]
Au	RDE	0.5	6.1	5.5	[424]
Pt	RDE	1.0	5.0	4.8	[425]
Pt	RCE	0.5	3.9	3.3	[426]
Au	RDE	0.5	6.16 ± 0.06	5.2 ± 0.3	*
Au	recessed RDE	0.5	6.07 ± 0.06	5.2 ± 0.4	*

* this work

comparison, the data of Benari et al. [425] are slightly lower due to more concentrated sulphuric acid being used. The study of Morrison et al. [426] was performed with a rotating cylinder electrode (RCE), which may explain the larger deviation from the present data. Critically, the measured diffusion coefficients were the same irrespective of the presence of the PTFE cap and adapter, when taking into account the computed standard deviation. Thus, the conditions of mass transfer appeared to be unaffected by the recess used within this work.

C Apparent valence of aluminium dissolution

In order to determine the apparent valence of dissolution of aluminium, samples 5.2 mm in diameter were dissolved at 75 °C in 85 % phosphoric acid for a cumulative charge of 100 C. Measurements were conducted in triplicate at two applied potentials, 1.4 and 5.4 V, at a rotation rate of 2500 rpm. Samples were weighted ten times each, before and after etching, to determine the contribution of the random error of the balance (Mettler Toledo, readability of 0.1 mg). A more in-depth description of the experimental setup can be found in Chapter 5.

The apparent valence of aluminium dissolution in concentrated phosphoric acid was calculated using Faraday's law, assuming a current efficiency of 100 % and a molecular weight of 26.98 g mol^{-1} for aluminium. The results together with the respective standard deviation are listed in Table C.1. They compare reasonably well with results obtained by Vidal and West [44] for high-purity aluminium.

Table C.1: Results of weight-loss experiments used to determine the mean value and the standard deviation of the apparent valence of dissolution of aluminium. All potentials are given relative to the SHE.

Purity (%)	Temp. (°C)	E_{appl} vs. SHE (V)	Weight loss (mg)	Charge (C)	Valence	Ref.
99.0	75	1.25	9.6 ± 0.2	100.0	2.92 ± 0.06	*
99.0	75	5.25	9.5 ± 0.2	100.0	2.93 ± 0.06	*
99.999	65	1.79	9.78	100.00	2.86	[44]
99.999	65	5.79	10.23	100.02	2.73	[44]

* this work

D Technical drawings

The following pages contain the manufacturing drawings for the two experimental setups described in Section 4.1. Therein, all dimensions are given in millimetres. The first two drawings relate to the RDE setup, while the other four drawings describe the parts for the plate-electrode setup. A summary of these drawings is given below:

- Drawing No. 1: 100 mL glass cell for RDE experiments
- Drawing No. 2: RDE adapter assembly for exchangeable disc samples
- Drawing No. 3: 1000 mL glass cell with water jacket
- Drawing No. 4: Polypropylene cell lid for 1000 mL glass cell
- Drawing No. 5: Glass sleeve (for the counter electrode) and Luggin capillary
- Drawing No. 6: PTFE sample holder and frame for plate samples

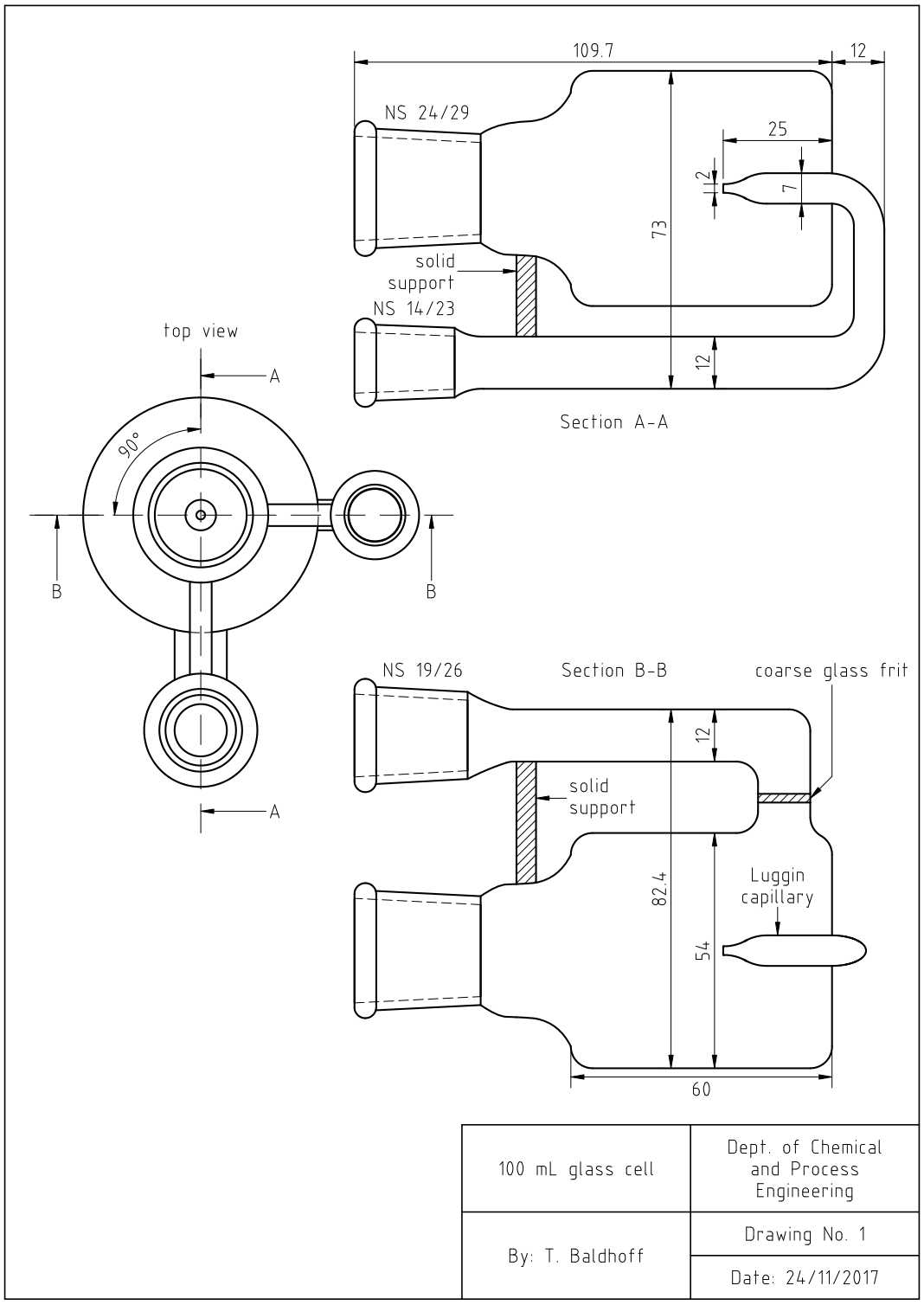
109.7
12
NS 24/29
25
2
7
73
solid
support
NS 14/23
12
Section A-A
top view
A
90°
B
B
A
NS 19/26
Section B-B
coarse glass frit
12
solid
support
82.4
Luggin
capillary
54
60
100 mL glass cell
Dept. of Chemical and Process Engineering
By: T. Baldhoff
Drawing No. 1
Date: 24/11/2017

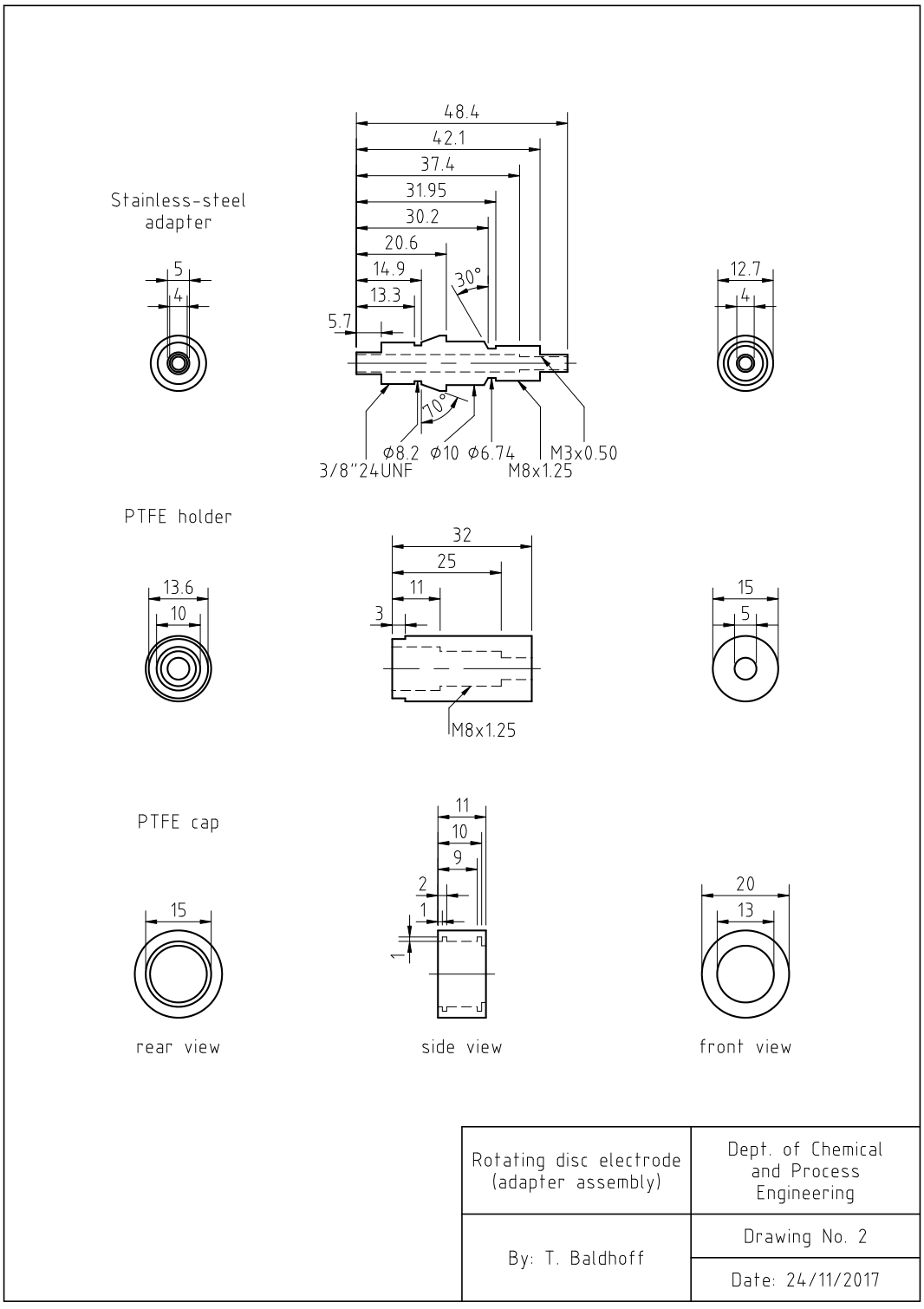
Stainless-steel adapter
48.4
42.1
37.4
31.95
30.2
20.6
14.9
13.3
5.7
30°
70°
5
4
12.7
4
ϕ8.2
ϕ10
ϕ6.74
M3x0.50
3/8"24UNF
M8x1.25
PTFE holder
32
25
11
3
13.6
10
15
5
M8x1.25
PTFE cap
11
10
9
2
1
1
15
20
13
rear view
side view
front view
Rotating disc electrode (adapter assembly)
Dept. of Chemical and Process Engineering
By: T. Baldhoff
Drawing No. 2
Date: 24/11/2017

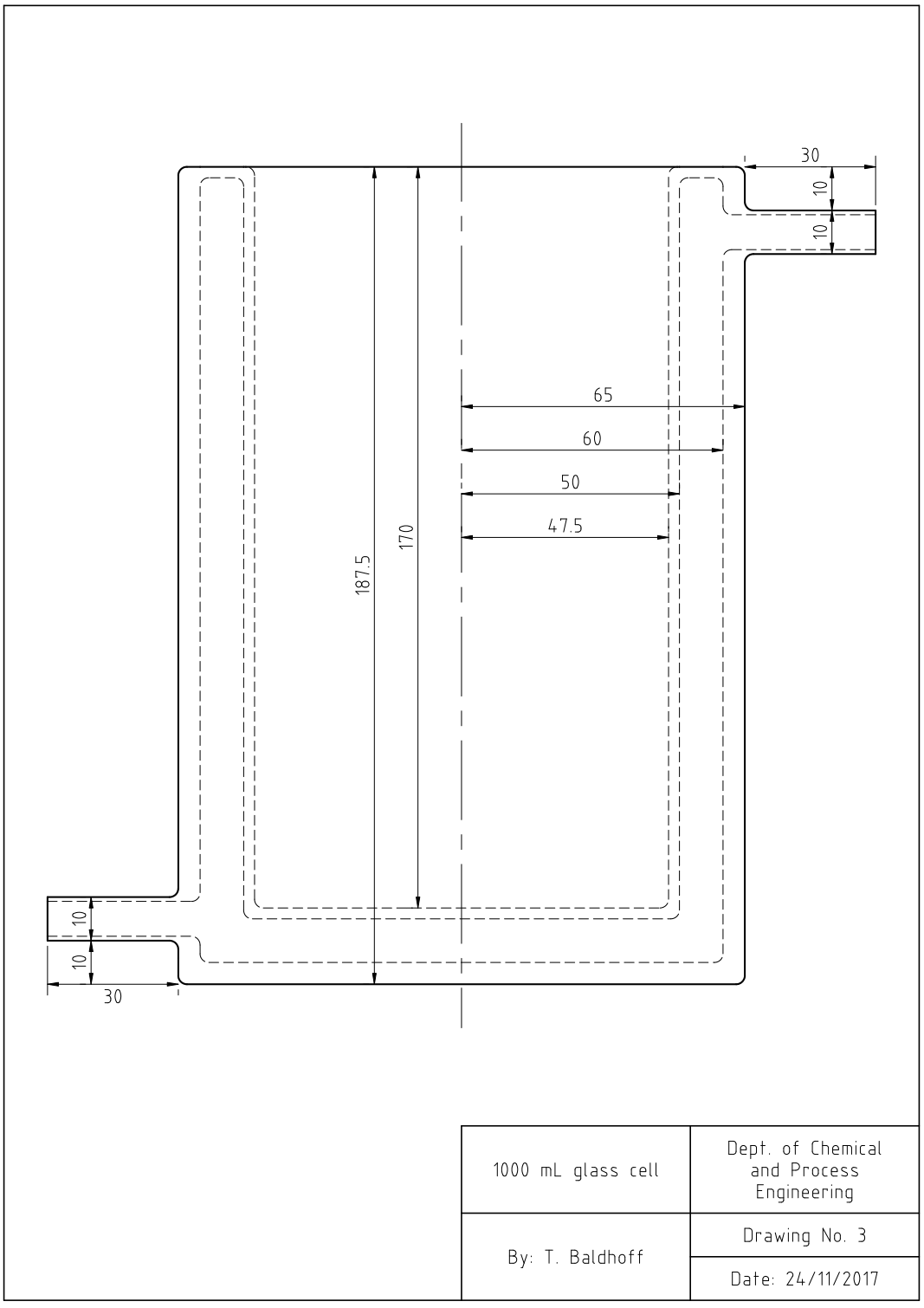

1000 mL glass cell	Dept. of Chemical and Process Engineering
By: T. Baldhoff	Drawing No. 3
	Date: 24/11/2017

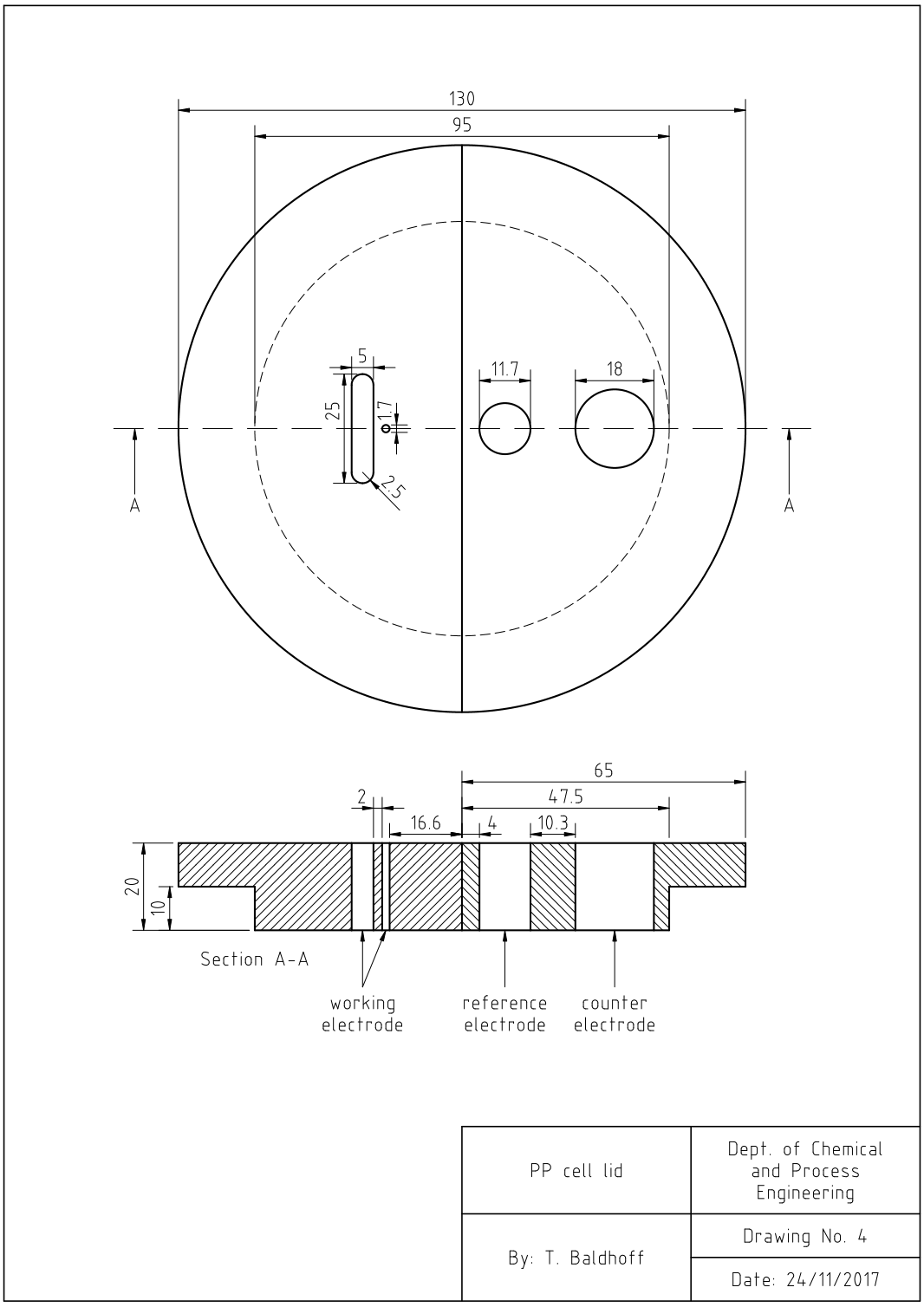

PP cell lid	Dept. of Chemical and Process Engineering
By: T. Baldhoff	Drawing No. 4
	Date: 24/11/2017

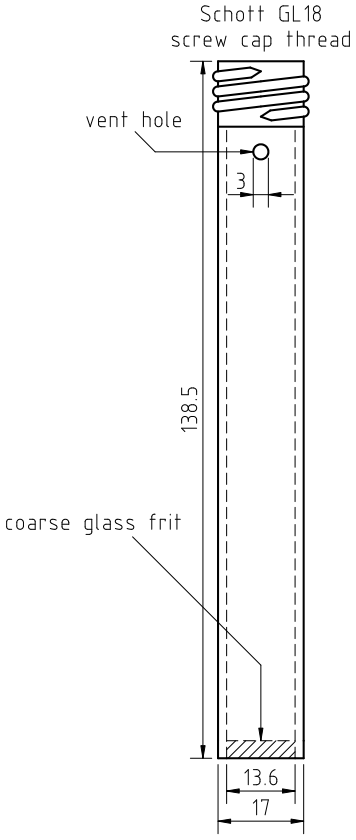

Glass sleeve

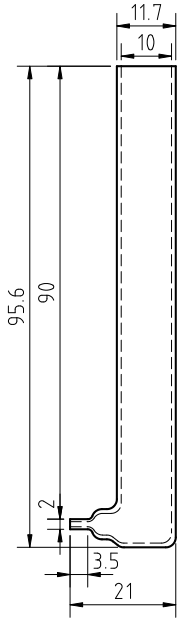

Luggin capillary

Glass sleeve and Luggin capillary	Dept. of Chemical and Process Engineering
By: T. Baldhoff	Drawing No. 5
	Date: 24/11/2017

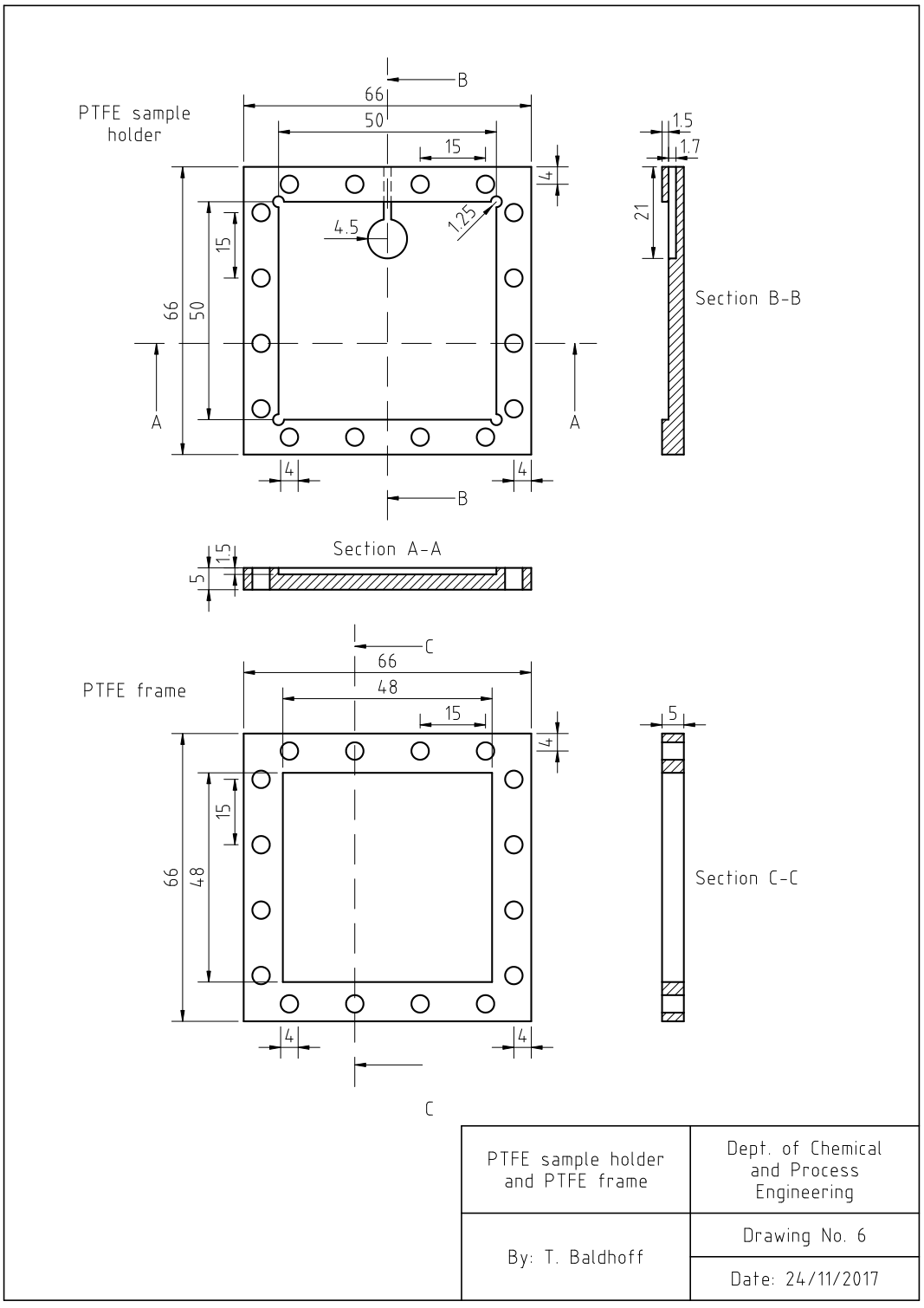
PTFE sample holder
B
66
50
15
4
4.5
1.25
15
66
50
A
A
4
4
B
1.5
1.7
21
Section B-B
Section A-A
1.5
5
C
PTFE frame
66
48
15
4
15
66
48
4
4
C
5
Section C-C
PTFE sample holder and PTFE frame
Dept. of Chemical and Process Engineering
By: T. Baldhoff
Drawing No. 6
Date: 24/11/2017

Bibliography

(1) Kolb, G. Review: Microstructured reactors for distributed and renewable production of fuels and electrical energy. *Chem. Eng. Process.* **2013**, *65*, 1–44.

(2) Ehrfeld, W.; Hessel, V.; Löwe, H. *Microreactors: New Technology for Modern Chemistry*; Wiley-VCH: Weinheim, Germany, 2000.

(3) Holladay, J. D.; Wang, Y.; Jones, E. Review of Developments in Portable Hydrogen Production Using Microreactor Technology. *Chem. Rev.* **2004**, *104*, 4767–4790.

(4) Kolb, G.; Hessel, V. Micro-structured reactors for gas phase reactions. *Chem. Eng. J.* **2004**, *98*, 1–38.

(5) Kockmann, N. *Transport Phenomena in Micro Process Engineering*; Heat and Mass Transfer; Springer: Berlin, 2008.

(6) *Microchemical Engineering in Practice*; Dietrich, T. R., Ed.; Wiley: Hoboken, NJ, 2009.

(7) Wegeng, R. S.; Call, C. J.; Drost, M. K. Chemical System Miniaturization. Presented at the 1996 Spring National Meeting of the AIChE, New Orleans, LA, 25th–29th Feb. 1996; Paper PNNL-SA-27317.

(8) Crämer, K.; Fürstenau, F.; Meyer, H. Mass Production of Microreactors on the Basis of Printed Circuit Board Technology and Electrochemistry. In *Proceedings / MICRO.tec 2000 : Applications, Trends, Visions / VDE World Microtechnologies Congress*, Hannover, Germany, 25th Sept. 2000–27th Sept. 2000; VDE Verlag: Berlin, 2000; Vol. 2, pp 775–777.

(9) Datta, M. Electrochemical Micromachining: the opportunities and challenges of through-mask electrochemical micromachining. *Electrochem. Soc. Interface* **1995**, *4*, 32–35.

(10) Datta, M.; Harris, D. Electrochemical micromachining: An environmentally friendly, high speed processing technology. *Electrochim. Acta* **1997**, *42*, 3007–3013.

(11) Madore, C.; Landolt, D. Electrochemical micromachining of controlled topographies on titanium for biological applications. *J. Micromech. Microeng.* **1997**, *7*, 270–275.

(12) Kusakabe, K.; Takahashi, M.; Maeda, H.; Morooka, S. Preparation of Thin Palladium Membranes by a Novel Method Based on Photolithography and Electrolysis. *J. Chem. Eng. Jpn.* **2001**, *34*, 703–705.

(13) McCrabb, H.; Lozano-Morales, A.; Snyder, S.; Gebhart, L.; Taylor, E. J. Through Mask Electrochemical Machining. *ECS Trans.* **2009**, *19*, 19–33.

(14) McCrabb, H.; Taylor, E. J.; Lozano-Morales, A.; Shimpalee, S.; Inman, M.; Van Zee, J. W. Through-Mask Electro-etching for Fabrication of Metal Bipolar Plate Gas Flow Field Channels. *ECS Trans.* **2010**, *33*, 991–1006.

(15) Shimpalee, S.; Lilavivat, V.; Van Zee, J. W.; McCrabb, H.; Lozano-Morales, A. Understanding the effect of channel tolerances on performance of PEMFCs. *Int. J. Hydrogen Energy* **2011**, *36*, 12512–12523.

(16) Madore, C.; Piotrowski, O.; Landolt, D. Through-Mask Electrochemical Micromachining of Titanium. *J. Electrochem. Soc.* **1999**, *146*, 2526–2532.

(17) Mineta, T. Basic characteristics of an electrochemical etching of Ni-Fe containing corrosion resistant alloys. *Sens. Actuators, A* **2004**, *114*, 536–542.

(18) Kikuchi, T.; Wachi, Y.; Sakairi, M.; Suzuki, R. O. Aluminum bulk micromachining through an anodic oxide mask by electrochemical etching in an acetic acid/perchloric acid solution. *Microelectron. Eng.* **2013**, *111*, 14–20.

(19) Allen, D. M. Electrolytic photoetching and its applications. In *Proceedings of the Technical Program, National Electronic Packaging and Production Conference (NEPCON West '87)*, Anaheim, CA, 24th Feb. 1987–26th Feb. 1987; Cahners Exposition Group: Des Plaines, IL, 1987; Vol. 2, pp 583–589.

(20) Shenoy, R. V.; Datta, M.; Romankiw, L. T. Investigation of Island Formation during Through-Mask Electrochemical Micromachining. *J. Electrochem. Soc.* **1996**, *143*, 2305–2309.

(21) Landolt, D.; Chauvy, P.-F.; Zinger, O. Electrochemical micromachining, polishing and surface structuring of metals: fundamental aspects and new developments. *Electrochim. Acta* **2003**, *48*, 3185–3201.

(22) Landolt, D. The role of surface films in electrochemical machining. In *International Symposium on ElectroChemical Machining Technology INSECT 2009: Proceedings*, Dresden, Germany, 26th Nov. 2009–27th Nov. 2009; Michaelis, A., Schneider, M., Eds.; Fraunhofer Verlag: Stuttgart, Germany, 2009; Vol. 1, pp 9–14.

(23) Raffelstetter, P.; Mollay, B.; Van den Bossche, B.; Nauer, G. E. Modeling Strategy for Predicting Current Density Distributions on PCBs and Other Complex Patterned Substrates. *J. Electrochem. Soc.* **2009**, *156*, D51–D57.

(24) Raffelstetter, P.; Mollay, B. On the modeling of shape evolution in through-mask electrochemical micromachining of complex patterned substrates. *Electrochim. Acta* **2010**, *55*, 2149–2157.

(25) Liauw, M. A.; Baerns, M.; Broucek, R.; Buyevskaya, O. V.; Commenge, J.-M.; Corriou, J.-P.; Falk, L.; Gebauer, K.; Hefter, H. J.; Langer, O.-U.; Löwe, H.; Matlosz, M.; Renken, A.; Rouge, A.; Schenk, R.; Steinfeldt, N.; Walter, S. Periodic Operation in Microchannel Reactors. In *Microreaction Technology: Industrial Prospects, IMRET 3: Proceedings of the Third International Conference on Microreaction Technology*, Frankfurt a. M., Germany, 18th Apr. 1999–21st Apr. 1999; Ehrfeld, W., Ed.; Springer: Berlin, 2000; pp 224–234.

(26) Ganley, J. C.; Seebauer, E. G.; Masel, R. I. Porous Anodic Alumina Microreactors for Production of Hydrogen from Ammonia. *AIChE J.* **2004**, *50*, 829–834.

(27) Ganley, J. C.; Seebauer, E. G.; Masel, R. I. Development of a microreactor for the production of hydrogen from ammonia. *J. Power Sources* **2004**, *137*, 53–61.

(28) Zech, T.; Hönicke, D.; Lohf, A.; Golbig, K.; Richter, T. Simultaneous Screening of Catalysts in Microchannels: Methodology and Experimental Setup. In *Microreaction Technology: Industrial Prospects, IMRET 3: Proceedings of the Third International Conference on Microreaction Technology*, Frankfurt a. M., Germany, 18th Apr. 1999–21st Apr. 1999; Ehrfeld, W., Ed.; Springer: Berlin, 2000; pp 260–276.

(29) Rebrov, E. V.; de Croon, M. H. J. M.; Schouten, J. C. Design of a microstructured reactor with integrated heat-exchanger for optimum performance of a highly exothermic reaction. *Catal. Today* **2001**, *69*, 183–192.

(30) Rebrov, E. V.; Duinkerke, S. A.; de Croon, M. H. J. M.; Schouten, J. C. Optimization of heat transfer characteristics, flow distribution, and reaction processing for a microstructured reactor/heat-exchanger for optimal performance in platinum catalyzed ammonia oxidation. *Chem. Eng. J.* **2003**, *93*, 201–216.

(31) Kursawe, A.; Dietzsch, E.; Kah, S.; Hönicke, D.; Fichtner, M.; Schubert, K.; Wießmeier, G. Selective Reactions in Microchannel Reactors. In *Microreaction Technology: Industrial Prospects, IMRET 3: Proceedings of the Third International Conference on Microreaction Technology*, Frankfurt a. M., Germany, 18th Apr. 1999–21st Apr. 1999; Ehrfeld, W., Ed.; Springer: Berlin, 2000; pp 213–223.

(32) Kiwi-Minsker, L.; Ruta, M.; Eslanloo-Pereira, T.; Bromley, B. Structured catalytic wall microreactor for efficient performance of exothermic reactions. *Chem. Eng. Process.* **2010**, *49*, 973–978.

(33) Sánchez, J. F.; Boldrini, D. E.; Tonetto, G. M.; Damiani, D. E. Palladium catalyst on anodized aluminum monoliths for the partial hydrogenation of vegetable oil. *Chem. Eng. J.* **2011**, *167*, 355–361.

(34) Pfeifer, P.; Schubert, K.; Liauw, M. A.; Emig, G. Electrically Heated Microreactors for Methanol Steam Reforming. *Chem. Eng. Res. Des.* **2003**, *81*, 711–720.

(35) Properties of Wrought Aluminum and Aluminum Alloys. In *ASM Handbook*, 10th ed.; ASM International: Materials Park, OH, 1990; Vol. 2, pp 62–122.

(36) Lossin, A. Copper. In *Ullmann's Encyclopedia of Industrial Chemistry*, Electronic Release; Wiley-VCH: Weinheim, Germany, 2001.

(37) Kerfoot, D. G. E. Nickel. In *Ullmann's Encyclopedia of Industrial Chemistry*, Electronic Release; Wiley-VCH: Weinheim, Germany, 2000.

(38) Wrought Stainless Steels. In *ASM Handbook*, 10th ed.; ASM International: Materials Park, OH, 1990; Vol. 1, pp 841–907.

(39) Albrecht, S.; Cymorek, C.; Andersson, K.; Reichert, K.; Wolf, R. Tantalum and Tantalum Compounds. In *Ullmann's Encyclopedia of Industrial Chemistry*, Electronic Release; Wiley-VCH: Weinheim, Germany, 2011.

(40) Sibum, H.; Güther, V.; Roidl, O.; Habashi, F.; Wolf, H. U.; Siemers, C. Titanium, Titanium Alloys, and Titanium Compounds. In *Ullmann's Encyclopedia of Industrial Chemistry*, Electronic Release; Wiley-VCH: Weinheim, Germany, 2017.

(41) US Geological Survey Online Publications Directory. https://pubs.usgs.gov/sir/2012/5188/tables/ (accessed 27th July 2017).

(42) Wießmeier, G.; Hönicke, D. Microfabricated components for heterogeneously catalysed reactions. *J. Micromech. Microeng.* **1996**, *6*, 285–289.

(43) Födisch, R.; Hönicke, D.; Xu, Y.; Platzer, B. Liquid phase hydrogenation of p-nitrotoluene in microchannel reactors. In *Microreaction Technology, IMRET 5: Proceedings of the Fifth International Conference on Microreaction Technology*, Strasbourg, France, 27th May 2001–30th May 2001; Matlosz, M., Ehrfeld, W., Baselt, J. P., Eds.; Springer: Berlin, 2001; pp 470–478.

(44) Vidal, R.; West, A. C. Aluminum and Aluminum Alloy Dissolution in Concentrated Phosphoric Acid. *J. Electrochem. Soc.* **1998**, *145*, 4067–4073.

(45) Wernick, S.; Pinner, R. *The Surface Treatment and Finishing of Aluminium and its Alloys*, 4th ed.; Robert Draper: Teddington, UK, 1972.

(46) Tegart, W. J. M. *The Electrolytic and Chemical Polishing of Metals in Research and Industry*; Pergamon Press: London, 1956.

(47) Datta, M. Anodic dissolution of metals at high rates. *IBM J. Res. Dev.* **1993**, *37*, 207–226.

(48) McGeough, J. A. *Principles of Electrochemical Machining*; Chapman and Hall: London, 1974.

(49) Bannard, J. Electrochemical machining. *J. Appl. Electrochem.* **1977**, *7*, 1–29.

(50) Hoar, T. P. The production and breakdown of the passivity of metals. *Corros. Sci.* **1967**, *7*, 341–355.

(51) Landolt, D. *Corrosion and Surface Chemistry of Metals*; CRC Press: Boca Raton, FL, 2007.

(52) Diggle, J. W.; Downie, T. C.; Goulding, C. W. Anodic oxide films on aluminum. *Chem. Rev.* **1969**, *69*, 365–405.

(53) Aladjem, A. Anodic oxidation of titanium and its alloys. *J. Mater. Sci.* **1973**, *8*, 688–704.

(54) Landolt, D. Fundamental aspects of electropolishing. *Electrochim. Acta* **1987**, *32*, 1–11.

(55) Wilson, J. F. *Practice and Theory of Electrochemical Machining*; Wiley-Interscience: New York, 1971.

(56) Pourbaix, M. *Atlas of Electrochemical Equilibria*; Pergamon Press: Oxford, UK, 1966; pp 168–176.

(57) *Perry's Chemical Engineers' Handbook*, 8th ed.; Perry, R. H., Green, D. W., Eds.; McGraw-Hill: New York, 2008.

(58) *CRC Handbook of Chemistry and Physics*, 91st ed.; Haynes, W. M., Ed.; CRC Press: Boca Raton, FL, 2010.

(59) *Corrosion Mechanisms in Theory and Practice*, 3rd ed.; Marcus, P., Ed.; CRC Press: Boca Raton, FL, 2012; p 274.

(60) *CRC Materials Science and Engineering Handbook*, 3rd ed.; Shackelford, J. F., Alexander, W., Eds.; CRC Press: Boca Raton, FL, 2001; p 959.

(61) Lohrengel, M. M. Thin anodic oxide layers on aluminium and other valve metals: high field regime. *Mater. Sci. Eng., R* **1993**, *11*, 243–294.

(62) Gerlagh, G.; Baeyens, P. A New Etchant for Photochemical Milling of Aluminium. *Trans. Inst. Met. Finish.* **1975**, *53*, 133–137.

(63) Chattergee, B.; Thomas, R. W. Chemical Etching of Aluminium in Caustic Soda Solutions. *Trans. Inst. Met. Finish.* **1976**, *54*, 17–24.

(64) Lenderink, H. J. W.; Linden, M. V. D.; De Wit, J. H. W. Corrosion of aluminium in acidic and neutral solutions. *Electrochim. Acta* **1993**, *38*, 1989–1992.

(65) Visser, A.; Junker, M. Sprühätzen von Aluminium: Vergleich zwischen sauren und alkalischen Ätzmedien unter Hochdruck-/Hochtemperatur-Bedingungen. *Galvanotechnik* **1993**, *84*, 1531–1540.

(66) Dražić, D. M.; Zečević, S. K.; Atanasoski, R. T.; Despić, A. R. The effect of anions on the electrochemical behaviour of aluminium. *Electrochim. Acta* **1983**, *28*, 751–755.

(67) Frers, S. E.; Stefenel, M. M.; Mayer, C.; Chierchie, T. AC-Impedance measurements on aluminium in chloride containing solutions and below the pitting potential. *J. Appl. Electrochem.* **1990**, *20*, 996–999.

(68) Bessone, J. B.; Salinas, D. R.; Mayer, C. E.; Ebert, M.; Lorenz, W. J. An EIS study of aluminium barrier-type oxide films formed in different media. *Electrochim. Acta* **1992**, *37*, 2283–2290.

(69) Hunter, M. S.; Fowle, P. Natural and Thermally Formed Oxide Films on Aluminum. *J. Electrochem. Soc.* **1956**, *103*, 482–485.

(70) Thompson, G. E. Porous anodic alumina: fabrication, characterization and applications. *Thin Solid Films* **1997**, *297*, 192–201.

(71) Lee, W.; Park, S.-J. Porous Anodic Aluminum Oxide: Anodization and Templated Synthesis of Functional Nanostructures. *Chem. Rev.* **2014**, *114*, 7487–7556.

(72) Zhang, Q.; Xu, J.; Fan, F.; Sun, D.; Xu, G.; Zhang, S.; Zhu, Z. Application of porous anodic alumina monolith catalyst in steam reforming of dimethyl ether: Cu/γ-Al_2O_3/Al catalyst degradation behaviors and catalytic activity improvement by pre-competition impregnation method. *Fuel Process. Technol.* **2014**, *119*, 52–59.

(73) Sulka, G. D. Highly Ordered Anodic Porous Alumina Formation by Self-Organized Anodizing. In *Nanostructured Materials in Electrochemistry*; Eftekhari, A., Ed.; Wiley-VCH: Weinheim, Germany, 2008; pp 1–116.

(74) Kikuchi, T.; Nakajima, D.; Nishinaga, O.; Natsui, S.; Suzuki, R. O. Porous Aluminum Oxide Formed by Anodizing in Various Electrolyte Species. *Curr. Nanosci.* **2015**, *11*, 560–571.

(75) Burgos, N.; Paulis, M.; Montes, M. Preparation of Al_2O_3/Al monoliths by anodisation of aluminium as structured catalytic supports. *J. Mater. Chem.* **2003**, *13*, 1458–1467.

(76) Sanz, O.; Echave, F. J.; Odriozola, J. A.; Montes, M. Aluminum Anodization in Oxalic Acid: Controlling the Texture of Al_2O_3/Al Monoliths for Catalytic Aplications. *Ind. Eng. Chem. Res.* **2011**, *50*, 2117–2125.

(77) O'Sullivan, J. P.; Wood, G. C. The morphology and mechanism of formation of porous anodic films on aluminium. *Proc. R. Soc. London, Ser. A* **1970**, *317*, 511–543.

(78) Chu, S. Z.; Wada, K.; Inoue, S.; Isogai, M.; Katsuta, Y.; Yasumori, A. Large-Scale Fabrication of Ordered Nanoporous Alumina Films with Arbitrary Pore Intervals by Critical-Potential Anodization. *J. Electrochem. Soc.* **2006**, *153*, B384–B391.

(79) Ono, S.; Saito, M.; Ishiguro, M.; Asoh, H. Controlling Factor of Self-Ordering of Anodic Porous Alumina. *J. Electrochem. Soc.* **2004**, *151*, B473–B478.

(80) Masuda, H.; Satoh, M. Fabrication of Gold Nanodot Array Using Anodic Porous Alumina as an Evaporation Mask. *Jpn. J. Appl. Phys.* **1996**, *35*, L126–L129.

(81) Masuda, H.; Yada, K.; Osaka, A. Self-Ordering of Cell Configuration of Anodic Porous Alumina with Large-Size Pores in Phosphoric Acid Solution. *Jpn. J. Appl. Phys.* **1998**, *37*, L1340–L1342.

(82) Nielsch, K.; Choi, J.; Schwirn, K.; Wehrspohn, R. B.; Gösele, U. Self-ordering Regimes of Porous Alumina: The 10% Porosity Rule. *Nano Lett.* **2002**, *2*, 677–680.

(83) Jessensky, O.; Müller, F.; Gösele, U. Self-Organized Formation of Hexagonal Pore Structures in Anodic Alumina. *J. Electrochem. Soc.* **1998**, *145*, 3735–3740.

(84) Hönicke, D. Comparative investigations of the catalytic properties of an anodic Al_2O_3-coated catalyst and of α- and γ-Al_2O_3 bulk catalysts. *Appl. Catal.* **1983**, *5*, 199–206.

(85) Hönicke, D. Partial Oxidation of 1,3-Butadiene on V_2O_5/Al_2O_3/Al-Coated Catalysts: Products and Reaction Routes. *J. Catal.* **1987**, *105*, 10–18.

(86) Hönicke, D. Partial Oxidation of 1,3-Butadiene on V_2O_5/Al_2O_3/Al-Coated Catalysts: Effects of Pore Lengths on Product Selectivities. *J. Catal.* **1987**, *105*, 19–25.

(87) Lichtenberger-Bajza, E. Die Untersuchung der Vorgänge beim elektrolytischen Polieren des Aluminiums und des Eisens. *Metalloberfläche* **1959**, *13*, 65–71.

(88) Lichtenberger-Bajza, E. Untersuchung der Korrosionsbeständigkeit elektropolierter Aluminiumspiegel und praktische Erfahrungen mit ihrer Anwendung. *Schleif- und Poliertech.* **1962**, *2*, 9–13.

(89) Elmore, W. C. Electrolytic Polishing. *J. Appl. Phys.* **1939**, *10*, 724–727.

(90) Hoar, T. P.; Mowat, J. A. S. Mechanism of Electropolishing. *Nature* **1950**, *165*, 64–65.

(91) Edwards, J. The Mechanism of Electropolishing of Copper in Phosphoric Acid Solutions: I. Processes Preceding the Establisment of Polishing Conditions. *J. Electrochem. Soc.* **1953**, *100*, 189C–194C.

(92) Crundwell, F. K. The anodic dissolution of copper in hydrochloric acid solutions. *Electrochim. Acta* **1992**, *37*, 2707–2714.

(93) Barcia, O. E.; Mattos, O. R.; Pebere, N.; Tribollet, B. Mass-Transport Study for the Electrodissolution of Copper in 1M Hydrochloric Acid Solution by Impedance. *J. Electrochem. Soc.* **1993**, *140*, 2825–2832.

(94) Vidal, R.; West, A. C. Copper Electropolishing in Concentrated Phosphoric Acid I. Experimental Findings. *J. Electrochem. Soc.* **1995**, *142*, 2682–2689.

(95) Jacquet, P. A. Electrolytic and chemical polishing. *Metall. Rev.* **1956**, *1*, 157–238.

(96) Maddin, R.; Mathewson, C. H.; Hibbard, W. R. Unpredicted Cross-slip in Single Crystals of Alpha Brass. *Trans. Am. Inst. Min., Metall. Eng.* **1948**, *175*, 86–105.

(97) Wilms, G. R. Note on the Use of Electropolishing in the Metallographic Study of Plastic Deformation. *J. Inst. Met.* **1949-1950**, *76*, 629–630.

(98) Raether, H. La structure et l'oxydation des surfaces d'aluminium polies électrolytiquement. *C. R. Hebd. Séances Acad. Sci.* **1948**, *227*, 1247–1249.

(99) Raether, H. Über die Struktur einer Metalloberfläche (Nach neueren Untersuchungen mittels Elektronenstrahlen). *Metalloberfläche* **1952**, *6*, A113–A119.

(100) Plateau, J.; Wyon, G.; Pillon, A.; Crussard, C. Contribution à l'étude du polissage électrolytique de l'aluminium. *Met.: Corros.-Ind.* **1951**, *26*, 235–249.

(101) Ma, D.; Li, S.; Liang, C. Electropolishing of high-purity aluminium in perchloric acid and ethanol solutions. *Corros. Sci.* **2009**, *51*, 713–718.

(102) Dunn, C. G.; Harris, L. A. Auger Electron Analysis of Electropolished High-Purity Aluminum. *J. Electrochem. Soc.* **1970**, *117*, 81–82.

(103) Lichtenberger-Bajza, E. Strukturuntersuchungen der beim elektrolytischen Polieren an der Aluminiumoberfläche entstandenen Oxydschichten. *Z. Phys. Chem.* **1960**, *214*, 280–287.

(104) Holló, M. G. A new interpretation of the substructure of electropolished aluminium surfaces. *Acta Metall.* **1960**, *8*, 265–268.

(105) Lichtenberger-Bajza, E. Strukturuntersuchungen von 0.1µ und 150-200µ dicken, electrolytisch erzeugten Oxydschichten auf Aluminium. *Metalloberfläche* **1961**, *15*, 38–41.

(106) Raub, E.; Baba, N. Über einige Eigenschaften der beim chemischen und anodischen Glänzen entstehenden Deckschichten. *Metalloberfläche* **1965**, *19*, 285–292.

(107) Brace, A. W.; Kape, J. M. Theoretical aspects of electrolytic and chemical polishing. In *Proceedings of a Conference on Anodising Aluminium*, Nottingham, UK, 12th Sept. 1961–14th Sept. 1961; Aluminium Development Association / University of Nottingham: London, 1962; pp 167–174.

(108) Arrowsmith, D. J.; Cunningham, P. J.; Dennis, J. K.; Survila, E. Icing on Electropolishing Aluminium. *Trans. Inst. Met. Finish.* **1981**, *59*, 13–16.

(109) Martin, S. (Oxy Metal Industries Corporation). Electropolishing aluminum and aluminum alloys. US Patent, 3,970,529, 1976.

(110) Neufeld, P.; Southall, D. M. The electropolishing of aluminium. *Electrodeposition Surf. Treat.* **1975**, *3*, 159–168.

(111) Clifford, A. W.; Arrowsmith, D. J. The Incidence and Avoidance of Gassing Defects in Chemical and Electropolishing of Aluminium. *Trans. Inst. Met. Finish.* **1978**, *56*, 46–50.

(112) Foley, R. T. Localized Corrosion of Aluminum Alloys—A Review. *Corrosion* **1986**, *42*, 277–288.

(113) Galvele, J. R.; de Micheli, S. M.; Muller, I. L.; de Wexler, S. B.; Alanis, I. L. Critical Potentials for Localized Corrosion of Aluminum Alloys. In *Proceedings U. R. Evans Conference on Localized Corrosion*, Williamsburg, VA, 6th Dec. 1971–10th Dec. 1971; Staehle, R. W., Brown, B. F., Kruger, J., Evans, U. R., Eds.; NACE: Houston, TX, 1974; Vol. NACE-3, pp 580–599.

(114) Kaesche, H. Untersuchungen über die gleichmäßige Auflösung und den Lochfraß von Aluminiumelektroden. *Z. Phys. Chem.* **1962**, *34*, 87–108.

(115) Hoar, T. P.; Mears, D. C.; Rothwell, G. P. The relationships between anodic passivity, brightening and pitting. *Corros. Sci.* **1965**, *5*, 279–289.

(116) Sautebin, R.; Froidevaux, H.; Landolt, D. Theoretical and Experimental Modeling of Surface Leveling in ECM under Primary Current Distribution Conditions. *J. Electrochem. Soc.* **1980**, *127*, 1096–1100.

(117) Levin, A. I.; Evseeva, M. A.; Nechaev, A. V. On the mechanism and peculiarities of electrochemical machining of metals at high current density. *Elektron. Obrab. Mater.* **1973**, *9*, 5–8.

(118) Nechaev, A. V.; Rossina, N. G.; Levin, A. I. Anodic dissolution of aluminum alloys in sodium chlorate solutions at high current densities. *Elektron. Obrab. Mater.* **1979**, *15*, 22–25.

(119) Rumyantsev, E. M.; Nevskli, O. I.; Volkov, V. I.; Grishina, E. P.; Lilin, S. A. Effect of surface films on the nature of anodic dissolution of metals at high current densities. *Elektron. Obrab. Mater.* **1980**, *16*, 17–21.

(120) Münninghoff, T. R. Mechanismen der anodischen Auflösung von Metallen und Legierungen bei extrem hohen Stromdichten. PhD Thesis, Heinrich-Heine Universität Düsseldorf, 2012.

(121) Bannard, J. E.; Duncan, J. R.; Lewis, G. Electrochemical machining as a method of preparing grained aluminium surfaces. *J. Appl. Electrochem.* **1981**, *11*, 253–259.

(122) Sellmyer, D. J.; Zheng, M.; Skomski, R. Magnetism of Fe, Co and Ni nanowires in self-assembled arrays. *J. Phys.: Condens. Matter* **2001**, *13*, R433–R460.

(123) Moon, S.-M.; Pyun, S.-I. The corrosion of pure aluminium during cathodic polarization in aqueous solutions. *Corros. Sci.* **1997**, *39*, 399–408.

(124) Nielsch, K.; Müller, F.; Li, A.-P.; Gösele, U. Uniform Nickel Deposition into Ordered Alumina Pores by Pulsed Electrodeposition. *Adv. Mater.* **2000**, *12*, 582–586.

(125) Sousa, C. T.; Leitao, D. C.; Proenca, M. P.; Ventura, J.; Pereira, A. M.; Araujo, J. P. Nanoporous alumina as templates for multifunctional applications. *Appl. Phys. Rev.* **2014**, *1*, 031102.

(126) Forrer, P.; Schlottig, F.; Siegenthaler, H.; Textor, M. Electrochemical preparation and surface properties of gold nanowire arrays formed by the template technique. *J. Appl. Electrochem.* **2000**, *30*, 533–541.

(127) Kondo, T.; Tanji, M.; Nishio, K.; Masuda, H. Cross-Striped Ordered Arrays of Au Nanoparticles in Anodic Porous Alumina Matrix. *Electrochem. Solid-State Lett.* **2006**, *9*, C189–C191.

(128) Pan, S. L.; Zeng, D. D.; Zhang, H. L.; Li, H. L. Preparation of ordered array of nanoscopic gold rods by template method and its optical properties. *Appl. Phys. A: Mater. Sci. Process* **2000**, *70*, 637–640.

(129) Gerein, N. J.; Haber, J. A. Effect of ac Electrodeposition Conditions on the Growth of High Aspect Ratio Copper Nanowires in Porous Aluminum Oxide Templates. *J. Phys. Chem. B* **2005**, *109*, 17372–17385.

(130) Platzer, B.; Xu, Y.; Roßmann, T.; Födisch, R.; Hönicke, D. Consideration of the Effect of Irregular Catalytic Active Component Distributions in Mesopores — Extension of a Model for Wall-Catalyzed Reactions in Microchannel Reactors. *Chem. Eng. Technol.* **2003**, *26*, 765–773.

(131) Wang, L.; Zhang, Q.; Sakurai, M.; Kameyama, H. Study on the Electro-Deposition of Platinum on Anodic Alumite Films for Catalytic Combustion of VOCs. *J. Chem. Eng. Jpn.* **2008**, *41*, 272–278.

(132) Bard, A. J.; Faulkner, L. R. *Electrochemical Methods: Fundamentals and Applications*, 2nd ed.; Wiley: New York, 2001.

(133) Levich, V. G. *Physicochemical Hydrodynamics*; Prentice-Hall International Series in the Physical and Chemical Engineering Sciences; Prentice-Hall: Englewood Cliffs, NJ, 1962; pp 60–72.

(134) Lasia, A. Electrochemical Impedance Spectroscopy and its Applications. In *Modern Aspects of Electrochemistry*; Conway, B. E., Bockris, J. O'M., White, R. E., Eds.; Kluwer Academic / Plenum Publishers: New York, 1999; Vol. 32, pp 143–248.

(135) Orazem, M. E.; Tribollet, B. *Electrochemical Impedance Spectroscopy*; The Electrochemical Society Series; Wiley: Hoboken, NJ, 2008.

(136) Savova-Stoynov, B.; Stoynov, Z. B. Analysis of the inductance influence on the measured electrochemical impedance. *J. Appl. Electrochem.* **1987**, *17*, 1150–1158.

(137) Mansfeld, F.; Lin, S.; Chen, Y. C.; Shih, H. Minimization of High-Frequency Phase Shifts in Impedance Measurements. *J. Electrochem. Soc.* **1988**, *135*, 906–907.

(138) Boukamp, B. A. A nonlinear least squares fit procedure for analysis of immittance data of electrochemical systems. *Solid State Ionics* **1986**, *20*, 31–44.

(139) *Impedance Spectroscopy: Theory, Experiment and Applications*, 2nd ed.; Barsoukov, E., Macdonald, J. R., Eds.; Wiley: Hoboken, NJ, 2005.

(140) Zoltowski, P. The error function for fitting of models to immittance data. *J. Electroanal. Chem. Interfacial Electrochem.* **1984**, *178*, 11–19.

(141) Bevington, P. R.; Robinson, D. K. *Data Reduction and Error Analysis for the Physical Sciences*, 3rd ed.; McGraw-Hill: Boston, MA, 2003.

(142) Marquardt, D. W. An algorithm for least-squares estimation of nonlinear parameters. *J. Soc. Ind. Appl. Math.* **1963**, *11*, 431–441.

(143) Datta, M.; Landolt, D. Fundamental aspects and applications of electrochemical microfabrication. *Electrochim. Acta* **2000**, *45*, 2535–2558.

(144) Allen, D. Electrolytic Photoetching. *PCMI J.* **1982**, *9*, 6.

(145) Allen, D. M.; Talib, T. N. Manufacture of stainless steel edge filters: an application of electrolytic photopolishing. *Precis. Eng.* **1983**, *5*, 57–59.

(146) Chatterjee, B. Fabrication of fine apertures in metal foils by photoelectrochemical milling. *Precis. Eng.* **1986**, *8*, 131–138.

(147) Buhlert, M.; Meier, K.; Plath, P. J. Photoelectropolishing of stainless steel. *PCMI J.* **2003**, *91*, 5–11.

(148) Datta, M.; Shenoy, R. V.; Romankiw, L. T. Recent Advances in the Study of Electrochemical Micromachining. *J. Eng. Ind.* **1996**, *118*, 29–36.

(149) Datta, M. Microfabrication by electrochemical metal removal. *IBM J. Res. Dev.* **1998**, *42*, 655–669.

(150) Datta, M.; Romankiw, L. T. Application of Chemical and Electrochemical Micromachining in the Electronics Industry. *J. Electrochem. Soc.* **1989**, *136*, 285C–292C.

(151) Van Osenbruggen, C.; de Regt, C. Electrochemical micromachining. *Philips Tech. Rev.* **1985**, *42*, 22–32.

(152) Datta, M.; Romankiw, L. T.; Vigliotti, D. R.; von Gutfeld, R. J. Jet and Laser-Jet Electrochemical Micromachining of Nickel and Steel. *J. Electrochem. Soc.* **1989**, *136*, 2251–2256.

(153) Datta, M.; Landolt, D. Electrochemical saw using pulsating voltage. *J. Appl. Electrochem.* **1983**, *13*, 795–802.

(154) Von Gutfeld, R. J.; Sheppard, K. G. Electrochemical microfabrication by laser-enhanced photothermal processes. *IBM J. Res. Dev.* **1998**, *42*, 639–653.

(155) Schuster, R.; Kirchner, V.; Allongue, P.; Ertl, G. Electrochemical Micromachining. *Science* **2000**, *289*, 98–101.

(156) Allen, D. M. *The Principles and Practice of Photochemical Machining and Photoetching*; Adam Hilger: Bristol, UK, 1986.

(157) Newman, J. S. *Electrochemical Systems*; Prentice-Hall International Series in the Physical and Chemical Engineering Sciences; Prentice-Hall: Englewood Cliffs, NJ, 1972; pp 301–352.

(158) Dukovic, J. O. Computation of current distribution in electrodeposition, a review. *IBM J. Res. Dev.* **1990**, *34*, 693–705.

(159) Dukovic, J. O. Current Distribution and Shape Change in Electrodeposition of Thin Films for Microelectronic Fabrication. In *Advances in Electrochemical Science and Engineering*; Gerischer, H., Tobias, C. W., Eds.; Wiley-VCH: Weinheim, Germany, 1994; Vol. 3, pp 117–161.

(160) West, A. C.; Madore, C.; Matlosz, M.; Landolt, D. Shape Changes during Through-Mask Electrochemical Micromachining of Thin Metal Films. *J. Electrochem. Soc.* **1992**, *139*, 499–506.

(161) Kwon, G.-J.; Sun, H.-Y.; Sohn, H.-J. Wall Profile Developments in Through-Mask Electrochemical Micromachining of Invar Alloy Films. *J. Electrochem. Soc.* **1995**, *142*, 3016–3020.

(162) Alkire, R.; Deligianni, H. The Role of Mass Transport on Anisotropic Electrochemical Pattern Etching. *J. Electrochem. Soc.* **1988**, *135*, 1093–1100.

(163) West, A. C.; Matlosz, M.; Landolt, D. Normalized and Average Current Distributions on Unevenly Spaced Patterns. *J. Electrochem. Soc.* **1991**, *138*, 728–735.

(164) Prentice, G. A.; Tobias, C. W. A Survey of Numerical Methods and Solutions for Current Distribution Problems. *J. Electrochem. Soc.* **1982**, *129*, 72–78.

(165) DeBecker, B.; West, A. C. Workpiece, Pattern, and Feature Scale Current Distributions. *J. Electrochem. Soc.* **1996**, *143*, 486–492.

(166) Lozano-Morales, A.; McCrabb, H.; Taylor, E. J.; West, A. C. Variation of Counterelectrode Size to Control Current Distribution in Parallel Plate Cells. *Plat. Surf. Finish.* **2008**, *95*, 34–38.

(167) Nouraei, S.; Roy, S. Electrochemical Process for Micropattern Transfer Without Photolithography: A Modeling Analysis. *J. Electrochem. Soc.* **2008**, *155*, D97–D103.

(168) Rosset, E.; Landolt, D. Experimental investigation of shape changes in electrochemical micromachining through photoresist masks. *Precis. Eng.* **1989**, *11*, 79–82.

(169) Rosset, E.; Datta, M.; Landolt, D. Electrochemical dissolution of stainless steels in flow channel cells with and without photoresist masks. *J. Appl. Electrochem.* **1990**, *20*, 69–76.

(170) Mehdizadeh, S.; Dukovic, J.; Andricacos, P. C.; Romankiw, L. T. Optimization of Electrodeposit Uniformity by the Use of Auxiliary Electrodes. *J. Electrochem. Soc.* **1990**, *137*, 110–117.

(171) Mehdizadeh, S.; Dukovic, J. O.; Andricacos, P. C.; Romankiw, L. T.; Cheh, H. Y. The Influence of Lithographic Patterning on Current Distribution in Electrodeposition: A Model for Microfabrication by Electrodeposition. *J. Electrochem. Soc.* **1992**, *139*, 78–91.

(172) Mehdizadeh, S.; Dukovic, J.; Andricacos, P. C.; Romankiw, L. T.; Cheh, H. Y. The Influence of Lithographic Patterning on Current Distribution in Electrodeposition: Experimental Study and Mass-Transfer Effects. *J. Electrochem. Soc.* **1993**, *140*, 3497–3505.

(173) Shenoy, R. V.; Datta, M. Effect of Mask Wall Angle on Shape Evolution during Through-Mask Electrochemical Micromachining. *J. Electrochem. Soc.* **1996**, *143*, 544–549.

(174) Ferri, Y.; Piotrowski, O.; Chauvy, P.-F.; Madore, C.; Landolt, D. Two-level electrochemical micromachining of titanium for device fabrication. *J. Micromech. Microeng.* **2001**, *11*, 522–527.

(175) Chauvy, P.-F.; Landolt, D. Unusual cavity shapes resulting from multistep mass transport controlled dissolution: Numerical simulation and experimental investigation with titanium using oxide film laser lithography. *J. Appl. Electrochem.* **2003**, *33*, 135–142.

(176) Kern, P.; Veh, J.; Michler, J. New developments in through-mask electrochemical micromachining of titanium. *J. Micromech. Microeng.* **2007**, *17*, 1168–1177.

(177) Volgin, V. M.; Kabanova, T. B.; Davydov, A. D. Modeling of through-mask electrochemical micromachining. *J. Appl. Electrochem.* **2015**, *45*, 679–688.

(178) Kuiken, H. K. A mathematical model for wet-chemical diffusion-controlled mask etching through a circular hole. *J. Eng. Math.* **2003**, *45*, 75–90.

(179) Kuiken, H. K. Etching: a two-dimensional mathematical approach. *Proc. R. Soc. London, Ser. A* **1984**, *392*, 199–225.

(180) Kuiken, H. K. Etching through a slit. *Proc. R. Soc. London, Ser. A* **1984**, *396*, 95–117.

(181) Vuik, C.; Cuvelier, C. Numerical Solution of an Etching Problem. *J. Comput. Phys.* **1985**, *59*, 247–263.

(182) Kuiken, H. K.; Kelly, J. J.; Notten, P. H. L. Etching Profiles at Resist Edges: I. Mathematical Models for Diffusion-Controlled Cases. *J. Electrochem. Soc.* **1986**, *133*, 1217–1226.

(183) Notten, P. H. L.; Kelly, J. J.; Kuiken, H. K. Etching Profiles at Resist Edges: II. Experimental Confirmation of Models Using GaAs. *J. Electrochem. Soc.* **1986**, *133*, 1226–1232.

(184) Sudirham, J. J. Space-Time Discontinuous Galerkin Methods for Convection-Diffusion Problems: Application to Wet-Chemical Etching. PhD Thesis, University of Twente, 2005.

(185) Shin, C. B.; Economou, D. J. Effect of Transport and Reaction on the Shape Evolution of Cavities during Wet Chemical Etching. *J. Electrochem. Soc.* **1989**, *136*, 1997–2004.

(186) Rath, P.; Chai, J. C.; Zheng, H.; Lam, Y. C.; Murukeshan, V. M.; Zhu, H. A fixed-grid approach for diffusion- and reaction-controlled wet chemical etching. *Int. J. Heat Mass Transfer* **2005**, *48*, 2140–2149.

(187) Rath, P.; Chai, J. C.; Zheng, H.; Lam, Y. C.; Murukeshan, V. M. Total concentration approach for three-dimensional diffusion-controlled wet chemical etching. *Int. J. Heat Mass Transfer* **2006**, *49*, 3408–3416.

(188) Shin, C. B.; Economou, D. J. Forced and Natural Convection Effects on the Shape Evolution of Cavities during Wet Chemical Etching. *J. Electrochem. Soc.* **1991**, *138*, 527–538.

(189) Higdon, J. J. L. Stokes flow in arbitrary two-dimensional domains: shear flow over ridges and cavities. *J. Fluid Mech.* **1985**, *159*, 195–226.

(190) Occhialini, J. M.; Higdon, J. J. L. Convective Mass Transport from Rectangular Cavities in Viscous Flow. *J. Electrochem. Soc.* **1992**, *139*, 2845–2855.

(191) Driesen, C. H. Simulation of convection-driven wet-chemical etching. PhD Thesis, University of Twente, 1999.

(192) Shin, C. B.; Economou, D. J. Mass transfer by natural and forced convection in open cavities. *Int. J. Heat Mass Transfer* **1990**, *33*, 2191–2205.

(193) Rath, P.; Chai, J. C. Modeling Convection-Driven Diffusion-Controlled Wet Chemical Etching Using a Total-Concentration Fixed-Grid Method. *Numer. Heat Transfer, Part B* **2007**, *53*, 143–159.

(194) Alkire, R. C.; Reiser, D. B.; Sani, R. L. Effect of Fluid Flow on Removal of Dissolution Products from Small Cavities. *J. Electrochem. Soc.* **1984**, *131*, 2795–2800.

(195) Alkire, R. C.; Deligianni, H.; Ju, J.-B. Effect of Fluid Flow on Convective Transport in Small Cavities. *J. Electrochem. Soc.* **1990**, *137*, 818–824.

(196) Kuiken, H. K.; Tijburg, R. P. Centrifugal Etching: A Promising New Tool to Achieve Deep Etching Results. *J. Electrochem. Soc.* **1983**, *130*, 1722–1729.

(197) Tijburg, R. P.; Ligthart, J. G. M.; Kuiken, H. K.; Kelly, J. J. Centrifugal Etching: An Experimental Study. *J. Electrochem. Soc.* **2003**, *150*, C440–C444.

(198) Kuiken, H. K. A free-convection boundary-layer model for the centrifugal etching of an axisymmetric cavity. *J. Eng. Math.* **1998**, *34*, 181–200.

(199) Almond, H.; Allen, D. M. Electrolytic machining of difficult-to-etch metals and alloys. In *Proceedings of the 20th International Conference on Computer-Aided Production Engineering (CAPE 2007)*, Glasgow, UK, 6th June 2007–8th June 2007; De Silva, A. K. M., Harrisson, D. K., Eds.; Glasgow Caledonian University / International Institution for Production Engineering Research: Glasgow, UK / Paris, 2007; pp 53–62.

(200) Datta, M. Microfabrication by High Rate Anodic Dissolution: Fundamentals and Applications. *ECS Trans.* **2015**, *66*, 1–18.

(201) Datta, M. Fabrication of an Array of Precision Nozzles by Through-Mask Electrochemical Micromachining. *J. Electrochem. Soc.* **1995**, *142*, 3801–3805.

(202) Datta, M.; Vega, L. F.; Romankiw, L. T.; Duby, P. Mass transport effects during electropolishing of iron in phosphoric-sulfuric acid. *Electrochim. Acta* **1992**, *37*, 2469–2475.

(203) Magaino, S.; Matlosz, M.; Landolt, D. An Impedance Study of Stainless Steel Electropolishing. *J. Electrochem. Soc.* **1993**, *140*, 1365–1373.

(204) Fushimi, K.; Stratmann, M.; Hassel, A. W. Electropolishing of NiTi shape memory alloys in methanolic H_2SO_4. *Electrochim. Acta* **2006**, *52*, 1290–1295.

(205) Konovalov, V. V.; Zangari, G.; Metzger, R. M. Highly Ordered Nanotopographies on Electropolished Aluminum Single Crystals. *Chem. Mater.* **1999**, *11*, 1949–1951.

(206) Piotrowski, O.; Madore, C.; Landolt, D. Electropolishing of Titanium and Titanium Alloys in Perchlorate-Free Electrolytes. *Plat. Surf. Finish.* **1998**, *85*, 115–119.

(207) Datta, M.; Landolt, D. On the role of mass transport in high rate dissolution of iron and nickel in ECM electrolytes—I. Chloride solutions. *Electrochim. Acta* **1980**, *25*, 1255–1262.

(208) Datta, M.; Landolt, D. On the role of mass transport in high rate dissolution of iron and nickel in ECM electrolytes—II. Chlorate and nitrate solutions. *Electrochim. Acta* **1980**, *25*, 1263–1271.

(209) Neufeld, P.; Southall, D. Gas Evolution and Pitting in Electropolishing. *Trans. Inst. Met. Finish.* **1976**, *54*, 40–44.

(210) Chauvy, P.-F. Electrochemical micromachining of titanium using oxide film laser lithography. PhD Thesis, École Polytechnique Fédérale de Lausanne, 2002.

(211) Piotrowski, O. Polissage électrochimique du titane. PhD Thesis, École Polytechnique Fédérale de Lausanne, 1999, p 64.

(212) Chauvy, P.-F.; Hoffmann, P.; Landolt, D. Applications of laser lithography on oxide film to titanium micromachining. *Appl. Surf. Sci.* **2003**, *208–209*, 165–170.

(213) Madou, M. *Fundamentals of Microfabrication: the Science of Miniaturization*, 2nd ed.; CRC Press: Boca Raton, FL, 2002; pp 1–76.

(214) Allen, D. M. Photochemical Machining: from 'manufacturing's best kept secret' to a $6 billion per annum, rapid manufacturing process. *CIRP Ann.—Manuf. Techn.* **2004**, *53*, 559–572.

(215) Nakamura, K. *Photopolymers: Photoresist Materials, Processes, and Applications*; Optics and Photonics, Vol. 10; CRC Press: Boca Raton, FL, 2015.

(216) Allen, D. M.; Gillbanks, P. J. The Photochemical Machining of some Difficult-to-Etch Metals. In *Proceedings of the Technical Program: NEPCON West Conference/Exhibition: Packaging, Production, Testing: National Electronic Packaging and Production Conference*, Anaheim, CA, 25th Feb. 1986–27th Feb. 1986; Cahners Exposition Group: Des Plaines, IL, 1986; Vol. 1, pp 487–494.

(217) Allen, D. M.; Brightman, J. R. C.; Gillbanks, P. J.; Smith, P. M.; Crookall, J. R. Three-Dimensional Photochemical Machining. *CIRP Ann.—Manuf. Techn.* **1987**, *36*, 91–94.

(218) Mineta, T. Electrochemical etching for micromachining of corrosion resistant alloys. In *12th International Conference on Solid State Sensors, Actuators and Microsystems (TRANSDUCERS '03)*, Boston, MA, 8th June 2003–12th June 2003; IEEE: 2003; Vol. 2, pp 1542–1545.

(219) Hao, X.; Wang, L.; Wang, Q.; Guo, F.; Tang, Y.; Ding, Y.; Lu, B. Surface micro-texturing of metallic cylindrical surface with proximity rolling-exposure lithography and electrochemical micromachining. *Appl. Surf. Sci.* **2011**, *257*, 8906–8911.

(220) Hao, X.; Pei, S.; Wang, L.; Xu, H.; He, N.; Lu, B. Microtexture fabrication on cylindrical metallic surfaces and its application to a rotor-bearing system. *Int. J. Adv. Manuf. Technol.* **2015**, *78*, 1021–1029.

(221) Chauvy, P.-F.; Madore, C.; Landolt, D. Electrochemical Micromachining of Titanium Through a Patterned Oxide Film. *Electrochem. Solid-State Lett.* **1999**, *2*, 123–125.

(222) Brevnov, D. A. Electrochemical etching of patterned Al (1 0 0) foils in HCl. *J. Micromech. Microeng.* **2008**, *18*, 087001.

(223) Chauvy, P.-F.; Hoffmann, P.; Landolt, D. Electrochemical Micromachining of Titanium Through a Laser Patterned Oxide Film. *Electrochem. Solid-State Lett.* **2001**, *4*, C31–C34.

(224) Chauvy, P.-F.; Hoffmann, P.; Landolt, D. Electrochemical micromachining of titanium using laser oxide film lithography: excimer laser irradiation of anodic oxide. *Appl. Surf. Sci.* **2003**, *211*, 113–127.

(225) Kikuchi, T.; Wachi, Y.; Takahashi, T.; Sakairi, M.; Suzuki, R. O. Fabrication of a meniscus microlens array made of anodic alumina by laser irradiation and electrochemical techniques. *Electrochim. Acta* **2013**, *94*, 269–276.

(226) Shin, H. S.; Chung, D. K.; Park, M. S.; Kim, B. H.; Chu, C. N. Electrochemical etching of stainless steel through laser masking. *J. Micromech. Microeng.* **2010**, *20*, 055030.

(227) Shin, H. S.; Chung, D. K.; Park, M. S.; Chu, C. N. Analysis of machining characteristics in electrochemical etching using laser masking. *Appl. Surf. Sci.* **2011**, *258*, 1689–1698.

(228) Shaw, J. M.; Gelorme, J. D.; LaBianca, N. C.; Conley, W. E.; Holmes, S. J. Negative photoresists for optical lithography. *IBM J. Res. Dev.* **1997**, *41*, 81–94.

(229) Qu, N.; Chen, X.; Li, H.; Zhu, D. Fabrication of PDMS micro through-holes for electrochemical micromachining. *Int. J. Adv. Manuf. Technol.* **2014**, *72*, 487–494.

(230) *Kunststoffe: Eigenschaften und Anwendungen*, 8th ed.; Domininghaus, H., Elsner, P., Eyerer, P., Hirth, T., Eds.; Springer: Heidelberg, Germany, 2012; p 1255.

(231) Chen, X.; Qu, N.; Li, H.; Guo, Z. Removal of islands from micro-dimple arrays prepared by through-mask electrochemical micromachining. *Precis. Eng.* **2015**, *39*, 204–211.

(232) Chen, X.; Qu, N.; Fang, X.; Zhu, D. Reduction of undercutting in electrochemical micro-machining of micro-dimple arrays by utilizing oxygen produced at the anode. *Surf. Coat. Technol.* **2015**, *277*, 44–51.

(233) Chen, X.; Qu, N.; Li, H.; Xu, Z. Electrochemical micromachining of micro-dimple arrays using a polydimethylsiloxane (PDMS) mask. *J. Mater. Process. Technol.* **2016**, *229*, 102–110.

(234) Chen, X.; Qu, N.; Hou, Z. Electrochemical micromachining of micro-dimple arrays on the surface of Ti-6Al-4V with $NaNO_3$ electrolyte. *Int. J. Adv. Manuf. Technol.* **2016**, *88*, 565–574.

(235) Datta, M. Fabrication of v-shaped nozzles in metal foils by through-mask electrochemical micromachining. In *Proceedings of the First International Symposium on Electrochemical Microfabrication*, Phoenix, AZ, 14th Oct. 1991–16th Oct. 1991; Datta, M., Sheppard, K., Snyder, D. D., Eds.; The Electrochemical Society: Pennington, NJ, 1992; Vol. 92-3, pp 61–79.

(236) Datta, M.; King, D. E.; Knight, A. D.; Sambucetti, C. J. (International Business Machines Corporation). Method for making a detachable electrical contact. US Patent, 5,105,537, 1992.

(237) Datta, M.; Romankiw, L. T. (International Business Machines Corporation). Electrochemical micromachining tool and process for through-mask patterning of thin metallic films supported by non-conducting or poorly conducting surfaces. US Patent, 5,284,554, 1994.

(238) Schönenberger, I.; Roy, S. Microscale pattern transfer without photolithography of substrates. *Electrochim. Acta* **2005**, *51*, 809–819.

(239) Chun, K.-H.; Jin, D.-S.; Kim, S.-H.; Lee, E.-S. Comparison between wire mesh and plate electrodes during Wide-pattern machining on invar fine sheet using through-mask electrochemical micromachining. *J. Mech. Sci. Technol.* **2017**, *31*, 1851–1859.

(240) Wang, G. Q.; Li, H. S.; Qu, N. S.; Zhu, D. Investigation of the hole-formation process during double-sided through-mask electrochemical machining. *J. Mater. Process. Technol.* **2016**, *234*, 95–101.

(241) Lu, X.; Leng, Y.; Zhang, X.; Xu, J.; Qin, L.; Chan, C. Comparative study of osteoconduction on micromachined and alkali-treated titanium alloy surfaces in vitro and in vivo. *Biomaterials* **2005**, *26*, 1793–1801.

(242) Lu, X.; Leng, Y. Electrochemical micromachining of titanium surfaces for biomedical applications. *J. Mater. Process. Technol.* **2005**, *169*, 173–178.

(243) Li, H.; Wang, G.; Qu, N.; Zhu, D. Through-mask electrochemical machining of a large-area hole array in a serpentine flow channel. *Int. J. Adv. Manuf. Technol.* **2017**, *89*, 933–940.

(244) Chen, X.; Qu, N.; Li, H. Improvement of dimensional uniformity on micro-dimple arrays generated by electrochemical micro-machining with an auxiliary electrode. *Int. J. Adv. Manuf. Technol.* **2015**, *80*, 1577–1585.

(245) Gokdel, Y. D.; Mutlu, S.; Yalcinkaya, A. D. Self-terminating electrochemical etching of stainless steel for the fabrication of micro-mirrors. *J. Micromech. Microeng.* **2010**, *20*, 095009.

(246) Wu, W.-T.; Shih, W.-H.; Wang, C.-T. Fabrication of a metal protector for a fiber sensor using through-mask electrochemical micromachining with pulse DC power. *Microsyst. Technol.* **2011**, *17*, 707–714.

(247) Winkelmann, C.; Lang, W. Influence of the electrode distance and metal ion concentration on the resulting structure in electrochemical micromachining with structured counter electrodes. *Int. J. Mach. Tool. Manu.* **2013**, *72*, 25–31.

(248) Winkelmann, C.; Lang, W. Sensorial Surfaces—Embedding Sensor Structures Into the Surface of Materials. *IEEE Sens. J.* **2014**, *14*, 2078–2083.

(249) Zhang, X.; Qu, N.; Li, H.; Xu, Z. Investigation of machining accuracy of micro-dimples fabricated by modified microscale pattern transfer without photolithography of substrates. *Int. J. Adv. Manuf. Technol.* **2015**, *81*, 1475–1485.

(250) Allen, D. M.; Talib, T. N.; Horne, D. F. Surface textures and process characteristics of the electrolytic photoetching of annealed AISI 304 stainless steel in hydrochloric acid. *Precis. Eng.* **1983**, *5*, 51–56.

(251) Allen, D. M.; Talib, T. N. Electrolytic photoetching of Vitrovac 6025 for the production of magnetic recording heads. *Precis. Eng.* **1984**, *6*, 125–128.

(252) James, B. D. Mechanization of the wafer fabrication process using air bearing handling techniques. In *Proceedings of the Technical Program: 1971 Semiconductor / IC Processing & Production Conference*, Anaheim, CA, 9th Feb. 1971–11th Feb. 1971; Industrial and Scientific Conference Management: Chicago, IL, 1971; pp 111–118.

(253) Hogg, H. A. C. Photo-etching molybdenum foil. *Proc. IEE-Part A: Radio Electron. Eng.* **1958**, *105*, 614–616.

(254) Wicke, W. C. Method of etching and composition thereof. US Patent, 2,990,282, 1961.

(255) Gottschling, M.; Löffelholz, J.; Albert, M.; Sadowski, G. (H. C. Starck GmbH). Process for the production of shaped articles of niobium or tantalum by electrochemical etching. US Patent, 7,090,763 B2, 2006.

(256) Frankenthal, R. P.; Eaton, D. H. Electroetching of Platinum in the Titanium-Platinum-Gold Metallization on Silicon Integrated Circuits. *J. Electrochem. Soc.* **1976**, *123*, 703–706.

(257) Gastol, D. A. Microfabrication processing of titanium for biomedical devices with reduced impact on the environment. PhD Thesis, Cranfield University, 2012.

(258) Kern, W.; Shaw, J. M. Electrochemical Delineation of Tungsten Films for Microelectronic Devices. *J. Electrochem. Soc.* **1971**, *118*, 1699–1704.

(259) Dasannacharya, B. S.; Murthy, K. K.; Rajagopal, I.; Rajagopalan, S. Photoelectrochemical Fabrication of Stainless Steel Filter Elements. *Indian J. Technol.* **1986**, *24*, 522–524.

(260) Ahn, J. B.; Ryu, H. Y.; Park, J. G. Fabrication of Bumping Mask for Flip-Chip Process on Stainless Steel Using Through Mask Electrochemical Micro Machining (TMEMM). *ECS Trans.* **2015**, *69*, 1–7.

(261) Zamin, M.; Mayer, P.; Murthy, M. K. On the Electropolishing of Molybdenum. *J. Electrochem. Soc.* **1977**, *124*, 1558–1562.

(262) Alanis, I. L.; Schiffrin, D. J. The influence of mass transfer on the mechanism of electropolishing of nickel in aqueous sulphuric acid. *Electrochim. Acta* **1982**, *27*, 837–845.

(263) Tian, H.; Corcoran, S. G.; Reece, C. E.; Kelley, M. J. The Mechanism of Electropolishing of Niobium in Hydrofluoric-Sulfuric Acid Electrolyte. *J. Electrochem. Soc.* **2008**, *155*, D563–D568.

(264) Anik, M.; Osseo-Asare, K. Effect of pH on the Anodic Behavior of Tungsten. *J. Electrochem. Soc.* **2002**, *149*, B224–B233.

(265) Allen, D. M.; Gillbanks, P. J. Manufacture of some SIMS components from tantalum foils by electrolytic photoetching. *Precis. Eng.* **1985**, *7*, 105–109.

(266) Allen, D. M. Methanol-sulphuric acid: a versatile non-aqueous etchant for use in electrolytic photoetching of difficult-to-etch materials. In *Proceedings of the Symposium on Electrochemical Technology in Electronics*, Honolulu, HI, 18th Oct. 1987–23rd Oct. 1987; Romankiw, L. T., Osaka, T., Eds.; The Electrochemical Society: Pennington, NJ, 1988; Vol. 88-23, pp 685–690.

(267) Zinger, O.; Chauvy, P.-F.; Landolt, D. Scale-Resolved Electrochemical Surface Structuring of Titanium for Biological Applications. *J. Electrochem. Soc.* **2003**, *150*, B495–B503.

(268) Allen, D. M.; Almond, H. J. A.; Wang, W.; Cobley, A.; Mason, T. J.; Paniwynk, L.; Jollie, M. Extending the process capability of electrolytic photoetching with ultrasonics and ultra-short voltage pulses. In *Proceedings of the 18th CIRP Design Conference*, Enschede, Netherlands, 7th Apr. 2008–9th Apr. 2008; van Houten, F. J. A. M., Miedema, J., Lutters, D., Eds.; Laboratory of Design, Production and Management, Faculty of Engineering Technology, University of Twente: Enschede, Netherlands, 2008.

(269) Mineta, T.; Mitsui, T.; Watanabe, Y.; Kobayashi, S.; Haga, Y.; Esashi, M. Batch fabricated flat meandering shape memory alloy actuator for active catheter. *Sens. Actuators, A* **2001**, *88*, 112–120.

(270) Mineta, T. Electrochemical etching of a shape memory alloy using new electrolyte solutions. *J. Micromech. Microeng.* **2003**, *14*, 76–80.

(271) Allen, D. M.; Chen, T. T. The electrochemical micromachining of microactuator devices from sputtered NiTi thin films. In *Proceedings of the Third International Symposium on Microstructures and Microfabricated Systems*, Montreal, Canada, 4th May 1997–9th May 1997; Hesketh, P. J., Barna, G., Hughes, H. G., Eds.; The Electrochemical Society: Pennington, NJ, 1997; Vol. 97-5, pp 72–78.

(272) Makino, E.; Shibata, T.; Allen, D. M. Electrochemical Micromachining of Shape Memory Alloy Sheets. *PCMI J.* **1997**, *70*, 13–17.

(273) Allen, D. M.; Impey, S. A.; Robin, R.; Chen, T. T. Nature and influence of surface layers and films on the chemical and electrochemical micromachining of NiTi shape memory alloys. In *Proceedings of SPIE, Design, Test and Microfabrication of MEMS and MOEMS*, Paris, 30th Mar. 1999–1st Apr. 1999; Courtois, B., Crary, S. B., Ehrfeld, W., Fujita, H., Karam, J. M., Markus, K. W., Eds.; SPIE: 1999; Vol. 3680, pp 478–485.

(274) Piotrowski, O.; Madore, C.; Landolt, D. Electropolishing of tantalum in sulfuric acid-methanol electrolytes. *Electrochim. Acta* **1999**, *44*, 3389–3399.

(275) Piotrowski, O.; Madore, C.; Landolt, D. The Mechanism of Electropolishing of Titanium in Methanol-Sulfuric Acid Electrolytes. *J. Electrochem. Soc.* **1998**, *145*, 2362–2369.

(276) Kim, Y.; Youn, S.; Cho, Y.-H.; Park, H.; Chang, B. G.; Oh, Y. S. A multi-step electrochemical etching process for a three-dimensional micro probe array. *J. Micromech. Microeng.* **2011**, *21*, 015019.

(277) Spencer, T.; Wilson, J. Engraving Metals by means of Voltaic Electricity. British pat., 8656, 1840.

(278) Walker, C. V. *Electrotpye Manipulation*, 25th ed.; Henry Carey Baird: Philadelphia, PA, 1852; pp 51–59.

(279) Grove, W. R. On a Voltaic Process for Etching Daguerreotype Plates. *Lond. Edinb. Dubl. Phil. Mag.* **1842**, *20*, 18–24.

(280) Grove, W. R. On a Voltaic Process for Etching Daguerreotype Plates. *J. Franklin Inst.* **1842**, *33*, 328–331.

(281) Osann, G. W. *Die Anwendung des hydroelektrischen Stromes als Aetzmittel*; Voigt und Mocker: Würzburg, Germany, 1842.

(282) Willson, C. G.; Dammel, R. A.; Reiser, A. Photoresist Materials: A Historical Perspective. In *Proceedings of SPIE, Optical Microlithography X*, Santa Clara, CA, 10th Mar. 1997–14th Mar. 1997; Fuller, G. E., Ed.; SPIE: 1997; Vol. 3051, pp 28–41.

(283) Briggs, G. R.; Tuska, J. W. Permalloy-Sheet Transfluxor-Array Memory. *J. Appl. Phys.* **1962**, *33*, 1065–1066.

(284) Romankiw, L. Pattern generation in metal films using wet chemical techniques: a review. In *Proceedings of the Symposium on Etching for Pattern Definition*; Hughes, H. F., Rand, M. J., Eds.; The Electrochemical Society: Princeton, NJ, 1976; Vol. 76-3, pp 161–193.

(285) Meek, R. L.; Schumaker, N. E. Anodic Dissolution and Selective Etching of Gallium Phosphide. *J. Electrochem. Soc.* **1972**, *119*, 1148–1152.

(286) Datta, M. Microfabrication by Through-Mask Electrochemical Machining. In *Proceedings of SPIE, Micromachining and Microfabrication Process Technology III*, Austin, TX, 29th Sept. 1997–30th Sept. 1997; Chang, S.-C., Pang, S. W., Eds.; SPIE: 1997; Vol. 3223, pp 178–184.

(287) Kohl, M.; Quandt, E.; Schüßler, A.; Trapp, R.; Allen, D. M. Characterization of NiTi shape memory microdevices produced by microstructure of etched sheets or sputter deposited films. In *Proceedings of the 4th International Conference on New Actuators (ACTUATOR '94)*, Bremen, Germany, 15th June 1994–17th June 1994; Borgmann, H., Lenz, K., Eds.; AXON Technologie Consult: Bremen, Germany, 1994; pp 317–320.

(288) Quandt, E.; Halene, C.; Holleck, H.; Feit, K.; Kohl, M.; Schloßmacher, P. Sputter deposition of TiNi and TiNiPd films displaying the two way shape memory effect. In *8th International Conference on Solid-State Sensors and Actuators (TRANSDUCERS '95)*, Stockholm, Sweden, 25th June 1995–29th June 1995; IEEE: 1995; Vol. 2, pp 202–205.

(289) Kohl, M.; Skrobanek, K. D.; Goh, C. M.; Allen, D. M. Mechanical characterization of shape memory micromaterials. In *Proceedings of SPIE, Microlithography and Metrology in Micromachining II*, Austin, TX, 14th Oct. 1996–15th Oct. 1996; Postek Jr, M. T., Friedrich, C. R., Eds.; SPIE: 1996; Vol. 2880, pp 108–118.

(290) Allen, D. M.; Leong, T.; Lim, S. H.; Kohl, M. Photofabrication of the Third Dimension of NiTi Shape Memory Alloy Microactuators. In *Proceedings of SPIE, Microlithography and Metrology in Micromachining III*, Austin, TX, 29th Sept. 1997–30th Sept. 1997; Friedrich, C. R., Umeda, A., Eds.; SPIE: 1997; Vol. 3225, pp 126–132.

(291) Chen, T.-T. Electrochemical micromachining of microdevices from NiTi shape memory alloys. PhD Thesis, Cranfield University, 1999.

(292) Kohl, M.; Skrobanek, K. D.; Miyazaki, S. Development of stress-optimised shape memory microvalves. *Sens. Actuators, A* **1999**, *72*, 243–250.

(293) Mineta, T.; Mitsui, T.; Watanabe, Y.; Kobayashi, S.; Haga, Y.; Esashi, M. An active guide wire with shape memory alloy bending actuator fabricated by room temperature process. *Sens. Actuators, A* **2002**, *97-98*, 632–637.

(294) Kohl, M.; Allen, D. M.; Chen, T. T.; Miyazaki, S.; Schwörer, M. Anisotropy in microdevices produced by micromachining of cold-rolled NiTi sheets. *Mater. Sci. Eng., A* **1999**, *270*, 145–150.

(295) Qian, S.; Zhu, D.; Qu, N.; Li, H.; Yan, D. Generating micro-dimples array on the hard chrome-coated surface by modified through mask electrochemical micromachining. *Int. J. Adv. Manuf. Technol.* **2010**, *47*, 1121–1127.

(296) Zhang, X.; Qu, N.; Chen, X. Sandwich-like electrochemical micromachining of micro-dimples. *Surf. Coat. Technol.* **2016**, *302*, 438–447.

(297) Madou, M. Si micromachining: the newest precision engineering tool. In *Proceedings of the Fourth International Symposium on Magnetic Materials, Processes, and Devices: Applications to Storage and Microelectromechanical Systems (MEMS)*, Chicago, IL, 9th Oct. 1993–12th Oct. 1993; Romankiw, L. T., Herman, D. A., Eds.; The Electrochemical Society: Pennington, NJ, 1996; Vol. 95-18, pp 236–252.

(298) Allen, D. M.; Gillbanks, P. J.; Palmer, A. J. The Selection of an Appropriate Method to Manufacture Thin Sheet Metal Parts based on Technical and Financial Considerations. In *Proceedings of the International Symposium for Electro-Machining (ISEM-9)*, Nagoya, Japan; Gakkai, D. K., Ed.; Japan Society of Electrical-Machining Engineers: Tokyo, 1989; pp 246–249.

(299) Matson, D. W.; Martin, P. M.; Tonkovich, A. L. Y.; Roberts, G. L. Fabrication of a stainless steel microchannel microcombustor using a lamination process. In *Proceedings of SPIE, Micromachined Devices and Components IV*, Santa Clara, CA, 20th Sept. 1998–24th Sept. 1998; French, P. J., Chau, K. H., Eds.; SPIE: 1998; Vol. 3514, pp 386–392.

(300) Matson, D. W.; Martin, P. M.; Stewart, D. C.; Tonkovich, A. L. Y.; White, M.; Zilka, J. L.; Roberts, G. L. Fabrication of Microchannel Chemical Reactors Using a Metal Lamination Process. In *Microreaction Technology: Industrial Prospects, IMRET 3: Proceedings of the Third International Conference on Microreaction Technology*, Frankfurt a. M., Germany, 18th Apr. 1999–21st Apr. 1999; Ehrfeld, W., Ed.; Springer: Berlin, 2000; pp 62–71.

(301) Hessel, V.; Ehrfeld, W.; Golbig, K.; Haverkamp, V.; Löwe, H.; Storz, M.; Wille, C. Gas / Liquid Microreactors for Direct Fluorination of Aromatic Compounds Using Elemental Fluorine. In *Microreaction Technology: Industrial Prospects, IMRET 3: Proceedings of the Third International Conference on Microreaction Technology*, Frankfurt a. M., Germany, 18th Apr. 1999–21st Apr. 1999; Ehrfeld, W., Ed.; Springer: Berlin, 2000; pp 526–540.

(302) Rouge, A.; Spoetzl, B.; Gebauer, K.; Schenk, R.; Renken, A. Microchannel reactors for fast periodic operation: the catalytic dehydration of isopropanol. *Chem. Eng. Sci.* **2001**, *56*, 1419–1427.

(303) Zapf, R.; Becker-Willinger, C.; Berresheim, K.; Bolz, H.; Gnaser, H.; Hessel, V.; Kolb, G.; Löb, P.; Pannwitt, A.-K.; Ziogas, A. Detailed Characterization of Various Porous Alumina-Based Catalyst Coatings Within Microchannels and Their Testing for Methanol Steam Reforming. *Chem. Eng. Res. Des.* **2003**, *81*, 721–729.

(304) Brandner, J. J. Fabrication of Microreactors Made From Metals and Ceramics. In *Microreactors in Organic Synthesis and Catalysis*; Wirth, T., Ed.; Wiley-VCH: Weinheim, Germany, 2008; pp 1–17.

(305) Markle, R. Effect of Nitric Acid Concentration on the Etch Rates and Surface Finish of Titanium: Part 1. http://www.chemcut.net/wp-content/uploads/2015/02/Etching-Titanium-with-HF-and-Nitric-Acid-Solutions-Part1.pdf (accessed 9th June 2018).

(306) Allen, D. M.; Hegarty, A. J.; Horne, D. F. Surface Textures of Annealed AISI 304 Stainless Steel Etched by Aqueous Ferric Chloride-Hydrochloric Acid Solutions. *Trans. Inst. Met. Finish.* **1981**, *59*, 25–29.

(307) Allen, D. M.; Beristain, L. S.; Gillbanks, P. J.; Crookall, J. R. Photochemical Machining of Molybdenum. *CIRP Ann.—Manuf. Techn.* **1986**, *35*, 129–132.

(308) Allen, D. M. Photochemical Machining (PCM) of Aluminium and its Alloys. In *Proceedings of the 2nd International & 23rd AIMTDR Conference*, Chennai, India, 15th Dec. 2008–17th Dec. 2008; Shunmugam, M. S., Ramesh Babu, N., Eds.; Indian Institute of Technology Madras: Chennai, India, 2008; pp 37–44.

(309) Rosset, E. Photodecoupage electrochimique en milieu salin neutre. PhD Thesis, École Polytechnique Fédérale de Lausanne, 1988.

(310) Allen, D. M.; Almond, H.; Logan, P. A technical comparison of micro-electrodischarge machining, microdrilling and copper vapour laser machining for the fabrication of ink jet nozzles. In *Proceedings of SPIE, Design, Test, Integration, and Packaging of MEMS/MOEMS*, Paris, 9th May 2000–11th May 2000; Courtois, B., Crary, S. B., Gabriel, K. J., Karam, J. M., Markus, K. W., Tay, A. A. O., Eds.; SPIE: 2000; Vol. 4019, pp 531–540.

(311) Compton, R. G.; Eklund, J. C.; Marken, F. Sonoelectrochemical Processes: A Review. *Electroanalysis* **1997**, *9*, 509–522.

(312) Hines, R. E. An Improved Technique for Etching Aluminium Interconnect Patterns on Integrated Circuits. *Microelectron. Reliab.* **1971**, *10*, 59.

(313) Lim, C. F. C. Electrochemical Reduction of Carbon Dioxide on Copper Electrodes. PhD Thesis, University of Canterbury, 2017.

(314) Baldhoff, T.; Marshall, A. T. Characterization of Surface Films Formed on Aluminum during Mass-Transfer Limited Anodic Dissolution in Phosphoric Acid. *J. Electrochem. Soc.* **2017**, *164*, C46–C53.

(315) West, A. C.; Deligianni, H.; Andricacos, P. C. Electrochemical planarization of interconnect metallization. *IBM J. Res. Dev.* **2005**, *49*, 37–48.

(316) Sakairi, M.; Yamada, M.; Kikuchi, T.; Takahashi, H. Development of three-electrode type micro-electrochemical reactor on anodized aluminum with photon rupture and electrochemistry. *Electrochim. Acta* **2007**, *52*, 6268–6274.

(317) Critchlow, G. W.; Brewis, D. M. Review of surface pretreatments for aluminium alloys. *Int. J. Adhes. Adhes.* **1996**, *16*, 255–275.

(318) Grimm, R. D.; West, A. C.; Landolt, D. AC Impedance Study of Anodically Formed Salt Films on Iron in Chloride Solution. *J. Electrochem. Soc.* **1992**, *139*, 1622–1629.

(319) Grimm, R. D.; Landolt, D. Salt films formed during mass transport controlled dissolution of iron-chromium alloys in concentrated chloride media. *Corros. Sci.* **1994**, *36*, 1847–1868.

(320) Matlosz, M. Modeling of impedance mechanisms in electropolishing. *Electrochim. Acta* **1995**, *40*, 393–401.

(321) Legrand, L.; Chassaing, E.; Chausse, A.; Messina, R. RDE and impedance study of anodic dissolution of aluminium in organic $AlCl_3$/dimethylsulfone electrolytes. *Electrochim. Acta* **1998**, *43*, 3109–3115.

(322) Keller, F.; Hunter, M. S.; Robinson, D. L. Structural Features of Oxide Coatings on Aluminum. *J. Electrochem. Soc.* **1953**, *100*, 411–419.

(323) Furneaux, R. C.; Rigby, W. R.; Davidson, A. P. The formation of controlled-porosity membranes from anodically oxidized aluminium. *Nature* **1989**, *337*, 147–149.

(324) Shimizu, K.; Kobayashi, K.; Thompson, G. E.; Wood, G. C. Development of porous anodic films on aluminium. *Philos. Mag. A* **1992**, *66*, 643–652.

(325) De Wit, H. J.; Wijenberg, C.; Crevecoeur, C. Impedance Measurements during Anodization of Aluminum. *J. Electrochem. Soc.* **1979**, *126*, 779–785.

(326) Bai, L.; Conway, B. E. Complex Behavior of Al Dissolution in Non-Aqueous Medium as Revealed by Impedance Spectroscopy. *J. Electrochem. Soc.* **1990**, *137*, 3737–3747.

(327) Brett, C. M. A. The application of electrochemical impedance techniques to aluminium corrosion in acidic chloride solution. *J. Appl. Electrochem.* **1990**, *20*, 1000–1003.

(328) Brett, C. M. A. On the electrochemical behaviour of aluminium in acidic chloride solution. *Corros. Sci.* **1992**, *33*, 203–210.

(329) De Wit, J. H. W.; Lenderink, H. J. W. Electrochemical impedance spectroscopy as a tool to obtain mechanistic information on the passive behaviour of aluminium. *Electrochim. Acta* **1996**, *41*, 1111–1119.

(330) Bojinov, M.; Betova, I.; Raicheff, R. Kinetics of formation and properties of a barrier oxide film on molybdenum. *J. Electroanal. Chem.* **1996**, *411*, 37–42.

(331) Bojinov, M.; Kanazirski, I.; Girginov, A. A model for surface charge-assisted barrier film growth on metals in acidic solutions based on ac impedance measurements. *Electrochim. Acta* **1996**, *41*, 2695–2705.

(332) Biaggio, S. R.; Rocha-Filho, R. C.; Vilche, J. R.; Varela, F. E.; Gassa, L. M. A study of thin anodic WO_3 films by electrochemical impedance spectroscopy. *Electrochim. Acta* **1997**, *42*, 1751–1758.

(333) Bojinov, M. The ability of a surface charge approach to describe barrier film growth on tungsten in acidic solutions. *Electrochim. Acta* **1997**, *42*, 3489–3498.

(334) Bojinov, M. Modelling the formation and growth of anodic passive films on metals in concentrated acid solutions. *J. Solid State Electrochem.* **1997**, *1*, 161–171.

(335) Cattarin, S.; Musiani, M.; Tribollet, B. Nb Electrodissolution in Acid Fluoride Medium: Steady-State and Impedance Investigations. *J. Electrochem. Soc.* **2002**, *149*, B457–B464.

(336) Metikoš-Huković, M.; Grubač, Z. The growth kinetics of thin anodic WO_3 films investigated by electrochemical impedance spectroscopy. *J. Electroanal. Chem.* **2003**, *556*, 167–178.

(337) Vázquez, G.; González, I. Diffusivity of anion vacancies in WO_3 passive films. *Electrochim. Acta* **2007**, *52*, 6771–6777.

(338) Metikoš-Huković, M.; Babić, R.; Grubač, Z. Passivation of Aluminum-Molybdenum Alloys in Hydrochloric Acid. *J. Electrochem. Soc.* **2009**, *156*, C435–C440.

(339) Chao, C. Y.; Lin, L. F.; Macdonald, D. D. A Point Defect Model for Anodic Passive Films I. Film Growth Kinetics. *J. Electrochem. Soc.* **1981**, *128*, 1187–1194.

(340) Lin, L. F.; Chao, C. Y.; Macdonald, D. D. A Point Defect Model for Anodic Passive Films II. Chemical Breakdown and Pit Initiation. *J. Electrochem. Soc.* **1981**, *128*, 1194–1198.

(341) Chao, C. Y.; Lin, L. F.; Macdonald, D. D. A Point Defect Model for Anodic Passive Films III. Impedance Response. *J. Electrochem. Soc.* **1982**, *129*, 1874–1879.

(342) Macdonald, D. D.; Urquidi-Macdonald, M. Theory of Steady-State Passive Films. *J. Electrochem. Soc.* **1990**, *137*, 2395–2402.

(343) Macdonald, D. D.; Biaggio, S. R.; Song, H. Steady-State Passive Films: Interfacial Kinetic Effects and Diagnostic Criteria. *J. Electrochem. Soc.* **1992**, *139*, 170–177.

(344) Macdonald, D. D. The Point Defect Model for the Passive State. *J. Electrochem. Soc.* **1992**, *139*, 3434–3449.

(345) Bojinov, M.; Betova, I.; Raicheff, R. Influence of molybdenum on the transpassivity of a Fe + 12% Cr alloy in H_2SO_4 solutions. *J. Electroanal. Chem.* **1997**, *430*, 169–178.

(346) Sikora, E.; Sikora, J.; Macdonald, D. D. A new method for estimating the diffusivities of vacancies in passive films. *Electrochim. Acta* **1996**, *41*, 783–789.

(347) Dignam, M. J. The Kinetics of the Growth of Oxides. In *Electrochemical Materials Science*; Bockris, J. O'M., Conway, B. E., Yeager, E., White, R. E., Eds.; Comprehensive Treatise of Electrochemistry, Vol. 4; Plenum Press: New York, 1981; pp 247–306.

(348) Fromhold Jr, A. T. Space-charge effects on anodic film formation. In *Oxides and Oxide Films*; Diggle, J. W., Vijh, A. K., Eds.; The Anodic Behavior of Metals and Semiconductors Series, Vol. 3; Marcell Dekker: New York, 1976; pp 1–272.

(349) Brug, G. J.; van den Eeden, A. L. G.; Sluyters-Rehbach, M.; Sluyters, J. H. The analysis of electrode impedances complicated by the presence of a constant phase element. *J. Electroanal. Chem. Interfacial Electrochem.* **1984**, *176*, 275–295.

(350) Baruffaldi, C.; Casellato, U.; Cattarin, S.; Musiani, M.; Tribollet, B.; Vercelli, B. Characterisation of the surface films formed on Nb during electrodissolution in aqueous alkali. *Electrochim. Acta* **2002**, *47*, 2989–2997.

(351) Chin, D.-T.; Chang, H. H. On the conductivity of phosphoric acid electrolyte. *J. Appl. Electrochem.* **1989**, *19*, 95–99.

(352) Newman, J. Resistance for Flow of Current to a Disk. *J. Electrochem. Soc.* **1966**, *113*, 501–502.

(353) Brosheer, J. C.; Lenfesty, F. A.; Anderson Jr, J. F. Solubility in the System Aluminum Phosphate-Phosphoric Acid-Water. *J. Am. Chem. Soc.* **1954**, *76*, 5951–5956.

(354) Egan Jr, E. P.; Luff, B. B. Density of Aqueous Solutions of Phosphoric Acid: Measurements at 15° to 80°C. *Ind. Eng. Chem.* **1955**, *47*, 1280–1281.

(355) Brebbia, C. A.; Telles, J. C. F.; Wrobel, L. C. *Boundary Element Techniques: Theory and Applications in Engineering*; Springer: Berlin, 1984.

(356) Brebbia, C. A.; Dominguez, J. *Boundary Elements: An Introductory Course*, 2nd ed.; Computational Mechanics Publications / McGraw-Hill: Southampton, UK / New York, 1992.

(357) Ang, W.-T. *A Beginner's Course in Boundary Element Methods*; Universal Publishers: Boca Raton, FL, 2007; pp 7–80.

(358) D'Errico, J. MATLAB Central File Exchange. https://au.mathworks.com/matlabcentral/fileexchange/34874-interparc (accessed 25th Apr. 2016).

(359) D'Errico, J. MATLAB Central File Exchange. https://au.mathworks.com/matlabcentral/fileexchange/34871-arclength (accessed 25th Apr. 2016).

(360) Becker, E. B.; Carey, G. F.; Oden, J. T. *Finite Elements: An Introduction*; The Texas Finite Element Series, Vol. 1; Prentice-Hall: Englewood Cliffs, NJ, 1981.

(361) Kwon, Y. W.; Bang, H. *The Finite Element Method using MATLAB*; CRC Press: Boca Raton, FL, 1997.

(362) Kattan, P. I. *MATLAB Guide to Finite Elements*; Springer: Berlin, 2003.

(363) Pozrikidis, C. *Introduction to Finite and Spectral Element Methods using MATLAB*; Chapman & Hall / CRC Press: Boca Raton, FL, 2005.

(364) Ivanov, A.; Mescheder, U. Primary Current Distribution Model for Electrochemical Etching of Silicon Through a Circular Opening. Presented at the 2015 COMSOL Conference, Grenoble, France, 14th–16th Oct. 2015.

(365) Baldhoff, T.; Nock, V.; Marshall, A. T. Through-Mask Electrochemical Micromachining of Aluminum in Phosphoric Acid. *J. Electrochem. Soc.* **2017**, *164*, E194–E202.

(366) Anxionnaz, Z.; Cabassud, M.; Gourdon, C.; Tochon, P. Heat exchanger/reactors (HEX reactors): Concepts, technologies: State-of-the-art. *Chem. Eng. Process.* **2008**, *47*, 2029–2050.

(367) Scotti, G.; Kanninen, P.; Kallio, T.; Franssila, S. Bulk-Aluminum Microfabrication for Micro Fuel Cells. *J. Microelectromech. Syst.* **2014**, *23*, 372–379.

(368) Mattsson, K. E. Surface micromachined scanning mirrors. *Microelectron. Eng.* **1992**, *19*, 199–202.

(369) Qian, S.; Ji, F. Investigation on the Aluminum-alloy Surface with Micro-pits Array Generating by through Double Mask Electrochemical Machining. In *Proceedings of the AASRI International Conference on Industrial Electronics and Applications (IEA 2015)*, London, UK, 27th June 2015–28th June 2015; Wu, Y., Deng, W., Eds.; Atlantis Press: 2015; Vol. 2, pp 59–62.

(370) Sudirham, J. J.; van Damme, R. M. J.; van der Vegt, J. J. W. Space-time discontinuous Galerkin method for wet-chemical etching of microstructures. Presented at the European Congress on Computational Methods in Applied Sciences and Engineering (ECCOMAS 2004), Jyväskylä, Finland, 24th–28th July 2004.

(371) Clerc, C.; Landolt, D. On the theory of anodic levelling: FEM simulation of the influence of profile shape and cell geometry. *Electrochim. Acta* **1984**, *29*, 787–795.

(372) Köhler, J. M. *Etching in Microsystem Technology*; Wiley-VCH: Weinheim, Germany, 1999; pp 41–84.

(373) Glarum, S. H.; Marshall, J. H. The Anodic Dissolution of Copper into Phosphoric Acid I. Voltammetric and Oscillatory Behavior. *J. Electrochem. Soc.* **1985**, *132*, 2872–2878.

(374) Zamin, M.; Mayer, P.; Murthy, M. K. Application of Wagner's Theory to the Electropolishing of Aluminum. *J. Electrochem. Soc.* **1976**, *123*, 1377–1379.

(375) Schönfeld, F.; Hardt, S. Simulation of Helical Flows in Microchannels. *AIChE J.* **2004**, *50*, 771–778.

(376) Rebrov, E. V.; Schouten, J. C.; de Croon, M. H. J. M. Single-phase fluid flow distribution and heat transfer in microstructured reactors. *Chem. Eng. Sci.* **2011**, *66*, 1374–1393.

(377) Amador, C.; Gavriilidis, A.; Angeli, P. Flow distribution in different microreactor scale-out geometries and the effect of manufacturing tolerances and channel blockage. *Chem. Eng. J.* **2004**, *101*, 379–390.

(378) Delsman, E. R.; de Croon, M. H. J. M.; Elzinga, G. D.; Cobden, P. D.; Kramer, G. J.; Schouten, J. C. The Influence of Differences Between Microchannels on Microreactor Performance. *Chem. Eng. Technol.* **2005**, *28*, 367–375.

(379) Hirata, H.; Hori, M. Gas-flow uniformity and cell performance in a molten carbonate fuel cell stack. *J. Power Sources* **1996**, *63*, 115–120.

(380) Ming, P.; Zhao, C.; Zhang, X.; Li, X.; Qin, G.; Yan, L. Investigation of foamed cathode through-mask electrochemical micromachining developed for uniform texturing on metallic cylindrical surface. *Int. J. Adv. Manuf. Technol.* **2018**, *96*, 3043–3056.

(381) Qian, S.; Ji, F.; Qu, N.; Li, H. Improving the Localization of Surface Texture by Electrochemical Machining with Auxiliary Anode. *Mater. Manuf. Processes* **2014**, *29*, 1488–1493.

(382) Tjerkstra, R. W. Isotropic etching of silicon in fluoride containing solutions as a tool for micromachining. PhD Thesis, University of Twente, 1999.

(383) Turner, H. L. (Union Carbide and Carbon Corporation). Electrolytic polishing of aluminium. US Patent, 2,708,655, 1955.

(384) Hessel, V.; Hardt, S.; Löwe, H. *Chemical Micro Process Engineering: Fundamentals, Modelling and Reactions*; Wiley-VCH: Weinheim, Germany, 2004; pp 258–261.

(385) Meille, V. Review on methods to deposit catalysts on structured surfaces. *Appl. Catal., A* **2006**, *315*, 1–17.

(386) Goerke, O.; Pfeifer, P.; Schubert, K. Water gas shift reaction and selective oxidation of CO in microreactors. *Appl. Catal., A* **2004**, *263*, 11–18.

(387) Klemm, E.; Döring, H.; Geisselmann, A.; Schirrmeister, S. Microstructured Reactors in Heterogenous Catalysis. *Chem. Eng. Technol.* **2007**, *30*, 1615–1621.

(388) Franz, A. J.; Ajmera, S. K.; Firebaugh, S. L.; Jensen, K. F.; Schmidt, M. A. Expansion of Microreactor Capabilites through Improved Thermal Management and Catalyst Deposition. In *Microreaction Technology: Industrial Prospects, IMRET 3: Proceedings of the Third International Conference on Microreaction Technology*, Frankfurt a. M., Germany, 18th Apr. 1999–21st Apr. 1999; Ehrfeld, W., Ed.; Springer: Berlin, 2000; pp 197–206.

(389) Walter, S.; Joannet, E.; Schiel, M.; Boullet, I.; Philipps, R.; Liauw, M. A. Microchannel Reactor for the Partial Oxidation of Isoprene. In *Microreaction Technology, IMRET 5: Proceedings of the Fifth International Conference on Microreaction Technology*, Strasbourg, France, 27th May 2001–30th May 2001; Matlosz, M., Ehrfeld, W., Baselt, J. P., Eds.; Springer: Berlin, 2001; pp 387–396.

(390) Bond, G. C.; Louis, C.; Thompson, D. T. *Catalysis by Gold*; Catalytic Science Series, Vol. 6; Imperial College Press: London, 2006.

(391) Ehrfeld, W.; Löwe, H.; Hessel, V.; Richter, T. Anwendungspotentiale für chemische und biologische Mikroreaktoren. *Chem. Ing. Tech.* **1997**, *69*, 931–934.

(392) Xhanari, K.; Finšgar, M. Organic corrosion inhibitors for aluminium and its alloys in acid solutions: a review. *RSC Adv.* **2016**, *6*, 62833–62857.

(393) Monticelli, C.; Brunoro, G.; Frignani, A.; Zucchi, F. Surface-active substances as inhibitors of localized corrosion of the aluminium alloy AA 6351. *Corros. Sci.* **1991**, *32*, 693–705.

(394) Zhao, T.; Mu, G. The adsorption and corrosion inhibition of anion surfactants on aluminium surface in hydrochloric acid. *Corros. Sci.* **1999**, *41*, 1937–1944.

(395) Taha, A. A.; Ahmed, A. M.; Rahman, H. H. A.; Abouzeid, F. M. The effect of surfactants on the electropolishing behavior of copper in orthophosphoric acid. *Appl. Surf. Sci.* **2013**, *277*, 155–166.

(396) Bommersbach, P.; Alemany-Dumont, C.; Millet, J.-P.; Normand, B. Hydrodynamic effect on the behaviour of a corrosion inhibitor film: characterization by electrochemical impedance spectroscopy. *Electrochim. Acta* **2006**, *51*, 4011–4018.

(397) Mahmud, T.; Haque, J. N.; Roberts, K. J.; Rhodes, D.; Wilkinson, D. Measurements and modelling of free-surface turbulent flows induced by a magnetic stirrer in an unbaffled stirred tank reactor. *Chem. Eng. Sci.* **2009**, *64*, 4197–4209.

(398) Lamarque, N.; Zoppé, B.; Lebaigue, O.; Dolias, Y.; Bertrand, M.; Ducros, F. Large-eddy simulation of the turbulent free-surface flow in an unbaffled stirred tank reactor. *Chem. Eng. Sci.* **2010**, *65*, 4307–4322.

(399) Velusamy, K.; Garg, V. K.; Vaidyanathan, G. Fully developed flow and heat transfer in semi-elliptical ducts. *Int. J. Heat Fluid Flow* **1995**, *16*, 145–152.

(400) Raffelstetter, P. Multiple Length-Scale Modeling of Through-Mask Electrochemical Micromachining of Complex PCBs. PhD Thesis, Universität Wien, 2010.

(401) Allen, D. M. *Photochemical Machining and Photoelectroforming*, ISBN 978-1-5262-0188-1, 2016.

(402) Walker, P.; Tarn, W. H. *CRC Handbook of Metal Etchants*; CRC Press: Boca Raton, FL, 1991; pp 80–113.

(403) Williams, K. R.; Gupta, K.; Wasilik, M. Etch Rates for Micromachining Processing—Part II. *J. Microelectromech. Syst.* **2003**, *12*, 761–778.

(404) MicroChemicals. General Properties of AZ/TI Photoresists. https://www.microchemicals.com/technical_information/photoresist_properties.pdf (accessed 22nd May 2018).

(405) Rao, P. N.; Kunzru, D. Fabrication of microchannels on stainless steel by wet chemical etching. *J. Micromech. Microeng.* **2007**, *17*, N99–N106.

(406) Sun, L.; Liang, J.; Liu, C.; Cao, Y.; Chen, L.; Liu, J. Effects of the initial stencil width on stainless steel wet chemical etching: combined model and experimental investigations. *J. Micromech. Microeng.* **2009**, *19*, 085023.

(407) Gabe, D. R. Anodic Polarization During Electrobrightening and Electropolishing of Aluminium. *Trans. Inst. Met. Finish.* **1973**, *51*, 32–38.

(408) Chatterjee, B. Chemical brightening of aluminium. *Mater. Chem. Phys.* **1984**, *10*, 357–364.

(409) Chin, D.-T.; Tsang, C.-H. Mass transfer to an impinging jet electrode. *J. Electrochem. Soc.* **1978**, *125*, 1461–1470.

(410) Chatterjee, S.; Ujihara, M.; Lee, D. G.; Chen, J.; Lei, S.; Carman, G. P. Spray etching 2 μm features in 304 stainless steel. *J. Micromech. Microeng.* **2006**, *16*, 2585–2592.

(411) Penniall, C. Fischer-Tropsch Based Biomass to Liquid Fuel Plants in the New Zealand Wood Processing Industry Based on Microchannel Reactor Technology. PhD Thesis, University of Canterbury, 2013.

(412) Wunsch, R.; Fichtner, M.; Görke, O.; Haas-Santo, K.; Schubert, K. Process of Applying Al_2O_3 Coatings in Microchannels of Completely Manufactured Microstructured Reactors. *Chem. Eng. Technol.* **2002**, *25*, 700–703.

(413) Gao, Q.; Lizarazo-Adarme, J.; Paul, B. K.; Haapala, K. R. An economic and environmental assessment model for microchannel device manufacturing: part 1 — Methodology. *J. Cleaner Prod.* **2016**, *120*, 135–145.

(414) Gao, Q.; Lizarazo-Adarme, J.; Paul, B. K.; Haapala, K. R. An economic and environmental assessment model for microchannel device manufacturing: part 2 — Application. *J. Cleaner Prod.* **2016**, *120*, 146–156.

(415) King, F.; Bailey, M. G.; Clarke, C. F.; Ikeda, B. M.; Litke, C. D.; Ryan, S. R. *A high-temperature, high-pressure, silver-silver chloride reference electrode*; Atomic Energy of Canada Ltd. Report AECL-9890; Pinawa, Canada: Whiteshell Nuclear Research Establishment, 1989.

(416) Bates, R. G.; Bower, V. E. Standard Potential of the Silver-Silver-Chloride Electrode from 0° to 95°C and the Thermodynamic Properties of Dilute Hydrochloric Acid Solutions. *J. Res. Natl. Bur. Stand. (US)* **1954**, *53*, 283–290.

(417) Greeley, R. S.; Smith Jr, W. T.; Stoughton, R. W.; Lietzke, M. H. Electromotive force studies in aqueous solutions at elevated temperatures. I. The standard potential of the silver-silver chloride electrode. *J. Phys. Chem.* **1960**, *64*, 652–657.

(418) Hamer, W. J.; Wu, Y.-C. Osmotic Coefficients and Mean Activity Coefficients of Uni-univalent Electrolytes in Water at 25°C. *J. Phys. Chem. Ref. Data* **1972**, *1*, 1047–1100.

(419) Dinan, T. E.; Matlosz, M.; Landolt, D. Experimental Investigation of the Current Distribution on a Recessed Rotating Disk Electrode. *J. Electrochem. Soc.* **1991**, *138*, 2947–2951.

(420) Rand, D. A. J.; Woods, R. The nature of adsorbed oxygen on rhodium, palladium and gold electrodes. *J. Electroanal. Chem. Interfacial Electrochem.* **1971**, *31*, 29–38.

(421) Darling, H. E. Conductivity of Sulfuric Acid Solutions. *J. Chem. Eng. Data* **1964**, *9*, 421–426.

(422) *Landolt-Börnstein: Zahlenwerte und Funktionen aus Physik, Chemie, Astronomie, Geophysik und Technik*, 6th ed.; Borchers, H., Hausen, H., Hellwege, K.-H., Schäfer, K., Schmidt, E., Eds.; Springer: Berlin, 1969; Vol. II 5a, p 310.

(423) Tobias, R. F.; Nobe, K. Electrochemical Behavior of Rotating Iron Disks: Effect of Fe(III). *J. Electrochem. Soc.* **1975**, *122*, 65–70.

(424) Angell, D. H.; Dickinson, T. The kinetics of the ferrous/ferric and ferro/ferricyanide reactions at platinum and gold electrodes: Part I. Kinetics at bare-metal surfaces. *J. Electroanal. Chem. Interfacial Electrochem.* **1972**, *35*, 55–72.

(425) Benari, M. D.; Hefter, G. T. Electrochemical characteristics of the iron(III)/iron(II) system in dimethylsulphoxide solutions. *Electrochim. Acta* **1991**, *36*, 471–477.

(426) Morrison, B.; Striebel, K.; Ross Jr, P. N.; Andricacos, P. C. Kinetic studies using a rotating cylinder electrode: Part I. Electron transfer rates in ferrous/ferric sulfate on platinum. *J. Electroanal. Chem. Interfacial Electrochem.* **1986**, *215*, 151–160.